Grain sorting processes in bed load transport : A theoretical and experimental study for gravel bed rivers

Costanza Carbonari

Communauté
UNIVERSITÉ Grenoble Alpes

UNIVERSITÀ
DEGLI STUDI
FIRENZE
DICEA
DIPARTIMENTO
DI INGEGNERIA CIVILE
E AMBIENTALE

THÈSE

Pour obtenir le grade de

DOCTEUR DE LA COMMUNAUTE UNIVERSITE GRENOBLE ALPES

DOTTORE DI RICERCA CIVIL AND ENVIRONMENTAL ENGINEERING

préparée dans le cadre d'une cotutelle *entre la Communauté Université Grenoble Alpes* et l'Università di Firenze

Spécialité : **Science de la Terre et Univers, Environnement**
Arrêté ministériel du 25 mai 2016

Présentée par

Costanza CARBONARI

Thèse dirigée par **Alain RECKING** et **Luca SOLARI**

préparée au sein de **Irstea Grenoble: Equipe ETNA: Erosion Torrentielle, Neige et Avalanches**
et **Dipartimento Ingegneria Civile e Ambientale Firenze**

dans les Écoles Doctorales **Terre Univers Environnement**
et **International Doctoral School in Civil and Environmental Engineering**

Processus de tri granulométrique dans le transport par charriage : une étude théorique et expérimentale pour les rivières à gravier

Thèse soutenue publiquement le 03 mai 2019,
devant le jury composé de :
M. Enio PARIS
Professeur Université de Florence, Président du jury
M. Günter BLÖSCHL
Professeur Université de Vienne, Membre du jury
M. Philippe FREY
Directeur de Recherche, Irstea Centre de Grenoble, Membre du jury M.
Renato MORBIDELLI
Maître de Conférence Université de Pérouse, Membre du jury
M. Alain RECKING
Directeur de Recherche, Irstea Centre de Grenoble, Directeur
M. Luca SOLARI
Maître de Conférence Université de Florence, Directeur

Résumé

Expériences de terrain et de laboratoire montrent que les rivières à gravier avec étendue granulométrique élevée et faible contrainte latérale, comme dans le cas des rivières à chenaux multiples, notamment les rivières en tresses, et des rivières à chenal unique avec une pleine mobilité latérale, comme les rivières à méandres, peuvent présenter simultanément variations du chenal actif à la fois dans le plan et dans la direction verticale, ainsi qu'un tri granulométrique planimétrique et vertical. En fait, les ajustements du chenal présentent une interaction complexe avec les processus de tri granulométrique: processus de transport et dépôt des mélanges de sédiments hétérogènes engendrent la formations de plusieurs motifs de tri, parmi lesquels patches qui migrent dans le chenal, notamment les sorting waves également connues sous le nom de bedload sheets. Ces sorting waves sont observées comme l'alternance des bandes de sédiments grossiers et fins dans la direction d'écoulement.

Cette thèse de doctorat étudie les processus de tri granulométrique d'une distribution granulométrique bimodale à la fois dans la direction latérale et verticale avec un accent particulier sur l'étude des bedload sheets. Ce projet vise également à étudier les effets du confinement latéral sur la morphodynamique du lit de la rivière et en particulier sur les processus de tri granulométrique; et en plus, vu que le tri granulométrique joue un rôle crucial en influant sur le profil en long de la rivière, ainsi que les motifs sédimentaires et le formes du lit, étant donné le lien étroit entre la topographie du lit et la composition sédimentaire du lit, nous voudrions apporter des simples analyses théoriques et outils capables de décrire les variations morphodynamiques du lit dues au tri granulométrique.

Différentes méthodologies ont étés appliquées pour attendre cet objectif avec succès. D'abord, a été faite une étude approfondie de l'état de l'art sur la morphodynamique des sédiments hétérogènes, les processus de tri granulométrique, les motifs de tri et les bedload sheets. Ensuite, une analyse de stabilité linaire 1D traite le problème de la formation des sorting waves en examinant la stabilité d'un écoulement en eau peu profonde sur lit mobile et érodable composé d'un mélange sédimentaire bimodale. Les résultats sont présentés en illustrant les survenant instabilités dominées par le tri granulométrique. Bien que le shallow-water framework monodimensionnel, le simple model d'écoulement adopté permet la formulation d'un problème aux valeurs propres algébrique qui peut être résolu analytiquement en permettant un aperçu approfondi sur les mécanismes qui entrainent les instabilités. Ensuite, des expériences de laboratoire en canal à échelle réduite ont été réalisées en reproduisant trois configurations qui diffèrent en contrainte latérale ; un mélange bimodale de sédiments naturels a été utilisé. Les trois configurations d'écoulement montrent des importantes fluctuations des paramètres caractérisant le lit en termes de composition sédimentaire, pente, largeur du chenal actif et taux de transport des sédiments. L'analyse de ces paramètres permet de définir des feedbacks entre les variables morphologiques. Les résultats de cette étude éclairent le rôle de la contrainte latérale sur les processus de tri granulométrique et la morphodynamique du lit nu des rivières.

Abstract

Field and laboratory investigations indicate that gravel bed rivers with poorly-sorted grain size distribution and low lateral confinement, such as in the case of multi-thread, braided and transitional rivers but also wandering single-thread rivers, can simultaneously present active channel variations, both in the planimetric and altimetric directions, together with planimetric and vertical sorting. Actually channel adjustments present a complex interaction with sorting processes: transport and depositional processes of heterogeneous sediment mixtures induce the formation of various sorting patterns, among which free migrating patches such as sorting waves also known as bedload sheets. Such sorting waves are mainly observed by the alternation of bands of finer and coarser material in the streamwise direction.

This PhD research investigates the sorting processes of a bimodal grain size distribution both in the lateral and in the vertical direction, with particular focus on the study of bedload sheets. This work also aims at investigating the effects of lateral confinement on river bed morphodynamics and in particular on grain sorting processes; and besides, given that grain sorting plays a crucial role in affecting longitudinal river profile, as well as sediment patterns and bed forms, being indeed the connection between bed topography and bed sediment composition close, we would like to provide simple theoretical analyses and tools able to predict morphodynamic bed river variations driven by sorting.

Different methodologies are applied to successfully achieve this purpose. Firstly, a deep investigation of the state of knowledge of mixed-size sediment morphodynamics, sorting processes, sorted sediment patterns and bedload sheets is carried out. Then, a 1D linear stability analysis addresses the problem of sorting waves' formation by investigating the stability of a uniform shallow-water flow above an erodible bed composed by a bimodal sediment mixture. Results are presented by illustrating the arising instabilities dominated by sorting. Although the monodimensional shallow-water framework, the simple flow model adopted allows for the formulation of an algebraic eigenvalue problem that can be solved analytically, allowing for a deep insight into the mechanisms that drive instabilities. Then, small scale flume experiments are carried out by reproducing three different flow confinement configurations and involving a bimodal mixture of natural sediments. All the configurations show large fluctuations of parameters characterising bed system in terms of bed sediment composition, slope, active channel width and sediment transport rate. The analysis of such parameters allows defining feedbacks among morphological variables. Results of such investigations shed light on the role of lateral confinement on sorting processes and morphodynamics of barebed rivers.

Acknowledgements

The present PhD research has been conducted thanks to a PhD scholarship given by the University of Florence (Italy) which is greatly acknowledged. I would like to express my special gratitude to Dr. Eng. Alain Recking and Prof. Dr. Eng. Luca Solari for allowing me to conduct the PhD study under their supervision in the National Research Institute of Science and Technology for Environment and Agriculture (Irstea), Grenoble, France and in the Department of Civil and Environmental Engineering, Florence (Italy) and for encouraging my research with their valuable suggestions. A special thank to Prof. Dr. Eng. Marco Colombini (Departement of Civil, Chemical and Environmental Engineering, University of Genoa) for his teachings, support, and unmatched availability. I am very grateful to Frédéric Ousset, Christian Eymond-Gris, and Eng. Hervé Bellot for their technical support in implementing the experimental setup at the Irstea Hydraulic Laboratory. The help with the experiments provided by my trainee Eng. Francesco Tanganelli is acknowledged. I thank Prof. Dr. Eng. Enio Paris, Prof. Dr. Philippe Frey, Dr. Eng. Didier Richard, Dr. Mélanie Bertrand, and Dr. Eng. Caroline Le Bouteiller for the profitable exchanges about my research activity. And a special thank to my friend and colleague Dr. Eng. Giulio Calvani with whom I shared passionate interest in our research field and many activities and experience for the whole duration of the PhD program.

Contents

Abstract iii

1 Introduction 1

2 Current state of knowledge and modelling 5
2.1 Gravel bed rivers . . . 5
2.2 Sediment heterogeneity and selective transport . . . 7
2.3 Bed patches . . . 13
2.3.1 Bedload sheets . . . 17
2.4 Recent advances in flume experiments and mathematical models on sediment sorting . . . 21
2.4.1 Mathematical models . . . 21
2.4.2 Flume experiments . . . 24
2.5 Thesis objectives and methodology . . . 32

3 Bedload transport of a sediment mixture: 1d linear stability analysis 35
3.1 An introduction to linear stability analysis in the context of river morphodynamics . . . 36
3.2 The flow equations . . . 41
3.3 The hydrodynamic instability . . . 46
3.3.1 The inviscid approximation . . . 47
3.3.2 The Saint-Venant equations . . . 47
3.3.3 The effect of dispersive stress . . . 48
3.3.4 The effect of viscous stress . . . 50
3.3.5 The effect of the Chézy perturbation in the bed shear stress . . . 53
3.3.6 The adopted form of the flow momentum equation . . . 54
3.4 The sediment equations . . . 55
3.5 Morphodynamic instability . . . 63
3.5.1 The quasi-steady problem . . . 63
The homogeneous sediment case . . . 64
The heterogeneous sediment case . . . 66
3.6 Conclusions and perspectives . . . 75

4 Experimental study of flows over a sediment mixture 77
4.1 The experimental setup . . . 78
4.1.1 The flume . . . 79
4.1.2 The sediment mixture . . . 81
4.2 Measurements and data acquisition . . . 82
4.2.1 The surface texture measurement with image processing . . . 82
4.2.2 The slope measurement and the bed topography . . . 87
4.2.3 The outlet solid discharge measurements . . . 89
4.2.4 The hydraulic measurements: flow depth, flow width, and flow velocity with Large Scale Particle Image Velocimetry . . . 90

4.3 Experimental procedure and conditions 93
4.4 Methodology 95
4.5 Results and discussion 99
4.5.1 Run 1 99
4.5.2 Run 2 103
4.5.3 Run 3 107
4.5.4 Runs' comparison 113
4.6 Conclusions and perspectives 123

5 Conclusions **125**

A Areal fraction content techniques for surface texture measurements **127**

B Color detection operations **131**

Bibliography **135**

List of Figures

1.1 Sandur river near Vatnajökull glacier, Iceland. Photo courtesy M. Rusnák. . . . 2
1.2 River Urslau in Austria. Photo courtesy D. Henner. . . . 2
1.3 River Tagliamento in north-east Italy. . . . 3

2.1 A reach of the Guadalfeo River: an example of coarse patches. . . . 7
2.2 Hypothetical GSD for the definition of different sediment mobility conditions for heterogeneous mixtures. . . . 9
2.3 Conceptual curves of how the ratio p_i/f_i varies with grain size for different mobility conditions. . . . 10
2.4 Examples of bed armoring and forced patches. . . . 12
2.5 Final bed facies map of the Tsukuba experiments illustrating patchiness in sediment supply limited condition. . . . 14
2.6 Final bed facies map of the Berkeley experiments illustrating patchiness in sediment supply limited condition. . . . 15
2.7 Sand bedforms developed over an immobile gravel bed; flume experiments by Kleinhans et al. (2002). . . . 18
2.8 Sketch of bedload sheets as reported by Whiting et al. (1988); (a) side and (b) plan view. . . . 19
2.9 Continuous outlet solid discharge and mean bed slope versus time for run 7 (slope 8.65 %; mixture: 2.3 mm 50 % and 4.9 mm 50 %) by Recking et al. (2009). . . . 26
2.10 Picture from run 1 (slope 1.8 %; mixture: 2.3 mm 50 % and 9 mm 50 %) by Recking et al. (2009). a) Smoothed bed; b) transitional bed; c) congested bed. From a) to c) the solid discharge is decreasing; actually the "blurriness" in a) is due to the huge amount of sefiments moving. . 26
2.11 Correlation between bedload sheet production, local bed topography changes, and Qs changes in run 7 (slope 8.65 %; mixture: 2.3 mm 50 % and 4.9 mm 50 %) by Recking et al. (2009). Fluctuations of the mean bed slope and of the total and fractional transport rates. . . . 27
2.12 The two bed states periodically observed by Leduc (2013). Left panel: smooth state with intense transport rate, well defined channel and bars pattern. Right panel: congested state with a wider main channel. . 30

3.1 Stability plot resulting from the linear stability analysis for dune and antidune formation by Colombini (2004). . . . 40
3.2 Sketch of a longitudinal profile of the flow configuration. . . . 41
3.3 The growth rate and the wave speed of the hydrodynamic eigenvalues in the case in which the viscous term is included. . . . 51
3.4 The growth rate and the wave speed of the hydrodynamic eigenvalues in the case in which the viscous term is neglected. . . . 52

3.5 The growth rate of the fast eigenvalue for the hydrodynamic problem; including and neglecting the viscous term. 52
3.6 The celerity and the growth rate of the bed eigenvalue for the morphodynamic problem under quasi-steady hypothesis, unisize sediment case. 65
3.7 The celerity and the growth rate of the bed eigenvalue for the morphodynamic problem under quasi-steady hypothesis, two-grain mixture case. 67
3.8 The celerity and the growth rate of the sorting eigenvalue for the morphodynamic problem under quasi-steady hypothesis, two-grain mixture case. 67
3.9 Stability plot of the sorting eigenvalue with varying C_0 value. 69
3.10 Unbounded and bounded region of instability depending on the C_0 value. 71
3.11 Region of instability depending on the C_0 value, when C_0 has large values. 72
3.12 The growth rate of the sorting eigenvalue, with and without viscous correction. 73
3.13 The growth rate of the sorting eigenvalue, with and without gravity correction. 73
3.14 The amplitude of the perturbations $B_1 W_{bed}$ and $B_1 W_{sort}$ when R_1 is set equal to 1. 74

4.1 The flume. A view from downstream to upstream and a scheme. . . . 80
4.2 The bimodal sediment mixture, left panel; the coarse and fine fractions separated, right panel. 81
4.3 The granulometric curve of the fine fraction (red), the coarse fraction (black), the mixture (green). 82
4.4 Digital Numbers' histograms for fine grains and coarse grains for each RGB channel. 84
4.5 An example of fractions' separation from Run 3. 84
4.6 An example of fractions' separation and patch detection from Run 1. . 85
4.7 The probability mass function of DNs for each of the three runs. The run specific threshold value is superimposed on the respective PMF. . 86
4.8 A picture of Run 1. The top figure is a the orthorectified image of the analyzed area of the flume bed. The bottom figure is the Digital Elevation Model classified using QGIS. 89
4.9 The three runs configurations. Left figure: Run 1, flume width 0.5 m. Central figure: Run 2, flume width 0.25 m. Right figure: Run 3, flume width 0.12 m. 91
4.10 Velocity measurement using Fudaa-LSPIV in Run 2. 93
4.11 Active channel width and bed surface covered by fine grains. 96
4.12 The signal % Fine and the signal % Area Fine 98
4.13 The three runs compared through demonstrative pictures aiming at illustrate the different "patchiness" of the three different configurations. 98
4.14 A photo sequence of pictures with $\Delta t = 1$ minute showing the rapid rearrangement of surface sediments during Run 1. 100
4.15 Run 1. The outlet solid discharge as a measure of the bedload transport. 100
4.16 Run 1. The slope signal and its average value (horizontal line), the latter equal to 3.26 %. 101

4.17 Run 1. The signals of the bed surface composition. 102
4.18 Run 1. Top figure: time series of the percentage of the coarse fraction of the bed surface, the fine fraction of the bed surface, and the total surface covered by patches of fines. Bottom figure: time series of the average bed slope and the outlet solid discharge. 103
4.19 Run 1. Time series of the outlet solid discharge and the total surface covered by patches of fines. 104
4.20 Run 2. The signals of the bed surface composition. 105
4.21 Run 2. The outlet solid discharge signal and the slope signal. 106
4.22 Run2. Top figure: the solid discharge and the slope signals. Bottom figure: the solid discharge and the % Fine signals. 106
4.23 Run 3. The outlet solid discharge signal and the slope signal. 107
4.24 Run 3. The signals of the bed surface composition. 108
4.25 Run3. Top figure: the solid discharge and the slope signals. Central figure: the slope and the % Coarse signals. Bottom figure: the solid discharge and the % Fine signals. 109
4.26 Run3. Photos of bedload sheets. 110
4.27 Run 3. Top views of bedload sheets; trains of bedload sheets, bed coarsening, bed fining. 111
4.28 The linear stability analysis for sorting waves applied to Run 3. 113
4.29 All runs. The signal % Coarse. 115
4.30 All runs. Box plots of the signal % Coarse. 115
4.31 All runs. The slope signal. 116
4.32 All runs. Box plots of the slope signal. 116
4.33 All runs. The signal of the outlet solid discharge. 117
4.34 All runs. Box plots of the signal of the outlet solid discharge. 118
4.35 All runs. The coefficient of variation for the signals % Coarse, slope and outlet solid discharge. 119
4.36 Main results of the linear stability analysis for bars formation performed for Run 2. The plots are obtained using the TREMTO tool. . . . 121
4.37 Main results of the linear stability analysis for bars formation performed for Run 3. The plots are obtained using the TREMTO tool. . . . 122

A.1 Digital Numbers' histograms of the two fractions in the blue channel. A threshold value is set on DNs. 129

B.1 A photo taken from the Run 1 configuration. Top figure: the original RGB photo in which coarse grains are white (light gray) and fine grains are orange. Central figure: the blue channel is a gray-scale image on which we performed thresholding. Bottom figure: the binary image resulting from the thresholded gray-scale image. 132
B.2 A photo taken during Run 1. (a) The original RGB photo; coarse grains are white (light gray) and fines are orange. (b) The binary image resulting from the thresholding; coarse grains are black and fines are white (reversed with respect to figure B.2). (c) The delimitation of the detected zone of fines. 133

List of Tables

3.1 The function $\Phi(\zeta)$ and the corresponding value of the critical Shields stress for several empirical relation. 58

4.1 Grain size characteristics of the bimodal mixture and of the single fractions. 81
4.2 Diameters and passing percentages values resulting from the sieving. These values are graphically represented in the granulometric curves. 81
4.3 Thresholds and error quantification for the operation of sediment fractions' separation. 87
4.4 Runs' characterization; what distinguish one run from another. 95
4.5 The parameters relevant for stability analysis with the measured values of Run 3. 112
4.6 All runs. Descriptive statistics for the signal % Coarse. 114
4.7 All runs. Descriptive statistics for the slope signal. 116
4.8 All runs. Descriptive statistics for the signal of the outlet solid discharge. 117

List of Symbols

b	exponent controlling the hiding effect in the formula of bedload transport	[-]
B	bed elevation	[-]
C	Chézy coefficient	[-]
d	grain size	[-]
d^*	dimensional grain size	m
d_g^*	dimensional median diameter	m
d_σ^*	dimensional diameter of a typical coarse grain	m
d_x	diameter for which x% of sample is finer than d_x	mm
D	water depth	[-]
D^*	dimensional water depth	m
F	mass density for the grain size ϕ in the active layer	[-]
F_a	mass density for the grain size ϕ_a in the active layer	[-]
F_b	mass density for the grain size ϕ_b in the active layer	[-]
Fr	Froude number	[-]
g	gravitational acceleration	$\mathrm{m\,s^{-2}}$
G	generic quantity of the governing equations	[-]
G_0	base state of the generic quantity of the governing equations	[-]
G_1	perturbation's amplitude of the generic quantity of the governing equations	[-]
i	imaginary unit	[-]
$Im(W)$	imaginary part of the eigenvalue	[-]
k	Von Karman constant	[-]
k_x	longitudinal wave number	[-]
k_y	transverse wave number	[-]
K	wave number for the 1D model	[-]
l	mixing length	[-]
L_a	active layer thickness	[-]
L_x^*	dimensional wave length in the streamwise direction	[-]
L_y^*	dimensional wave length in the spanwise direction	[-]
$\mathcal{O}(\varepsilon^0)$	equation's terms proportional to the zero power of ε	[-]
$\mathcal{O}(\varepsilon)$	equation's terms proportional to the first power of ε	[-]
p_s	sediment porosity	[-]
q_s	volumetric sediment discharge per unit width	[-]
q_u	transport density per unit content	[-]
r	bed roughness	[-]
R	roughness height	[-]
Re	Reynolds number	[-]
$Re(W)$	real part of the eigenvalue	[-]
Re_p	particle Reynolds number	[-]
s	relative density of the sediment	[-]
S	bed slope	[-]

T_d	dispersive stress	[-]
T_n	depth-averaged normal Reynolds stress	[-]
T_t	bed shear stress	[-]
u	flow velocity	[-]
u^*	dimensional flow velocity	$\mathrm{m\,s^{-1}}$
u_f^*	dimensional friction velocity	$\mathrm{m\,s^{-1}}$
W	complex wave speed (the eigenvalue)	[-]
β	width-to-depth ratio	[-]
γ	small parameter representing the ratio between the characteristic time scale of the flow discharge and of the flux of sediment	[-]
ε	small parameter	[-]
ζ	dummy parameter of the function Φ	[-]
μ	Fredsøe constant	[-]
ν_t	eddy viscosity	[-]
θ	Shields stress	[-]
θ_c	critical Shields stress	[-]
ρ	water density	$\mathrm{kg\,m^{-3}}$
σ_m	standard deviation of the F distribution	[-]
ϕ	grain size according to the sedimentological ϕ scale	[-]
ϕ_a	grain size of the finest fraction of the bimodal mixture	[-]
ϕ_b	grain size of the coarsest fraction of the bimodal mixture	[-]
ϕ_m	mean grain size of the F distribution	[-]
Φ	function depending on the empirical relation of bedload transport	[-]
ω	bed forms' migration celerity	[-]
Ω	bed forms' growth rate	[-]

1 Introduction

Rivers in mountain regions represent a fundamental resource as they provide water and energy for human settlement and they are an invaluable ecosystem. However mountain regions, as for instance Alpine areas, experienced an intense socio-economic development which resulted in an appreciable aggregation of settlements and infrastructure facilities (Wohl, 2006), whilst safe regions suitable for development are relatively sparse in mountain regions, and thus those assets are increasingly exposed to natural hazards arising from the unsteady character of rivers (Church and Ferguson, 2015). Hence a better understanding of river dynamics is a crucial issue in order to improve river management with its task of facing natural hazard and protecting endangered areas through mitigation measures, designing hydraulic structures and infrastructures facilities close to rivers, and preserving riverine ecological systems (Wohl, 2006).

In mountain regions rivers flow over coarse alluvial substrata, thereby they are classified as gravel bed rivers (Church, 2010). In this kind of streams the flow and the channel morphology have a complex mutual interaction through mechanisms governed by sediment transport (Church, 2006). Indeed gravel bed rivers have this peculiar feature: they are alluvial systems formed in sediments they have transported and deposited. This means that gravel bed rivers are self-formed channels: their morphology is a direct consequence of bedload transport (Pitlick et al., 2013).

Another peculiar feature of gravel bed rivers is their grain size distribution typically characterized by poorly-sorted sediments. These different size fractions of sediments differently interact with flow: during bedload transport, heterogeneous sediments typically undergo the process of sorting so that the grain size distribution of river beds displays significant spatial structures.

Bed surface and subsurface heterogeneity may also be a primary control on sediment transport rates, and because bed material exerts a strong control on the near bed hydraulic environment, patches may have important implications for aquatic ecology. Moreover sediment segregation patterns in gravel bed rivers can also have complex feedbacks with both slope and channel width adjustments, as it is the case of low laterally confined flows. Examples of this kind of streams are reported in figure 1.1 representing a multi-thread river in a rather large alluvial plane, and figure 1.2 representing a single-thread river in a mountain valley.

It is therefore clear that a proper understanding of the complex dynamics of gravel bed rivers is essential for river management, given that anthropic activities and interventions are numerous in the river buffer area where the hydraulic, geomorphologic, and ecologic effects of the river are relevant. Indeed the cases of natural river reaches are nowadays few in our European regions, and we like to show an exception in 1.3, the Tagliamento river in north-east Italy, a braided river which flows from the Alps to the Adriatic Sea and which is pristine in almost its length.

Indeed what are the the effects of lateral confinement on river bed morphodynamics and in particular on grain sorting processes?

FIGURE 1.1: Sandur river near Vatnajökull glacier, Iceland. Photo courtesy M. Rusnák.

FIGURE 1.2: River Urslau in Austria. Photo courtesy D. Henner.

FIGURE 1.3: River Tagliamento in north-east Italy. A wide area of the river basin is sparsely populated and settlements and infrastructure facilities are few, whereby the river flows in rather natural and unconfined conditions resulting in spectacular anabranches.

And in particular what are these effects in presence of drastic reductions of the river bed's width? Indeed when dealing with the morphodynamics of low confined rivers for which a key point is the lateral mobility of the main channel, it is, unfortunately, rather common to witness anthropic interventions reducing the lateral space naturally pertinent to rivers.

And in case of widening, as commonly undertaken by river restoration operations?

Although design strategies adopted in river restoration and flood protection increasingly reflect the view that an increase in river width is needed to improve bed morphological complexity and ecological quality (e.g. Rohde et al., 2004; Rohde et al., 2005), few studies provide detailed quantitative information on the effect of different width constraints on river bed topography, and these few studies do not take into account sediment heterogeneity (Garcia Lugo et al., 2015).

Fluvial geomorphologists have long explored the relationship between river planform style and external controlling parameters and this topic continues to be debated. However, the focus of this mainly empirical, field-based, research is usually the natural state of a river rather than its state when constrained by embankments, other engineering structures, or by natural inerodible valley walls. Other studies have considered the effect of different widths on alternate and multiple bar formation (Fujita, 1989) or on braided river sediment transport (Marti and Bezzola, 2006), but a detailed investigation on the morphological changes induced by lateral confinement is lacking, and even scarcer when sediment sorting of heterogeneous sediments is included in the analysis.

Moreover, in such context, given that grain sorting plays a crucial role in affecting longitudinal river profile, as well as sediment patterns and bed forms, being indeed the connection between bed topography and bed sediment composition close, it is possible to provide simple theoretical analyses and tools able to predict morphodynamic bed river variations driven by sorting?

In the attempt of implementing an analytical tool for predicting morphodynamic bed river variations driven by sorting, we are aware that the analytical theories (such as those for bar formation) are based on the hypothesis that the entire channel width is actively transporting sediments (Garcia Lugo et al., 2015). Whereby their application in cases where the active width is smaller than the wetted width and even dry areas are present in the river bed (namely the cases of braiding and in general low lateral confinement illustrated above) is problematic. Hence the analytical tool we developed (dealt with in chapter 3) does not claim to overcome this limitation: it however provides a valuable contribution in theoretical analysis of sorting processes of gravel bed rivers morphodynamics.

2 Current state of knowledge and modelling

The current knowledge on the understanding of bedload dynamics and river morphodynamics with heterogeneous sediments is reviewed and analyzed in this chapter. The focus is on the main mechanisms of the bedload transport of heterogeneous sediment mixture and on the formation of sorting patterns, morphodynamic changes, and bedload transport rates fluctuations; no less, we bring to focus experimental investigations on such issues as well as mathematical modelling for prediction of mixed sediment morphodynamics. First we describe the context of gravel bed rivers in section 2.1. The key elements of bedload transport of heterogeneous sediment mixtures, selective transport depending upon shear stress conditions, and examples of associated grain sorting phenomena are presented in section 2.2. Section 2.3 analyses in details a particular sorting phenomenon observed in gravel bed rivers: bed patches, among which bedload sheets, their occurrence and features are illustrated. Section 2.4 deals with both experimental investigations and mathematical modelling of mixed sediment: subsection 2.4.1 provides an overview of mathematical modelling dealing with river morphodynamics in presence of heterogeneous sediment mixtures; subsection 2.4.1 illustrates laboratory flume experiments on sorting phenomena. As a main result of the literature study, the gaps of knowledge are identified and the implications for the present research are drawn, and finally the objectives and methodology of the work are specified (section 2.5).

2.1 Gravel bed rivers

Gravel bed rivers are self-formed channels in coarse alluvial substrata; their dynamics results from the feedback between the flow and the morphology through sediment transport (Church, 2010).

Sediment transport in gravel bed rivers essentially occurs in the form of bedload, which is the transport mode more closely interacting with the bed. As a result bedload transport has a major role in shaping the channel morphology (Church, 2006); bedload is also characterized by an unsteady, intermittent nature (Gomez et al., 1989; Singh et al., 2009). Indeed the pulsating character of bedload transport in gravel bed rivers has been observed also under steady external conditions (Recking et al., 2009; Dhont, 2017), besides, bedload transport varies depending on sediment supply (Recking, 2012).

The morphology of gravel bed rivers on bed gradients in a range from 1% to 3% is characterized by bars morphology and braided morphology; however the morphology of gravel bed rivers is affected also by sediment supply (Madej et al., 2009; Venditti et al., 2012) and not only by the bed slope.

In particular an increase in sediment supply may induce the transition from single thread to braided morphology, the flow tends to be divided into a number of sub-channels around bars yielding to a braided configuration (Church, 2006) generally associated with steeper bed slopes (Madej et al., 2009). This transition from single thread to braided morphology has complex feedbacks with river bed variables such as the slope, the grain size distribution, the channel width, and the sediment supply and transport. In particular, the relation between bed forms presence and morphological changes and both sediment supply and transport is an issue still needing further investigation (Francalanci et al., 2012; Recking et al., 2016).

Hence we shortly outlined how changes in sediment supply can affect bed rivers morphology; however it is more common that gravel bed rivers accommodate changes in sediment supply through adjustments in bed surface sediment composition (Pfeiffer et al., 2017; Venditti et al., 2017). From this point of view, a key role in gravel bed rivers' morphodynamics is played by grain sorting processes. Such processes are a direct effect of sediment heterogeneity and non-equal bedload transport. Indeed gravel bed rivers are characterized by poorly-sorted sediments which are differently mobilized depending on the shear stress value. Hence, the interaction between moving and static grains, mobile and less mobile grains leads to self-organized bed (Church, 2006).

We illustrate the fact that sediment supply affects the surface composition of gravel bed rivers by choosing the example of a reduction in sediment sediment supply; precisely we will compare sand-bedded and gravel-bedded channels in limited sediment supply conditions and we will highlight that gravel-bedded rivers, because of pronounced sediment heterogeneity, have a degree of freedom that generally does not exist in sand-bedded rivers. If the supply to a sand-bedded channel is reduced, the bed will erode to compensate for the sediment flux divergence. In a gravel-bedded channel, erosion of the bed will also occur, but as the bed erodes, the bed can become coarser under selective mobility conditions reducing and stabilizing the erosion (Venditti et al., 2017).

Figure 2.1 shows an example of a gravel bed river with clear sorting patterns: evident sediments deposits characterized by different grain size distribution.

Sorting processes tend to become less and less important as equal mobility state is approached (Parker and Klingeman, 1982). This occurs during intense flow conditions such as flood events. Given that moderate flow conditions are much more common than flood events sorting processes and patterns are almost ubiquitous in gravel bed rivers, indeed such sorting patterns take place in all the channel-scale morphologies characterizing gravel bed rivers, i.e. in step-pool morphology, bars, braiding. Gravel bed rivers actually develop a distinct suite of bed features intrinsically related to sorting which are larger than individual clasts and smaller than channel-scale features (e.g. bars or step-pool features) (Venditti et al., 2017). These bed features include (i) gravel dunes (e.g. Carling, 1999), (ii) mobile, migrating patches typically referred to as bedload sheets (e.g. Whiting et al., 1988; Recking et al., 2009), (iii) sand bedforms developed over an otherwise immobile gravel bed (sand ribbons, barchans and dunes; e.g. Kleinhans et al., 2002), (iv) pebble clusters (e.g. Brayshaw, 1985), (v) stone lines (Laronne and Carson, 1976) or transverse ribs (e.g. Allen, 1984), and (vi) reticulate stone cells (e.g. Hassan and Church, 2000).

Given these examples of bed features intrinsically related to sorting, in section 2.2 we move to the explanation of the mechanisms of sediment sorting processes, their origin lying in non-equal mobility of different sediment size fractions. Then, in

FIGURE 2.1: A reach of the Guadalfeo River in the Sierra Nevada, Spain; photo courtesy M. Burguet. In the foreground a deposit of coarse pebbles deposit, fine sediments are present in the interstices and below this coarse surface. On the right side of the photo a deposit composed of boulders.

section 2.3, we provide more details about particular sediment sorting patterns: bed patches, among which bedload sheets.

2.2 Sediment heterogeneity and selective transport

Sediments in nature can seldom be considered as homogeneous, river beds indeed present different size fractions of sediments. Generally, these different size fractions differently interact with flow, since grain mobilization depends firstly on grain size, with the exception of very intense transport events during which mobility differences on a grain-by-grain basis disappear. A more detailed illustration about the conditions of equal mobility, near-equal mobility, and non-equal mobility of different grain sizes depending on stress range will be provided in a while.

Despite sediment heterogeneity, among the many simplifying assumptions usually adopted in the modeling of sediment transport, the one of well-sorted material is probably the most common. Following this approach, the dynamics of the sediment mixture is modeled as if it were composed by a single grain size, typically chosen as the median diameter of the mixture, i.e. the average particle diameter of the sample by mass or weight. If the sediment is moving as bedload, a single sediment mass conservation equation (known as the Exner equation) is then usually introduced to represent the bed dynamics. Moreover, equilibrium bedload transport is assumed, whereby sediment discharge equals the transport capacity of the flow. Once coupled

with the set of equations of a suitable flow model, Exner equation provides the simplest possible tool to study morphodynamic problems. Actually in many cases of morphodynamic modelling, usually when performing friction and transport laws, and in general bedload formulas, the definition of the critical thresholds of motion is approached through the use of a single, representative grain size to characterize the grain size distribution of bed sediment.

This assumption could be right when dealing with uniform sediment or with sand-bed rivers at high intensity of transport. But in coarse-bed streams, bed sediment is poorly sorted (Iseya and Ikeda, 1987; Church, 2006) and grain size distributions are defined by a wide range of grain sizes (gravel, cobble, sand), indeed, gravel-bed rivers present grain size distributions, hereafter GSD, much more extended with respect to sand-bed rivers' GSD .

Under these bed-state conditions, it seems unrealistic to approach the bedload transport by using a single, representative grain-size, or more precisely depending on the objective this simplification could be inappropriate. This is the case when dealing with sorting effects which are completely wiped out from an analysis with a single, representative grain-size approach.

The transport mode of sediments linked to sorting is bedload transport since it greatly interacts with the bed (more than suspended load)(Church, 2006). It influences and controls the arrangements of bed material, the morphology and the roughness of the bed, and in turn, they influence it.

Hence, during bedload transport heterogeneous sediment mixtures undergo the process of sorting so that the grain size distribution of river beds displays significant spatial structures, both in the surface texture (planimetric grain segregation) and in the stratigraphy (vertical grain segregation), giving rise to several kinds of patterns occurring at different spatial scales (river profile, reach, unit). Examples of sorting patterns in gravel bed rivers have been given in section 2.1. Other details of particular sorting patterns are provided in this section dealing with bed armoring (an example of vertical sorting) and in section 2.4 dealing with bed patches (an example of planimetric sorting). Indeed segregation of grains during processes of erosion, transport, and deposition gives rise to spatial grain-sorting phenomena such as coarse bed surface layers, downstream fining, coarser-grained riffles in straight channels, and finer-grained point bars in meandering rivers. Grain sorting also affects the longitudinal river profile, as well as the patterns and dimensions of bars, riffles, and pools. The close connection between bed topography and bed sediment composition makes sediment composition a central element in river morphology (Mosselman, 2012).

So we presented the conditions in which grain sorting occurs and we stated that sorting is inevitably wiped out if a single-size modelling is adopted. However in some cases in which sorting takes place, it can be acceptable not to model it by adopting a single-size approach. For instance this is the case in the study of bed forms, when the focus is on the instability of the bed interface as a whole and sorting is passively driven by changes in bed elevation, simply producing an accumulation of finer (coarser) material on crests (troughs) or viceversa. On the contrary, this is obviously inappropriate when the formation of the bed form itself is inherently associated with, or dominated by, the effect of sorting, the heterogeneity of the sediment being the crucial mechanism driving the instability (Livesey et al., 1998; Seminara, 1995). This is the case of the sorting waves named "bedload sheets" after Whiting et al. (1988), which appear as rhythmic alternations of finer and coarser bands of the

bed material aligned across the flow, characterized by downstream migration and negligible amplitude (Venditti et al., 2008). In subsection 2.3.1, we will illustrate in details the sorting waves named "bedload sheets".

The sorting patterns we listed here and in section 2.1 result from non-equal mobility experienced by gravel mixtures; however the terms full, partial, selective, and equal mobility are terms that do not have precise definitions, indeed universally accepted definitions have not been adopted in literature (Venditti et al., 2017).

In their work Venditti et al. (2017) report two criteria to distinguish between different mobility conditions: a common criterion based on the comparison between shear stress and critical shear stress, and a criterion by Parker (2008b) based on the shape of the GSDs of bedload, bed surface, and subsurface.

According to the first criterion, partial mobility occurs when $\theta/\theta_{c84} < 1$ (where θ and θ_{c84} are respectively the Shields stress and the critical Shields stress (i.e. the shear stress required to move a particular grain size) for the representative coarse grain diameter) because the shear stress is not competent to move the large grain sizes on the bed (Venditti et al., 2017). Increasing values of the ratio θ/θ_{c84} identify conditions of selective mobility and equal mobility; precisely selective mobility occurs when $\theta/\theta_{c84} > 1$, whereas when $\theta/\theta_{c84} > 2.1$ all grains are equally mobile.

Parker (2008b) defines different mobility conditions by comparing the hypothetical GSD of bedload, bed surface, and subsurface. Venditti et al. (2017) sum up and graphically illustrate (figure 2.2) Parker's definitions and here we report the schemes by Venditti et al. (2017).

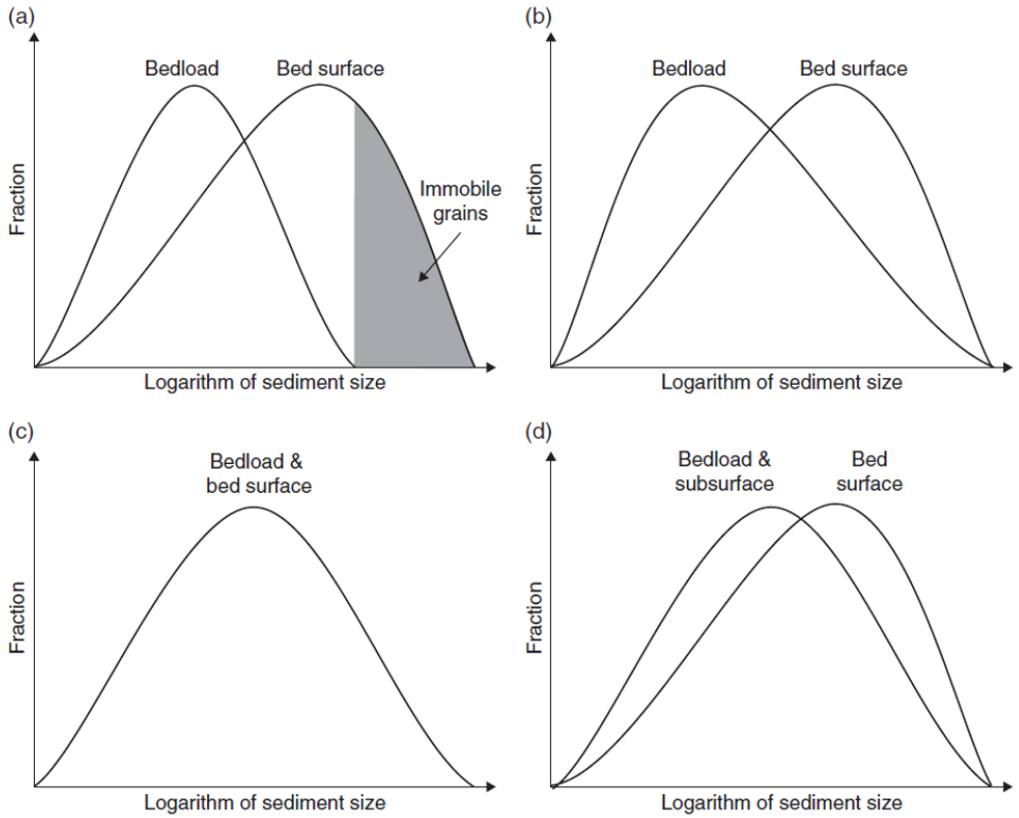

FIGURE 2.2: Illustration from Venditti et al. (2017). Hypothetical GSDs for (a) partial, (b) selective and (c) equal mobility in gravel-bed rivers based on Parker (2008b). Panel (d) depicts a special case of selective mobility where transport is equally mobile with respect to the subsurface sediment.

Partial transport occurs when the coarse tail of the bedload size distribution is finer than that of the bed surface (panel (a) figure 2.2). Selective transport occurs when all grain sizes on the bed are found in the bedload, but the bedload size distribution is finer than the bed surface (panel (b) figure 2.2). Equal mobility occurs when the size distributions of the bedload and the bed surface are the same (panel (c) figure 2.2). Equal mobility of the bedload with respect to the subsurface sediment (rather than the surface) can occur in the presence of a coarse surface layer which is a special case of selective mobility (panel (d) figure 2.2) (Venditti et al., 2017).

According to Venditti et al. (2017) the condition of partial mobility is characteristic of many gravel bed rivers during flows below bankfull, whereas such streams are characterized by selective mobility during bankfull flows. Hence equal mobility appears rare (if not the widespread use of hiding correction in sediment transport formula would not be justified). More specifically the authors identify thie equal mobility condition as the condition of equal bedload's GSD and surface's GSD: precisely the fraction of particle size i in the bedload p_i and the fraction of that size on the bed f_i are the same for all grain sizes (i.e. absence of coarse surface). Whereby the equal mobility condition is identified by $p_i/f_i = 1$, and, moreover, we can identify selective and partial mobility as well making use of the ratio p_i/f_i (figure 2.3).

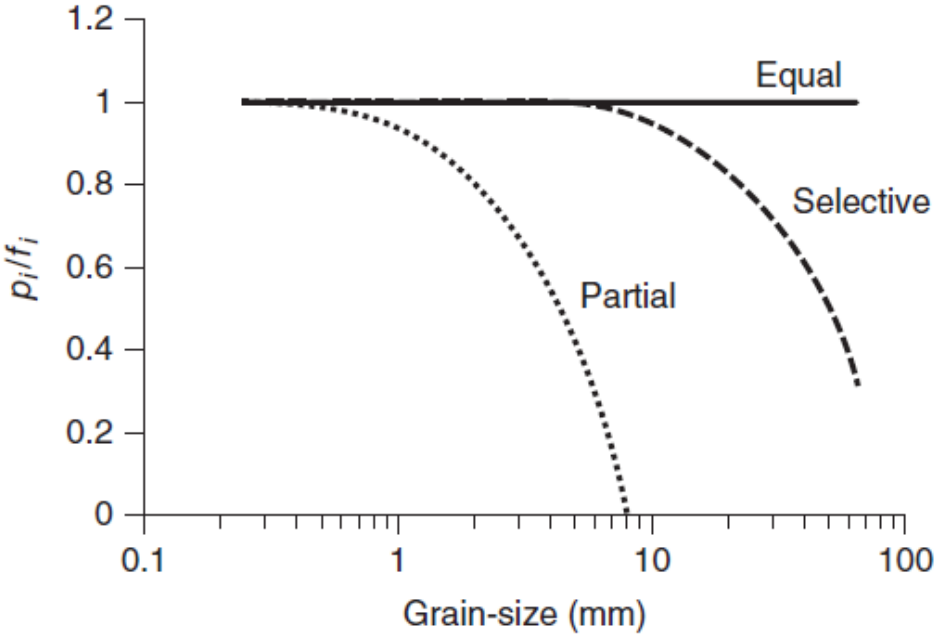

FIGURE 2.3: Illustration from Venditti et al. (2017). Conceptual curves of how the ratio p_i/f_i varies with grain size for different mobility conditions: solid line represents equal mobility, dashed line represents selective mobility, dotted line represents partial mobility.

The plot of p_i/f_i values against grain-size (figure 2.3) presents the conceptual curve for selective mobility characterised for large grain size by $0 < p_i/f_i < 1$, whereas the conceptual curve for partial mobility has in the same range of large grain size $p_i/f_i = 0$.

We recall that such analysis is hypothetical, conceptual and definitely requires detailed measurements of both the bedload and the bed surface GSDs, whereas the use of θ/θ_{c84} is an expedite method of assessing mobility conditions.

After these rigorous criteria of assessing mobility conditions, we want to focus on a clear example of sorting: fluvial armor. This can be considered the more relevant vertical sorting effect in gravel bed rivers. Bed armoring consists in a coarse surface and fine material embedded in the substrate. In addition, the surface layer is usually coarser than the mean annual load of transported gravel (Parker, 2008a).

It is worth analyzing bed armoring because it has close connections with rhythmical fluctuations of both the bed level and the bedload transport rate also under steady conditions, with the presence of longitudinal grain sorting with and without bed forms, and with selective transport by size fraction. Our objective is not the study of bed armoring, but the latter is a suitable opportunity to illustrate clearly selective transport of non-uniform sediments which is a key feature of the present work.

Bed armoring and selective transport

The current paragraph deals with armoring making the distinction between static and mobile armor. Secondly, we provide an explanation of why we are mainly interested in mobile armor. Mobile and static armor are also termed by some authors "kinetic" and "standard" armor respectively (Recking, 2013). We specify that the type of vertical sorting more closely related to the fluctuations of bed elevation and of bedload transport rate, as well as to the presence of longitudinal grain sorting with and without bed forms is kinetic sorting, in opposition to standard sorting. The term kinetic sorting (the term "kinematic sorting" was also used for describing these effects in granular flows) seems appropriate (Frey and Church, 2011) because in these experiments sorting occurred in a moving mixture (in opposition to standard sorting by "hiding exposure" effects where the coarse fraction is immobile) (Recking, 2013).

The tendency toward selective transport by size fraction and the possibility of armor formation are two of the processes interacting between each other when we deal with bedload transport of non-uniform sediments (Parker and Sutherland, 1990). Armor layer can take place as static armor or as mobile armor and the occurrence of static and mobile armor basically depends on sediment supply conditions, examples of bed armoring are shown in figure 2.4.

Static armor layers form by selective erosion as a result of the action of clear water flows corresponding to vanishing or near-vanishing sediment supply conditions, while mobile armor layers occur in the presence of an upstream sediment supply (Parker and Sutherland, 1990). A mobile-bed armor gives way to a static armor as the sediment supply tends toward zero (Parker, 2008a), so that we can state that static armor constitutes a limiting state of mobile armor, reached as sediment transport is reduced (Parker and Sutherland, 1990).

The main different effect of static versus mobile armor is that the former does not interact with the substrate, while the latter interacts with the substrate provoking changes in it. In the following is provided a short explanation of the previous statement.

When mobile armor occurs the flow and sediment transport conditions make the coarse fraction mobile. Hence, large grains can be dislodged from the bed surface. The dislodged coarse grain leaves a “hole” in the bed of comparable size. Small grains that fall into the hole may work their way below the pavement and reduce their probability of reerosion. Therefore, in this case a “vertical winnowing” process

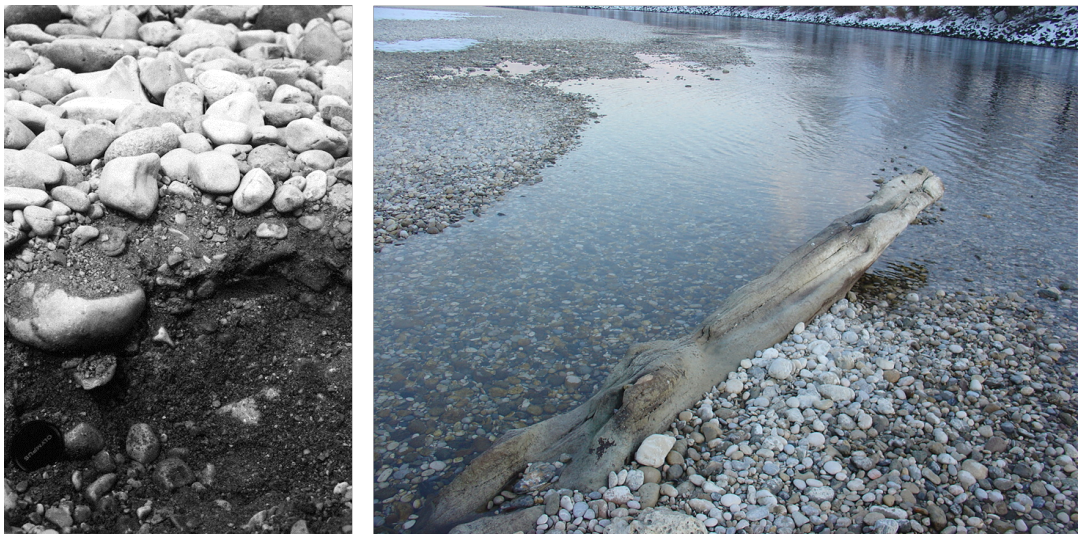

FIGURE 2.4: Examples of bed armoring. Left panel: bed sediments of the Wharfe River, U.K., showing a pronounced surface armor, photo courtesy D. Powell. Right panel: A paved reach of the Sava River, Croatia, photo courtesy D. Oskorus. Patches can also be forced by topographic control such as large woody debris (Nelson et al., 2009).

occurs (Parker and Klingeman, 1982), such a process characterizing only mobile armor is also named by some researchers "kinetic sieving" (Recking et al., 2009; Bacchi et al., 2014). To sum up only when mobile armor occurs there is an evolution of a bias in the surface layer toward coarser grains relative to the substrate (Parker and Klingeman, 1982).

We are mainly interested in mobile armor rather than in static armor, because the former is the type of vertical sorting that involves all the compartments of the bed (so it is more interesting from the point of view of morphodynamic changes) and because mobile armor is more common, more frequently observed in natural gravel-bed streams (Parker, 2008a). Static armor is typically observed in the context of degradation of poorly sorted bed sediment downstream of a dam (Vericat et al., 2006). The cessation of sediment supply drives simultaneous bed degradation and surface coarsening toward an asymptotic static state (Parker and Sutherland, 1990).

Now that a description of bed armoring has been provided we illustrate the reason why in particular mobile armor occurs.

Most gravel-bed rivers display a mobile armor (Parker, 2008a). These streams display a pavement at low flow, that is to say during typical transport events capable of moving all available sizes. During transport events characterized by bed shear stresses not far above the critical value for sporadic mobilization of pavement grains, coarser particles are intrinsically harder to move than finer particles even including hiding effects (Parker and Sutherland, 1990; Parker and Toro-Escobar, 2002). If bedload and substrate are observed to have similar grain size distributions, it follows that the coarse half of the substrate moves through the system at a rate near that of the fine half, i.e. the two halves are of near-equal mobility. This observed near-equality can only be accounted for by assuming that the stock of coarse grains available for motion at the surface is enhanced just so as to approximately counter their lower intrinsic mobility. This enhancement is realized in the form of pavement; it is achieved by a vertical winnowing process (Parker and Klingeman, 1982).

When stresses are well above critical stress [1], mobility differences on a grain-by-grain basis are reduced; the differences disappear asymptotically. Thus a coarse pavement should not form. The low-Shields stress range for which pavement is required is typical of gravel-bed streams; the high-Shields stress range where it should not occur is typical of sand-bed streams (Parker and Klingeman, 1982).

The explanation provided in this paragraph have quantitative support obtained by measurements in Oak Creek, Oregon, and data from other three field streams agree with the mechanism just described (Parker and Klingeman, 1982), while flume tests conducted by Parker and Toro-Escobar confirmed this explanation (Parker and Toro-Escobar, 2002).

We stated that armor is the response to ensure near-equal mobility during "common" flows (transport events characterized by bed shear stresses not far above the critical value for sporadic mobilization of coarser particles). We conclude the context specifying that in the case of extremely high gravel transport rates, no armor is necessary to enable the coarse half of the gravel load to move through at the same rate as the fine half (Parker, 2008a).

2.3 Bed patches

The beds of nearly all gravel bed rivers are frequently arranged into patches of distinct grain size hence sorted patterns of sediments. The term patches refer to facies of common size distributions, namely significant spatial structures of grain size distribution on the surface of channel beds.

In the classification of these facies Nelson et al. (2009) identify some patches which can be texturally stable for many years (even after considerable bedload flux) and remain in a fixed location in the channel, while other patches may migrate downstream as a distinct grain size varying pulse of sediments. The relatively stable (in space) patches appear to arise from shear stress divergences that are forced by topographic controls, such as bar morphology and flow obstructions such as large woody debris (right picture of figure 2.4).

In systems with decreasing sediment supply, spatially persistent zones of coarse sediment can emerge as a consequence of weaker topographic influences such as grain interactions and general coarsening (Lisle et al., 1993), (left picture of figure 2.4). Downstream migrating zones of distinct clustering of sediment sizes may organize into thin mappable features referred to as bedload sheets (Whiting et al., 1988; Recking et al., 2009). These features develop from interactions between coarse and fine grains (Whiting et al., 1988; Seminara et al., 1996; Recking et al., 2009). Following the terminology proposed for bar types (e.g. Seminara, 1998), Nelson et al. (2009) refer to these end-member types of patches as "forced patches" (spatially persistent associated with strong topographic controls), "fixed patches" (spatially persistent because of weak topographic influences and coarsening), and "free patches" (migrating patches, typically bedload sheets in gravel bed rivers).

Venditti et al. (2008) and Nelson et al. (2009) investigate the relationship between sediment supply and bed surface patchiness by analysing two sets of experiments, the Tsukuba experiments and the Berkeley experiments, which reproduced flows

[1] It is widespread to use the concept of "reference Shields stress" rather than that of "critical Shields stress", the former value slightly above the critical value. The reason of this choice and the formulation of the reference Shields stress can be found in Parker and Klingeman (1982).

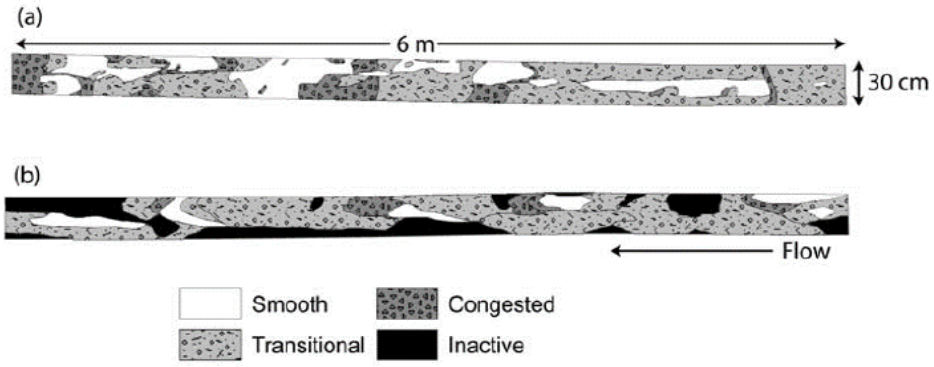

FIGURE 2.5: Illustration from Nelson et al. (2009). Bed facies map of the Tsukuba experiments at the end of the (a) 17.4 and (b) 6.1 g/min cm sediment feed runs. The terms smooth, transitional, congested, and inactive identify bed surface coarser and coarser (increasing values of d_{50}, the two extremes are smooth areas (composed of fines) and inactive areas (coarse zones with no active bedload transport). (see Iseya and Ikeda (1987) for a more detailed discussion of the terms).

over sediment mixtures in conditions of limited sediment supply. These flume experiments explore the response of bedload and bed-surface texture to reductions in sediment supply, till zero sediment feeding rate. They first reproduce conditions in which the sediment supply is nearly equivalent to the transport capacity of the channel, then they focus on reproducing at length conditions of reduced sediment supply (figure 2.5 and 2.6).

It appears that when the sediment supply is nearly equivalent to the transport capacity of the channel, active bedload transport takes place across much of the channel width, and more specifically, given the flow and sediment supply conditions (sand-gravel mixture in the Tsukuba experiments and (sand-free) gravel mixture in the Berkeley experiments) the bedload transport takes place with the presence of bedload sheets.

The reduction of the sediment supply narrows the zone of active transport, the bedload fines and the mean bed surface grain-size becomes coarser (figure 2.5 and 2.6). When sediment supply is reduced, but still non-zero, bedload sheets still occur but in a central narrow corridor rather than on the entire channel width. Therefore the authors conclude that sediment supply controls the relative abundance of fixed and free patches and determines the scaling and dynamics of bedload sheets (details concerning bedload sheets' occurrence, scaling and dynamics are provided in subsection 2.3.1). In both the sets of experiments, reductions in sediment supply led to an expansion of coarse patches at the expense of finer ones and a narrowing of the corridor through which nearly all bedload transport occurred. Reduced sediment supply led to a decrease in sheet migration rate and an increase in the spacing between sheets. Complete elimination of sediment supply resulted in a nearly total loss of bed surface heterogeneity, a uniformly coarse bed and elimination of bedload sheets (Nelson et al., 2009). This outcome agrees with what we previously presented in section 2.2 dealing with bed armoring.

We recall that actually the sets of experiments analyzed by Venditti et al. (2008) and Nelson et al. (2009) mainly focus on fixed patches which develop in supply limited conditions (actual bedload sheets quickly disappear as they decrease sediment feeding), and these experimental conditions and observations are reproduced by a morphodynamic model developed by the same authors in Nelson et al. (2015). In

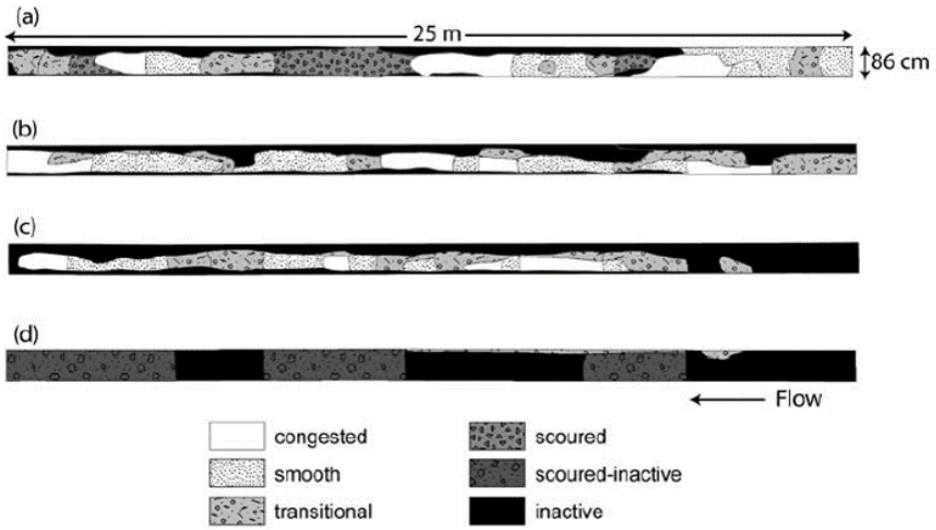

FIGURE 2.6: Illustration from Nelson et al. (2009). Facies map of the bed of the Berkeley experiments at the end of the (a) 23.3, (b) 15.5, (c) 9, and (d) 0 g/min cm sediment feed runs. The terms smooth, transitional, congested, scoured, scoured-inactive, and inactive identify bed surface coarser and coarser (increasing values of d_{50}, the two extremes are smooth areas (composed of fines) and inactive areas (coarse zones with no active bedload transport).

their 2D morphodynamic model Nelson et al. (2015) examine the mechanisms responsible for the development of forced bed surface patches and the coevolution of bed morphology and bed surface patchiness. In this model they consider only forced patches developing on a single bar configuration, namely sediment patches forming because of a topographic controls, precisely a bar morphology. In the discussion of their morphodynamic model Nelson et al. (2015) arise an interesting issue stating that "it is unclear how much the degree of bed surface patchiness may depend upon subsurface heterogeneity" and citing Kinerson (1990)'s field study of several gravel bed channels found relatively little variation in the subsurface material despite considerable surface patchiness.

We provide a more detailed analysis of bedload sheets occurrence and characteristics in subsection 2.3.1, while we conclude the current section with the presentation of the thesis proposed by Venditti et al. (2008) about mixed-size sediment patterns as a phenomenon controlled by sediment supply (rather than hydraulically controlled).

According to Venditti et al. (2008) bedload sheets and in general mixed-size sediment patterns are not hydraulically controlled (from the point of view of their occurrence and their characteristics such as wavelength and migration rate), they are rather sediment supply controlled. The authors argue that "there have been a number of attempts to include bedload sheets into the bedform phase diagrams used to predict bedform occurrence in sandy sediments (Carling, 1999; Kleinhans et al., 2002). The results of these exercises have only been partially successful at distinguishing between bedform types in poorly sorted sediments (Kleinhans, 2002). Indeed, bedload sheets commonly fall into the dune existence field on bedform phase diagrams. This has provided some evidence of the linkage between bedload sheets and dunes formed in coarse sediments [2] (gravel and sand-gravel mixes)."

[2]While recognising that the distinction between dunes with sorting and bedload sheets is difficult to make (Carling, 1999), we do not agree on the linkage between bedload sheets and dunes formed in coarse sediments (as proposed by Venditti et al. (2008)), neither to consider bedload sheets as some sort of 'precursor' of dunes (Bridge, 1993) (see subsection 2.3.1). Basically, wavelength, wavespeed, and amplitude of bedload sheets differ greatly from those of dunes.

The authors state that the partial failure to place bedload sheets into the bedforms phase diagrams used for sandy sediments comes from the assumption that the occurrence of bedload sheets (and in general bedforms of heterogeneous sediments) is hydraulically controlled. According to the authors, this assumption is appropriate for sandy sediment bedforms whereas it is not appropriate for bedforms of heterogeneous sediments. In order to predict the occurrence of bedforms of heterogeneous sediments Venditti et al. (2008) and Venditti et al. (2017) find more appropriate phase diagrams based on the following two parameters: a mobility parameter and a sediment supply parameter. The former is basically based on the quantification of the excess shear stress; the latter is accounted for by comparing the sediment supply (evaluated as the measured transport in flume experiments) with the transport capacity (computed with a transport formula), the sediment supply parameter is whereby defined as $q^* = supply/capacity$ [3]. Hence, through the use of the q^* parameter, three conditions are identified: balance between sediment supply and transport capacity, $q^* = 1$; limited supply conditions, i.e. when sediment supply is lower than transport capacity and hence degradational conditions occur, $q^* < 1$; sediment supply greater than transport capacity with consequent aggradation, $q^* > 1$.

We raise some objections to the analysis of the occurrence of bedforms of mixed-size sediments in such conditions far from dynamic equilibrium conditions (which correspond to $q^* = 1$).

Indeed, no matter the homogeneity or the heterogeneity of sediments, phase diagrams for bedforms occurrence are in the parameter space of hydraulic parameters and sediment mobility parameters, and without a sediment supply parameter because there is the initial hypothesis, basis of the entire study of bedforms occurrence, of sediment supply that equals transport capacity. For instance, stability analysis (successfully achieved for bedforms occurrence even in the case of mixed sediments) are based on the perturbation of a base state that is a uniform flow with sediment supply equal to transport capacity and without aggradation nor degradation (see chapter 3). Indeed this state is the one reasonably analysed when dealing with morphodynamics (both in analytical and numerical studies as well as in the majority of experiments). Moreover, the study of morphodynamics bedforms' occurrence and characteristics is univocal only under conditions of a balance between sediment supply and transport capacity; in case of unbalance what values of deficit or surplus of sediment supply with respect to transport capacity one chooses among the infinite possible values? And besides, while the cases of real rivers with limited sediment supply conditions are quite frequent, the cases presenting sediment supply greater than transport capacity are rare. The latter are very site-specific and episodic (Cui et al., 2003; Madej et al., 2009) and thus of interest for specific case study rather than general morphodynamic investigations.

We conclude our discussion of the thesis proposed by Venditti et al. (2008) about mixed-size sediment patterns as a phenomenon controlled by sediment supply (rather than hydraulically controlled) with the following last objection. Why bedforms only if in mixed sediment conditions should be affected by sediment supply (in terms of occurrence and characteristics such as wavelength and celerity)? There is no reason

[3] According to us, this choice of the sediment supply parameter presents a crucial limitation: q^* can be determined only if it is possible to measure sediment transport (as it was done by Kleinhans (2002) who first accounted for this sediment supply parameter in phase diagrams). Whereby only in laboratory experiments and some field cases it is possible to carry out the diagram phase proposed (sediment supply parameter vs mobility parameter). Hence such diagram phase can not be the outcome of a pure theoretical analysis to compare with experimental results.

why bedforms in uniform sediment conditions would not be affected by sediment supply. In other words, if the sediment supply parameter is the controlling parameter for the occurrence and dynamics of bedforms' with heterogeneous sediments, it must play a key role for unisize sediment bedforms (the sandy bedforms after Venditti et al. (2008)) as well.

Dealing with the partial mobility regime experienced by sand-gravel mixtures, Venditti et al. (2017) present the case of sandy bedforms developed over an immobile gravel bed, and precisely they take as an example the flume experiments by Kleinhans et al. (2002) (figure 2.7).

The authors show that the occurrence of a particular type of sand bedforms depends on the values of the sediment supply parameter q^*. More specifically, increasing values of q^* correspond to the occurrence of sand ribbons, barchans, barchanoids, and dunes, in that order (figure 2.7). We find that the authors are contradictory since first they state that mixed-size sediments bedforms are sediment supply controlled, in contrast to sandy bedforms which are hydraulically controlled, and then they use as an example sandy bedforms stating that they are sediment supply controlled. The flume experiments shown for that purpose are carried out using only sand developing bedforms over a Plexiglas bed (figure 2.7). And besides, the authors even "speculate that sandy bedforms developed over an otherwise immobile gravel bed can be sustained only if the gravel supply is terminated" (Venditti et al., 2017) actually describing unisize sediment conditions.

Actually, according to us, both homogeneous sediments and heterogeneous sediments bedforms are hydraulically controlled and citing Kleinhans et al. (2002)'s summury about their own experiments "during low flow most of the sediment is immobile, leading to strong sediment supply-limited conditions with sand ribbons. With increasing flow strength and sediment transport, sand ribbons evolve into barchans, barchanoids, and finally dunes" we support the thesis that flow conditions (i.e. hydraulic control) together with mobility parameter are the controlling parameters for both homogeneous and heterogeneous sediments bedforms.

2.3.1 Bedload sheets

Bedload sheets are highly mobile and very low-relief bed forms present in moderate, poorly-sorted material; they are few coarse grain diameter thick and they appear to be rhythmic alternations of finer and coarser bands of the bed material aligned across the flow, and they propagate in the downstream direction.

Bedload sheets have been observed both in the laboratory (Iseya and Ikeda, 1987; Kuhnle and Southard, 1988; Bennett and Bridge, 1995; Recking et al., 2009; Nelson et al., 2009) and in the field (Whiting et al., 1988; Cudden and Hoey, 2003) sometimes superimposed on the stoss side of dunes and bars (Whiting et al., 1988; Livesey et al., 1998; Bennett and Bridge, 1995; Rice et al., 2009).

Venditti et al. (2008) and Nelson et al. (2009) analyse experimental observations on bedload sheets and surface patchiness (as we illustrated in section 2.3) and they argue that bedload sheets dynamics is primarily scaled by sediment supply, and actually a reduction in sediment supply until condition below and far below transport capacity of the channel causes the absence of bedload sheets: free migrating patches are not observed anymore giving way to fixed coarse patches (figure 2.5 and 2.6). Hence, according to Venditti et al. (2008) and Nelson et al. (2009) bedload sheets' occurrence and characteristics are primarily affected by sediment supply (a detailed

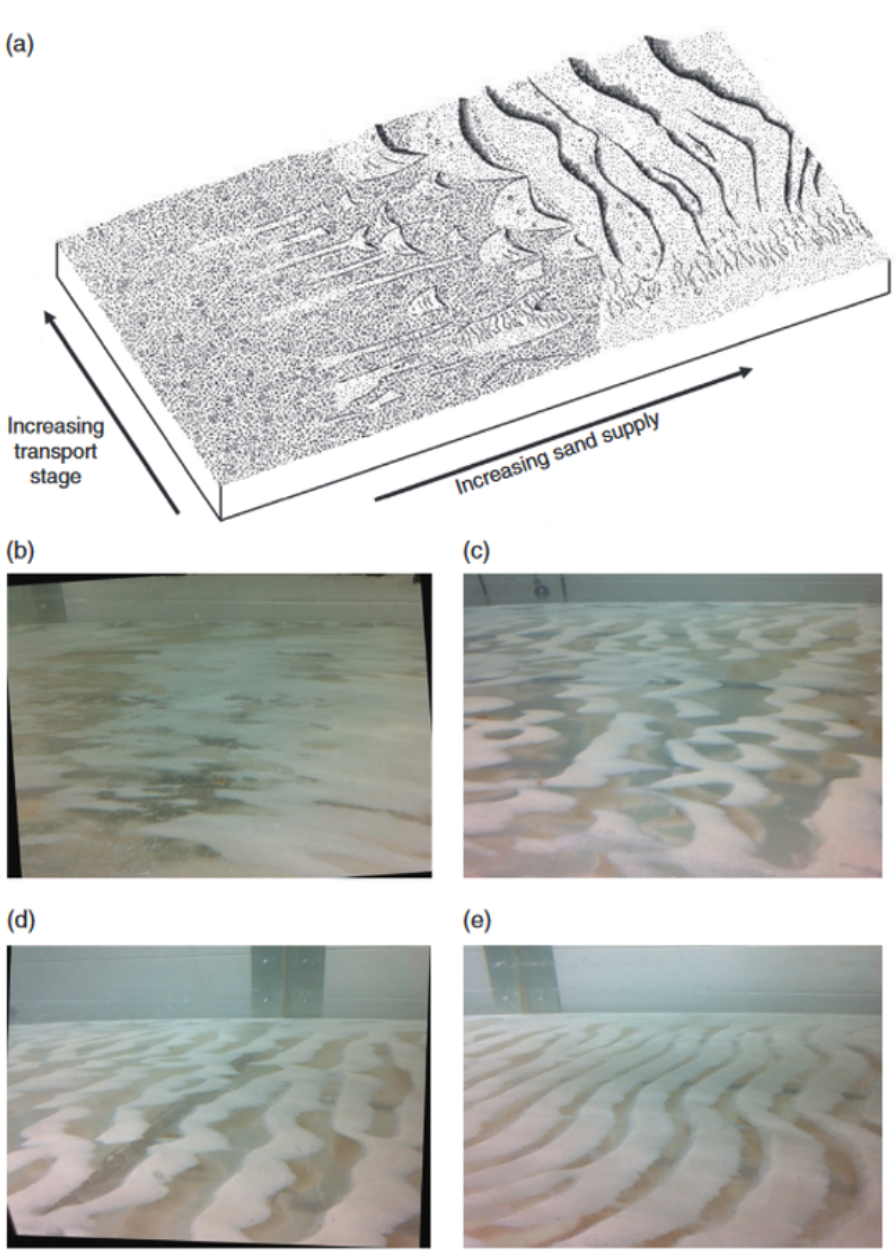

FIGURE 2.7: Illustration from Venditti et al. (2017).(a) Kleinhans et al. (2002) conceptual model of sand bedforms developed over an otherwise immobile gravel bed showing the influence of transport stage and sediment supply: flow is left to right. (Modified from Kleinhans et al. (2002).). Sequence of bedforms developed of over a Plexiglas bed with increasing sand supply showing (b) patches of sand akin to sand ribbons, (c) barchan dunes, (d) interconnected barchan dunes, and (e) laterally continuous dunes: flow is right to left.

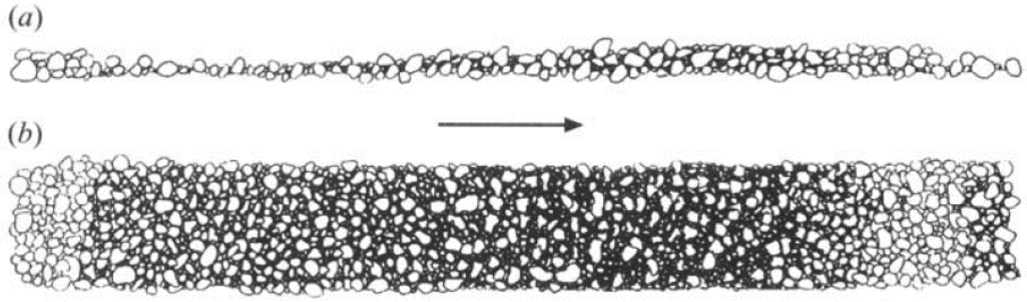

FIGURE 2.8: Sketch of bedload sheets as reported by Whiting et al. (1988); (a) side and (b) plan view.

illustration of that thesis has been provided in section 2.3). More specifically Venditti et al. (2008) outlining the domain of bedload sheets state that this kind of sorting patterns are situated between aggradation and degradation extremes, between high and low q^* values (hence around $q^* = 1$), in the full mobility regime. Concerning bedload sheets dynamics Nelson et al. (2009), trough the analysis of the Tsukuba and Berkeley experiments (see section 2.3), state that reduced sediment supply lead to a decrease in sheet migration rate and an increase in the spacing between sheets, and zero sediment supply results in a uniformly coarse bed surface and elimination of bedload sheets. Hence reduced sediment supply and zero sediment supply cause a kind of inhibition of bedload sheets and suppression of bedload sheets, respectively.

We illustrated in section 2.3 our objections to such thesis according to which bedload sheets and in general mixed-size sediment patterns as a phenomenon controlled by sediment supply. Actually, other authors too (Recking et al., 2009) think that bedload sheets have not to be studied in conditions far from dynamic equilibrium conditions (which correspond to $q^* = 1$). According to Recking et al. (2009) bedload sheets' occurrence and characteristics has not to be investigated at varying (more precisely several cases of limited sediment supply) sediment supply conditions. All the experiments carried out by Recking et al. (2009) reproduce conditions of balance between sediment supply and transport capacity, i.e. dynamic equilibrium. According to Recking et al. (2009) bedload sheets' characteristics rather depend on channel slope. The authors state that amplitude and migration rate depend on slope: the gentler the slope, the smaller bedload sheets' amplitude and migration rate.

About bedload sheets' occurrence, there is (at least) a point that finds a general agreement in scientific community: the grain interaction between sediments of different size is crucial for bedload sheets to take place. Nelson et al. (2009) show that bedload sheets take place not only in sand-gravel mixtures (Tsukuba experiments) but also in sand-free mixtures (Berkeley experiments): in particular bedload sheets of the Berkeley experiments take place in a unimodal gravel (unimodal but still heterogeneous). Hence Nelson et al. (2009) conclude that the presence of sand in the sediment mixture is not essential for bedload sheets to take place, whereas the important parameter is the ratio between the coarse diameter and the fine diameter; the authors speculate that the lower limit of such ratio is 4 for bedload sheets occurrence. Recking et al. (2009)'s experiments too prove that bedload sheets occur in sand-free gravel mixtures, and besides the ratio between the coarse diameter and the fine diameter can be smaller than 4; actually this last point show that the 'degree of heterogeneity' for the occurrence of bedload sheets can be moderate, and we add that more in general grain sorting takes place for very slight degrees of heterogeneity.

The propagation of bedload sheets has been associated with bedload pulses frequently observed in gravel bed rivers (Reid et al., 1985; Iseya and Ikeda, 1987; Kuhnle and Southard, 1988; Recking et al., 2009). Actually the way of displacement and propagation of bedload sheets is related to the strong fluctuations in bedload rates recorded in coarse bed channels and to fluctuations in bed slope, whit both these fluctuations being difficult to explain with the classical models of river hydraulics. Indeed, classical formulations of river hydraulics are based on the equilibrium concept (Lane, 1954) for which an equilibrium slope could be defined for a particular channel attending to its grain size, sediment load and discharge; namely, given a sediment grain size, a flow discharge, and a solid discharge, the system will adjust its power (by modifying its energy slope) to equalize the rate of the transporting work. In particular, in flume experiments this occurs when the flow adjusts its slope, the latter attaining a constant value, until the outlet solid discharge equals the feeding rate (Recking, 2006). Whereas this is verified in flume experiments with uniform materials, it is not the case for experiments with non-uniform sediments. Indeed, experimental and field measures show that equilibrium slope is never reached when dealing with non-uniform sediment, and at the same time it has been observed that bedload rates strongly fluctuate around the bedload rate corresponding to the equilibrium slope (Hoey and Sutherland, 1991; Iseya and Ikeda, 1987; Kuhnle and Southard, 1988). Besides, the presence of sand has been widely reported, both in the flume and in the field, to increase gravel transport efficiency (Gilbert and Murphy, 1914; Iseya and Ikeda, 1987; Ferguson et al., 1989; Wilcock et al., 2001; Cui et al., 2003; Curran and Wilcock, 2005). In particular, Iseya and Ikeda (1987) carried out several experiments with constant feeding rate both for the liquid and solid discharge, varying the proportion of sand in the in a sand-gravel mixture. They concluded that less flow power is necessary for transportation of a mixture of sand and gravel than for transportation of sand only. This confirms that the equilibrium concept cannot be applied for sediment mixtures. Hence is not surprising that the sorting waves named bedload sheets are characterized by a propagation concomitant with bedload fluctuations, precisely "bedload pulses". The propagation of bedload sheets seems to be not only related to bedload pulses, but it also seems the main responsible of fluctuations at different temporal scales concerning aggradation and erosion stages of the bed. Actually, experimental observations (Kuhnle and Southard, 1988; Whiting et al., 1988) show that local aggradation and erosion phases alternates in the channel bed during a transport episode, and that channel equilibrium is a dynamical concept. Regarding bedload sheets propagation, several authors (Livesey et al., 1998; Cudden and Hoey, 2003) have highlighted how difficult is, from an experimental point of view, to distinguish among the different spatial and temporal scales associated with bed and sorting waves. This led Livesey et al. (1998) to conclude that "the interactions between bed topography, flow structure and surface sorting patterns remains poorly understood despite their central role in controlling mixed-size entrainment dynamics and fractional bedload transport rates". In particular, the distinction between dunes with sorting and bedload sheets is difficult to make (Carling, 1999) so that often the latter has been considered as some sort of 'precursor' of the former (e.g. Bridge, 1993), adding confusion to the confusion. In fact, observations have shown that both the wavelength and the wavespeed of dunes (with sorting) and bedload sheets can be remarkably different one from another, the former being typically longer and slower than the latter (Kuhnle et al., 2006). The most distinctive character remains indeed the height of the bed form, which is almost negligible for bedload sheets as compared to dunes and bars.

From a theoretical point of view, linear stability analyses are known to be the perfect tool to shed light on the mechanisms hidden underneath the formation of patterns of any kind, so it is not surprising that in the nineties several attempts were made to include sorting into existing studies on bed forms, initially developed for well-sorted sediment (see Colombini and Parker, 1995; Seminara et al., 1996; Lanzoni and Tubino, 1999, among others). These analyses were mainly focused on the formulation of coupled sediment transport and flow models valid for heterogeneous mixtures, thus including the effect of hiding and of the local surface roughness. The appearance of sorting waves was in fact acknowledged, but the distinct nature of the sorting and the bed eigenvalues did not receive the attention it deserved, mainly because the focus was more on the effect of sorting on bed forms than on the formation of sorting waves. The only notable exception is the work of Seminara et al. (1996), where the formation of bedload sheets was investigated in detail. However, in order for the bedload sheet mode to emerge, in Seminara et al. (1996) the dune mode was artificially ruled out from the analysis, by assuming that the perturbation of bed elevation scales with the (small) standard deviation of the grain size distribution.

2.4 Recent advances in flume experiments and mathematical models on sediment sorting

2.4.1 Mathematical models

Mathematical models of river morphodynamics compute changes in both bed elevation and bed sediment composition as a result of open channel hydraulics and sediment transport. These models compute the flow using a Reynolds-averaged momentum equation, but excursions into large-eddy simulation have been made. Direct numerical simulation has come within reach for the motion of sediment, but customary models remain based on empirical transport relations and a volumetric sediment balance or Exner equation (Mosselman, 2012). In particular, the tools used to model the flow and sediment transport depend upon the scales of interest. At the scale of dunes and ripples, the mechanics of sediment transport must be coupled with the Reynolds equations (appropriately closed for turbulence). For bars and in general at larger scales, however, the shallow-water equations are quite adequate to model the flow, and thus, sediment transport and river mechanics are commonly addressed through 1D, 2D (depth averaged) Saint-Venant-Exner shallow water system of equations (later on we will show in the present work that the modelling of bars needs a 2D Saint-Venant-Exner shallow water system of equations as it is well known, whereas for the sorting waves modelling a 1D Saint-Venant-Hirano shallow water system of equations is sufficient).

The cases in which sediment non-uniformity must be taken into account have been presented at the beginning of this chapter; they basically are the cases in which grain sorting is the main morphological feature of the investigated phenomenon, as in sediment stratigraphy, an example of which is bed armoring, or as in bed patchiness (planimetric sorting as described in Nelson et al. (2009)), an example of which is representeed by bedload sheets. In this section, we outline the main elements of non-uniform sediment modelling.

As set out in Mosselman (2012), the classical approach to modelling river morphology with non-uniform sediment is based on: (i) division of the sediment mixture into separate fractions, (ii) transport formulae and mass conservation equations

for each of the separate fractions, (iii) hiding-and-exposure corrections to the critical shear stress of each of the fractions (Egiazaroff, 1965; Ashida and Michiue, 1972; Ashida and Michiue, 1973), and (iv) an active layer or transport layer affected by erosion and sedimentation (Hirano, 1971).

Concerning point (iii) of the above list, we can state that hiding-and-exposure corrections account for the interactions between different size fractions; after Einstein (1950), several correction parameters and functions (Egiazaroff, 1965; Parker and Klingeman, 1982) have been included into the transport equations to address this grain scale or relative size effects of sorting. In particular, hiding corrections reduce the mobility of fine grains in the mixture compared to the unisize-sediment case, whereas exposure corrections make coarse grains more easily entrained because they protrude more. Thus, hiding-and-exposure corrections promote conditions closer to equal mobility with respect to the case without hiding-and-exposure corrections. By the way, the different size fractions are still characterized by different transport capacities and therefore grain size selectivity of transport is maintained. Actually, grain size selectivity of transport is the standard condition in rivers from low to relatively high transport conditions, and it must be retained in the analysis in order to properly appreciate the features of the mathematical model. About hiding and exposure, we can finally remark that they act not only on the critical shear stress, but also on the effective bed shear stress (Einstein and Qian, 1953; referenced by Ribberink, 1987), which depends on the surface roughness of the bed (Mosselman, 2012). This roughness varies in a complex manner with bed sediment composition under conditions of non-equal mobility.

Regarding the active layer formulation, it represents the most widespread sediment continuity model used to describe the interaction between grain size selectivity of transport, vertical sorting profile within the bed, and changes in bed elevation. In the active layer model by Hirano (1971) the sediments are discretized through a finite number of classes each of which characterized by a single grain size value. As for the bed, it is divided into a fully mixed top layer, i.e. the active layer also called exchange layer, and in a substrate layer underneath which is inactive. Only sediments in the active layer interact with the flow giving rise to bedload fluxes; sediment fluxes between the active layer and the substrate take place only when there is a change in the average bed elevation.

The active layer formulation remains the most used model for mixed-sediment morphodynamics, despite more refined multiple-layer models and vertical-continuous models for size stratification have been propose later on (e.g. Ribberink, 1987; Parker et al., 2000; Blom and Parker, 2004; Blom et al., 2008; Viparelli et al., 2017).

Authors, such as Mosselman (2012) and Stecca et al. (2014), who performed a mathematical analysis of the Hirano active layer model, remarked the sensitivity of morphological computations to the oversimplified single active layer. In this regard, for instance, they observed that computations depend much upon the thickness of the active layer. In particular, Stecca et al. (2014) dealing with the celerity of "sorting waves", i.e. the speed associated with a model for the evolution of the average diameter in the mixture, found that such celerity is proportional to the inverse of the active layer thickness. Therefore, sorting celerity can be in principle arbitrarily increased by setting thinner active layer.

In order to overcome this type of shortcoming characterizing the Hirano model, authors proposed the addition of a further exchange layer as Ribberink (1987) did in his two-layer model and the introduction of depth-continuous models for vertical

sediment exchange as for instance in Parker et al. (2000), the latter model applied in Viparelli et al. (2017).

Among the aforementioned works the study by Ribberink (1987) is of particular interest for two main reasons: first, it is one of the not so numerous theoretical analysis, with respect to numerical ones, of river morphodynamics with non-uniform sediment, and secondly, it is the first work reporting that the Hirano model can become conceptually unsuitable for morphodynamic predictions due to a switch in its mathematical character under some conditions. Regarding the first point, it is worth recalling that mathematical modelling consists in not only numerical solution of mathematical equations but also analytical solution of equations under special conditions. The two approaches are complementary as the analytical solutions offer valuable insights into the fundamental behaviour of the corresponding physical system. In this context, we have already recalled in the section devoted to bedload sheets the theoretical analyses on mixed-sediment morphodynamics consisting in stability analyses; whereas Ribberink (1987) does not perform a stability analysis. He integrates mass conservation equations for individual sediment size fractions over the full sediment mixture and combines the resulting equation for sediment composition with quasi-steady flow equations and the sediment balance or Exner equation, assuming capacity-limited sediment transport as a function of depth-averaged flow velocity and bed sediment composition, without lag effects. He then carries out an analysis of characteristics of the set of equations, which reveals how information propagates in the mathematical system (Mosselman, 2012). The analysis focuses on the celerities of the perturbation in bed level, called "bed wave" and of the perturbation in bed sediment composition, called "sorting wave". A summary of Ribberink's work can be found in Mosselman (2012). The significance of Ribberink's work also lies in saying, the first, that the Hirano model consisting in the Saint-Venant equations coupled with the Exner equation with the active layer formulation become ill-posed in certain conditions. Actually, Ribberink reports that in some particular conditions the Saint-Venant-Hirano system of equations become unsuitable for morphodynamic predictions. Ribberink's analysis concerns the roots of his system of equations; these roots are the celerities of the bed wave (i.e. the perturbation in bed level) and of the sorting wave (i.e. the perturbation in bed sediment composition). When these wavespeeds have real values, the system is hyperbolic and thus appropriate for representing time-advancing problems, which are fully determined by the initial, and boundary conditions (Stecca et al., 2014). On the other hand, Ribberink finds that in the particular case of the active layer degrading into a finer substrate, the celerities have complex values; thus, the problem becomes elliptic and therefore no more adequate for representing morphodynamic changes. Detailed explanations about the switching mathematical character of the Saint-Venant-Hirano model can be found in Stecca et al. (2014) and in Siviglia et al. (2017).

Closing this overview about theoretical analyses, we can state that the studies of the mathematical behaviour of the Saint-Venant-Hirano model (Ribberink, 1987; Sieben, 1997; Stecca et al., 2014) can display similarities with linear stability analyses of the same system of equations. Although in the first kind of studies the focus is on the mathematical character of the system (elliptic, hyperbolic or parabolic), whereas the linear stability analyses investigate the stability of the system, both analyses rely on a linearization in terms of small-amplitude hydro-morphodynamic waves. Hence, some similarities in results of these two kind of studies are not surprising and they will be discussed later on dealing with the linear stability analysis we propose in the present work (chapter 3).

2.4.2 Flume experiments

The current section presents laboratory flume experiments on sorting phenomena occurring in non-uniform sediments, both narrowly graded sediments such as bimodal mixtures, and widely graded sediments. The flume experiments here reported concern models of gravel bed rivers; we present them starting with narrow flume experiments and then reporting investigations about larger flow configurations.

In our work we aim at studying morphodynamic equilibrium states of flows over non-uniform sediments and the eventual evolution of the bed variables such as bed slope, sorting patterns, and bedload transport rate in dynamic equilibrium conditions. Having this objective, the experimental works in literature that mainly are of interest to us are those studies modeling equilibrium conditions, thus having long duration and steady external conditions (constant feeding rates both for flow and sediment discharge) and reproducing conditions of balance between sediment supply and transport capacity.

The observations of narrow flume tests concern both vertical and longitudinal sorting and variation in composition and fluctuations in intensity of bedload transport as well. In particular the selection of the case studies here reported is about pulsations in bedload transport rates induced by longitudinal sorting without noticeable bed forms (Iseya and Ikeda, 1987), pulsations in bedload transport rates associated to bedload sheets (Recking et al., 2009; Recking, 2013; Bacchi et al., 2014) and mobile and static armor (Bacchi et al., 2014).

The experiments by Iseya and Ikeda (1987) with a sand-gravel mixture are conducted at equilibrium conditions, the latter identified by the authors through two criteria: the near-equality of feed and trap rates of both sediment fractions, for an extended period of time; and a rather constant water surface slope. As for the first criterion, the authors observe that the longitudinal sorting causes variations in this comparison even at an apparent stable condition, and thus the constant value approached by the water surface slope is set as benchmark for equilibrium conditions.

Iseya and Ikeda (1987) perform 9 runs with different combinations of the feed rates of the sand and gravel. The water discharge is fixed at 400 cc/sec for all runs, constant value during each run duration, and the sediment as well was fed with a constant value during each run duration. The sediments used for mixture are subangular gravels with median grain size of 2.6 mm and medium sand with median grain size of 0.37 mm.

A first clear result is that bedload transport rate of gravel increases when transported within a mixture rather than without sand [4]. Furthermore gravel transport rate increases as the content of sand within the mixture increases. Both the outcomes are an evidence of higher mobility of the mixture because of the mixing effects of smoothing, exposure and collision.

[4]The authors quantified this behaviour measuring the water surface slope capable of transporting all the sediments supplied. The equilibrium slope is in inverse proportion to the mobility of sediment, because the water discharge was constant for all runs. The greater the mobility of sediment, the smaller the equilibrium slope. In Iseya and Ikeda (1987) flume configuration, incipient motion for a fixed amount of gravel only begins at water surface slope of 3%; the same amount of gravel (with the same water discharge) is transported with a halved value of water surface slope when to the gravel feed rate is added the same value of sand feed rate. Actually the slope decreased in spite of an increasing total load which has to be transported by the flow (Iseya and Ikeda, 1987).

The effects of smoothing, exposure and collision do not operate evenly through the length of the flume. Along the channel distinct bed states were observed, in particular three bed states. The congested state, i.e. pavement characterized by steep slopes; the smooth state, i.e. plane bed with majority of sand particles and characterized by gentle slopes; the transitional state. These three bed states repeatedly occurred in an orderly manner; this alternation occurred as well at a given cross-section. This phenomenon is the longitudinal grain sorting described by the authors, and it is also associated with rhythmical transport rate fluctuations. Indeed the importance of the work by Iseya and Ikeda (1987) lies in the description of the three bed states occurring cyclically and constituting a longitudinal sediment sorting, see figure 2.10. The latter induce a changing availability of bed materials and also produce the rhythmic pulsation of bedload transport rate.

Laboratory observations of sediment sorting related to bedload sheets can be found in Recking et al. (2009) and in Bacchi et al. (2014), both reproducing gravel mixture bedload transport under quasi-steady flow conditions.

The experimental set up in Recking et al. (2009) has the following features:

- 20 runs
- 8-m-long tilting flume; width from 0.05 to 0.15 (in order to avoid divagations and to ensure 2D flows); slope from 0.8 to 9 %
- constant ingoing flow and sediment discharge (with feed system)
- gravel mixtures of 2 grain sizes (varying composition of $d_1 = 2.3mm$, $d_2 = 4.9mm$, $d_3 = 9mm$)

The experimental set up in Bacchi et al. (2014) has the following features:

- 2 long runs (about 100 hours each)
- 6-m-long, 0.1-m-wide flume; slope 12 %
- constant ingoing flow and sediment discharge (with feed system)
- sediment mixture composed of nearly uniform mixtures whose median size was 1.0, 2.1, 4.9, 9.0, 12.5, 18.7 $mm \rightarrow$ GSD: $d_{16} = 1.8\ mm$, $d_{30} = 2.1\ mm$, $d_{50} = 3.2\ mm$, $d_{84} = 9.0\ mm$, $d_m = 6.0\ mm$

Recking et al. (2009) measure for all runs, large fluctuations of both the slope and the outlet solid discharge, Qs, although feeding rates are maintained constant (figure 2.9).

In all runs, is observed aggradation associated to reduced gravel mobility (reduced transport rate) and efficient longitudinal and vertical sorting. This vertical sorting during aggradation manifests itself with coarsening and successive paving surface; subsurface fining. Aggradation continues until the attainment of a maximum local slope. The stage of aggradation stops with the attainment of a maximum local slope, at this moment a violent erosion with armor destruction takes place: this local "sediment purge" coincide with bedload sheet departure. These alternating stages repeat several times, hence we can sum up that at a given cross section, a cyclic behaviour is observed (alternating bed states and bedload conditions):

a) smooth bed; high solid transport of all gravel fractions;

b) transitional bed; half way through aggradation stage;

c) congested bed; low solid transport over paved bed;

d) strong local erosion; maximum solid transport.

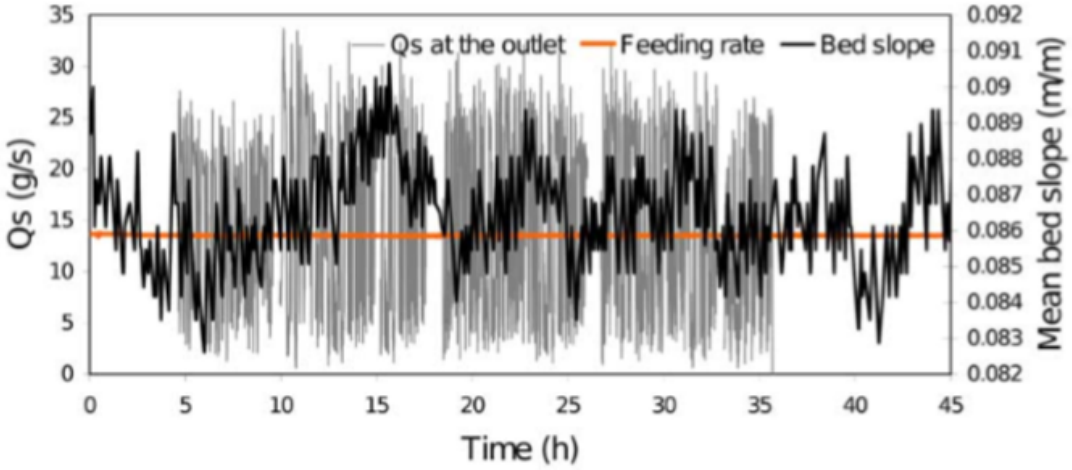

FIGURE 2.9: Continuous outlet solid discharge and mean bed slope versus time for run 7 (slope 8.65 %; mixture: 2.3 mm 50 % and 4.9 mm 50 %) by Recking et al. (2009).

Indeed Recking et al. (2009) monitor the cyclical bed states previously observed by Iseya and Ikeda (1987) related to the fluctuation of bedload transport rate (figure 2.10).

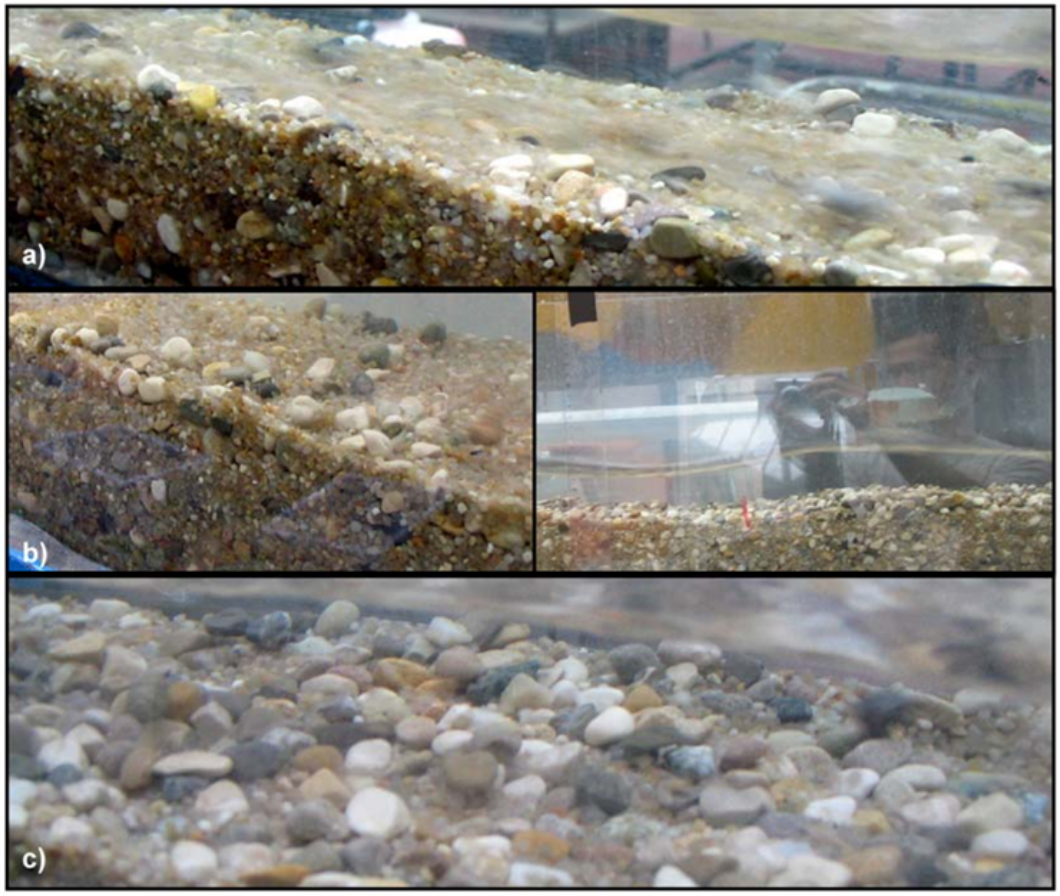

FIGURE 2.10: Picture from run 1 (slope 1.8 %; mixture: 2.3 mm 50 % and 9 mm 50 %) by Recking et al. (2009). a) Smoothed bed; b) transitional bed; c) congested bed. From a) to c) the solid discharge is decreasing; actually the "blurriness" in a) is due to the huge amount of sefiments moving.

In the analysis of the measurements, Recking et al. (2009) relat to each other the

main three elements observed: the bedload sheets production and displacement, the local bed topography changes and the transport rate variations. The outcome shows that aggrading bed associated with low outlet solid discharge; most peaks associated with degrading bed (figure 2.11). A Spectral analysis with Fourier transform of temporal signals $Qs(t)$, solid discharge, and $S(t)$, mean bed slope, is provided as well. The analysis shows that both signals have approximately the same frequency signature: this confirms that Qs fluctuations are correlated with S fluctuations.

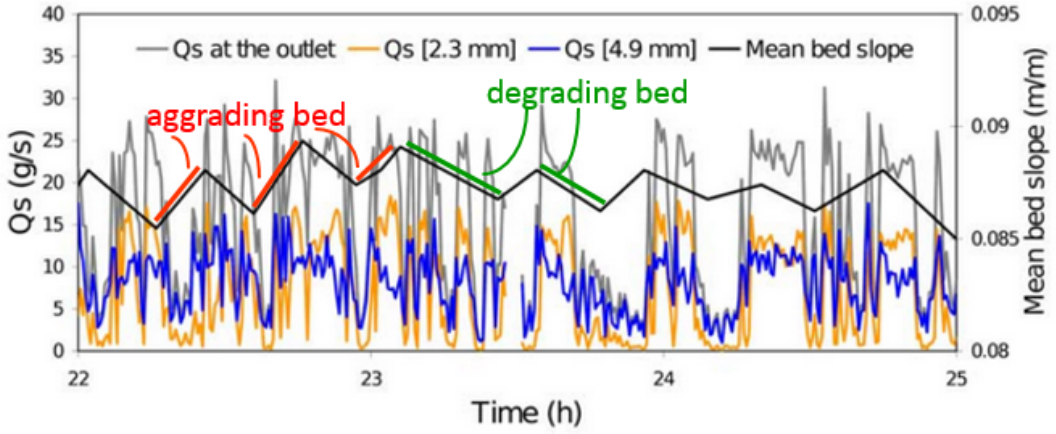

FIGURE 2.11: Correlation between bedload sheet production, local bed topography changes, and Qs changes in run 7 (slope 8.65 %; mixture: 2.3 mm 50 % and 4.9 mm 50 %) by Recking et al. (2009). Fluctuations of the mean bed slope and of the total and fractional transport rates.

As for solid transport of a mixture, the authors analyze fractional transport rates compared to transport capacities for the two uniform mixtures. They conclude that coarse grains have a greater mobility when they are transported in a mixture with fines rather than when they are alone. Fine gravels transport rate attains its uniform transport capacity only during the passage of a bedload sheet.

These experimental observations are summarized in a conceptual model based on the energy conservation principle (Recking et al., 2009; Recking, 2013).

Using the Bagnold equation (Bagnold, 1966) the authors state that when the feeding rates (Q, Q_s) are kept constant, energy conservation imposes that the product of the bedload rate efficiency e and the slope S is constant as well

$$eS = \phi\left(Q, Q_s\right) = C^{te} \tag{2.1}$$

This formulation supports the existence of periodical slope and bedload transport rate fluctuations, as the transport rate efficiency e (which depends upon the sediment mixture composition) is time-varying because of sorting effects. In particular e has a maximum value during bedload sheets passage, when sediment transport (of the coarse fraction and of the whole mixture) is indeed very efficient.

In Bacchi et al. (2014) two long runs (about 100 hours each) are performed with the experimental set up previously illustrated.

First we focus our attention on run 2: the long run with $\theta^*_{84}/\theta^*_{c84} > 1$ i.e. the high flow condition run. This run is characterized by kinetic sorting. Recking's experimental observations about bed slope and solid discharge fluctuations are confirmed. The slope peaks at the final stage of long aggradation processes, followed by sharp

and rapid bed erosion coincident with a bedload sheet departure. A wavelet analysis shows a correlation between rates of bedload sheet production and the slope signal. Bedload sheets were not observed in run 1 i.e. the low flow condition run (with $\theta^*_{84}/\theta^*_{c84} < 1$). As in Recking et al. (2009) a very efficient vertical sorting is observed.

On the other hand, run 1 performed by Bacchi et al. (2014) the run at low flow conditions ($\theta^*_{84}/\theta^*_{c84} < 1$), does not manifest any cycles of armoring and erosion. In this run was rather observed a permanent armoring, which is effect of a static sorting. In run 1 the flow was not strong enough to entrain the coarser fraction of the mixture and consequently kinetic sorting was negligible (whereas in run 2 the flow was strong enough to entrain the coarser particles, producing indeed kinetic sorting).

To sum up, narrow flume experiments demonstrate interactions between channel slope adjustments, vertical and longitudinal sorting, and fluctuations of bedload transport rate. In particular, the experimental observation we presented show significant fluctuations of slope and outlet solid discharge and how such fluctuations are related to bedload sheets. These laboratory observations confirmed and extend the field investigations by Whiting et al. (1988) on the sorting phenomenon of bedload sheets and the associated fluctuations of bedload transport rates.

As for experimental works with larger flume configurations with regard to grain sorting, the investigations concern sorting patterns and their relation with bed forms such as bars and braiding systems, as well as fluctuations in bedload transport rates (Lisle et al., 1991; Lisle et al., 1993; Lanzoni et al., 1994; Lanzoni, 2000b; Cui et al., 2003; Madej et al., 2009; Leduc, 2013).

Among these studies, however, there are some (Lisle et al., 1993; Cui et al., 2003; Madej et al., 2009) that do not have steady external conditions and thus are less interesting to us from the point of view of dynamic equilibrium. Actually such works analyze specific cases such as channel response to a decrease in sediment supply (Lisle et al., 1993) and disturbances in sediment supply like sediment pulses reproducing landslide in the channel bed (Cui et al., 2003), and cycles of intense sediment supply and sediment starvation simulating specific case studies of flood and post-flood events (Madej et al., 2009).

In particular, the flume experiment by Madej et al. (2009) model aggradation and degradation cycles in a specific steep gravel-bed channel with alternate bars, the Emerald Creek, California. Each phase of the experiment has a short duration and it is not in equilibrium conditions.

The experiments by Cui et al. (2003) reproduce a gravel-bedded, straight, single-thread channel with alternate bars characterized by high transport rate perturbed by occasional landslides and debris flows, the latter two modeled in the flume with sediment pulses consisting in bumps put in the channel bed.

Indeed these two studies have an approach of "channel recovery after disturbances" and they do not deal with morphodynamic equilibrium. However in Cui et al. (2003) the run with the pulse finer than the prepulse bed material is of particular interest to us since the finer prepulse is responsible of the destruction of the surface armor layer, and of the increased transport rate of gravel; furthermore this run exhibits significant pulse translation in addition to dispersion, and such sediment pulse translation is indeed identified by the authors as migrating bedload sheets. "The evidence for translation was embodied in clearly visible leading and

trailing edges that migrated downstream. The sand from the pulse elevated the transport rate of the ambient gravel, a phenomenon earlier noted by Wilcock (1998). The presence of the sand thus abetted a morphodynamic response similar to the "gravel sheets" observed experimentally by Iseya and Ikeda (1987) and Whiting et al. (1988) and studied theoretically by Seminara et al. (1996)."

Interesting observations in Madej et al. (2009) concern coarsening during degradational cycles and bedload sheets. The latter take place only during aggradational phases; the mechanism provided by bedload sheets in enhancing bed mobility is recognized; and lastly the authors find the presence of bedload sheets a good indicator of high sediment loads in gravel bed channels.

Hence, experimental works with large flume configurations studying grain sorting in dynamic equilibrium conditions remain not so numerous. Indeed there are also cases such as Dhont (2017) in which very long experiments (up to 600 h) with heterogeneous sediment mixtures are performed; this study deals with bedload fluctuations in gravel bed streams with alternate bars. Such experiments ensure dynamic equilibrium conditions in the flume and the observation of all potential types of bedload transport rate fluctuations at different time scales, but unfortunately do not provide a follow-up of sorting phenomena even if they take place. Dhont (2017) states that "Little attention was paid to grain sorting although we observed some of its effect in the bed. For instance, bar heads were made of coarse particles and the bottom of the pools featured special arrangements of fine grains. Moreover, the mechanisms of bedload transport and the changes in bed morphology we described are somehow related to grain sorting effects. Among the main reasons for not documenting this phenomenon we point: the moderately-sorted sediment mixture used, the difficulty to quantify its effects given the limited range of grain sizes (for instance compared to mixtures with sand and gravel), and the priority to carry out long experimental runs without stopping the water flow (which is generally needed to assess grain sorting in the bed)."

Lisle et al. (1991), Lanzoni et al. (1994), Lanzoni (2000a), Lanzoni (2000b), and Leduc (2013) study the influence of sediment heterogeneity on bars' dynamics. Experiments suggest that sediment heterogeneity, going with selective transport and subsequent grain sorting, can lead to a modification in the balance between stabilizing and destabilizing effects. In particular various contributions related to sediment heterogeneity cause stabilizing effects on bottom development, reduction of bar amplitude (i.e. height) and shortening of bar wavelength in a wide range of the dimensionless control parameters, namely the Shields parameter θ, the width-to-depth ratio β, and the relative bed roughness d_s, as confirmed by the theoretical analysis by Lanzoni and Tubino (1999).

In this regard, Lisle et al. (1991) conduct a flume experiment about bars with constant feeding rates; the hydraulic and sedimentological conditions are those typical of gravel-bedded, steep, natural channels, in particular the authors use a moderately to poorly-sorted, log-normally distributed mixture of sand and gravel (range, 0.35–8 mm; median size, 1.4 mm) and the slope is of 3%. The authors document alternate steady bars with coarse particles covering bar heads, preventing bar head erosion and thus migration. The authors identify as other causes of bars steadiness the steep slope and the low relative submergence. Two main objections can be raised up to Lisle et al. (1991) contribution: first of all the experiment duration is rather short, 10 hours, and a longer duration would ensure a dynamic equilibrium and more reliable observation about eventual bars steadiness; second, as for steep slope it is more

reasonable the hypothesis that it can reduce bars dynamic (intended as migration speed) rather than inhibit bars dynamic. Indeed in steep slope secondary flow is less important than in a channel with unchanged conditions but with a a milder slope, and the key role in bars dynamics played by secondary flow is acknowledged: the relative importance of lateral gravitational forces on the cross-stream component of sediment transport is a primary control on the amplitude of the bars (Nelson et al., 2015).

Leduc (2013) investigates influence of sediment heterogeneity on bars dynamic with almost the same experimental conditions of Lisle et al. (1991) but with a longer duration, 100 hours, in order to understand if the bars steadiness observed by Lisle et al. (1991) is imputable to the to much short experiment duration. Leduc (2013) observes the absence of stationarity of bed forms and cyclicity of bed states accompanied by planimetric variations of the channel. Precisely Leduc (2013) observes two different bed patterns associated with this cyclical bar migration phenomenon. The first bed state corresponds to a smooth state (figure 2.12 left panel), with a high sediment transport rate and a well-identified channel, including both shallow and deep pools. The associated alternate bars were clearly visible with their tops significantly above the mean water level. The second bed state was congested, with a pool-riffle-like morphology, showing a wider main channel and steep slopes close to the pool (figure 2.12 right panel). The smooth bed corresponds to erosion while the congested bed corresponds to deposition. Throughout the entire experiment, no equilibrium slope, constant bedload transport rate or constant bed pattern is reached. Instead, Leduc (2013) observes a quasi-periodic cyclical behavior.

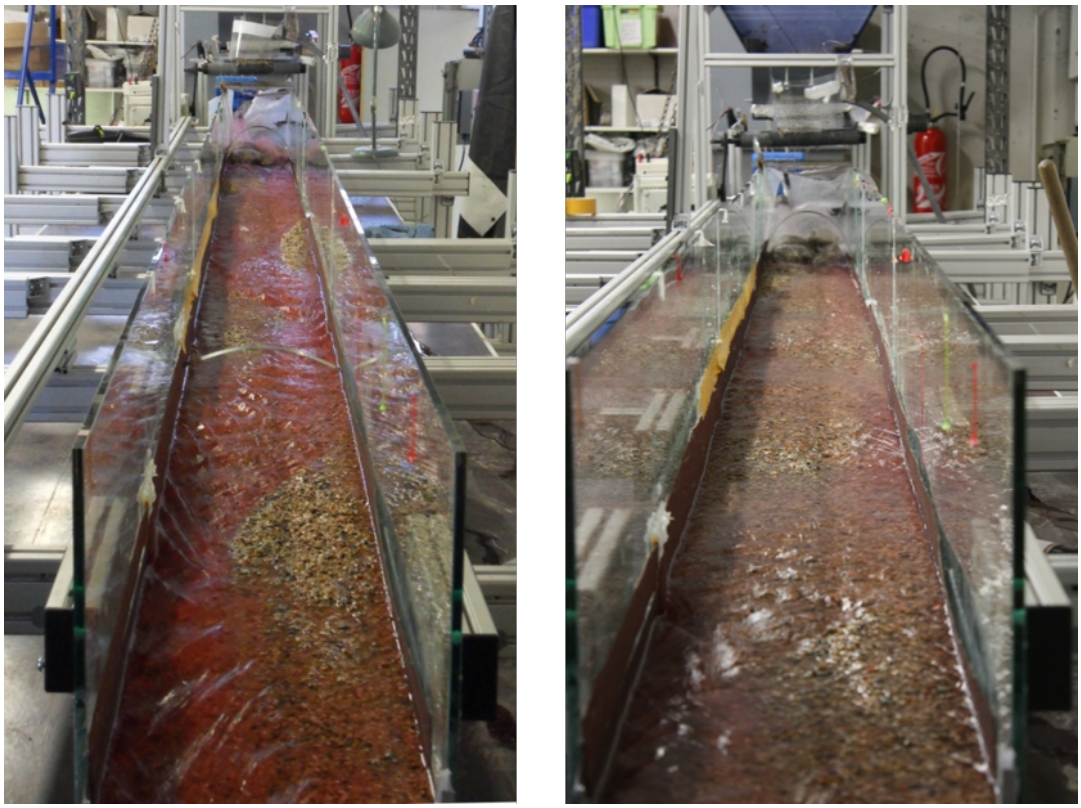

FIGURE 2.12: The two bed states periodically observed by Leduc (2013). Left panel: smooth state with intense transport rate, well defined channel and bars pattern. Right panel: congested state with a wider main channel.

Lanzoni carries out flume experiments on alternate bars with uniform sediments

(Lanzoni, 2000a) and with graded sediments (Lanzoni, 2000b) in order to bring out what is the effect of sediment heterogeneity on bars dynamics.

The two cases have the same conditions of discharge, slope, Shields parameter, width-to-depth ratio, and the bimodal mixture of the graded experiment has the same mean diameter of the sediments used in the uniform test. In so doing the comparison is designed with unchanged values of the dimensionless governing parameter θ, β, and d_s. Unfortunately two issues in these tests cause different values of θ and d_s in the non-uniform sediment case with respect to the uniform one. In the uniform case ripples and dunes are present on bars, whereas they do not take place in the graded sediment case. The resulting different flow resistance cause different θ values. θ and d_s values are different between the uniform case and the non-uniform case (and the bias increases with time as the non-uniform sediment experiments go on) also because of the coarsening of the transported sediment with respect to the bulk mixture composition, this coarsening is related to the winnowing of finer grains into the bed substrate, and recirculation feeding system appears not suitable in this case. Indeed in a recirculation feeding system the composition of transported sediment is significantly affected not only by dynamical armor but also by the intense longitudinal and vertical sorting due to bar formation. Anyway a subset of the experiments with uniform sediments is comparable with a subset of the experiments with non-uniform sediments.

As for the test with high values of shear stress and thus with both the grain fractions mobile migrating bars are observed. Sediment heterogeneity has a damping effect on bar height and and bar growth rate with respect to the uniform sediments case. The damping effect due to sorting weakens as θ increases, namely when equal mobility is approached. On the other hand, Lanzoni (2000b) observe no different values of bar wavelength in the comparison between the uniform sediment case and the graded one.

Finally we find worth recalling also the tests by Lanzoni (2000b) with low value of shear stress. These test are characterized by partial transport and no bars growth nor migration is observed. Only steady bars with similar wavelength of that of forced bars with uniform sediments (Lanzoni, 2000a) are present. The explanation given by Lanzoni is that these bars may be triggered by spatially growing disturbances originating from nonuniform initial conditions in the lateral distribution of grain sizes. The extremely low mobility of coarser particles, in fact, made it quite difficult to ensure a perfectly symmetrical feeding of the recirculated sediment. The formation of asymmetrical patches of coarse particles near the walls of the flume then induced a slight but permanent deflection of the flow which, in turn, enhanced the development of the observed long steady bars. This remark is worth-recalling since it draws attention on forcing terms which always have to be accounted for and recognized both in the field and in the laboratory when dealing with bars dynamics and river morphodynamics in general.

Lastly we report the study of Leduc (2013) and Garcia Lugo et al. (2015) about a flume configurations larger than alternate bars configurations. Leduc (2013) also reproduces a braided system with a slope of 1.5% using a bimodal mixture consisting of coarse and fine sands, ranging between 1.5 mm to 3 mm with a mean diameter of 1.8 mm, in order to study grain sorting phenomena in such unconfined flow configuration. These long experiments of more than 400 hours are compared with uniform sediment test on braiding patterns previously performed by Leduc (2013), in the attempt to shed some light on the effect of sorting in such flow configuration.

In each anabranch considered individually armoring process is observed; and fluctuations of channels width are relevant. A comprehensive follow-up of the channel evolution is indeed very difficult. The comparison of the two sets of experiments (the uniform sediment experiments and the non-uniform ones) results difficult and complex since the two series of tests seem characterized by different mechanisms concerning for instance the confluence of two active channels and in general the evolution of morphology.

Finally the experimental work by Garcia Lugo et al. (2015) is of interest to our research since it investigate the effect of lateral confinement on the different morphologies typical of gravel bed rivers.

The authors carry out a set of large flume experiments in conditions of dynamic equilibrium reproducing different bed morphologies by varying the channel width and the discharge. The experimental observations aim at understanding:

- how channel morphology change depending on the channel width and on the discharge;
- if bed elevation frequency distribution, obtained from Digital Elevation Models for a detailed 3D topography of the river bed, can be a good predictor for planform morphology;
- if the extent of dry areas within the active channel and the extent of the channel itself are related to channel configuration.

The above-listed objectives have elements in common with our research goals (introduced in chapter 1, outlined in section 2.5 and at the very beginning of chapter 4): Garcia Lugo et al. (2015) explore the effects of lateral constraint on channel morphologies performing experiments with uniform sediments; our experimental activity, focused on sorting, aims at investigating morphodynamic equilibrium states of flows over non-uniform sediments at varying lateral confinement, with a particular interest in sorting patterns.

2.5 Thesis objectives and methodology

Our literature review on mathematical modelling of mixed sediments morphodynamics revealed in the analytical domain the appearance of sorting waves, i.e. the instability driven by sorting, is acknowledged, but the distinct nature of the sorting and the bed eigenvalues did not receive the attention it deserved, mainly because the focus was more on the effect of sorting on bed forms than on the formation of sorting waves. We can find an exception in Seminara et al. (1996) in which bedload sheets are studied in details even if with a complex flow model suitable for dunes formation and dynamics, and this latter element makes the analysis rather complex and less focused on sorting waves. In this context, therefore we performed a stability analysis revisiting Seminara et al. (1996) with a simpler flow model. The latter allows for the formulation of an algebraic eigenvalue problem that can be solved analytically, allowing for a deep insight into the mechanisms that drive both topography-driven and roughness-driven instabilities and their interaction. This part of the thesis work is dealt with in chapter 3.

Our overview of experimental studies of flows over non-uniform sediments aiming at investigate dynamic equilibrium conditions revealed that they are not so numerous, and among them a targeted documentation of bed sediment composition

and thus sorting patterns occurring in the bed is lacking. Moreover a comprehensive understanding of flow confinement and "morphological print" on sorting features is still missing (a wide experimental activity on the dependence of channel morphologies on the lateral confinement has been performed in homogeneous sediment conditions (Garcia Lugo et al., 2015)). In this regard the present study aims at identifying grain sorting processes in the case of different degrees of flow confinement, considering first low constrained flows and then a confined flow. We performed three long morphodynamic runs differing from one another in respect of the flow lateral confinement. In each of them we aimed at investigating the feedback between the river bed variables, i.e. bed slope, bed sediment composition, active channel width, sediment transport rate. Particular attention is given to grain sorting processes and patterns. The set of experiments, whose configuration varies in flow lateral constraint, aimed at studying how the aspect ratio affects the "bed system" dynamics. With the objective of investigating the influence of lateral confinement on bed morphodynamics in general, and on grain sorting processes in particular, we decided to perform three runs varying the flume's width only, and maintaining all the other conditions unchanged. The experimental part of this thesis is reported in chapter 4.

3 Bedload transport of a sediment mixture: 1d linear stability analysis

Sediment sorting in rivers is almost ubiquitous since river beds have heterogeneous sediments which are transported by the flow in a different way, a selective way, during common flow conditions. Indeed, as illustrated in section 2.2, non-equal mobility and near-equal mobility conditions of bedload transport of heterogeneous sediments are the most common conditions, being the equal-mobility conditions characteristics of intense flood events.

Selective transport of heterogeneous sediments provokes sorting patterns on the river bed which in turn affect the sediment transport itself; and both sediment transport and sorting patterns have complex feedbacks with bed rivers parameters such as the slope and the channel width.

Moreover sorting also interacts with river bed forms, affecting their formation, morphology and migration, as it has been observed in bars and in braided patterns. There are even bed forms that do not seem to occur if sediments are homogeneous: bedload sheets are described, in field and in laboratory observations, as forms dominated by the effect of sorting (see subsections 2.3.1, 2.4.1 and 2.4.2).

Bedload sheets are precisely the bed forms we want to investigate through our stability analysis; we aim at a better understanding of those sediment patterns for which heterogeneity of sediments is a crucial mechanism for instability.

From a theoretical point of view linear stability analyses are an effective tool to shed light on the mechanisms playing a role in the formation of patterns of many kinds, and thus they represent an approach pretty applied for the study of river bed forms. In such context stability analyses were even performed dealing with heterogeneous sediments but not focusing on sorting; such analyses actually payed attention on topography driven perturbations (e.g. dunes, bars), see subsection 2.4.1.

On the contrary, we aim at performing a linear stability analysis focusing on instabilities arising from sorting. In particular, we will study a system consisting of a flow over an erodible bed composed of two sediment fractions. The equilibrium state of such system is the steady uniform flow in a infinitely wide channel with active sediment transport. We will superimpose to this equilibrium state two different perturbations: a perturbation of the bed elevation and a perturbation of the superficial concentration of the two sediment species. The latter is particularly important: we actually explore the case in which sediments undergo segregation processes, thus the grain size distribution of the bed surface is perturbed, and bed roughness depends on the grain size distribution of the bed surface. Hence we will express the granulometric perturbation as a roughness perturbation, in so doing we will introduce and deal at length an element of novelty in linear stability analysis of river

bed forms [1]. We will study the evolution over time of this twofold perturbation (i.e. bed elevation and bed roughness) in the framework of a sediment model with size-specific bedload transport.

3.1 An introduction to linear stability analysis in the context of river morphodynamics

The wide domain of river morphodynamics includes a large variety of fluvial bed forms, which are sediment patterns that develop and evolve at different space and time scales. These sediment patterns are of particular interest when they represent the morphology that freely takes place in unconfined alluvial rivers, indeed we restrict our study to some features of free bed forms.

The prediction of the morphodynamics of bed forms is possible using mathematical theories that consider a uniform flow over an erodible bed, the latter is assumed initially flat and free bed forms can arise from instabilities of the flow-bed interface.

The variety of bed forms can be classified in terms of the geometric (e.g. wavelength, amplitude, shape) or kinematic (e.g. upstream or downstream migration) characteristics of the bed form itself, in terms of the characteristics of the flow (e.g. subcritical or supercritical, hydraulically smooth or rough regime, amplitude and phase of the free-surface wave with respect to the bed wave) or of the sediments (e.g. finer or coarser material, transport as bedload or as suspended load). In general, more than one aspect is needed to mark the distinction.

Therefore, given a set of relevant flow and sediment parameters, predicting which of all sediment patterns will form is not an easy task (Colombini and Stocchino, 2012).

In this respect, linear stability analyses are a tool able to explore the mechanism responsible of sediment patterns formation (Colombini and Stocchino, 2012). In fact, linear analyses identify first, the relevant parameters controlling possible instability (e.g. width-to-depth ratio for bars, Froude number for dunes and antidunes, particle Reynolds number for ripples) and second, the range of values of such parameters for which sediment patterns are expected to form (as a result of instability arising from growing perturbations).

In order to understand where instability actually comes from we provide the explanation given by Colombini and Stocchino (2012) for which the origin of instability can be identified in the linearized form of the sediment mass-balance equation. Indeed, the linearized Exner equation contains a balance between stabilizing and destabilizing terms: gravity, which favours downhill motion of sediments, acts as a stabilizing effect, whereas the bed shear stress can be either destabilizing or stabilizing depending on its lag with respect to the bed profile. Other effects can be added to the two basic just mentioned, one of particular interest is the sorting effect which we will consider in the present work.

[1] We will perform a perturbation of the bed elevation and a perturbation of the bed roughness, whereas we will not perturb the Chézy coefficient and hence the Shields parameter; the reasons for that are provided in subsections 3.3.5 and 3.3.6. In order to investigate instabilities arising from sorting, the bed roughness perturbation is sufficient since the roughness height depends on the local value of the size density. As a consequence, a local increase of the coarser (finer) fraction implies a larger (smaller) roughness height, thus creating the necessary feedback between the bed composition and the flow.

However, non-linear stability analyses are needed to go beyond the information of the onset of bed forms formation, since at a linear level is only possible to determine if a certain pattern will form or not, and for which range of relevant parameters it will form. However, once established that in a region of the parameter space, the perturbations grow and thus instability drives bed forms formation, in order to know the amplitude of bed forms non-linear effects must be taken into account; for this, non-linear stability analyses are undertaken. Non-linear analyses not only provide information about the amplitude of bed forms but also provide corrections on celerity of propagation (with respect to the celerity obtained at the linear level) and information concerning possible interactions between different bed forms.

The parameter space

In the context of stability analyses of bed forms, the common relevant flow and sediment parameters are the Froude number Fr, the Shields number θ, the particle Reynolds number Re_p, and the dimensionless grain size d:

$$Fr = \frac{U^*}{\sqrt{gD^*}} \qquad \theta = \frac{u_f^{*2}}{(s-1)gd^*} \qquad Re_p = \frac{\sqrt{(s-1)gd^*}d^*}{\nu} \qquad d = \frac{d^*}{D^*} \tag{3.1}$$

where U^* is the dimensional flow velocity, D^* is the dimensional flow depth, u_f^* is the dimensional friction velocity, d^* is the dimensional grain diameter, g is the gravitational acceleration, s is the relative density of the sediment, and ν is the kinematic viscosity. We point out that star superscript denotes dimensional quantities. Fr, θ, Re_p, and d are interrelated with formulas, among which we provide the following familiar examples in 3.2; the first shows the conductance Chézy coefficient (its interrelation with the dimensionless grain size is easily identifiable) and the second shows the Shields parameter [2] as we are used to express it:

$$C = \frac{U^*}{u_f^*} = \frac{1}{k} ln\left(\frac{11.09D}{r}\right) \qquad \theta = \frac{Fr^2}{(s-1)dC^2} \tag{3.2}$$

in 3.2 k is the von Karman constant, taken as 0.4; r is the bed roughness and the roughness height R is typically set equal to one thirtieth of r; r in turns depends on the local value of the grain size d.

Furthermore, for the uniform flow the following equation applies

$$S = \frac{Fr^2}{C^2} \tag{3.3}$$

[2]The expression of the Shields parameter as in equation 3.2 is readily obtained starting from the definition of the Shields parameter, $\theta = \frac{T_t^*}{\rho(s-1)gd^*}$ where T_t^* and ρ are the dimensional bed shear stress and the water density, respectively; making use of the following definitions, $u_f^* = \sqrt{T_t^*/\rho}$, $C = \frac{U^*}{u_f^*}$, $d = \frac{d^*}{D^*}$; performing the following steps:

$$\theta = \frac{T_t^*}{\rho(s-1)gd^*} = \frac{\rho u_f^*}{\rho(s-1)gd^*} = \frac{U^{*2}}{(s-1)gd^*C^2} = \frac{U^{*2}}{(s-1)gdD^*C^2} = \frac{Fr^{*2}}{(s-1)dC^2}$$

Thus, given all these interrelation between such parameters and assuming hydraulically rough regime conditions, as it is usual for river bed forms (except for ripples (Colombini and Stocchino, 2011)), only two parameters are to be set to identify the state of the system: one between the dimensionless sediment grain size d and the conductance Chézy coefficient C, which are related by the first expression of 3.2, and one among the Froude number Fr and the Shields stress θ, which are related by the second expression of 3.2. This couple of parameters represents the parameter space, which has to be explored seeking the regions of instability.

Finally, we introduce the wavenumbers, which are functions of the wavelengths of bed forms (we recall that the latter present spatial periodicities). The longitudinal and transverse wavenumbers are

$$k_x = \frac{2\pi D^*}{L_x^*} \quad , \qquad k_y = \frac{2\pi D^*}{L_y^*} \tag{3.4}$$

where L_x^* and L_y^* are the wavelengths in the streamwise and spanwise direction, respectively. The longitudinal wavenumber applies to those bed forms periodic in the longitudinal streamwise direction (dunes, antidunes, ripples, roll-waves); the transverse wavenumber applies to those bed forms periodic in the transverse spanwise direction (sand ribbons); both the wavenumbers are necessary for the patterns that are periodic in both directions (alternate bars, oblique dunes).

The functioning of linear stability analysis

In the following, we outline what linear stability analysis of river bed forms is all about.

We consider a system that, for some values of its variables and parameters, is in equilibrium (the so-called base state). We slightly alter this base state through the superposition of a set infinitesimal disturbances on the base state itself. The linear stability analysis explores the stability of the base state, looking for the temporal evolution of the perturbations. Perturbations amplitude can grow or decay in time thus, the equilibrium is respectively stable or unstable with respect to the perturbations themselves.

In the context of river bed forms the base state consist of a steady uniform flow in an infinitely wide channel with active sediment transport. If in a certain region of the parameter space the base state is found to be unstable with respect to disturbances, it means that the uniform flow over a flat bed will not persist and the system will evolve towards a new equilibrium state characterized by the presence of bed forms.

Perturbations are assigned a specific spatial structure, in particular a periodic structure; depending on which perturbation we consider the spatial periodicity can be in the longitudinal streamwise direction (dunes, antidunes, ripples, roll-waves), in the transverse spanwise direction (sand ribbons), or in both the directions (alternate bars, oblique dunes). Perturbations also have a temporal structure that allows them to grow or decay in amplitude during propagation.

Hence, first the problem is formulated through a suitable set of equations for both the flow and sediment transport (a further discussion on the equations appropriately describing the dynamics of the flow-bed system is dealt with in sections 3.3, 3.4 and 3.5. Then we perform for each quantity of the equations the following expansion

using complex numbers

$$G(x,y,z,t) = G_0(z) + \varepsilon G_1(z) exp[ik_x(x - Wt) + ik_y] + c.c. \tag{3.5}$$

where G_0 represents the base state, ε is a small parameter, G_1 is the amplitude of the perturbation, i is the imaginary unity, W is the complex wave speed and k_x, k_y are the longitudinal and transverse wavenumbers, respectively. The notation $c.c.$ stands for the complex conjugate of the preceding quantity $\mathcal{O}(\varepsilon^0)$.

This expansion applied to each variable of the governing system, composed of equations and boundary conditions, is actually the linearization procedure. Then, terms with the same power in ε are collected. Equations describing the base state (a steady uniform flow in an infinitely wide channel) are obtained at $\mathcal{O}(\varepsilon^0)$, whereas at $\mathcal{O}(\varepsilon)$ a so-called eigenvalue problem is recovered, which allows for the determination of the complex wave speed W (the eigenvalue) as a function of the wavenumbers of the perturbations and of all the parameters appearing in the set of equations and boundary conditions that governs the system at hand.

The real and imaginary parts of the complex wave speed are linked to the bed forms' migration celerity and growth (or amplification) rate respectively.

$$\omega = \mathrm{Re}(W) \qquad \Omega = k_x \mathrm{Im}(W) \tag{3.6}$$

To sum up the substitution of the perturbations' functional structure 3.5 into the governing system allows quantifying how bed forms' growth rate and celerity depend on the relevant uniform flow parameters and on the bed forms' wavenumber.

About celerity, it quantifies bed forms' migration in time: a positive celerity corresponds to downstream propagation; a negative one corresponds to upstream propagation.

About amplification rate, it sets whether the base state is stable or not with respect to perturbations, i.e. it sets whether the bed forms do not develop or develop respectively. In particular, information about stability can be represented graphically through stability plots. Stability plots are contour plots representing the ranges of unstable (positive growth rate) and stable (negative growth rate) wavenumbers. Marginal (vanishing growth rate) curves mark the borders between stable and unstable regions. The wavenumber of maximum growth rate identifies the wavelengths that are likely to be selected by the instability process.

We illustrate these information about celerity and growth rate of bed forms in figure 3.1 adapted from Colombini (2004).

Colombini (2004) performs a linear stability analysis for dune and antidune formation and compares its model with the experimental data of Guy et al. (1966) as reported by Fredsøe (1974). Figure 3.1 is a stability plot which represents the growth rate for dunes, antidunes and ripples. The plot contains information about celerity as well.

As for the growth rate, white regions represent regions of the parameter space where bed forms are not expected to form (negative values of the growth rate, $\Omega < 0$), whereas colored regions are regions of instability (positive values of the growth rate, $\Omega > 0$). Thick solid line is the marginal curve ($\Omega = 0$).

As for the celerity, dashed lines are the curves of vanishing celerity ($\omega = 0$). In the upper right corner and in the "wedge" in the top of the plot the celerity is negative

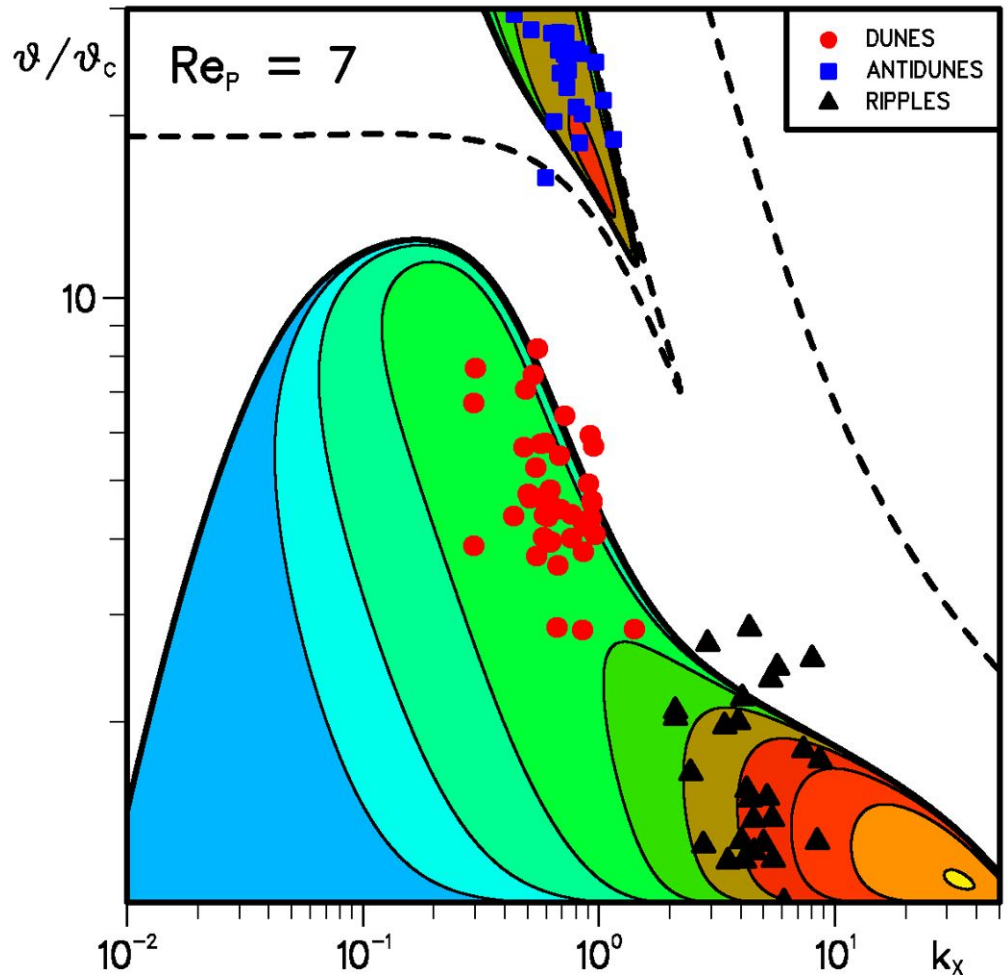

FIGURE 3.1: Stability plot resulting from the linear stability analysis for dune and antidune formation by Colombini (2004). The contourplot is the outcome of the mathematical model; markers represent experimental data by Guy et al. (1966).

implying an upstream migration (in accordance with experimental observations on antidunes); in the rest of the figure the celerity is positive and thus the migration of bed forms is in the downstream direction (as experimentally observed for dunes and ripples).

Here we settle for this short description of the principles of linear stability analysis; more details about the wavenumber selection and more detailed aspects of linear stability analysis in general will be discussed in the following sections dealing with our particular case study. This chapter deals with the hydrodynamic and morphodynamic instabilities in 1D shallow water flows; in particular the stability of a uniform flow over an erodible bed composed by a bimodal mixture of sediments is investigated by means of linear analysis.

In section 3.2 and 3.4 we provide the problem formulation; in particular, section 3.2 presents the flow equations starting with the governing equations and the closure relations until the conduct of the linearization procedure, whereas section 3.4 does the same with the sediment equations. Then sections 3.3 and 3.5 deal with the solution of a sequence of sub-cases of the whole problem formulated in sections 3.2 and 3.4. Namely section 3.3 addresses the hydrodynamic instability; section 3.5 deals with the morphodynamic instability, first considering the homogeneous sediment

case and then investigating the heterogeneous sediment case. Lastly, we provide a discussion of the analyses' results in section 3.6.

3.2 The flow equations

In this section the flow model is presented and thus the hydrodynamic instability is discussed. Indeed, the starting point of our analysis is the 1-D form of the governing equations of hydrodynamics in a straight channel. The triplet composed by the fluid density ρ, and by the uniform depth-averaged flow velocity U^* and depth D^* is used for nondimensionalization. In the following, a star apex denotes dimensional variables. It is convenient to write the equations in the Cartesian coordinate system sketched in figure 3.2, sloping with slope S. Three different interfaces are displayed in the picture. The curve $z = B(x,t)$ is the actual bed and the curve $z = B(x,t) + R(x,t)$ represents the reference level, R being the roughness height, i.e. the distance above the bed at which the logarithmic vertical profile of velocity conventionally vanishes. Moreover, we stipulate that the reference level sets the lower boundary of the flow, so that the free surface is represented by the curve $z = B(x,t) + R(x,t) + D(x,t)$, where D is the nondimensional local flow depth. When dealing with sediment sorting, it is particularly important to set the reference level as the sum of the bed elevation and the roughness height, since roughness is proportional to (coarse) grain diameters and thus a perturbation of the bed surface sediment composition (nothing but sorting!) corresponds to a perturbations of the bed roughness.

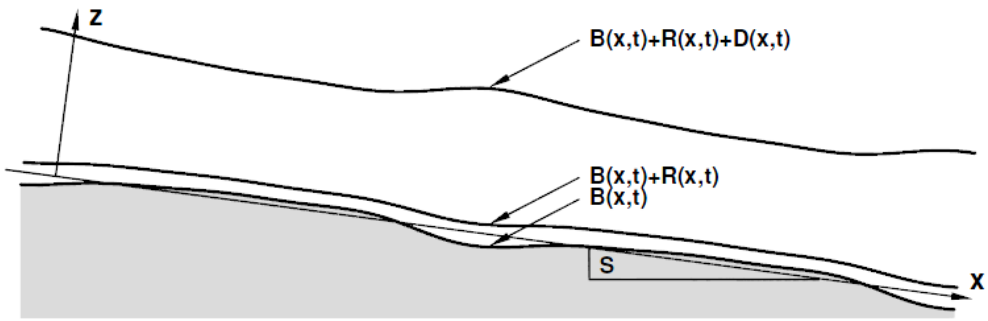

FIGURE 3.2: Sketch of a longitudinal profile of the flow configuration.

The appropriate flow model for our aim is a 1D depth-averaged flow model consisting of the nondimensional forms of the continuity and the unsteady Saint-Venant and equations

$$D_{,t} + UD_{,x} + DU_{,x} = 0 \tag{3.7}$$

$$U_{,t} + U_{,x} - \frac{S}{Fr^2} + \frac{1}{Fr^2}\left(B + R + D\right)_{,x} + \frac{T_t}{D} - \frac{1}{D}\left[\left(T_n - T_d\right)D\right]_{,x} = 0 \tag{3.8}$$

where D and U are the local values of the flow depth and velocity, S is the averaged bed slope and Fr is the Froude number of the base uniform flow, such that

$$Fr^2 = \frac{U^{*2}}{gD^*} \tag{3.9}$$

B and R are the bed and the roughness height respectively, and their sum gives the reference level that we just defined and sketched in figure 3.2; the bed shear stress is evaluated at the reference level (i.e. above the roughness).

Finally T_t, T_n and T_d represent the bed shear stress, the depth-averaged normal Reynolds stress and the dispersive stress, respectively. We have by definition

$$U = \frac{1}{D}\int_{B+R}^{B+R+D} u\,\mathrm{d}z \qquad T_t = u_f^2 = \frac{U^2}{C^2} = (\nu_t u_{,z})_{B+R}$$

$$T_n = \frac{2}{D}\int_{B+R}^{B+R+D} \nu_t u_{,x}\,\mathrm{d}z \qquad T_d = \frac{1}{D}\int_{B+R}^{B+R+D} (u-U)^2\,\mathrm{d}z$$

where u and ν_t are the vertical velocity and eddy viscosity respectively. Moreover, we stipulate that the vertical velocity profile is set equal to the one obtained under uniform condition, with the local value of U, C, R, B, D.

We introduce the following coordinates' transformation, which maps the channel, sketched in figure 3.2 in a rectangular domain. By this choice, the upper and lower boundaries are identified by a constant value of the transformed vertical coordinate ς; the upper boundary is the free surface represented by $\varsigma = 1$, the lower boundary is the reference level represented by $\varsigma = 0$.

$$\varsigma = \frac{z - B - R}{D}$$

Thus, we set a mixing length equal to

$$l = k(R + \varsigma D)(1-\varsigma)^{1/2}$$

which close to the bed is proportional to the distance from the bed and tends to vanish at the free surface with a half-power law.

This enable us to obtain the following relations expressed using the transformed vertical coordinate for the vertical velocity profile and the eddy viscosity respectively:

$$u = \frac{U}{kC} ln\left(\frac{R+\varsigma D}{R}\right) \qquad \nu_t = l^2 u_{,z} = \frac{kU}{C}(\varsigma D + R)(1-\varsigma) \tag{3.10}$$

The latter expressions allow us to write the depth-averaged flow velocity, the conductance Chézy coefficient, and the stresses in the transformed coordinate system:

$$U = \int_0^1 u\,\mathrm{d}\varsigma = \frac{U}{kC}\int_0^1 ln\left(\frac{R+\varsigma D}{R}\right)\mathrm{d}\varsigma \qquad C = \frac{1}{k}\left[ln\left(\frac{D}{R}\right) - 1\right]$$

$$T_d = \frac{1}{D}\int_0^1 (u-U)^2\,\mathrm{d}\varsigma = \frac{U^2}{k^2C^2} \qquad T_n = 2\int_0^1 \nu_t u_{,x}\,\mathrm{d}\varsigma = \frac{U^2}{C^2}\left[\left(\frac{U_{,x}}{U} - \frac{C_{,x}}{C}\right)\frac{D}{3}\left(kC_0 + \frac{1}{6}\right) - B_{,x} - \frac{1}{3}\frac{D}{R}R_{,x}\right]$$

The Chézy expression just provided applies in the limit $R << D$; moreover by setting $R = r/30$ we obtain

$$C = \frac{1}{k} ln \left(\frac{30D}{eR} \right) = \frac{1}{k} ln \left(\frac{11.04D}{r} \right)$$

which is the Keulegan relation for open-channel flow in infinitely-wide channels.

In short, after some algebra, the final expressions (in the transformed coordinate system) of the stresses and of the Chézy coefficient are set out below. Such expressions are the ones that we will perturb in the linearization procedure.

$$T_t = \frac{U^2}{C^2} \tag{3.11}$$

$$T_d = \frac{U^2}{k^2 C^2} \tag{3.12}$$

$$T_n = \frac{U^2}{C^2} \left[\left(\frac{U_{,x}}{U} - \frac{C_{,x}}{C} \right) \frac{D}{3} \left(kC_0 + \frac{1}{6} \right) - B_{,x} - \frac{1}{3} \frac{D}{R} R_{,x} \right] \tag{3.13}$$

$$C = \frac{1}{k} \left[ln \left(\frac{D}{R} \right) - 1 \right] \tag{3.14}$$

Now that the hydrodynamic problem is formulated in its equations and closure relations, the linearization procedure can be undertaken by expanding the generic quantity G as

$$G(x, y, z, t) = G_0(z) + \varepsilon G_1(z) exp[iK(x - Wt)] + c.c. \tag{3.15}$$

where ε is a small parameter, K and W are wavenumber and complex growth rate of the perturbation and *c.c.* stands for complex conjugate. (Comparing 3.5 to 3.15 we introduce a slight different notation about the longitudinal streamwise wavenumber denoted k_x in 3.5 and K in 3.15. Since we deal with a $1D$ only the wavenumber in the longitudinal direction can be considered, hence the reason of our simplified notation of 3.15).

Collecting terms with the same power of ε the following problems arise.

Base flow: $\mathcal{O}(\varepsilon^0)$

Substituting the splitting 3.15 into the nondimensional forms of the unsteady Saint-Venant and continuity equations and collecting terms of $\mathcal{O}(\varepsilon^0)$ we obtain the base state that consist of a uniform flow, so that, by definition we have:

$$U_0 = D_0 = 1 \tag{3.16}$$

$$T_{t0} = \frac{S}{Fr^2} = \frac{1}{C_0^2} \qquad C_0 = \frac{1}{k} ln \left(\frac{11.09}{r_0} \right) \tag{3.17}$$

$$R_0 = \frac{r_0}{30} = \frac{2.5 d_{50}}{30} = \frac{d_{50}}{12} \tag{3.18}$$

$$T_{d0} = \frac{1}{k^2 C_0^2} \qquad T_{n0} = 0 \tag{3.19}$$

where the median diameter d_{50} has been made nondimensional with the uniform flow depth D^*.

Linear level: $\mathcal{O}(\varepsilon)$

Substituting the splitting 3.15 into the nondimensional forms of the unsteady Saint-Venant and continuity equations and collecting terms of $\mathcal{O}(\varepsilon)$ the following set of algebraic equations is obtained

$$-iKWU_1 + iKU_1 + \frac{iK}{Fr^2}(B_1 + R_1 + D_1) + T_{t1} - T_{t0}D_1 - iK(T_{n1} - T_{d1} - T_{d0}D_1) = 0$$

$$-iKWD_1 + iKD_1 + iKU_1 = 0 \tag{3.20}$$

where

$$T_{t1} = 2T_{t0}\left(U_1 - \frac{C_1}{C_0}\right) \qquad T_{n1} = \frac{iK}{C_0^2}\left[\left(U_1 - \frac{C_1}{C_0}\right)N - B_1 - \frac{1}{3}\frac{R_1}{R_0}\right] \qquad T_{d1} = \frac{2}{k^2 C_0^2}\left(U_1 - \frac{C_1}{C_0}\right) \tag{3.21}$$

where

$$N = \frac{1}{3}\left(kC_0 + \frac{1}{6}\right)$$

Using the extended expressions of the Chézy coefficient and of the bed roughness at the linear level the stresses can be expanded as follows:

$$T_{t1} = \frac{2}{C_0^2}\left(U_1 - \frac{1}{kC_0}D_1 + \frac{1}{kC_0R_0}R_1\right) \tag{3.22}$$

$$T_{d1} = \frac{2}{k^2 C_0^2}\left(U_1 - \frac{1}{kC_0}D_1 + \frac{1}{kC_0R_0}R_1\right)$$

$$T_{n1} = \frac{iK}{C_0^2}\left(NU_1 - \frac{1}{kC_0}ND_1 - B_1 + \frac{1}{18}\frac{1}{kC_0R_0}R_1\right) \tag{3.23}$$

This enable us to rewrite the flow equations 3.20 isolating as coefficients U_1, D_1, B_1, and R_1, respectively the perturbations of the flow velocity, the water depth, the bed elevation, and the roughness height.

$$\begin{aligned}
&\left[1+\frac{2}{k^2C_0^2}-\frac{i}{KC_0^2}(2+K^2N)-W\right] \quad U_1 \quad + \\
&\left[1+\frac{1}{Fr^2}-\frac{2}{k^3C_0^3}(2+KN)+\frac{1}{k^2C_0^2}+\frac{i}{KC_0^2}\left(\frac{2+K^2}{kC_0}+1\right)\right] \quad D_1 \quad + \\
&\left[1+\frac{1}{Fr^2}+\frac{i}{KC_0^2}K^2\right] \quad B_1 \quad + \\
&\left[1+\frac{1}{Fr^2}+\frac{2}{k^3C_0^3R_0}-\frac{i}{KC_0^2}\left(\frac{2+K^2/18}{kC_0R_0}\right)\right] \quad R_1 \quad = 0 \\
&[1] \quad U_1 \quad + \quad [1-W] \quad D_1 \quad = 0
\end{aligned} \tag{3.24}$$

The flow equations can be rearranged in the following matrix form

$$\begin{pmatrix} a_{1U}-W & a_{1D} & a_{1B} & a_{1R} \\ 1 & 1-W & 0 & 0 \end{pmatrix} \begin{pmatrix} U_1 \\ D_1 \\ B_1 \\ R_1 \end{pmatrix} = 0 \tag{3.25}$$

where, according to equation 3.24, the entries of the matrix are

$$a_{1U} = 1+\frac{2}{k^2C_0^2}-\frac{i}{KC_0^2}(2+K^2N)-W$$

$$a_{1D} = 1+\frac{1}{Fr^2}-\frac{2}{k^3C_0^3}(2+KN)+\frac{1}{k^2C_0^2}+\frac{i}{KC_0^2}\left(\frac{2+K^2}{kC_0}+1\right)$$

$$a_{1B} = 1+\frac{1}{Fr^2}+\frac{i}{KC_0^2}K^2$$

$$a_{1R} = 1+\frac{1}{Fr^2}+\frac{2}{k^3C_0^3R_0}-\frac{i}{KC_0^2}\left(\frac{2+K^2/18}{kC_0R_0}\right)$$

The system 3.25 is an algebraic homogeneous system with complex entries; it is an eigenvalue problem, and the eigenvalues W are complex as well, namely they are the complex wave speeds, so that the growth rate and the celerity of the perturbations are linked to the imaginary and real part of W according to 3.6.

To sum up system 3.25 is the hydrodynamic problem, outcome of the linearization of the flow equations.

In section 3.4 we will carry out the same procedure for the sediment equations, thereby achieving the morphodynamic problem. However, before addressing the whole morphodynamic problem, it is worth analyzing the hydrodynamic problem (3.3), since a better understanding of the flow equation considering their terms (for instances the stresses) enables us to identify which components of the flow equations are essential and which are negligible in the framework of stability analysis. In so doing we can adopt the best form of the flow equations fitting our purpose; this particular form of the flow equations will be subsequently coupled to the sediment phase equations, and thus the complete morphodynamic problem obtained.

3.3 The hydrodynamic instability

This section address the hydrodynamic problem studying its solution in many subcases, from the most simplified to the most complex.

We study the hydrodynamic problem defined by the submatrix composed of the first two rows and the first two columns of 3.25 and no disturbances of the bed elevation and roughness height, namely $B_1 = R_1 = 0$ corresponding to a flow over a flat bed of constant roughness. Such configuration is described by the system set out below

$$\begin{pmatrix} a_{1U} - W & a_{1D} \\ 1 & 1 - W \end{pmatrix} \begin{pmatrix} U_1 \\ D_1 \end{pmatrix} = 0 \tag{3.26}$$

which can be rewritten in compact form as

$$(\mathbf{A} - W\mathbf{I})\,\mathbf{x}_1 = \{0\} \tag{3.27}$$

where $\mathbf{x}_1 = (U_1 D_1)^T$ is the vector of the unknowns. The system admits a non-trivial solution only for those specific values of W for which

$$\det(\mathbf{A} - W\mathbf{I}) = 0 \tag{3.28}$$

where $det()$ stands for the determinant of the array.

The eigenvalues are the roots of the quadratic eigenrelation

$$W^2 - \mathrm{tr}(\mathbf{A})W + \det(\mathbf{A}) = 0$$

$$\mathrm{tr}(\mathbf{A}) = 1 + a_{1U} \qquad \det(\mathbf{A}) = a_{1U} - a_{1D}$$

The coefficients of the 2x2 matrix $\mathbf{A}$ being complex, two complex eigenvalues are obtained as roots of the eigenrelation and we call them hydrodynamic eigenvalues:

$$W_h = \frac{1}{2}\left[(1 + a_{1U}) \pm \sqrt{(1 - a_{1U}^2 + 4a_{1D}}\right]$$

The two eigenvalues are easily found, but the complete solution is not particularly instructive, but rather, recalling that the growth rate and the celerity of the perturbations are linked to the imaginary and real part of the eigenvalues according to 3.6, is more interesting to extract the real and the imaginary parts of the eigenrelation as follows

$$\begin{cases} \omega^2 - \dfrac{\Omega^2}{K^2} - (1 + a_{1U}^r)\,\omega + a_{1U}^i \dfrac{\Omega}{K} + a_{1U}^r - a_{1D}^r = 0 \\ 2\omega\dfrac{\Omega}{K} - (1 + a_{1U}^r)\,\dfrac{\Omega}{K} - a_{1U}^i\omega + a_{1U}^i - a_{1D}^i = 0 \end{cases}$$

and to investigate the behaviour of the eigenrelation in some simplified cases, in order of increasing complexity. This will enable us to understand the way single terms of the flow equations affect the hydrodynamic instability. The terms that we will switch off and on in such analysis, by making the hydrodynamic problem

gradually more complex, are: the bed shear stress, the dispersive stress, the depth averaged normal Reynolds stress, the conductance Chézy coefficient. In particular, the conductance Chézy coefficient will be dealt with in the inviscid case, i.e. when it tends to infinity; when it has a constant value; and when it varies as a function of the water depth, according to the expression 3.2.

3.3.1 The inviscid approximation

In the case of the inviscid approximation we consider an ideal fluid, i.e. a frictionless flow. We can define such condition in proper, synthetic, mathematic terms: $C \to \infty$; indeed the Chézy coefficient is a measure of flow conductance or efficiency (that is, it is the inverse of flow resistance). In the inviscid case C is maximum and the stresses are zero.

$$T_{t0} = T_{d0} = 0 \qquad T_{t1} = T_{n1} = T_{d1} = 0$$

$$a_{1U} = 1 \qquad a_{1D} = -\frac{1}{Fr^2}$$

The system consisting of the real and imaginary part of the eigenrelation reads

$$\begin{cases} (\omega - 1)^2 - \dfrac{\Omega^2}{K^2} - \dfrac{1}{Fr^2} = 0 \\ (\omega - 1)\dfrac{\Omega}{K} = 0 \end{cases}$$

which provides

$$\Omega C_0^2 = 0 \qquad \omega = 1 \pm \frac{1}{Fr} \tag{3.29}$$

In this case the system is always marginal, i.e. the perturbations neither decay nor amplify. The celerity is dependent on the Froude number alone: the "fast" eigenvalue (the one with celerity given by $\omega = 1 + \frac{1}{Fr}$) always propagates downstream, whereas the "slow" eigenvalue (the one with celerity given by $\omega = 1 - \frac{1}{Fr}$) propagates downstream (upstream) for $Fr > 1$ ($Fr < 1$).

3.3.2 The Saint-Venant equations

In this subsection we pursue a line of argument aimed at assessing the effect of the individual stresses on the evolution of the perturbations. In particular we will not treat the flow as a frictionless flow anymore; we will add piece by piece the bed shear stress, the dispersive stress, and the depth-averaged normal Reynolds stress, making the momentum equation of the flow system gradually more and more complex. All the cases that we are about to discuss are characterized by a Chézy coefficient with a finite value. Such finite value can be constant or it can be dependent on the water depth.

First we discuss the simplest possible case just taking into account the bed shear stress, i.e. we disregard both the turbulent stress and the dispersive stress.

$$T_{d0} = 0 \qquad T_{d1} = T_{n1} = 0 \qquad T_{t1} = \frac{2}{C_0^2} U_1$$

$$a_{1U} = 1 - \frac{2i}{KC_0^2} \qquad a_{1D} = \frac{1}{Fr^2} + \frac{i}{KC_0^2}$$

$$\begin{cases} \left[(\omega - 1)^2 - \dfrac{1}{Fr^2} \right] K^2 - \Omega \left(\Omega + \dfrac{2}{C_0^2} \right) = 0 \\ 2 (\omega - 1) \left(\Omega C_0^2 + 1 \right) = 0 \end{cases}$$

We consider the behaviour of celerity and growth rate in the limits $K \to 0$ and $K \to \infty$; the limit $K \to 0$ is called the long wave limit corresponding to perturbation with large wavelength (and small wavenumber K given the definition in 3.4), the limit $K \to \infty$ is called the short wave limit corresponding to perturbation with short wavelength (and high values of the wavenumber).

Long wave limit: $K \to 0$

For $K \to 0$ the above system provides

$$\Omega C_0^2 \to -1 \pm 1 \qquad \omega \to 1 \pm \frac{1}{2} \tag{3.30}$$

In the long wave limit the fast eigenvalue is marginal, whereas the slow one is stable. Both the eigenvalues propagate downstream.

Short wave limit: $K \to \infty$

For $K \to \infty$ the above system provides

$$\omega \to 1 \pm \frac{1}{Fr} \qquad \Omega C_0^2 \to -1 \pm \frac{1}{2} Fr \tag{3.31}$$

In the short wave limit the celerities of the eigenvalues are the same that in the inviscid case.

The slow eigenvalue is always stable, whereas the fast eigenvalue becomes unstable in the supercritical regime, when $Fr > 2$ thus recovering roll-wave instability. It is worth noting that once the above threshold is exceeded, all the wavenumbers are simultaneously unstable and there is no mechanism of wavelength selection.

3.3.3 The effect of dispersive stress

Now we add to the simple case just discussed a non-zero dispersive stress, so that in the Saint-Venant equations both the bed shear stress and the dispersive stress are taken into account. No turbulent stress is considered nor any function of the Chézy coefficient which remains a constant value. Indeed we want to understand, in the context of hydrodynamic instability, the role of single additional terms of stresses

and Chézy expansion with respect to the reference case of the simple Saint-Venant equations. The Saint-Venant equations are actually widely used in river morphodynamics and it is worth figure out if we loose relevant information by neglecting the dispersive stress, the viscous stress, the depth-averaged normal Reynolds stress, and the dependence of the Chézy coefficient on the water depth.

Hence, in this case in which we want to investigate the role of the dispersive stress we have

$$T_{d0} = \frac{1}{k^2 C_0^2} \qquad T_{d1} = \frac{2}{k^2 C_0^2} U_1 \qquad T_{t1} = \frac{2}{C_0^2} U_1 \qquad T_{n1} = 0$$

$$a_{1U} = 1 + \frac{2}{k^2 C_0^2} - \frac{2i}{K C_0^2} \qquad a_{1D} = \frac{1}{Fr^2} + \frac{1}{k^2 C_0^2} + \frac{i}{K C_0^2}$$

In this case the system consisting of the real and the imaginary parts of the eigenrelation reads

$$\begin{cases} \left[\left(\omega - 1 - \dfrac{1}{k^2 C_0^2} \right)^2 - \dfrac{1}{k^4 C_0^4} - \dfrac{1}{k^2 C_0^2} - \dfrac{1}{Fr^2} \right] K^2 - \Omega \left(\Omega + \dfrac{2}{C_0^2} \right) = 0 \\ 2 \left(\omega - 1 - \dfrac{1}{k^2 C_0^2} \right) \left(\Omega C_0^2 + 1 \right) - 1 + \dfrac{2}{k^2 C_0^2} = 0 \end{cases}$$

As before, we consider the behaviour of celerity and growth rate in the long wave limit and in the short wave limit.

Long wave limit: $K \to 0$

For $K \to 0$ the above system provides

$$\Omega C_0^2 \to -1 \pm 1 \qquad \omega \to 1 + \frac{1}{k^2 C_0^2} \pm \frac{1}{2} \left(1 - \frac{2}{k^2 C_0^2} \right) \tag{3.32}$$

Short wave limit: $K \to \infty$

For $K \to \infty$ the above system provides

$$\begin{aligned} \omega &\to 1 + \frac{1}{k^2 C_0^2} \pm \sqrt{\frac{1}{Fr^2} + \frac{1}{k^2 C_0^2} + \frac{1}{k^4 C_0^4}} \\ \Omega C_0^2 &\to -1 \pm \frac{1}{2} \frac{1 - \frac{1}{k^2 C_0^2}}{\sqrt{\frac{1}{Fr^2} + \frac{1}{k^2 C_0^2} + \frac{1}{k^4 C_0^4}}} \end{aligned} \tag{3.33}$$

The dispersive stress provides a small correction of $\mathcal{O}(1/(k^2 C_0^2))$, the most important effect of which is to slightly increase the threshold of instability, which becomes

$$Fr \geq \frac{2}{\sqrt{1 - \frac{8}{k^2 C_0^2}}}$$

3.3.4 The effect of viscous stress

In this case we investigate the effect of the viscous stress on celerity and growth rate of the hydrodynamic eigenvalues. Hence we consider the Saint-Venant equations plus the depth-averaged normal Reynolds stress, whereas the dispersive stress is disregarded. As in the previous cases, the Chézy coefficient has no expansion, i.e. it has a constant value.

$$T_{d0} = 0 \qquad T_{d1} = 0 \qquad T_{t1} = \frac{2}{C_0^2} U_1 \qquad T_{n1} = \frac{iK}{C_0^2} N U_1$$

$$a_{1U} = 1 - \frac{2i}{K^2 C_0^2}\left(1 + K^2 \frac{N}{2}\right) \qquad a_{1D} = \frac{1}{Fr^2} + \frac{i}{K^2 C_0^2}$$

The system consisting of the real and imaginary parts of the eigenrelation reads

$$\begin{cases} \left[(\omega - 1)^2 - \dfrac{1}{Fr^2} - \dfrac{N}{C_0^2}\Omega\right] K^2 - \Omega\left(\Omega + \dfrac{2}{C_0^2}\right) = 0 \\ 2(\omega - 1)\left(\Omega C_0^2 + 1 + K^2 \dfrac{N}{2}\right) - 1 = 0 \end{cases}$$

In the long wave limit we recover the same solution obtained in the reference case of the simple Saint-Venant equation in which we have the bed shear stress only 3.30, so it is interesting to analyze only the short wave limit, where the viscous term plays an important role.

Short wave limit: $K \to \infty$

We set $\alpha = 1/K^2$ so that $\alpha \to 0$

$$\begin{cases} \left[(\omega - 1)^2 - \dfrac{1}{Fr^2} - \dfrac{N}{C_0^2}\Omega\right] - \alpha\Omega\left(\Omega + \dfrac{2}{C_0^2}\right) = 0 \\ 2(\omega - 1)\left[\alpha\left(\Omega C_0^2 + 1\right)\dfrac{N}{2}\right] - \alpha = 0 \end{cases}$$

From the second equation it follows

$$\omega = 1 \tag{3.34}$$

so that setting $\alpha = 0$ the first equation provides

$$\Omega = -\frac{C_0^2}{Fr^2 N} \tag{3.35}$$

We note that the small parameter α multiplies the higher-order term of the eigenrelation, and this suggests the possibility of a singular perturbation problem. Indeed, the missing root tends to infinity as $\alpha \to 0$.

If we expand the growth rate as

$$\Omega = \Omega_0 + \frac{\Omega_1}{\alpha} + \frac{\Omega_2}{\alpha^2} + \dots$$

the two roots are found to be

$$\Omega^+ = -\frac{C_0^2}{nFr^2} \qquad \Omega^- = -\frac{2}{C_0^2} + \frac{C_0^2}{NFr^2} - \frac{N}{C_0^2\alpha} \tag{3.36}$$

In the short wave limit ($K \to \infty, \alpha \to 0$) both the growth rates are negative and this imply that the viscous term has a damping effect.

Furthermore, since the growth rate of the fast eigenvalue, for any $Fr > 2$, vanishes for $K \to 0$, is positive for intermediate values of K and negative for large K, there must be a maximum in the growth rate that marks the wavelength that will be linearly selected.

Hence the viscous term related to the depth-averaged Reynolds normal stress is to be held responsible for providing the wavelength selection mechanism in the roll-wave instability.

Both the damping effect and the wavelength selection due to the viscous term related to the depth-averaged Reynolds normal stress are displayed graphically in the following.

The growth rate and the wave speed associated with the two hydrodynamic eigenvalues are plotted in figure 3.3, for several values of the Froude number, as a function of the wavenumber. The curves of one eigenvalue called "fast eigenvalue" are plotted in solid lines, the curves of the second eigenvalues the so called "slow eigenvalue" are plotted in dashed lines. The two eigenvalues are labelled "fast" and "slow" respectively because comparing their celerity with unity (i.e. with the depth-averaged, uniform flow velocity used for nondimensionalization), the former is characterized by the plus sign, the latter by the minus. In the long wave limit ($K \to 0$), both perturbations travel downstream (a positive celerity corresponds to downstream propagation), the slow one being always stable (a negative growth rate corresponds to an exponentially decaying perturbation), the fast one being marginal (a vanishing growth rate corresponds to a perturbation who neither amplifies nor decays). In the short wave limit ($K \to \infty$), the fast perturbation always travels downstream, whereas the slow perturbation travels upstream (downstream) for Froude numbers smaller (larger) than unity (i.e. in the subcritical (supercritical) flow regime).

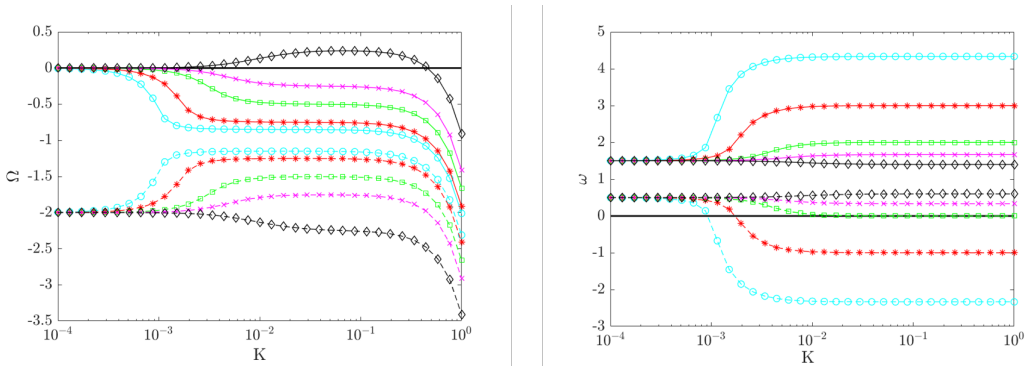

FIGURE 3.3: The growth rate (left panel) and the wave speed (right panel) of the fast (solid upper lines) and slow (dashed bottom lines) hydrodynamic eigenvalues are plotted versus the wavenumber for several values of the base Froude number (black diamonds, Fr = 2.5; magenta crosses, Fr = 1.5; green squares, Fr = 1; red stars, Fr = 0.5; cyan circles, Fr = 0.3), $C_0 = 17$. These solutions are computed including the viscous term.

The growth rate of the fast and slow eigenvalues decreases significantly in the range

of large wavenumbers, actually the growth rate drops towards negative values. We can safely affirm that this damping effect is originated by the viscous term related to the depth-averaged Reynolds normal stress: it is sufficient to compare the left panel of figure 3.3 with the left panel of figure 3.4.

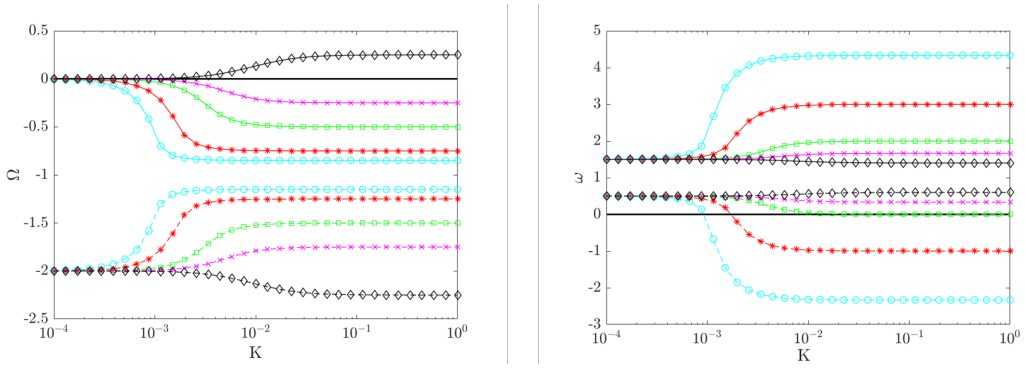

FIGURE 3.4: The growth rate (left panel) and the wave speed (right panel) of the fast (solid upper lines) and slow (dashed bottom lines) hydrodynamic eigenvalues are plotted versus the wavenumber for several values of the base Froude number (black diamonds, Fr = 2.5; magenta crosses, Fr = 1.5; green squares, Fr = 1; red stars, Fr = 0.5; cyan circles, Fr = 0.3), $C_0 = 17$. These solutions are computed neglecting the viscous term.

Figure 3.4 represents the solutions computed without taking into account the viscous term (i.e. when $T_n = 0$) and it shows that the growth rate does not decrease for large wavenumbers. Then the viscous term actually acts as a stabilizing effect, whereas it has no effect on the celerity of the perturbations (right panel of figures 3.3 and 3.4).

Furthermore, we can visualize the stabilizing effect of $T_n \neq 0$ looking at the stability plot of the fast eigenvalue, i.e. the contour plot of the growth rate associated with the fast eigenvalue (it is possible to observe, left panel of figures 3.3 and 3.4, that the slow eigenvalue is always stable, whereas the fast eigenvalue is unstable for $Fr > 2$).

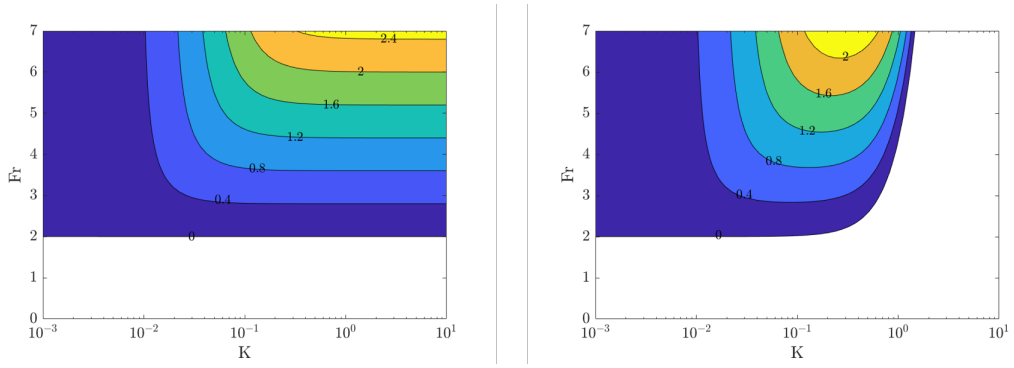

FIGURE 3.5: The growth rate of the fast eigenvalue for the hydrodynamic problem. Left panel: the viscous term is neglected ($T_n = 0$). Right panel: the viscous correction is taken into account ($T_n \neq 0$). The solution is computed for $C_0 = 17$.

Figure 3.5 not only shows the stabilizing effect due to the viscous correction in the range of large wavenumbers, it also shows that the viscous term leads to a cut-off mechanism (a range of wavelengths is cut off) and to a wavelength selection mechanism. The cut-off due to the viscous term is of particular importance: if T_n is neglected, as soon as the Froude number exceeds the critical threshold all the modes

in the short wave range are equally unstable. In such case the physical interpretation of the stability results is not particularly appealing because no wavelength of maximum amplification is selected by means of a normal mode analysis.

Thus is therefore necessary to keep the term T_n in the flow momentum equation because of its double relevant role in linear analysis of hydrodynamic instability and then of morphodynamic instability as well.

Nevertheless, we finally point out that the physical meaningfulness of the stability results is achieved when considering T_n, but the mathematical meaningfulness is still present when T_n is neglected. Indeed also when T_n is neglected (left panel of figure 3.5) the unstable region is bounded, namely the growth rate associated to the eigenvalue has a finite upper bound, independently of the wavenumber. The problem is adequate from a mathematical if unstable regions are bounded; in fact bounded unstable regions make the problem regular in the sense of Birkhoff (1954) and thus the problem is mathematically well-posed.

3.3.5 The effect of the Chézy perturbation in the bed shear stress

In order to complete our investigation on the role of different stresses and possible Chézy expansion on growth rate and celerity of the hydrodynamic eigenvalues, we study in the following the effect of considering the Chézy coefficient not as a constant but rather dependent on the water depth. In this scenario we have the dispersive and viscous terms of the stresses set equal to zero and a more refined expression of the bed shear stress which has a part coming from the expansion of the Chézy coefficient; indeed we are considering the case simple Saint-Venant equations plus dependence of C on D. Thereby we set

$$T_{d0} = 0 \qquad T_{d1} = T_{n1} = 0 \qquad T_{t1} = \frac{2}{C_0^2}\left(U_1 - \frac{1}{kC_0^2}D_1\right)$$

$$a_{1U} = 1 - \frac{2i}{KC_0^2} \qquad a_{1D} = \frac{1}{Fr^2} + \frac{i}{KC_0^2}\left(\frac{2}{kC_0^2} + 1\right)$$

The system consisting of the real and the imaginary parts of the eigenrelation reads

$$\begin{cases} \left[(\omega-1)^2 - \dfrac{1}{Fr^2}\right]K^2 - \Omega\left(\Omega + \dfrac{2}{C_0^2}\right) = 0 \\ (\omega-1)\,\Omega C_0^2 + \omega - \dfrac{3}{2} - \dfrac{1}{kC_0} = 0 \end{cases}$$

Long wave limit: $K \to 0$

For $K \to 0$ the above system provides

$$\Omega C_0^2 \to -1 \pm 1 \qquad \omega \to 1 \pm \frac{1}{2}\left(1 + \frac{2}{kC_0}\right) \tag{3.37}$$

Short wave limit: $K \to \infty$

For $K \to \infty$ the above system provides

$$\omega \to -1 \pm \frac{1}{Fr} \qquad \Omega C_0^2 \to 1 \pm \frac{1}{2} Fr \left(1 + \frac{2}{kC_0}\right) \tag{3.38}$$

Considering the dependence of the Chézy coefficient on flow depth, a small correction of $\mathcal{O}(1/(kC_0))$ is found. The general behaviour of the eigenvalues remains the same.

3.3.6 The adopted form of the flow momentum equation

The study of the subcases addressed in the subsections 3.3.2, 3.3.3, 3.3.4, 3.3.5 is necessary in order to understand which is the degree of refinement the flow momentum equation must have for the purpose of a 1D linear stability analysis of mixed sediment morphodynamics. Actually by analyzing the effect of each term of the flow momentum equation on the hydrodynamic stability, it is possible to find the stabilizing/destabilizing effect of single terms, precisely the stresses terms (subsections 3.3.3, 3.3.4) and the terms arising from considering the Chézy coefficient not constant (subsection 3.3.5).

As for the stresses terms, we analyzed the case in which the flow momentum equation consist in the Saint-Venant equation (subsection 3.3.2), hence only the bed shear stress is present, and we compared this "basic" case with the case "flow momentum equation with both bed shear stress and dispersive stress" (subsection 3.3.3) and with the case "flow momentum equation with both bed shear stress and viscous stress" as well (subsection 3.3.4).

In the case "flow momentum equation with both bed shear stress and dispersive stress" (subsection 3.3.3) we found that the dispersive stress has a very slight stabilizing effect, compared to the case with the bed shear stress only; hence we can consider its contribution negligible.

In the case "flow momentum equation with both bed shear stress and viscous stress" (subsection 3.3.4) we found that the viscous term arising from to the depth averaged normal Reynolds stress has two relevant effects compared to the case with the bed shear stress only. First, the viscous term has a damping effect in the short wave range; second, it provides a cut-off and a wavelength selection mechanism. Hence we account for the viscous stresses in the flow momentum equation.

As for the perturbation of the Chézy coefficient (subsection 3.3.5) we analyzed the effect of considering the Chézy coefficient dependent on the flow depth compared to the case of considering the Chézy coefficient constant. We found that in the two cases the general behaviour of the eigenvalues remains the same, thus the perturbations of the Chézy coefficient does not yield an appreciable effect on instability mechanisms. We therefore consider the Chézy coefficient as a constant (reasonably acceptable as long as C is large compared to R).

To sum up, we neglect:

- the dependence on the flow depth of the Chézy coefficient, then $C = C_0 = constant$;

- the role of the dispersive stresses, then $T_{D0} = T_{D1} = 0$.

We obtain therefore simpler expressions of T_{t1} and T_{n1} compared to equations 3.22 and 3.23

$$T_{t1} = \frac{2}{C_0^2} U_1 \tag{3.39}$$

$$T_{n1} = \frac{iK}{C_0^2} \left(N U_1 - B_1 - \frac{1}{3} \frac{R_1}{R_0} \right) \tag{3.40}$$

and consequently, the following "new version" of the flow equations:

$$\begin{aligned}
&\left[1 - \frac{i}{KC_0^2}(2 + K^2 N) - W\right] \quad U_1 \quad + \\
&\left[\frac{1}{Fr^2} + \frac{i}{kC_0^2}\right] \quad D_1 \quad + \\
&\left[\frac{1}{Fr^2} + \frac{iK}{C_0^2}\right] \quad B_1 \quad + \\
&\left[\frac{1}{Fr^2} + \frac{iK}{3C_0^3 R_0}\right] \quad R_1 \quad = 0 \\
&[1] \quad U_1 \quad + \quad [1 - W] \quad D_1 \quad = 0
\end{aligned} \tag{3.41}$$

Indeed the stresses in 3.39 and 3.40 are simpler than their expression in 3.22 and 3.23 respectively. Accordingly flow equations in 3.41 have a simpler formulation than 3.24. However this simpler formulation does not represent an oversimplification: indeed we maintain all the terms, in their more appropriate form, which play a relevant role in stability analysis.

3.4 The sediment equations

As for the sediment transport model, the minimal ingredients are the Exner equation and a suitable relationship that provides the amount of sediment moving as bedload, a relation in terms of the Shields stress. If transport in suspension has to be considered, then an additional equation for the sediment concentration along the depth must be introduced.

Thus the simplest sediment transport model is the one consisting of just one equation, the Exner equation, i.e. only a mass balance equation when sediments are all the same size and only transported as bedload.

Conversely considering the bedload transport of an heterogeneous mixture of sediment of different sizes and thus studying sorting processes, we need a more complex formulation for the sediment transport model, since the continuous grain size distribution is approximated by a finite number of steps and a set of Exner-like equations is introduced for each sediment fraction. As a result of the sorting process, finer and coarser sediment tend to accumulate in different positions along the bed form, altering the value of the local roughness with respect to the well-mixed

uniform base state. As a consequence, also the flow model should be able to provide a response to variation of bed roughness as well as bed elevation.

Since our aim is to investigate sorting processes, we use a complex formulation of the sediment model taking into account a sediment mixture. We restrict our case study to a bimodal sediment mixture.

We provide a grain-size specific nondimensional Exner equation from which we obtain two Exner-like equations at the linear level. The latter together with the flow equations form the morphodynamic system, the study of which provides information about the morphodynamic instabilities. To treat the bedload transport of our bimodal sediment mixture, a simple three-layer model is used, which implements the concept of 'active layer' of Hirano (1971), defined as the layer of sediment close to the bed interface which is available for entrainment into bedload and that is affected by depositional processes.

The active layer model of Hirano is a mass conservation model for mixed-size sediments where sediments' distribution provides for a vertical structure. Indeed three sediments' layers are present in the active layer model of Hirano: the bedload layer (in the water column), the active layer (the topmost part of the bed), and the substrate (below the active layer). These three layers have different sediment compositions, i.e. different volume fraction contents. For each fraction of the sediment distribution, sediment transfer is considered through the interface between the substrate and the active layer, and specific functional forms for transfer are taken into account both during degradation and aggradation.

Our aim is not to describe the vertical flux of sediments originating from changes in elevation of the interface between the active layer and the substrate as considered in the Hirano model, rather we just want to point out that the Hirano model has a vertical structure from the point of view of sediment fraction content.

Conversely in our stability analysis we neglect any vertical structure inside the sediment layers: bedload layer and bed layers, in particular the active layer, have the same grain size distribution. We warrant this point of our analysis by the fact that first, the active layer has no vertical structure, i.e. it is well mixed as in the Hirano model, and second, there is no interaction between the active layer and substrate assuming that only a minimal amount of aggradation and degradation takes place.

To characterize the size distribution of the mixture composing the bed, we make use of d^*_{50}, introducing the sedimentological $\phi-$scale as:

$$d^*(\phi) = d^*_{50} 2^{-\phi+\phi_{50}} \tag{3.42}$$

The mass density for the grain size ϕ in the active layer is denoted as $F(\phi; x, t)$, where, by definition

$$\int_{-\infty}^{\infty} F(\phi) \mathrm{d}\phi = 1 \tag{3.43}$$

The first and second moment of the density provide the mean grain size ϕ_m and standard deviation σ_m (on the $\phi-$scale) of the F distribution as

$$\phi_m = \int_{-\infty}^{\infty} \phi F(\phi) \mathrm{d}\phi \qquad \sigma_m^2 = \int_{-\infty}^{\infty} (\phi - \phi_m)^2 F(\phi) \mathrm{d}\phi \tag{3.44}$$

from which the characteristic diameters d^*_g and d^*_σ can be calculated

$$d_g^* = d_{50}^* 2^{-\phi_m+\phi_{50}} \qquad d_\sigma^* = d_{50}^* 2^{-\phi_m+\phi_{50}+\sigma_m} \tag{3.45}$$

It is just worth noting that in the case of a log-normally distributed sediment

$$\phi_m = \phi_{50} \qquad d_g^* = d_{50}^* \qquad d_\sigma^* = d_{50}^* 2_{\sigma_m} = d_{84}^* \tag{3.46}$$

where d_{84}^* is the size such that 84 percent of the mass of a sample is finer. This grain size is close to d_{90}^*, which is often considered as representative of both the roughness of the bed and the thickness of the active layer. However, in the present work we want to investigate the mechanisms which drive and are driven by sorting and, to this end, we are particularly interested in well-sorted mixtures which exhibit only a small degree of heterogeneity (and prove that even in this condition sorting instabilities arise). Since, in the following, we are going to restrict our attention to the case of weak sorting, defined as $\sigma_m << 1$, we can safely make use of d_g^* instead of d_σ^* in the determination of roughness and of the active layer thickness.

The bed shear stress and the volumetric grain-specific sediment discharge per unit width are made nondimensional using d_{50}^*

$$\theta = \frac{T_t^*}{\rho(s-1)gd_{50}^*} \qquad q_s = \frac{q_s^*}{\sqrt{(s-1)gd_{50}^*}d_{50}^*} \tag{3.47}$$

where θ is the Shields stress, ρ is the fluid density and s is the relative density of the sediment.

Imposing sediment mass conservation, a grain-size specific nondimensional Exner equation is obtained that reads

$$FB_{,t} + L_a F_{,t} + \gamma q_{s,x} = 0 \tag{3.48}$$

where $F(\phi)$ is the mass density for the grain size ϕ in the active layer, L_a is the active layer thicknes, $q_s(\phi)$ is the nondimensional volumetric sediment discharge per unit width and

$$\gamma = \frac{\sqrt{(s-1)gd_{50}^*}d_{50}^*}{(1-p_s)U^*D^*} = \frac{\sqrt{(s-1)d_{50}^3}}{Fr(1-p_s)} \tag{3.49}$$

is a small parameter of the order $\mathcal{O}(10^{-3})$ that represents the ratio between the characteristic time scales of the flow discharge and of the flux of sediment motion; p_s is the sediment porosity.

The nondimensional volumetric sediment discharge per unit width $q_s(\phi)$ is expressed in terms of grain-size specific sediment discharge as follows

$$q_s(\phi) = q_u(\phi)F(\phi) \tag{3.50}$$

where q_u is the transport density per unit content in the active layer. A closure equation is needed for q_u, which is assumed to depend on the fraction grain size through one of the many empirical relationships available in the literature for homogeneous sediment. More precisely we adopt the fractional approach from Parker et al. (1982)

$$
\begin{aligned}
q_u(\phi) &= \theta^{3/2}\Phi\left[\zeta(\phi)\right] \qquad \zeta(\phi) = \frac{\theta}{\theta_c}\frac{d^*_{50}}{d^*_g}\left(\frac{d^*_g}{d^*(\phi)}\right)^b \\
\theta &= \frac{T^*_t}{\rho(s-1)gd^*_{50}} = \frac{T_t Fr^2}{(s-1)d_{50}}
\end{aligned}
\tag{3.51}
$$

where θ_c is the critical Shields stress for sediment motion and the effect of hiding is included in the definition of $\zeta(\phi)$.

The function $\Phi(\zeta)$ depends on the empirical relation adopted; we take the relation of Wong and Parker (2006) coming from a reanalysis and correction of the bedload relation of Meyer-Peter and Müller [3]. It reads

$$
\Phi(\zeta) = 3.97\left(1 - \frac{1}{\zeta}\right)^{3/2} \tag{3.52}
$$

For completeness we summarize in table 3.1 the most used relations for the function $\Phi(\zeta)$ together with the corresponding values of the critical Shields stress.

TABLE 3.1: The function $\Phi(\zeta)$ and the corresponding value of the critical Shields stress for several empirical relation.

Meyer-Peter and Müller (1948)	$8(1-1/\zeta)^{1.5}$	0.047
Ashida and Michiue (1972)	$17(1-1/\zeta)(1-1/\sqrt{\zeta})$	0.06
Parker (1978)	$11.2(1-1/\zeta)^{4.5}$	0.03
Wilcock and Crowe (2003)	$14(1-1/\sqrt{\zeta})^{4.5}$	0.0288
Wong and Parker (2006)	$3.97(1-1/\zeta)^{1.5}$	0.0495

Note that the perturbation approach followed herein requires Φ to be continuous with continuous derivatives, so that we have assumed the function to be valid in the whole interval $\zeta > 1$, accepting a small error in the limit $\theta \to \theta_c$, where the function Φ is known to become less accurate.

The exponent b in 3.51 controls the hiding effect. Two limiting cases are of relevance: when b vanishes, the 'equal mobility' case is recovered, whereby the transport densities of the fractions are all equal to each other and depend on the local value of the Shields stress built upon the geometric mean size. On the contrary, when b is set to unity, the transport density of each fraction depends on the local value of the Shields stress built upon the fraction grain size, as if the bed were composed by that sediment alone. We set b to the value of 0.095, as in Parker (1990), so that even if the same function Φ is used for all grain sizes, the mobility of each fraction is not exactly identical. Indeed, a small positive value of b corresponds to finer material being slightly more mobile than the coarser one. As a consequence, under uniform conditions the bed surface is coarser than the bedload and selective transport of surface grains can take place whenever uniform conditions are perturbed.

[3] We adopted the Wong and Parker (2006) relation after careful thought; indeed at first we wanted to use the Parker and Sutherland (1990) bedload relation for mixtures. However, the latter defines $\Phi(\zeta)$ as a step function; but actually in linear (and non linear as well) stability analyses it is better to deal with continuous functions with continuous derivatives. Indeed the problem at the linear level, $\mathcal{O}(\varepsilon)$ terms, (as well as at the non-linear level,$\mathcal{O}(\varepsilon^2)$ terms) requires deriving all the quantities of the governing equations.

Finally, we show in the following the way we can account for the effect of gravity on grains, whereby grains move more easily downhill than uphill: we reduce the critical Shields stress of an amount proportional to the local slope

$$\theta_c = \theta_{ch} - \mu\,(S - B_{,x}) \qquad \theta_{ch} = 0.0495 \tag{3.53}$$

where θ_c is the constant value appearing in table 2.1 and the constant μ has been set equal to 0.1 after Fredsøe (1974).

Now that the morphodynamic problem is formulated since we set the nondimensional grain-size specific Exner equation and a closure equation for the transport density per unit content, we can undertake the linearization procedure.

We recall that the result of the of the linearization procedure at the linear level consists of two Exner-like equations that together with the flow equations form the morphodynamic problem.

Hence we expand the generic quantity of the Exner equation as

$$G(x,y,z,t) = G_0(z) + \varepsilon G_1(z) exp[iK(x - Wt)] + c.c.$$

where ε is a small parameter, K and W are the wavenumber and the complex growth rate of the perturbation respectively and *c.c.* stands for complex conjugate. Collecting terms with the same power of epsilon the following problems arise.

Base flow: $\mathcal{O}(\varepsilon^0)$

The base state consists, as already stated, in a uniform flow, so that the Exner equation does not provide any additional information, since, under uniform flow conditions, the bed neither experiences aggradation nor degradation. The following relationships hold

$$\phi_{m0} = \phi_{50} \qquad d_{g0} = d_{50} \qquad \text{by definition}$$

$$q_{u0}(\phi) = \theta_0^{3/2}\Phi\left[\zeta_0(\phi)\right] \qquad \zeta_0(\phi) = \frac{\theta_0}{\theta_{c0}} 2^{b(\phi-\phi_{m0})} \tag{3.54}$$

$$\theta_0 = \frac{T_{t0}Fr^2}{(s-1)d_{g0}} = \frac{Fr^2}{C_0^2(s-1)d_{g0}} \qquad \theta_{c0} = \theta_{ch} - \mu S = \theta_{ch} - \mu\frac{Fr^2}{C_0^2} \tag{3.55}$$

$$q_{s0}(\phi) = F_0(\phi) q_{u0}(\phi) \qquad L_{a0} = 2d_{g0} \tag{3.56}$$

$$\int_{-\infty}^{\infty} F_0(\phi)\mathrm{d}\phi = 1 \qquad \phi_{m0} = \int_{-\infty}^{\infty} F_0(\phi)\phi\mathrm{d}\phi \qquad \sigma_0^2 = \int_{-\infty}^{\infty} F_0(\phi)\phi^2\mathrm{d}\phi \; - \phi_{g0}^2 \tag{3.57}$$

Linear level: $\mathcal{O}(\varepsilon)$

Substituting the splitting 3.15 in 3.48 and collecting terms of $\mathcal{O}(\varepsilon)$ we obtain

$$-WF_0B_1 - WL_{a0}F_1 + \gamma q_{s1} = 0 \tag{3.58}$$

where

$$q_{s1} = q_{u0}F_1F_0q_{u1} \qquad q_{u1} = \theta_0^{3/2}\left\{\frac{3}{2}\Phi_0\frac{\theta_1}{\theta_0} + \Phi_0'\zeta_0\left[\zeta_0\frac{\theta_1}{\theta_0}\frac{\theta_{c1}}{\theta_{c0}} - (1-b)\frac{d_{g1}}{d_{g0}}\right]\right\} \tag{3.59}$$

$$\frac{\theta_1}{\theta_0} = \frac{T_{t1}}{T_{t0}} \qquad \theta_{c1} = iK\mu B_1 \qquad \frac{d_{g1}}{d_{g0}} = \frac{r_1}{r_0} = \frac{R_1}{R_0} = -ln(2)\phi_{m1} \tag{3.60}$$

where Φ' denotes the derivative of Φ with respect to ζ.

Finally:

$$\int_{-\infty}^{\infty} F_1(\phi)\mathrm{d}\phi = 0 \qquad \phi_{m1} = \int_{-\infty}^{\infty} F_1(\phi)\phi\mathrm{d}\phi \qquad \sigma_1 = \frac{1}{2\sigma_0}\int_{-\infty}^{\infty} F_1(\phi)\phi^2\mathrm{d}\phi \; - 2\phi_{m0}\phi_{m1} \tag{3.61}$$

Equation 3.58 can be integrated in ϕ leading to

$$-WB_1 + \gamma q_{s1} = 0 \tag{3.62}$$

where

$$q_{s1} = \int_{-\infty}^{\infty} q_{s1}(\phi)\mathrm{d}\phi \tag{3.63}$$

is the perturbation of the total sediment discharge per unit width.

Equation 3.62 can be substituted in equation 3.58 leading to

$$-WL_{a0}F_1(\phi) + \gamma q_{s1} - \gamma F_0(\phi)q_{s1} = 0 \tag{3.64}$$

Equations 3.62 and 3.64 are the sediment equations of the linear system that control morphodynamic instabilities.

Assuming that the size distribution of the mixture can be approximated by means of N fractions, there are N eigenvalues and the associated eigenvectors are composed by N unknowns: the amplitude of the bed perturbation B_1 plus those of the size densities $F_1(\phi_i)$, with $i = 1, 2, \ldots, N$-1, the last density $F_1(\phi_N)$ being determined by the condition that the summation of all F_1 must vanish.

Consistently we have N-1 equations from equation 3.64 and one from 3.62.

As already stated, we consider the simplest possible case of heterogeneous sediment mixture: a bimodal mixture composed by two fractions in the same proportion.

Hence

$$F_0^a = F_0^b = \frac{1}{2} \qquad F_1^a = -F_1^b \tag{3.65}$$

$$\phi_a = \phi_{m0} + \sigma_0 \qquad \phi_b = \phi_{m0} - \sigma_0 \qquad \phi_{m1} = 2\sigma_0 F_1^a \tag{3.66}$$

where the apexes a and b refer to the finest and the coarsest fractions, respectively. Moreover, recalling equation 3.60, the mean grain size at the linear level ϕ_{m1}, the perturbation of the grain size distribution F_1^a, and the bed roughness R are interrelated as follows

$$F_1^a = -\frac{R_1}{2\sigma_0 ln(2) R_0} \tag{3.67}$$

the expressions of the of the perturbed fraction specific sediment flux q_{u1} and of the perturbed total sediment flux q_{s1} become

$$q_{s1}^n = q_{u0}^n F_1^n + F_0^n q_{u1}^n \qquad n = a, b$$

$$q_{s1} = q_{s1}^a + q_{s1}^b = \left(q_{u0}^a - q_{u0}^b\right) F_1^a + \frac{1}{2}\left(q_{u0}^a + q_{u0}^b\right)$$

and we can put them in the two Exner-like equations 3.62 and 3.64.

Furthermore we introduce the following synthetic notations

$$q_{ui}^S = \frac{1}{2}\left(q_{u0}^a + q_{u0}^b\right) \qquad q_{ui}^D = \frac{1}{2}\left(q_{u0}^a - q_{u0}^b\right) \qquad i = 0, 1$$

$$q_{u0}^n = \frac{2}{3}\alpha^n \qquad q_{u0}^n = \alpha^n \frac{\theta_1}{\theta_0} + \beta^n \left[\frac{\theta_1}{\theta_0} + \frac{\theta_{c1}}{\theta_{c0}} - (1-b)\frac{d_{g1}}{d_{g0}}\right]$$

$$\alpha^n = \frac{3}{2}\theta_0^{3/2}\Phi_0^n \qquad \beta^n = \theta_0^{3/2}\Phi_0'^n \zeta_0^n$$

where

$$\frac{\theta_1}{\theta_0} = \frac{T_{t1}}{T_{t0}} = 2U_1 \qquad \theta_{c1} = iK\mu B_1$$

$$\frac{d_{g1}}{d_{g0}} = \frac{r_1}{r_0} = \frac{R_1}{R_0} = -2\sigma_0 ln(2) F_1^a$$

The sediment equations can be rewritten in the following matrix form

$$\begin{pmatrix} \gamma a_{3U} & 0 & \gamma a_{3B} - W & \gamma a_{3R} \\ \gamma' a_{4U} & 0 & \gamma' a_{4B} & \gamma' a_{4R} - W \end{pmatrix} \begin{pmatrix} U_1 \\ D_1 \\ B_1 \\ R_1 \end{pmatrix} = 0 \tag{3.68}$$

where

$$\gamma' = \frac{\gamma ln(2) R_0}{L_{a0}} \tag{3.69}$$

$$a_{3U} = 2\left(\alpha^S + \beta^S\right) \qquad a_{3B} = -\beta^S \frac{iK\mu}{\theta_{c0}} \qquad a_{3R} = -\beta^S \frac{(1-b)}{R_0} - \frac{2}{3}\frac{\alpha^D}{\sigma_0 ln(2) R_0} \tag{3.70}$$

$$\begin{aligned} a_{4U} = -2\sigma_0\left(\alpha^D + \beta^D\right) \qquad a_{4B} = \sigma_0 \beta^D \frac{iK\mu}{\theta_{c0}} \\ a_{4R} = \sigma_0 \beta^D \frac{(1-b)}{R_0} + \frac{2}{3}\frac{\alpha^S}{\gamma ln(2) R_0} \end{aligned} \tag{3.71}$$

Adding to the system 3.68 the flow equations as in 3.41 we obtain the complete eigensystem for the morphodynamic problem of a bimodal mixture, as follows

$$\begin{pmatrix} a_{1U} - W & a_{1D} & a_{1B} & a_{1R} \\ 1 & 1 - W & 0 & 0 \\ \gamma a_{3U} & 0 & \gamma a_{3B} - W & \gamma a_{3R} \\ \gamma' a_{4U} & 0 & \gamma' a_{4B} & \gamma' a_{4R} - W \end{pmatrix} \begin{pmatrix} U_1 \\ D_1 \\ B_1 \\ R_1 \end{pmatrix} = 0 \tag{3.72}$$

The submatrix composed of the first two rows and the first two columns (corresponding to $B_1 = R_1 = 0$) defines the hydrodynamic eigenvalue problem that controls roll-waves instability. Indeed only the flow equations and only the perturbations on flow velocity and flow depth are considered. Actually we obtain the hydrodynamic problem addressed in section 3.3.

The non-zero perturbations of bed elevation and roughness height are considered introducing the sediment equations and thus the study of morphodynamic instabilities. In the discussion of the morphodynamic problem we will show that in the case of homogeneous sediment only the bed elevation perturbation is possible and, clearly, no roughness height perturbation is possible; whereas in the case of heterogeneous sediment mixture both B_1 and R_1 are possible. In particular, R_1 comes from a local perturbation of the surface texture composition in terms of different granulometric fractions. The latter not only affects the roughness height but also the conductance Chézy coefficient (3.2) (as well as the sediment flux), thus creating the necessary feedback between the bed composition and the flow.

Precisely the submatrix composed of the first three rows and the first three columns (corresponding to $R_1 = 0$) defines the coupled morphodynamic eigenvalue problem that controls bed form instability for homogeneous sediment. This last problem provides three complex eigenvalues, two related to the evolution of the hydrodynamic perturbations and one related to the evolution of the bed elevation perturbation. The three eigenvalues are obtained as roots of the following cubic eigenrelation

$$\begin{aligned} W^3 - \left(1 + a_{1U} + \gamma a_{3B}\right) W^2 + \left[a_{1U} - a_{1D} + \gamma\left(a_{3B} + a_{3B} a_{1U} - a_{1B} a_{3U}\right)\right] W + \\ \gamma\left[a_{1B} a_{3U} + a_{3B}\left(a_{1D} - a_{1U}\right)\right] = 0 \end{aligned} \tag{3.73}$$

The morphodynamic problem for homogeneous sediments is dealt with in the first

part of section 3.5.

Lastly the whole system (3.72) describes the morphodynamic problem for heterogeneous sediments in which both the perturbations of the sediment phase are considered, $B_1 \neq 0$ and $R_1 \neq 0$. This case is dealt with by choosing as heterogeneous sediment mixture a bimodal mixture; the problem is addressed in the second part of section 3.5.

Dealing with the morphodynamic problem, both the homogeneous sediment case and the heterogeneous sediment case, two possible approaches are possible: the first consists of a decoupling of the equations, splitting the hydrodynamic and morphodynamic equations, following the quasi-steady approximation, and the second provides for a fully coupled problem treating the problem as fully unsteady.

In this thesis work we address the morphodynamic instabilities following the quasi-steady approach illustrated in its principles and in its particular application to our case study in section 3.5.

3.5 Morphodynamic instability

3.5.1 The quasi-steady problem

The quasi-steady assumption, widely adopted in the literature, is based on the fact that the characteristic time scales of the flow and of the sediment transport are quite different one from the other, the latter being much longer than the former.

The quasi-steady hypothesis consists in the assumption whereby the flow instantaneously adapts to changes in bed elevation and roughness. Hence the time derivatives are neglected in the flow equations and therefore we deal with the steady non-dimensional form of the Saint-Venant and continuity equations.

The quasi-steady problem provides in our case only two 'morphodynamic' eigenvalues coming from a quadratic problem whose solution consists of two complex eigenvalues related to the bed perturbation and sorting perturbation. We recall that the sorting perturbation is interrelated to the roughness perturbation as in 3.60. Indeed roughness depends on grain size of sediments on the bed surface and we explore the case in which these sediments undergo grain segregation processes, thus the grain size distribution in the bed is perturbed.

Hence, enforcing the quasi-steady hypothesis, the flow equations are in their steady form and can be rewritten in the following matrix form

$$\begin{pmatrix} a_{1U} & a_{1D} & a_{1B} & a_{1R} \\ 1 & 1 & 0 & 0 \end{pmatrix} \begin{pmatrix} U_1 \\ D_1 \\ B_1 \\ R_1 \end{pmatrix} = 0 \tag{3.74}$$

The system 3.74 in turn can be expressed in the following non-homogeneous system representing the forced problem describing the flow response to the perturbations of bed elevation and bed roughness

$$\begin{pmatrix} a_{1U} & a_{1D} \\ 1 & 1 \end{pmatrix} \begin{pmatrix} U_1 \\ D_1 \end{pmatrix} = -B_1 \begin{pmatrix} a_{1b} \\ 0 \end{pmatrix} - R_1 \begin{pmatrix} a_{1R} \\ 0 \end{pmatrix} \tag{3.75}$$

The system 3.75 can be split in two problems, the solution of which is the flow response (in terms of U_1 and D_1) to a unit perturbation of the bed elevation (first problem in 3.76) and to a unit perturbation of the roughness (second problem in 3.76)

$$\begin{pmatrix} a_{1U} & a_{1D} \\ 1 & 1 \end{pmatrix} \begin{pmatrix} U_{1B} \\ D_{1B} \end{pmatrix} = -B_1 \begin{pmatrix} a_{1B} \\ 0 \end{pmatrix} = - \begin{pmatrix} a_{1B} \\ 0 \end{pmatrix}$$
$$\begin{pmatrix} a_{1U} & a_{1D} \\ 1 & 1 \end{pmatrix} \begin{pmatrix} U_{1R} \\ D_{1R} \end{pmatrix} = -R_1 \begin{pmatrix} a_{1R} \\ 0 \end{pmatrix} = - \begin{pmatrix} a_{1R} \\ 0 \end{pmatrix} \tag{3.76}$$

Precisely (U_{1B}, D_{1B}) and (U_{1R}, D_{1R}) are the solution of the first and second system in 3.76 respectively. The solution of the non-homogeneous system with both the bed elevation perturbation and the roughness perturbation (3.75) is given by

$$U_1 = U_{1B}B_1 + U_{1R}R_1 \qquad D_1 = D_{1B}B_1 + D_{1R}R_1$$

$$U_{1B} = -D_{1B} = -\frac{a_{1B}}{a_{1U} - a_{1D}} \qquad U_{1R} = -D_{1R} = -\frac{a_{1R}}{a_{1U} - a_{1D}}$$

Not only U_1 and D_1 but also all the other flow quantities can be expressed as the composition of a part proportional to B_1 and a part proportional to R_1, in particular the bed shear stress T_{t1} can be expressed as stated in the following

$$T_{t1} = 2T_{t0}U_1 = 2T_{t0}\left(U_{1B}B_1 + U_{1R}R_1\right) = T_{t0}\left(T_{t1B}B_1 + T_{t1R}R_1\right)$$

$$T_{t1B} = 2U_{1B} = -2\frac{1 + iKFr^2/C_0^2}{Fr^2 - 1 - iFr^2\left(3 + K^2N\right)/KC_0^2}$$

$$T_{t1R} = 2U_{1R} = -2\frac{1 + iKFr^2/3C_0^2R_0}{Fr^2 - 1 - iFr^2\left(3 + K^2N\right)/KC_0^2}$$

Hence the sediment equations can be rewritten as follows

$$\begin{pmatrix} \gamma\left(a_{3B} + a_{3U}U_{1B}\right) - W & \gamma\left(a_{3R} + a_{3U}U_{1R}\right) \\ \gamma'\left(a_{4B} + a_{4U}U_{1B}\right) & \gamma'\left(a_{4R} + a_{4U}U_{1R}\right) - W \end{pmatrix} \begin{pmatrix} B_1 \\ R_1 \end{pmatrix} = 0 \tag{3.77}$$

The sediment problem in 3.77 can be studied in the uni-size sediment case, thus considering only a bed elevation perturbation, and can be studied as well considering not only a bed elevation perturbation but also a granulometric perturbation, and so study the two-size sediment mixture case. Both the cases are addressed and compared in the present subsection.

The homogeneous sediment case

In the study of the morphodynamic quasi-steady problem described by 3.77 we obtain the uni-size case by imposing $R_1 = 0$ and then recovering the single eigenvalue

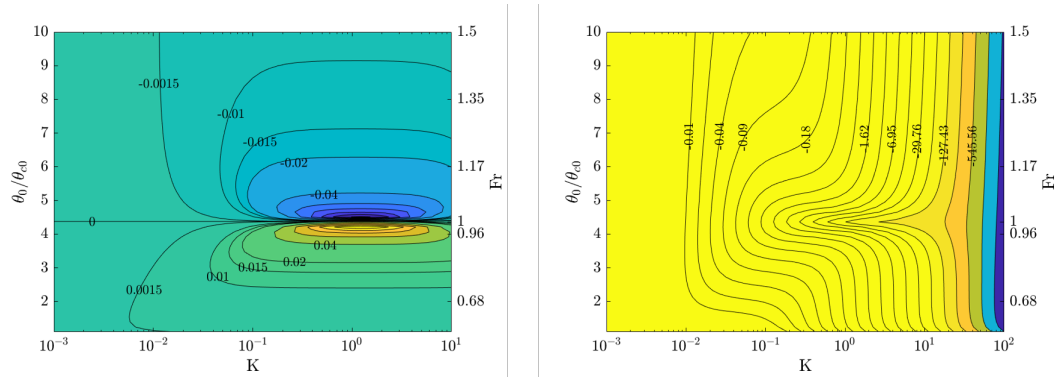

FIGURE 3.6: The celerity (left panel) and the growth rate (right panel) of the bed eigenvalue for the morphodynamic problem under quasi-steady hypothesis, unisize sediment case. The solution is computed for $C_0 = 14.5$.

$$W = \gamma \left(a_{3B} + a_{3U} U_{1B} \right) = \gamma \left[\left(\alpha^S + \beta^S \right) \frac{T_{t1B}}{T_{t0}} - \beta^S \frac{iK\mu}{\theta_{c0}} \right] \tag{3.78}$$

Recalling the definition in 3.6 we can analyze the growth rate and the celerity of the bed elevation perturbation linked respectively to the imaginary part and real part of the eigenvalue as follows

$$\begin{aligned} \Omega = K\mathrm{Im}(W) = \gamma K^2 \left[\left(\alpha^S + \beta^S \right) \frac{\mathrm{Im}\left(T_{t1B} \right)}{K T_{t0}} - \beta^S \frac{\mu}{\theta_{c0}} \right] \\ \omega = \mathrm{Re}(W) = \gamma \left(\alpha^S + \beta^S \right) \frac{\mathrm{Re}\left(T_{t1B} \right)}{T_{t0}} \end{aligned} \tag{3.79}$$

Growth rate and celerity of the single eigenvalue given by the equation 3.78, which we label "bed eigenvalue", are represented graphically in figure 3.6.

Both the expressions in 3.79 show that both the growth rate and of the celerity are proportional to γ, implying that the timescale on which bed waves evolve and propagate is much longer than that of the flow perturbations, as expected.

The expression of Ω in 3.79 shows that stability is related to the imaginary part of the bed shear stress, $\mathrm{Im}\left(T_{t1B} \right)$, and in particular the latter must be positive for instability to take place. Actually, the sign of the growth rate, and thus the growing or decay of the perturbation, is governed by a subtle balance between the term $\mathrm{Im}\left(T_{t1B} \right)$ and the term $\beta^S \frac{\mu}{\theta_{c0}}$, associated with the effect of gravity, which favours downhill motion of sediments. The expression of Ω in 3.79 also shows that gravity acts as a stabilizing effect so that a necessary condition for instability is that the imaginary part of the bed shear stress must be positive. Specifically for the morphodynamic problem under quasi-steady hypothesis in the unisize sediment case the growth rate is consistently negative, i.e. the balance between the imaginary part of the bed shear stress and the term associated with the effect of gravity always results negative. This implies a decay of bed perturbations of any wavelength, independently of the Froude number.

As for the celerity, it is controlled by the real part of the bed shear stress as formulated in the expression of ω in 3.79. In particular a positive value of the celerity corresponds to downstream propagation, a negative value to upstream migration,

as represented in figure 3.6.

Setting, for simplicity, $T_{n1} = 0$ we have

$$T_{t1B} = -2\frac{1}{Fr^2 - 1 - 3iFr^2/KC_0^2}$$

$$\mathrm{Im}\left(T_{t1B}\right) = \frac{-6/KC_0^2}{\left(1-Fr^2\right)^2 + 9/KC_0^2} \qquad \mathrm{Re}\left(T_{t1B}\right) = \frac{2\left(1-Fr^2\right)}{\left(1-Fr^2\right) + 9/KC_0^2}$$

Hence the bed eigenvalue is always stable and propagates upstream for supercritical flows and downstream for subcritical flows.

Note that in the short wave range $K \to \infty$ the imaginary and real part of the bed shear stress turn out

$$\mathrm{Im}\left(T_{t1B}\right) \to \frac{-6}{KC_0^2\left(1-Fr^2\right)^2} \qquad \mathrm{Re}\left(T_{t1B}\right) \to \frac{2}{\left(1-Fr^2\right)}$$

and a resonance appears as $Fr \to 1$ whereby

$$\begin{array}{lllll} \text{for} & Fr \to 1^+ & \omega \to -\infty & \Omega \to -\infty \\ \text{for} & Fr \to 1^- & \omega \to +\infty & \Omega \to -\infty \end{array}$$

Whereas far from the resonance the celerity of the bed eigenvalue (i.e. the single eigenvalue in the uni-size sediment case) turns out

$$\omega = \gamma\left(\alpha^S + \beta^S\right)C_0^2\frac{2}{1-Fr^2}$$

The heterogeneous sediment case

In the study of the morphodynamic quasi-steady problem 3.77 we obtain the two-size mixture case considering the whole system of the two Exner-like equations, namely considering both the bed elevation perturbation and the granulometric perturbation non-zero: $B_1 \neq 0, R_1 \neq 0$.

For this case the eigenrelation reads

$$\begin{aligned} W^2 - \left[\gamma\left(a_{3B} + a_{3U}U_{1B}\right) + \gamma'\left(a_{4R} + a_{4U}U_{1R}\right)\right]W \quad + \\ +\gamma\gamma'\left[\left(a_{3B} + a_{3U}U_{1B}\right)\left(a_{4R} + a_{4U}U_{1R}\right) - \left(a_{3R} + a_{3U}U_{1R}\right)\left(a_{4B} + a_{4U}U_{1B}\right)\right] \quad = \quad 0 \end{aligned} \tag{3.80}$$

Hence, two solutions are obtained and they consist of two distinct eigenvalues, one eigenvalue associated to the bed elevation perturbation and one eigenvalue associated to the granulometric perturbation (i.e. a bed sediment composition perturbation, corresponding to a bed roughness perturbation, see equation 3.67); the two eigenvalues are labelled respectively "bed eigenvalue", W_{bed}, and "sorting eigenvalue", W_{sort}.

The bed eigenvalue does not change remarkably with respect to the homogeneous sediment case. Figure 3.7 shows the same behaviour of both the celerity and the growth rate of the bed eigenvalue obtained for the homogeneous sediment case (figure 3.6); however the plots in figure 3.6 are not identical to those in 3.7 since in the latter, representing the two-grain mixture case, the bed eigenvalue and the sorting eigenvalue are not independent and the granulometric perturbation affects the bed elevation perturbation.

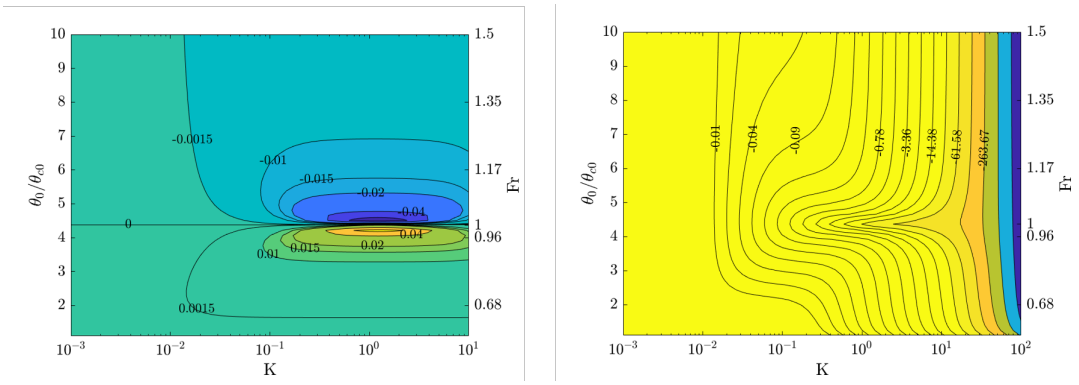

FIGURE 3.7: The celerity (left panel) and the growth rate (right panel) of the bed eigenvalue for the morphodynamic problem under quasi-steady hypothesis, two-grain mixture case. The solution is computed for $C_0 = 14.5$ and $\sigma_0 = 10^{-3}$.

The sorting eigenvalue has a behaviour very different from the bed eigenvalue and much more interesting, both concerning the wave speed and the growth rate.

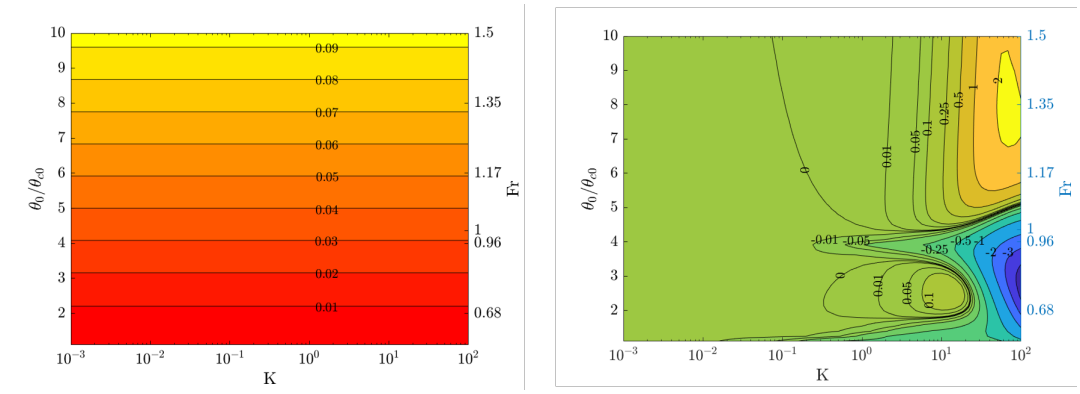

FIGURE 3.8: The celerity (left panel) and the growth rate (right panel) of the sorting eigenvalue for the morphodynamic problem under quasi-steady hypothesis, two-grain mixture case. The solution is computed for $C_0 = 14.5$ and $\sigma_0 = 10^{-3}$.

The celerity of the sorting eigenvalue, on the left in figure 3.8, is always positive, sorting waves' celerity is larger than bed waves' celerity, but it is smaller than flow perturbations' celerity (see for instance the celerity of the "fast" eigenvalue in the right panel of figure 3.3). This ensures that sorting sorting and bed perturbations do not travel faster than flow perturbations, a quite unrealistic and unphysical result. However this line of reasoning can be pursued more rigorously by means of an order of magnitude analysis, the objective of which is to provide the order of the flow perturbations, the bed perturbation, and the sorting perturbation. Such order of magnitude analysis is not shown in this work; we think however that it is an interesting point to add to the stability analysis and, thus, it is among the perspectives of the thesis. We would stress that the celerity of the sorting eigenvalue is

larger than the celerity of the sorting eigenvalue (compare the left panel of figures 3.7 and 3.8 in accordance with Stecca et al. (2014). This means that the perturbation of the bed sediment composition travels always downstream and much faster than the bed elevation perturbation. The celerity increases with the Froude number and is insensitive to the wavenumber.

The growth rate of the sorting eigenvalue becomes positive, leading to instability, as opposite to the bed eigenvalue, which is invariably negative. In particular, figure 3.8 shows for Chézy equal to 14.5 two regions of instability arising one for subcritical flows and one for supercritical flows. Both the unstable regions are bounded. Instability takes place for wavenumbers rather large. The upper ($Fr > 1$) unstable region clearly presents a wavelength mechanism, as the minima of the isolines show. Similarly, the lower ($Fr < 1$) unstable region presents a wavelength mechanism, as the maxima of the isolines show.

The stability plot in figure 3.8 is computed for $\sigma_0 = 10^{-3}$, hence instability arises even when sorting is constrained to be weak by the condition of a small standard deviation of the two-grain mixture. Precisely the value of $\sigma_0 = 10^{-3}$ is small with respect to ϕ_{g0}, the median grain size in the sedimentological ϕ-scale, or in general with respect to the size of the two grains of the mixture, the finer $\phi_a = \phi_{g0} + \sigma_0$ and the coarser $\phi_b = \phi_{g0} - \sigma_0$ (equation 3.66).

Whereas the celerity does not change its behaviour for varying Chézy value, the growth rate remarkably change depending on C_0. Hence we do not represent the wave speed for different values of C_0, it is always positive and not dependant on K, we rather report in figure 3.9 the stability plots for $C_0 = 13.5, 14.5, 15.5, 16.5, 17.2, 17.55$, these Chézy values respectively characterize the plots from top left to bottom right.

We can first observe that all the unstable regions in the stability plots of figure 3.9 are bounded, i.e. the growth ate has a maximum value in the short wave range: for each unstable wavenumber a maximum value of the amplification rate is found.

All the unstable regions present a cut-off mechanism except the top left plot for $C_0 = 13.5$; indeed the mechanism of wavelength selection as described for figure 3.8 is always present except the top left plot for $C_0 = 13.5$. In all the cases instability takes place for large values of wavenumbers.

For $C_0 = 13.5$, top left panel, only one region of instability is present, namely in the parameter space for $Fr > 1$. Increasing the Chézy coefficient an unstable region for subcritical flows appears while the unstable region for supercritical flows gets narrow, top right panel of figure 3.9. Continuing to increase C_0 the subcritical unstable region widens and the supercritical unstable region narrows. For intermediate values of C_0 as those of the central plots of figure 3.9, 15.5 and 16.5 in the left and right panel respectively, the "closing" [4] of the upper unstable region is more evident and the wavelength selection is clear for both the unstable regions. Finally for $C_0 = 17.55$, bottom right plot, only a lower unstable region appears, for the range θ_0/θ_{c0} we adopted, and it is the biggest compared to the other cases of figure 3.9.

Indeed the supercritical flows are not represented in the bottom right plot of figure 3.9. However this plot is obtained for a large value of C_0 which implies small values of roughness and large value of water depth (see equation 3.17 where r_0 is the dimensionless roughness which is the ratio between the roughness and the uniform

[4] What we termed "the closing of the unstable region" is the way the cut-off graphically appears in a stability plot. The unstable regions are closed with respect to the wavenumber: the largest wave number are cut off.

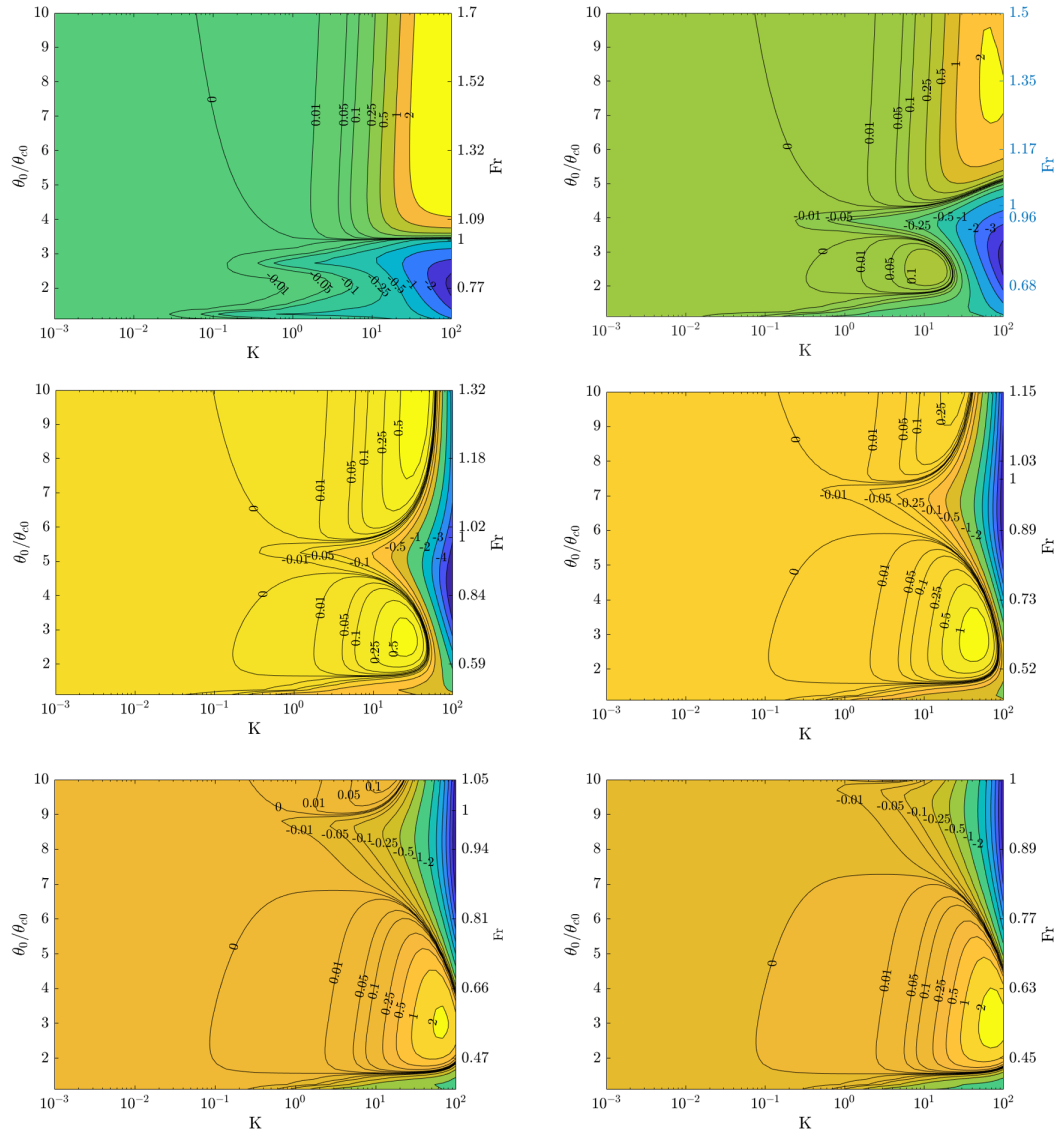

FIGURE 3.9: Stability plot of the sorting eigenvalue with varying C_0 value and constant $\sigma_0 = 10^{-3}$. Top panels: left $C_0 = 13.5$, right $C_0 = 14.5$. Central panels: left $C_0 = 15.5$, right $C_0 = 16.5$. Bottom panels: left $C_0 = 17.2$, right $C_0 = 17.55$.

water depth [5]). Hence in this condition it is reasonable to only account for subcritical flows and not taking into account supercritical flows, which would correspond to very large values of bed shear stress, thus exceeding the range θ_0/θ_{c0} we adopted.

It is interesting to analyse the reason why in the top left plot of figure 3.9 obtained for the smallest of the Chézy coefficient ($C_0 = 13.5$) the isolines characterising the unstable region are horizontal, that is to say the graphical representation of the absence of a cut-off and of wavelength selection mechanisms.

In subsection 3.3.4 we outlined the concept of unstable regions' boundedness tied to the problem of well-posedness, as well as the concept of cut-off mechanism tied to physical meaningfulness of the problem.

Here we provide a follow-up of these two concepts: we better explain the reason why in general a not bounded region of instability and the absence of a cut-off in the short wave limit corresponds to an inadequate functioning of a model, and afterwards we illustrate why our specific model presents such a failure (for certain values of the Chézy coefficient).

As for the not bounded unstable region in the short wave limit, a clear discussion is provided by Joseph (1990) and Truzzolillo and Cipelletti (2017) who face hydrodynamic instabilities in miscible fluids. Indeed their field of investigation differs from ours, but it however represents two layers of two different mediums and the instabilities occurring at the interface (the analogy with flowing water and erodible bed is clear); besides, the authors' analysis about not bounded unstable region in the short wave limit as a sign of ill-posedness is valid in general.

Joseph (1990) and Truzzolillo and Cipelletti (2017) state that short wave instabilities with a growth rate that increases without bound as the wavelength tends to zero are cases representing a so-called ill-posed problem: the model does not capture the real physical phenomenon and catastrophically diverge in numerical analysis. Indeed such instabilities are a catastrophe for numerical analysis since the finer is the mesh, the worse is the result. For sake of clarity, we point out that it is possible to have short wave instabilities with $K \to \infty$ without ill-posedness. This is the case when the growth rates are bounded with a maximum growth rate for the shortest waves: $K \to \infty$ (Joseph, 1990). We recover such condition in all the plots of figure 3.9, thus our problem is always well-posed and therefore suitable from a mathematical point of view. Unstable regions also present a cut-off mechanism in all the plots of figure 3.9 except the top left one. Hence our model presents a failure, in the sense illustrated in subsection 3.3.4, for small values of the Chézy coefficient, more precisely smaller than about 14, as shown in figure 3.9 and in more detail in figure 3.10.

It turns out that we have unstable regions with a cut-off for large C_0 values (precisely for C_0 larger than about 14) which implies small values of r (see equation 3.17) the dimensionless roughness which is the ratio between the roughness and the uniform water depth. Thus, a cut-off mechanism is present for small values of roughness and large values of water depth. Conversely, for large values of roughness and small values of water depth (precisely for C_0 smaller than about 14) our model does not work properly (absence of cut-off in figures 3.9 and 3.10). Indeed our stability analysis uses the shallow-water flow model that is not adequate for a macroroughness regime (from a "morphological point of view" small Chézy values are generally associated with mountain streams with shallow flow depth). In

[5] The definition of the conductance Chézy coefficient is an increasing monotonic function of the ratio between the water depth, D, and the roughness, r. Hence C can vary because only one between D and r varies while the other remains constant.

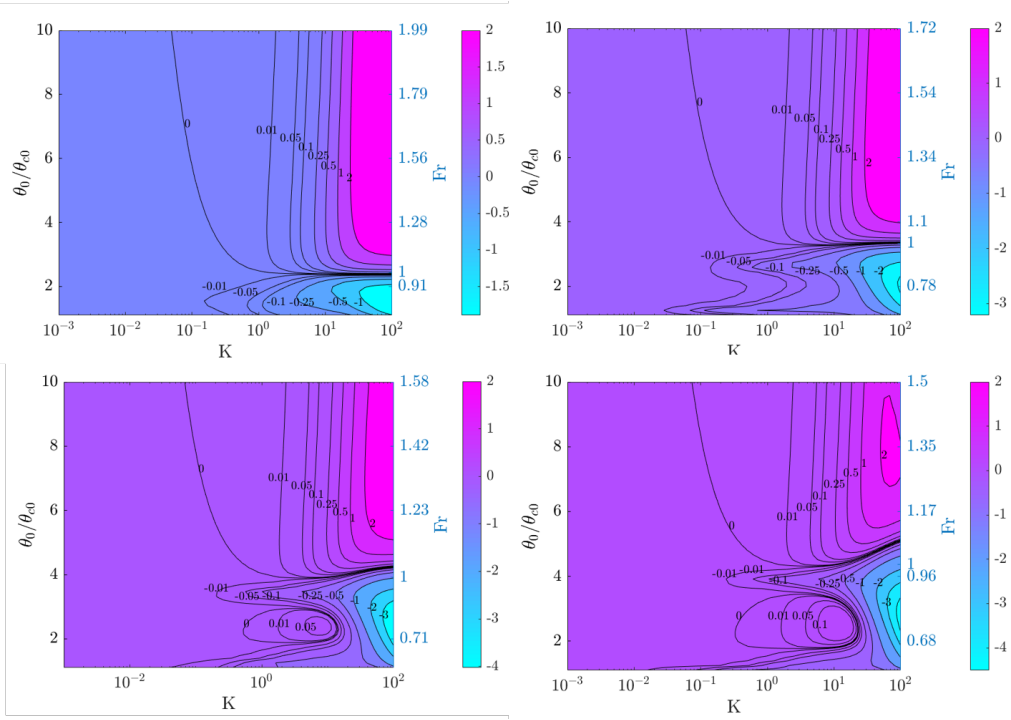

FIGURE 3.10: Stability plot of the sorting eigenvalue with relatively small C_0 values. Top panels: left $C_0 = 12.1$, right $C_0 = 13.4$. Bottom panels: left $C_0 = 14.1$, right $C_0 = 14.5$.

a macroroughness regime the feedback between the erodible bed and the flow is complex and not properly accounted for by a shallow-water flow model. Indeed in the shallow-water model the feedback between the erodible bed and the flow is accounted for using stresses whose closure relations rely on eddy viscosity and on a logarithmic vertical profile for water velocity. Hence, we can state that we identified a lower limit for the Chézy coefficient in order to safely apply our model.

We can similarly investigate whether there is an upper limit in terms of Chézy values for the applicability of our model. We can explore this possible upper limit stating from the bottom plots of figure 3.9 representing unstable regions for large values of the Chézy coefficient, 17.2 and 17.55 for the left and right plot, respectively. Here, with respect to the plots obtained for smaller values of the Chézy coefficient, the subcritical unstable region widens but also flattens, as it is clearly visible looking at the marginal curve (the isoline representing a zero growth rate), this implies a tendency to a less accurate mechanism of wavelength selection as C increases. Moreover looking at figure 3.9 it seems that for increasing values of C the supercritical unstable region does not disappear. We verify this hypothesis by plotting the growth rate of the sorting eigenvalue for values of Fr and θ_0/θ_{c0} larger than those of figure 3.9.

Figure 3.11 shows the supercritical unstable region that does not disappear for increasing C values: we can observe it by widening the region of the parameter space: indeed we represented an upper limit for θ_0/θ_{c0} of 20 (figure 3.11) instead of 10 (figure 3.9). The fact that for large C values the supercritical unstable region does not disappear in contrast to what happens for small C values when the subcritical unstable region disappears, together with the flattening of the isolines make us "suspect" that our analysis does not fit the conditions of large C values. Our interpretation is that for large C values (namely for small values of roughness and large values

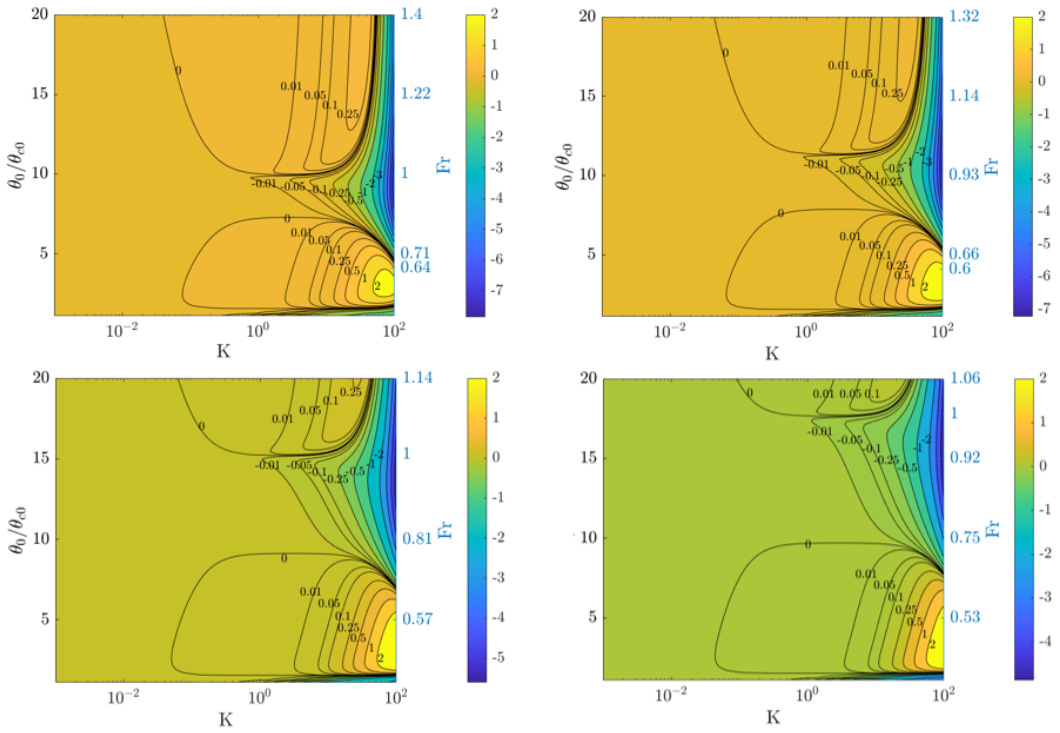

FIGURE 3.11: Stability plot of the sorting eigenvalue with relatively large C_0 values. Top panels: left $C_0 = 17.55$, right $C_0 = 18$. Bottom panels: left $C_0 = 19$, right $C_0 = 19.5$.

of the water depth) the sediment transport can also take place in suspension (reasonably, for large C values transport in suspension occurs at least when the Shields stress exceeds many times the critical Shields stress, even if high values of the ratio Shields stress over critical Shields stress are not a rigorous criterion which would rather be the Bagnold criterion for incipient suspension), and our model does not account for suspension [6]. As mentioned in section 3.4, if transport in suspension has to be considered, the model needs additional equations for the sediment concentration along the flow depth. Since our model only accounts for bedload transport, it is not surprising that it has not a proper functioning when suspension is likely to occur.

Hence we can conclude that our model has the following range of applicability: flow regimes where sediments are transported as bedload and where the Chézy coefficient has intermediate values, neither too small (lower than about 14) corresponding to macroroughness regimes, nor too large (exceeding 19) corresponding to conditions in which suspension should be taken into account.

Here it is interesting to observe both the role of the viscous term related to the depth averaged normal Reynolds stress and the role of the term associated to gravity, and then exploring the effect they have on instability in this scenario consisting of the morphodynamic problem for the two-grain mixture case. These two elements have been addressed in the previous analyses: the role of the viscous term arising from the depth averaged normal Reynolds stress in the discussion of the hydrodynamic instability (subsection 3.3.4); the role of the term associated to gravity in the study of

[6] From a morphological point of view large C values are generally associated to lowland rivers and large flow depths; such conditions are generally characterized by the presence of suspended load.

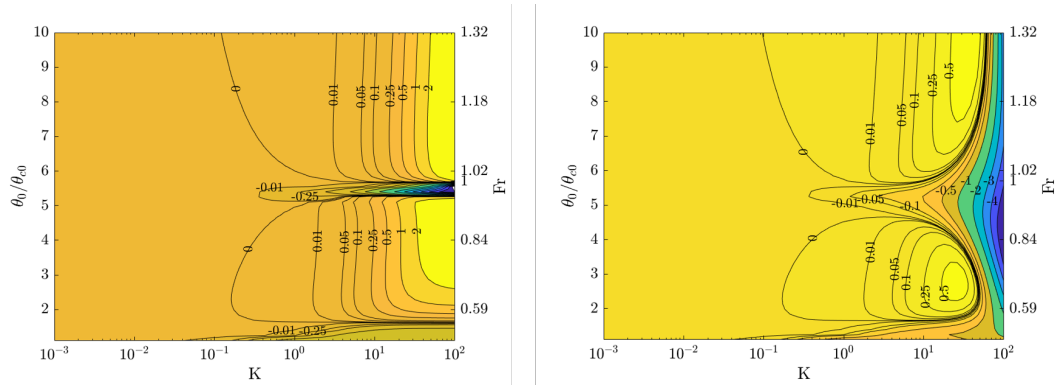

FIGURE 3.12: The growth rate of the sorting eigenvalue. Left panel: the viscous term is neglected ($T_n = 0$). Right panel: the viscous correction is taken into account ($T_n \neq 0$). The solution is computed for $C_0 = 15.5$ and $\sigma_0 = 10^{-3}$.

the morphodynamic problem for the uni-size sediment case (subsection 3.5.1, equation 3.53).

In figure 3.12 we compare the growth rate of the sorting eigenvalue, for $C_0 = 15.5$ and $\sigma_0 = 10^{-3}$, in two different cases: when neglecting T_n, left panel, and when accounting for T_n, right panel.

Without viscous correction the unstable regions are wider and they are not "closed", this meaning that the viscous term has a damping effect on the growth rate, actually reducing its value and narrowing the unstable regions. We observed thus the same behaviour found for the growth rate of the fast eigenvalue in the hydrodynamic problem (see figure 3.5).

Moreover, without viscous correction no wavelength selection is possible, and this fact as well confirms what we observed for the hydrodynamic instability as figure 3.5 shows.

As for the effect of gravity on morphodynamic instability, similarly to the study of the viscous correction, we plot the growth rate Ω_{sort} with and without considering the terms associated to gravity.

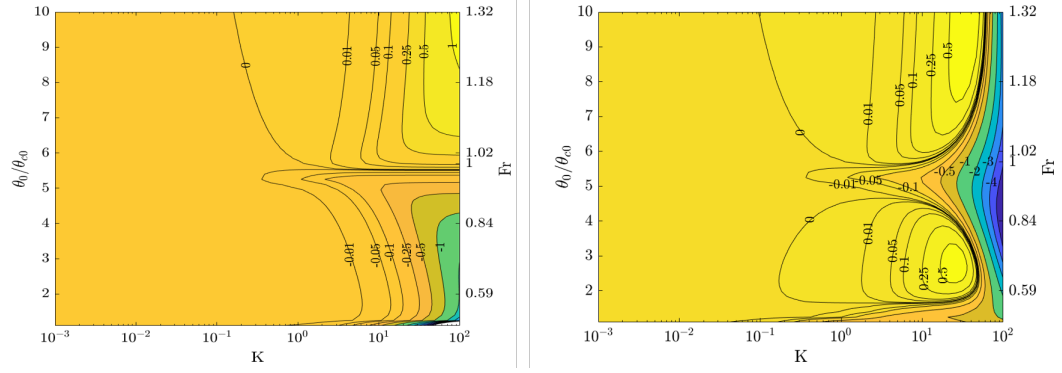

FIGURE 3.13: The growth rate of the sorting eigenvalue. Left panel: the terms associated to gravity are not accounted for. Right panel: the terms associated to gravity are taken into account. The solution is computed for $C_0 = 15.5$ and $\sigma_0 = 10^{-3}$.

When gravity is wiped out from the analysis we obtain a stability plot with no lower ($Fr < 1$) unstable region and with an upper ($Fr > 1$) unstable region large. Hence gravity acts as a stabilizing effect in the supercritical region of the parameter

space, confirming what expressed in equation 3.79 and discussed dealing with the morphodynamic problem for uniform sediment.

Furthermore when terms associated to gravity are not considered the unstable region does not have a closing for the long wave limit and no pronounced wavelength selection mechanism are observed.

Finally we can discuss the effect of the two eigenvalues W_{bed} and W_{sort} on the perturbations B_1 and R_1. Indeed, in reference to the morphodynamic problem expressed by the system 3.77 the eigenvectors associated with each eigenvalue determines the relative amplitude of the two perturbations expressed by

$$B_1 = -\frac{\gamma'\left(a_{4R} + a_{4U}U_{1R}\right) - W}{\gamma'\left(a_{4B} + a_{4U}U_{1B}\right)}R_1 \tag{3.81}$$

or expressed altogether equivalently by

$$B_1 = -\frac{\gamma\left(a_{3R} + a_{3U}U_{1R}\right)}{\gamma\left(a_{3B} + a_{3U}U_{1B}\right) - W}R_1$$

With heterogeneous sediments B_1 and R_1 are always both present: B_1 and R_1 both amplify if one of the two eigenvalues is unstable. However, the way how the two eigenvalues affect B_1 and R_1 is different since the eigenvectors associated with W_{bed} and W_{sort} are remarkably different one from the other in terms of amplitude (figure 3.14).

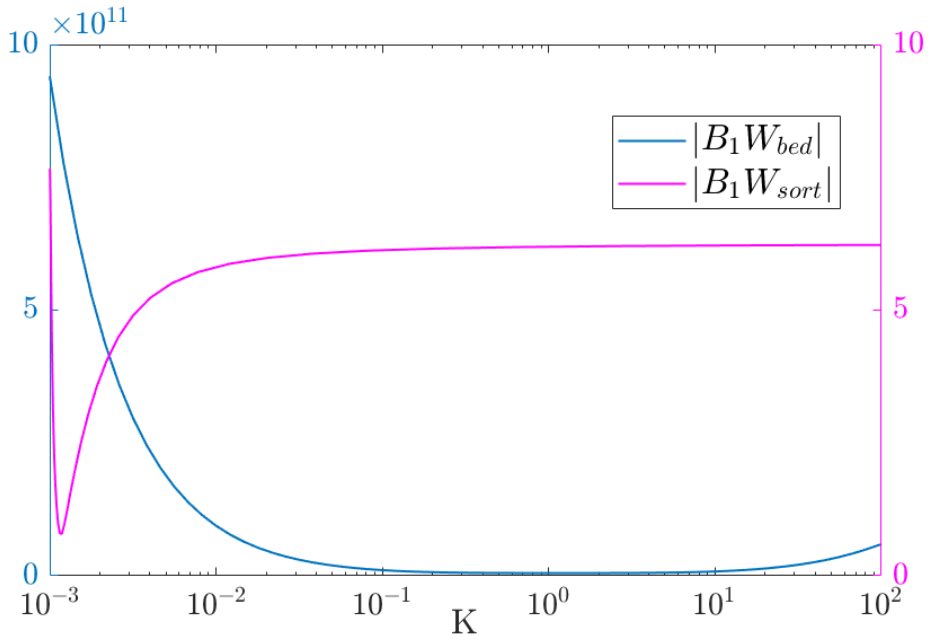

FIGURE 3.14: The amplitude of the perturbations B_1W_{bed} and B_1W_{sort} when R_1 is set equal to 1.

By imposing a unitary roughness perturbation, $R_1 = 1$, in equation 3.81 and by substituting W once by W_{bed} and then by W_{sort}, it is possible to obtain the perturbation B_1 induced once by W_{bed} and then by W_{sort}, these two latter labelled B_1W_{bed} and B_1W_{sort}. B_1W_{bed} and B_1W_{sort} are complex quantities of which we can compute the amplitude and the phase. We compare the amplitude of B_1W_{bed} and B_1W_{sort} in figure 3.14 where the two perturbations are computed with the following values of the relevant parameters: $Fr = 1$, $C_0 = 15.5$, $\sigma_0 = 10^{-3}$.

The amplitude of $B_1 W_{bed}$ is many order of magnitude larger than the amplitude of $B_1 W_{sort}$. This means that the eigenvalue W_{sort} induces a very small perturbation in terms of bed elevation. Indeed this justifies the name given to the particular bed forms taking place only in presence of heterogeneous sediments, bed forms with a negligible height and driven by sorting. This analysis theoretically gives a context to sorting waves and bedload sheets.

3.6 Conclusions and perspectives

We developed a simple but effective model consisting in a 1D linear stability analysis able to catch instabilities sorting dominated. We emphasise the fact we were able to describe sorting waves with the simplest (but not oversimplified!) possible model: the governing equations are in a simple form, we did not need to implement a rotational 2D flow model, and not even a 2D model.

Here we provide a deeper reflection on instabilities in 1D and 2D dynamics and hence in 1D and 2D flow models. We recall that we used in our analysis the shallow-water flow model, which has limitations in linear analysis of some bed forms' dynamics: the shallow-water model can not be properly applied to processes occurring over distances larger than the flow depth. As a result, the 2D dynamics of alternate bars, the wavelength of which scales with the channel width (typically at least ten times larger than the flow depth), is handled satisfactorily (Colombini et al., 1987), whereas the 1D dynamics of dunes and antidunes, the wavelength of which scales with flow depth, cannot be captured equally well (Lanzoni et al., 2006; Balmforth and Vakil, 2012). Indeed, the only 1D waves caught by the shallow-water model and found to be unstable are those corresponding to the formation of roll waves, whereby the process driving the instability has to be sought in the interactions between the flow and the free-surface more than in the interactions of the flow with the erodible bed. Conversely, we showed (section 3.5) that the solution of the morphodynamic problem (even under quasi-steady approximation) revealed the appearance of an instability of the bedload-sheet kind: a sorting wave which manifests itself as a streamwise periodic perturbation of the surface composition of the bed, travelling downstream with only a very small change in bed elevation.

We described instabilities arising when sorting is constrained to be weak by the condition of a small standard deviation of the two-grain mixture. This is an important result since it means that sorting waves take place even for weak sorting, and this applies a fortiori when sorting is not weak.

Our model gives a theoretical context for bedload sheets: it provides a theoretical justification of depicting bedload sheets as bed forms sorting driven and with negligible amplitude (as described in field and laboratory observations, see subsections 2.3.1, 2.4.1 and 2.4.2).

By summarising and further commenting the main results of our analysis, illustrated in section 3.5 (in particular figures 3.8, 3.9, 3.10, 3.11), we can better specify the ability of the model to predict the occurrence of bedload sheets and their characteristics, as well as the range of applicability of our model, and thus its limitations.

Concerning figure 3.8, it appears that sorting waves always propagate downstream (the celerity is positive for each value of the relevant parameters of the analysis) in accordance with literature on bedload sheets (subsection 2.3.1). Moreover, sorting waves propagate faster than bed waves, as the comparison between figure

3.7 and figure 3.8 clearly shows, and this outcome too is in accordance with literature (Stecca et al., 2014).

As for figure 3.9, a first result is that instabilities take place for large values of wavenumbers, hence according to our analysis, bedload sheets have short wavelengths (recalling the definition of the wavenumber K, $K = (2\pi D^*)/L^*$ where D^* and L^* are the dimensional water depth and wavelength, respectively). Unfortunately, few experimental studies report measurements of bedload sheets' wavelengths; one of these is the work by Whiting et al. (1988) where the authors monitored in Muddy Creek and in Duck Creek bedload sheets characterised by large wavenumbers: about 4.5 and 2.5, respectively. We too monitored bedload sheets during one of the runs of our set, dealt with in the experimental part of this thesis (chapter 4), precisely during Run 3 (subsection 4.5.3). In this experiment too the wavenumber charcterizing bedload sheets was about 1, a relatively large value. The matching of our experimental results on bedload sheets and our stability analysis is illustrated in the discussion concerning Run 3 (see subsection 4.5.3).

However, looking at the unstable regions of the sorting eigenvalue represented in figure 3.9, we observed not only that all of them are present for large values of the wavenumber but also that for certain values of the Chézy coefficient they do not present a cut-off mechanism nor a sufficiently accurate mechanism of wavelength selection; this condition, graphically represented by the stability plots, is interpreted as an inappropriateness of the model and it occurs for small and large values of the Chézy coefficient (figure 3.10 and 3.11, respectively). Whereby we could identify the lower and upper limit in terms of Chézy values for our model to be safely applied. From a physical point of view, our model suits flow regimes where sediments are transported as bed load and characterize by intermediate Chézy values, such that macroroughness regimes as well as regimes where transport in suspension occurs are excluded.

Lastly, an important perspective about the model presented in this chapter consists of performing our stability analysis dealing with fully unstable equations, in so doing we could figure out the "error" we made by adopting the quasi-steady approximation.

4 Experimental study of flows over a sediment mixture

The experimental part of this thesis relies on the analysis of three flume experiments carried out under steady flow conditions over long durations (each experiment is about 60 hours). Steady flow conditions over long durations are usually depicted as conditions of "dynamic equilibrium", being the latter a convenient term to characterize the behaviour of alluvial channels under steady external conditions (typically constant flow and sediment feed rates) given the controversial use and portray of river equilibrium (Bracken and Wainwright, 2006). In particular we use the term of dynamic equilibrium to depict the oscillations of the system parameters (e.g., bed slope fluctuations) around mean values (e.g., the average bed slope).

We performed three long morphodynamic runs in a mobile-bed flume reproducing a flow over a bimodal sediment mixture; the flow is characterized by constant values of inlet water and sediment discharge. In all the experiments we aim at modelling a gravel bed river, i.e. a self-formed channel in a coarse alluvial substratum. The dynamic of such a system results from the feedback between the flow and the morphology through sediment transport; and in particular dealing with morphology, a self-formed channel that is allowed to wander in the alluvial substratum can adjust its width to an equilibrium value. In two experiments we reproduced this condition: the flume width (distance separating the flume walls) was greater than the channel width. Actually the channel could wander in the large alluvial bed, i.e. the flow was low constrained. Starting from the lowest confined configuration (Run 1) we decreased the flume width, corresponding to an increasing flow confinement (Run 2: configuration with an intermediate flow confinement; Run 3: confined flow). Indeed in the lowest confined configuration (Run 1) we observed and documented an equilibrium channel width that we interpreted as the "width of the self-formed channel". We varied the flow lateral constraint from one run to another having the "width of the self-formed channel" as a guiding principle.

Actually, we empirically verified that the criterion of a constant active width characterizing flows with different lateral confinement (with the other variables such as the slope and sediment size kept constant) is also valid in conditions of heterogeneous sediments undergoing sorting processes. Garcia Lugo et al. (2015) performed a large set of flume experiments at dynamic equilibrium conditions with uniform sediments reproducing different gravel bed rivers morphologies (confined single thread, alternate bars configurations, wandering, braiding) by varying the channel width (hence the lateral confinement) and for each channel width by varying the formative discharge (three values of Q). They observed that "for the three largest widths, the active width remained almost constant for all three discharges, indicating that the combinations of gradient, flux, and grain size are able to maintain the same active channel width". Whereby we verified that this also applies to heterogeneous sediment conditions (bimodal sediment mixture typical of gravel bed rivers).

Hence, the three flume experiments differ from one another in respect of the flow lateral confinement. The sole external parameter we varied from one run to another was the flume width, moving one channel wall and maintaining the other wall at a fixed position. The other external conditions (namely the feeding rates and the flume slope) were maintained unchanged.

We pursued the objective of investigating the influence of lateral confinement on bed morphodynamics, i.e. on feedback between the river bed variables such as the bed slope, the bed sediment composition, the active channel width, and the sediment transport rate. Particular attention is given to grain sorting processes and patterns. Indeed we wanted to study how sorting phenomena may vary depending on flow lateral confinement: thus we wanted to document when sorting takes place on the surface, when vertical sorting is present or not, which are the characteristics of bed surface patches.

In this chapter we first report our experimental setup (section 4.1) presenting the physical devices (subsection 4.1.1) and the material (subsection 4.1.2) we used. Then we illustrate in section 4.2 all the measurements and data acquisition techniques we carried out and implemented; particular attention is devoted to the measurements aimed at determining the bed surface sediment composition (subsection 4.2.1), about such measurements a follow-up is provided in Appendix A and Appendix B. We deal with the experimental procedure and the experimental conditions characterising the three runs we carried out in section 4.3; whereas the methodology for data analysis is described in section 4.4. Section 4.5 contains results and discussion, first dealing with the runs one by one, and secondly comparing them with each other. Finally the summing-up of the experimental activity of the thesis is provided in section 4.6.

4.1 The experimental setup

All runs were performed in the Hydraulic Laboratory of the Institut national de recherche en sciences et technologies pour l'environnement et l'agriculture, the Irstea research institute, center of Grenoble. With the objective of studying grain sorting processes and bed patterns related to such processes it was very important to ensure

- fraction specific data capturing techniques, i.e.tools and protocol measurements able to capture and distinguish different size sediment fractions of the bed;
- a highly constant feeding rate both in terms of flow rate and in terms of sediment discharge (considering the sediment discharge composition as well). Indeed, since we are interested in the evolution of bed sediment composition (and its feedback with other river bed variables such as the bed slope, the active channel width, the transport rate), the feeding conditions must be kept as constant as possible in order to observe the evolution of the river bed variables independently from any variation of the inlet.

Thus before starting the experiments great care was taken to develop the experimental setup, i.e. mainly the sediment feeding adjustments and control, and above all the devices and protocol of measurements for the bed sediment composition.

4.1.1 The flume

The experimental setup (figure 4.1) consists of a 6-m-long flume with a maximum width of 0.5 m. The flume is tilting but we set its slope at the fixed value of of 3.18 % for all the experiments we performed; whereas from one experiment to another the flume width was varying. We set this value of the flume slope because together with our values of feeding rates (section 4.3) and the characteristics of the adopted sediment mixture (subsection 4.1.2) it ensures a rapid river bed dynamics being at the same time representative of a natural gravel bed river. However we specify that we did not focus on the scaling of a particular river, we are rather interested in analyzing the physical processes associated to bedload transport of heterogeneous sediment mixture.

We set in the entire flume a layer of well mixed sediments which constituted the erodible mobile bed. This layer is composed of the same sediment mixture used for the inlet solid discharge; further information about this mixture is provided in the following. The outlet section consisted of a control section with a central rectangular opening and drains giving continuity to the filtration flow from sediment layer (figure 4.1) . Each run was performed at the dynamic equilibrium slope, with the liquid and solid discharge kept constant over an initial flat bed whose thickness varied from 5 to 7 cm from one run to another. Thereby, before each run the bed filtration rate was systematically measured and deduced from the total inlet flow rate.

The water was supplied from a reservoir positioned at the end of the flume and it was recirculated by a pump. The flow rate at the flume inlet was controlled since the water reservoir had a constant head ensured by an overflow system; the flow rate was measured by an electromagnetic flow-meter.

As for the sediments, the system was an open circuit, i.e. no sediment recirculation. At the upstream section, the sediments entered the flume by means of a hopper; the solid discharge was controlled through the opening of the hopper itself and through the speed of the conveyor belt, which was at the flume entrance. Sediments were collected at the flume outlet and separated from water through a sieve placed in a bucket.

In order to allow a regular sediment motion into the hopper particular attention was paid to wetting the sediment with an additional constant water discharge whose optimal value was found equal to 0.045 l/s (approximately equal to the filtration discharge). This latter is fundamental because it guarantees that the effective solid discharge entering in the flume depends exclusively on the rotation speed of the conveyor belt driven by a visual program based on a system of calibration laws between engine tension and rotation speed and between rotation speed and solid discharge. We point out that both the base flow and the additional discharge for sediment wetting were carefully quantified.

Since the sediment utilized in this experiment consisted of a mixture of different grains in a precise proportion, it was crucial to ensure that no sorting processes took place into the hopper and that the grain proportion of the mixture was statistically maintained, we ensured this by controlling the sediments composition through numerous samplings (samples at the flume inlet) all runs long. For details on the sediment feeding device see Recking (2006). Furthermore, sediments were mixed by hand, and the mixture collected at the flume outlet were stored in large quantities, tested by sieving and readjusted if necessary. A certain amount of the two separated uniform materials was available to maintain the exact proportion of the mixture.

FIGURE 4.1: The flume. A view from downstream to upstream and a scheme.

FIGURE 4.2: The bimodal sediment mixture, left panel; the coarse and fine fractions separated, right panel.

TABLE 4.1: Grain size characteristics of the bimodal mixture and of the single fractions.

Fine fraction	Coarse fraction	Mixture
$d_{16} = 0.6\,mm$	$d_{16} = 1.4\,mm$	$d_{16} = 0.7\,mm$
$d_{50} = 0.7\,mm$	$d_{50} = 1.8\,mm$	$d_{50} = 1.5\,mm$
$d_{84} = 0.9\,mm$	$d_{84} = 2.2\,mm$	$d_{84} = 2.1\,mm$

4.1.2 The sediment mixture

The sediment mixture is a bimodal mixture. In order to account for sediment heterogeneity and to observe sorting processes a bimodal mixture is preferred since it facilitates observation and it is also representative of natural gravel bed sediments (Kuhnle, 1996; Smith et al., 1997; Recking, 2006). The 60% of the bimodal mixture consists of the coarse fraction, characterized by a d_{50} equal to 1.8 mm; the remaining 40% is the fine fraction which has a d_{50} equal to 0.7 mm. We characterized the mixture through a granulometric analysis by sieving carried out both for the mixture itself and for each fraction separately. Figure 4.2 shows the mixture used in our runs; table 4.1 collects the information of the mixture and the fractions in terms of relevant grain sizes. The granulometric curves for both the fractions and the mixture are provided in figure 4.3. We report in table 4.2 the values resulting from the sieving with which the curves are obtained.

Both fine and coarse fraction consist of natural sediments, but the fine fraction is artificially colored in order to enhance its natural orange color. Indeed this was essential in order to create an automatic procedure able to separate the two grain sizes

TABLE 4.2: Diameters and passing percentages values resulting from the sieving. These values are graphically represented in the granulometric curves.

Fine fraction		Coarse fraction		Mixture	
D	% Pass	D	% Pass	D	% Pass
0.4	0	1	0	0.4	0
0.5	5.3	1.25	5.5	0.5	4.9
0.63	26.8	2	68	0.63	11.3
0.7	51.1	2.5	98	0.9	32.3
0.9	73.1	3	100	1.25	38.8
1	100	4	100	2	79.8
				2.5	98
				3	100

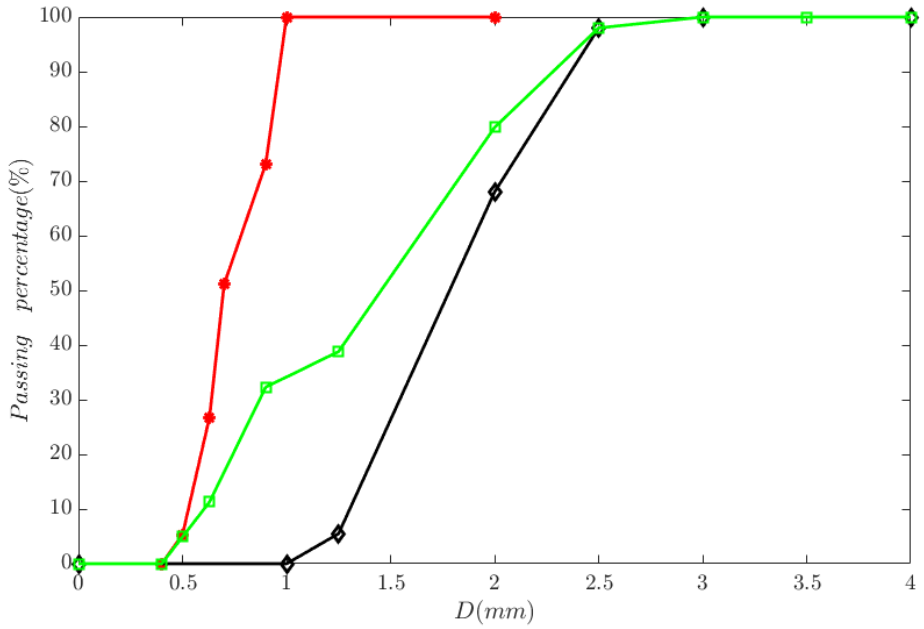

FIGURE 4.3: The granulometric curve of the fine fraction (red), the coarse fraction (black), the mixture (green).

constituting the mixture with the overall objective of identifying the bed surface percentage of coarse and fine grains.

Basically we took photos of the bed all runs long; the different colors of sediment fractions was reflected in a different radiance of photos' pixels; thus the distinction and separation of sediment fractions was achieved through an image analysis procedure. A detailed explanation of this procedure is provided in the following section.

4.2 Measurements and data acquisition

The bed surface sediment composition (subsection 4.2.1) is a morphodynamic bed variable with a feedback with other important variables defining the bed state, such as the slope. Slope measurement is therefore essential to map out the bed state (subsection 4.2.2).

In the context of the complex mutual dependence of bed state variables also bedload transport rate (subsection 4.2.3) plays an important role, whereas hydraulic measurements such as flow depth and flow velocity measurements (subsection 4.2.4) are necessary in order to define the flow conditions (through the use of relevant non-dimensional numbers such as the Froude number, the Shields number, the width-to depth ratio).

4.2.1 The surface texture measurement with image processing

The areal images taken during the runs were processed with an image analysis algorithm that was written using Matlab. The code is based on color detection and provides the areal fraction content of a surface area covered by a certain color, i.e. a certain grain size.

In this subsection we describe the instrumental equipment for the surface texture measurements; we provide the basis of image processing through color detection and we briefly illustrate through color detection and we briefly illustrate its application to our case study; lastly we illustrate the way we evaluated the accuracy of the operations of color detection we performed. In appendix A we provide a wider context of image processing for surface texture measurements: we illustrate areal fraction content measurements. In appendix B we provide the details of the color detection operations we performed.

As for the instrumental equipment, we took photos using a camera placed 2.5 meters above the flume. The camera support was a structure able to move sliding on a rail along the flume, but we set it at a fixed position for this specific shooting aimed at the surface texture measurements.

The camera is a Canon 450D; the focal length was of 24 mm; the horizontal resolution of the image as well as the vertical one was of 72 dpi. The camera was equipped with a polarizing filter (an HOYA cir-polarizing filter) able to reduce water reflections. Indeed the strength of our surface texture analysis relies on achieving this sediment composition study with flowing water and sediment transport, all runs long, and without intrusive techniques. For instance, other experimental investigations carried out image analysis based on color segmentation of drained bed and of submerged bed but with still water (Orru et al., 2014). In yet others, image analysis for areal fraction content has been carried out during laboratory runs, thus with flowing water and solid transport (Orru et al., 2014); (Orru et al., 2016). But the image analysis of both these studies first, was in conditions of partial solid transport (coarse fraction immobile) and lack of sediment supply, i.e. in flow and sediment transport conditions less "tricky" with respect to ours; and secondly but no less important, they employed an equipment to take pictures rather intrusive, in the authors' opinion, consisting of a carriage for the camera installed on a floating device even partially submerged.

Lastly the remaining information concerning our camera settings are its precise position and framed area with respect to the flume, the ad hoc lighting system we implemented, and the shooting frequency.

The camera is positioned above the central part of the flume, precisely it frames the central 2.8 meters of the flume length. Given the position of the camera together with its focal length, we had a ground pixel size of 1.266 mm.

We designed an ad hoc lighting system in order to ensure an homogeneous illumination and minimize the shaded areas (mainly due to the presence of the flume walls). The homogeneous lighting system of the framed area was essential because light affects sediment grains' color and thus pixels' radiance. To this end three photo diffuser umbrellas and two LED lamps were installed near the central part of the flume.

Finally, we took photos every minute all runs long; this high shooting frequency enable us to catch also very rapid morphodynamic changes.

The two sediment fractions of our mixture (subsection 4.1.2) captured in the photos had different colors, and thus different radiances. Radiance is an information "stored" in the photos' pixels. Indeed pixels have values, called Digital Numbers (DN), which have a one-to-one correspondence with radiance (a follow-up about this topic is provided in appendix A).

By applying these basic concepts to our case study, we analyzed images of our

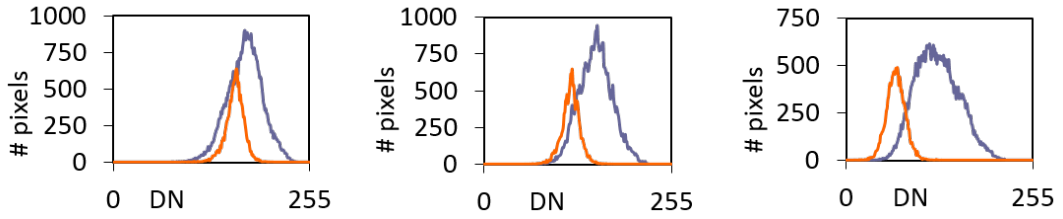

FIGURE 4.4: Digital Numbers' histograms for fine grains in orange, and coarse grains in blue. In the left panel the DNs' histograms in the red channel; in the central panel the DNs' histograms in the green channel; in the right panel the DNs' histograms in the blue channel.

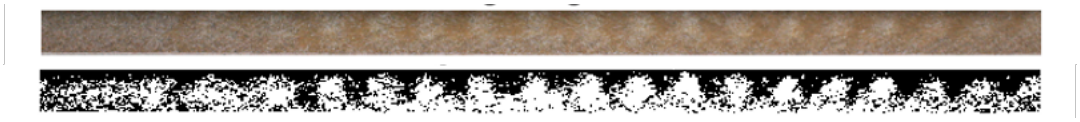

FIGURE 4.5: A picture of Run 3, namely the run with minimum flume width (0.12 m). The entire flume width is framed and the central 2.8 m of the flume length are framed; flow is from left to right. The top figure is the original RGB photo, coarse grains are white, fines are orange. The bottom figure is the binary image where the two fractions are separated: coarse grains-white-1, fines-black-0.

two sediment fractions with the objective of distinguish and separate them in the photos of the flume's bed taken all runs long.

We run preliminary experiments with both water and sediment feeding at the same conditions characterizing the subsequent actual runs. This way we obtained grain segregated patterns similar to those we observed later during actual runs. We took a large amount of target photos during these preliminary tests. In these images we took interrogation areas of patterns of fine grains alone and of patterns of coarse grains alone, and we analyzed the histograms of fine grains and coarse grains in the three bands of the RGB photos (figure 4.4). We found that in the blue channel fine grains and coarse grains have DNs' (and thus radiance) histograms with the minimum overlapping. It is therefore possible to set a threshold on DNs' histograms in the blue channel and thus distinguish and separate coarse grains from fines.

Once separated the two fractions, we can determine the areal fraction content of coarse grains and fines in each photo and thus determine the bed surface sediment composition in terms percentage of coarse grains and percentage of fines. Figure 4.5 shows an example of the outcome of the fractions' separation we were able to perform for every picture. In particular figure 4.5 shows bedload sheets, the sorting patterns we observed during Run 3 (section 4.5.3). Bedload sheets clearly manifested themselves as a periodical alternation in the streamwise direction of coarse and fine grains. We will describe and discuss at length in section 4.5.3, here we just point out that the forms shown in figure 4.5 are not antidunes (as one could suppose given the high value of the slope and supercritical conditions, see table 4.4) since they migrate downstream at fast pace as observed in literature concerning bedload sheets; moreover, the water depth was small (table 4.4) so as not to give rise to any problems for the detection of the bed surface composition.

The separation of coarse grains from fines can be achieved not only at the "grain scale" (determining fractions' percentage), but also at the "pattern scale". Indeed we can identify and isolate patches of coarse grains as well as patches of fines, and we can get information such as patches' extension. These analyses at the pattern scale are achieved through morphological operations. Figure 4.6 shows an example of patterns detection for a patch of coarse grains resulting from specific morphological

operations; similar but not identical morphological operations allow us to identify patches of fines.

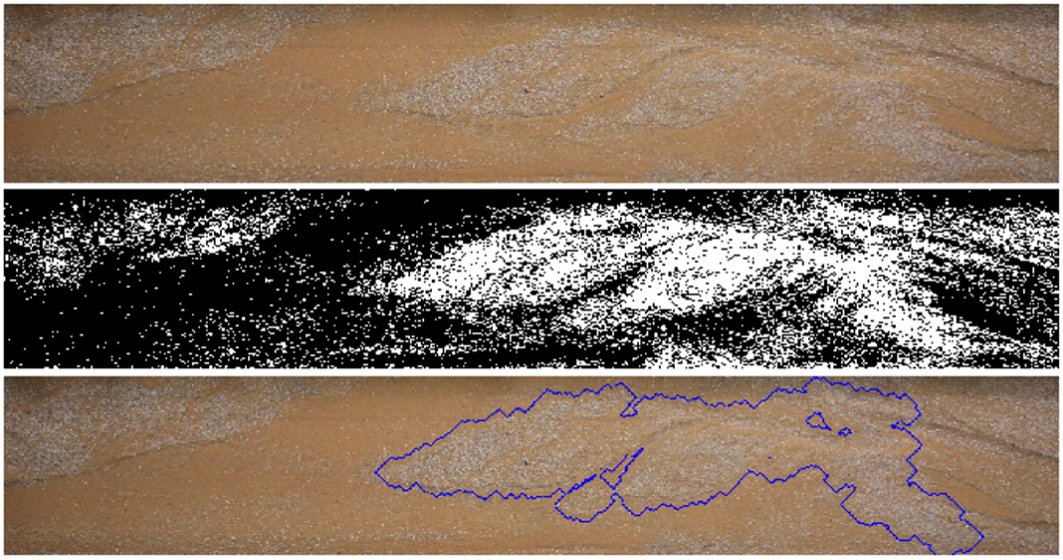

FIGURE 4.6: A picture of Run 1, namely the run characterized by the maximum flume width (0.5 m). The central 2.8 m of the flume length are framed. Top panel: the original RGB photo; central panel: the binary image in which the two fractions are separated; bottom panel: a patch of coarse grains is detected.

All the operations aimed at determining the surface texture composition and at identifying homogeneous sediment patches were achieved writing on purpose Matlab codes and using Matlab's Image Processing Toolbox. The details of such operations as well as the evaluation of their accuracy are provided in Appendix B.

Lastly we illustrate the evaluation of the accuracy of the operation of fractions' separation in our image processing. This accuracy evaluation is about the threshold values and, as well as for their determination, it is run specific.

For each run we took several photos in which we considered several interrogation areas framing coarse grains as well as interrogation areas framing fines, paying attention to taking interrogation areas with similar amounts of pixels. Then we could obtain as many DNs' histograms and performing an ensemble average whose outcome is a probability mass function of DNs. Figure 4.7 shows for each run the probability mass function (PMF) carried out for the accuracy evaluation compared with the threshold value.

The evaluation of the accuracy of the operation of fractions detection consists in quantifying the error committed in detecting fractions by applying the specific thresholds we defined. Indeed, by applying a certain threshold value we identify as fine grains all the pixels whose DN is lower than the threshold and we identify as coarse grains all the pixels whose DN is higher than the threshold.

However we committed an error since a few coarse grains actually have pixels' DN lower than the threshold and they are detected as fines, and there are a few fine grains which actually have pixels' DN higher than the threshold. Therefore we committed an error on coarse grains erroneously detected as fines, and similarly an error on fine grains erroneously detected as coarse ones. Table 4.3 contains the outcomes of this error quantification.

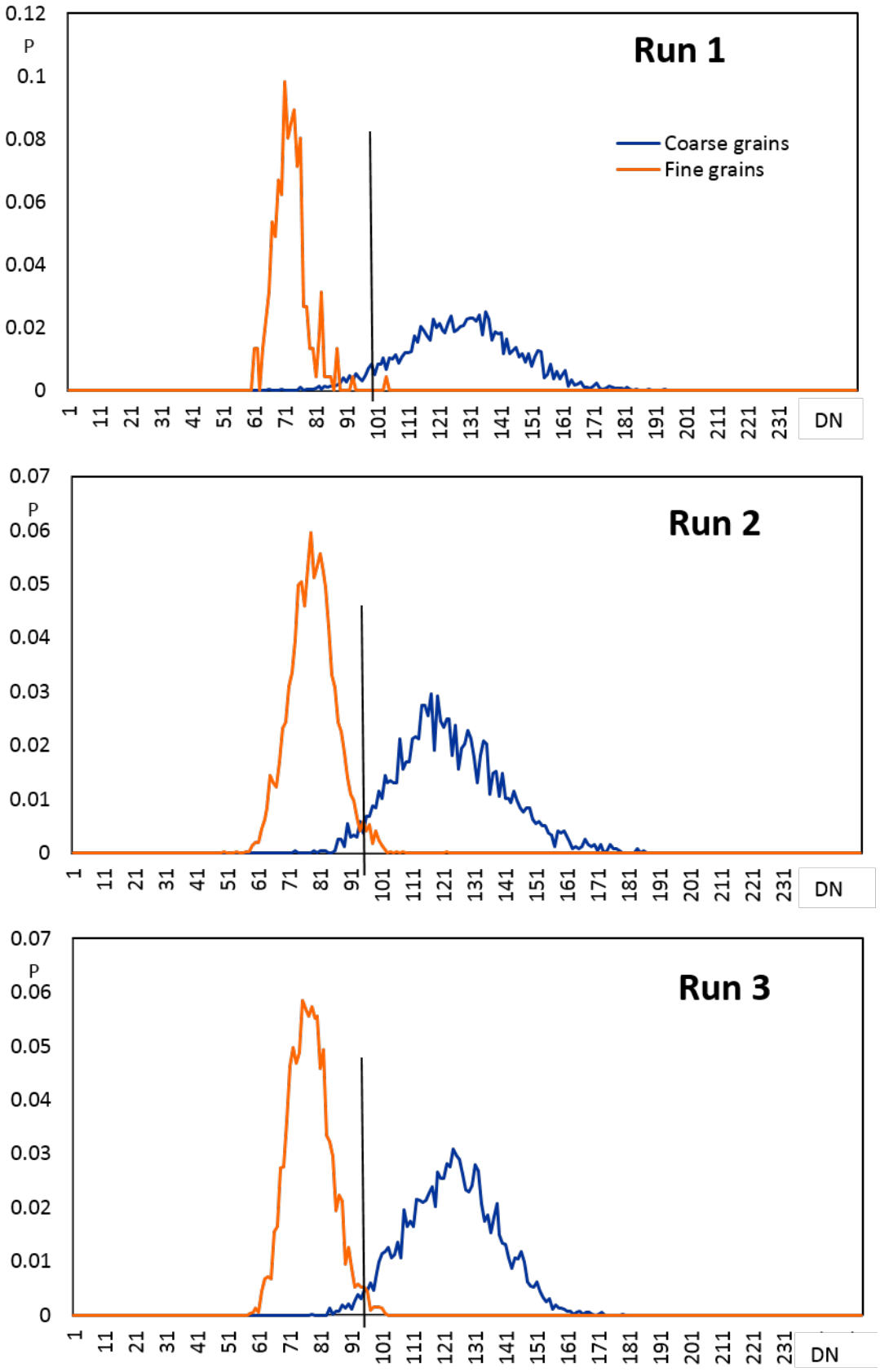

FIGURE 4.7: The probability mass function of DNs for each of the three runs. The run specific threshold value is superimposed on the respective PMF.

TABLE 4.3: Thresholds and error quantification for the operation of sediment fractions' separation.

Run 1	
Threshold value on pixels' DN	100
Error on fine grains	0.45 %
Error on coarse grains	6.8 %
Overall error	5.12 %
Run 2	
Threshold value on pixels' DN	95
Error on fine grains	2.15 %
Error on coarse grains	3.35 %
Overall error	2.78 %
Run 3	
Threshold value on pixels' DN	96
Error on fine grains	0.74 %
Error on coarse grains	2.9 %
Overall error	1.91 %

In table 4.3 errors are calculated with respect to the probability mass functions of figure B.4. Errors are expressed in percentage since they are quantified as the ratio between pixels erroneously detected and the total amount of pixels; this ratio is both fraction specific (error on fine grains, error on coarse grains) and for the sum of the two fractions (overall error).

4.2.2 The slope measurement and the bed topography

Bed slope was inferred using two different techniques:

(i) manual measurements;

(ii) bed topography reconstruction from a set of photos using the Structure from Motion technique performed using the software Agisoft PhotoScan.

Manual measurements (i) allowed us to measure the bed slope frequently and without interrupting the runs. We used a digital depth gauge to measure the bed elevation (and bed thickness obtained by difference knowing the elevation of flume's bottom) in various section (several points per section) allowing to determine the slope of the bed itself both for local reaches and for the entire length of the flume (in the following we will call the latter "mean bed slope"). This monitoring was rather frequent: we measured the bed slope every 30 minutes.

The bed topography reconstruction from a set of photos using the Structure from Motion technique (ii) allows very precise topographic measurements. The bed topography reconstruction through Structure from Motion technique generates a textured 3D model of the investigated area by means of photos.

First of all, a correct design of the photographic campaign was determined. The photos taken are the input for the whole process, therefore the precision in the results strongly depends on the quality of these photos. Attention must be paid to the correct spatial arrangements of photos and to an adequate resolution in order to guarantee a high quality 3D reconstructed object.

As for the photos spatial arrangement, in order to ensure the correct functioning of the software Agisoft Photoscan photos had a lateral overlapping of 60 % and a forward overlapping of 80 %.

Moreover, in order to obtain not only a 3D reconstruction but also quantitative measurements on the 3D model, we set a reference system based on ground reference points. The latter were markers we put along the flume. Markers' coordinates were determined with a $\pm$ 1 mm accuracy using a topographical total station. The markers were used for the creation of a local 3D Cartesian coordinate system but also for an optimization of the alignment of the photos (in laboratory studies a local coordinate system is appropriate, whereas in field campaigns georeferencing is needed).

As for the characteristics and setting of the cameras and the resolution of the photos, we used a fixed focal length of 50 mm and we positioned the two cameras 2.5 m above the flume, this way we ensured a good photo resolution and a foreground frame of the object of interest; precisely the horizontal resolution as well as the vertical resolution of the images was of 72 dpi, and the ground pixel size was of 0.1 mm. The two cameras were positioned on the same support of the Canon 450D used for image processing, that is the support sliding on the rail parallel to the flume. The cameras for the topography reconstruction were two Canon 100D slightly tilted differently choosing convergent directions (i.e. 10 and 15 degrees towards each others). We put marks on the rail every 30 cm; this was the spacing used to move the cameras between two adjacent pairs of photos. Thus, the overlapping criteria have been respected, in particular, for each topographic measurement campaign, a set of 38 photos has been created.

The procedure, from photos acquisition to the generation of the 3D model, consists in four main steps:

1. Cameras alignment. PhotoScan searches for the common points on the photos, calculates and determines the position of the cameras for each image and refines the calibration parameters of the cameras. As a result of this first step, a sparse point cloud is generated together with a set of camera estimated positions.
2. Generation of a dense point cloud based on the estimated cameras shooting positions and photos themselves.
3. Construction of the mesh. PhotoScan reconstructs a 3D polygon mesh that represents the framed object. This latter operation is based on the dense point cloud obtained from the previous calculation.
4. Finally, the reconstructed geometry (e.g. the mesh), can be structured or used for the orthophotos generation. Furthermore, tiff. file can be generated and exported in Geographic Information Systems (e.g. QGIS) for further elaborations as point cloud decimating or surface and volume measurements.

Among the output files of Agisoft Photoscan we can generate an orthorectified photo of the entire object framed (starting from 38 photos in our case, outcome of the photographic capturing and loaded at the beginning as input of the software).

Agisoft Photoscan can generate as well a Digital Elevation Model (DEM) of the framed zone. The DEM is realized in raster format, associating to each pixel the elevation value of the relative pixelized area in the real object. Figure 4.8 shows an example of these outputs.

Since we had a high-quality camera, a relatively small area to measure, and all

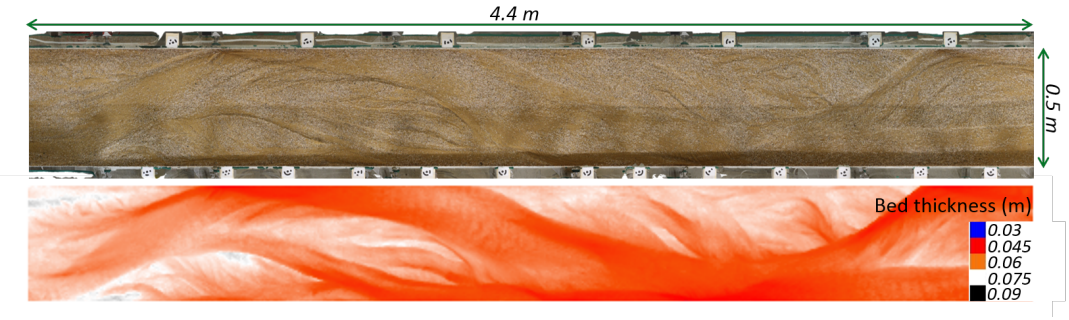

FIGURE 4.8: A picture of Run 1. The top figure is a the orthorectified image of the analyzed area of the flume bed. The bottom figure is the Digital Elevation Model classified using QGIS.

the parameters of the Structure from Motion (SfM) procedure chosen to optimize the algorithms of the software, we got a high-quality result in the output reconstruction. Indeed each DEM cell corresponds to a metrics of 1.2 mm, meaning that for instance in Run 1, namely the run with maximum width that is 0.5 m, each transect of the flume had about 400 bed elevation values.

Among the two techniques used to infer the bed slope, we actually used the slope measurements coming from the manual monitoring in order to have a long data series of bed slope evolution in time. Actually the reconstruction of the entire bed topography, using the SfM procedure, could not have been achieved frequently since it required a good deal of time to take all the areal photos needed and above all since topography reconstruction can be achieved with drained bed only. Conversely we wanted to stop our long morphodynamic runs the least possible. Interruptions were inevitable at the end of an experimental day, that is to say every 6-7 hours of run, because being the sediment feeding an open circuit, the hopper needed to be refilled by hand. Thus every time we stopped the run for this reason we took the pictures necessary for the topography reconstruction. However we realized that many different bed states in terms of slope changes and in general topographic evolution have taken place during the 6-7 hours time interval intervening between two photo capturing for topography reconstruction. Indeed bed topography evolution in our case study was a more rapid morphodynamic change. Thereby it was preferable to have more limited topographic information, namely the bed slope of our manual measurements, but with a higher frequency monitoring.

4.2.3 The outlet solid discharge measurements

Bedload transport rate is among the morphodynamic variables we monitored all runs long. We could measure it in terms of outlet solid discharge. We measured it every 20 minutes by weighing the exiting sediments collected in buckets from which water alone could flow in the water reservoir. This value was not an instantaneous value of the outlet solid discharge, but a value averaged on the time interval of 20 minutes. Indeed we would have liked to get also the information concerning the composition of the transported material, i.e. the fractions' percentage of the outlet solid discharge but because of some practical limitations we did not carry out such a measurement. We could not install devices for the measurement of the total and fractional solid discharge at the flume outlet like the device used in Recking et al. (2009) (transparent ramp placed above an illuminated waterproof box, a video camera placed above the plate and operated in backlighted mode and final identification

of grain sizes after image analysis techniques). We recall that we had a feeding system consisting of an open circuit for sediments which were collected at the flume outlet, weighted by hand, mixed by hand in the boxes containing the stock of the sediment mixture, and reintroduced in the hopper upstream at the flume inlet. This sequence took place in few minutes and it was obviously repeated all the runs long and it was very energy and time demanding for the person in charge; a further operation of drying, sieving and weighting of the outlet solid discharge would have been very demanding, above all considering that it would have been necessary to carry it out with big quantities of sediments analysed and with high frequencies in order to get a meaningful information. Finally we recall that this kind of fraction content would have been a volume fraction content and not an areal fraction content (see subsection 4.2.1 and appendix A) and thus a conversion model would have been needed.

4.2.4 The hydraulic measurements: flow depth, flow width, and flow velocity with Large Scale Particle Image Velocimetry

As for the hydraulic measurements, we gauged the flow depth, the flow width and the flow velocity. They represented necessary information in order to characterize the flow, namely for the determination of subcritical/supercritical flow conditions, sediment transport conditions (incipient motion/non equal mobility/equal mobility), lateral flow constraint.

All three runs were characterized by small water depths with respect to the grain diameter. The lateral confinement varied from one run to another, and before describing the hydraulic measurements we performed it is worth remarking some flow features characterizing the low lateral confined configurations we reproduced.

The three runs were carried out maintaining the same constant values of water and sediment discharge and varying the flume width, as illustrated in figure 4.9 and reported in table 4.4 (for the sake of completeness the flume width, the discharge per unit width, and the width to average flow depth ratio varied from one run to another). In so doing Run 1 and Run 2, flume width 0.5 m and 0.25 m respectively, had configurations with low lateral confinement; Run 1 had a configuration of a braiding system, whereas Run 2 had a central/multiple bars configuration [1]. In both cases the channel could wander in the alluvial bed and the flow did not take place from wall to wall in the flume, conversely a transversal section from wall to wall exhibited emerged zones. On the contrary, the narrower configuration of Run 3 was characterized by a flow as wide as the flume.

Hence, in Run 3 the flow width was constant and always equal to the flume width. As for the flow depth and the flow velocity, they were measured knowing that they did not vary in the spanwise transversal direction.

On the other hand, with the aim of hydraulically characterizing the flow, in the low confined runs we decided to measure the flow depth, the flow width, and the flow velocity where the flow actually took place, i.e. in the main active channel; that is to say, for the hydraulic flow characterization, in the configurations were emerged zones were present, the latter were not concerned by any measurements. Lastly, with "main active channel" we mean the channel with flowing water and sediment (for

[1] A discussion about the flow configuration of the runs is provided in section 4.5 where we perform a linear stability analysis for alternate bars formation using the values of the parameters characterising our runs.

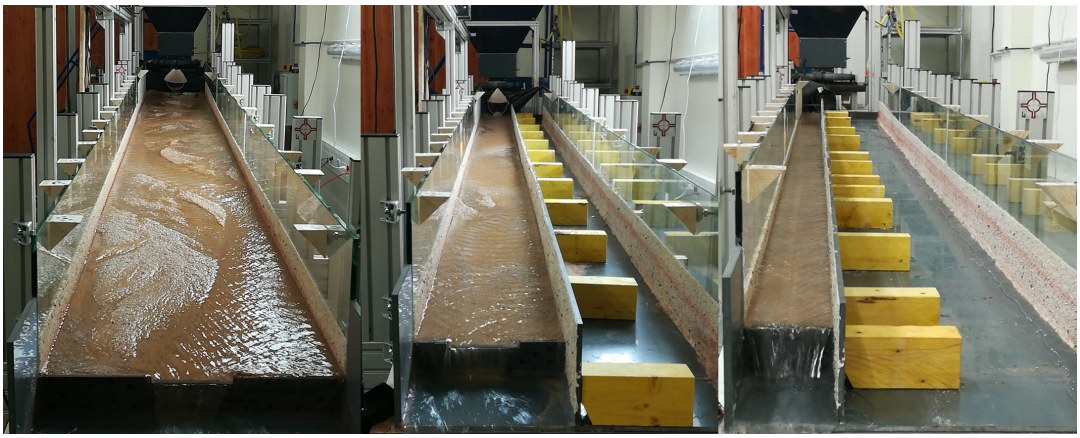

FIGURE 4.9: The three runs configurations. Left figure: Run 1, flume width 0.5 m. Central figure: Run 2, flume width 0.25 m. Right figure: Run 3, flume width 0.12 m.

instance in Run 1 the braided configuration were also characterized, at certain sections in certain moments, by a main active channel, secondary channels with flowing water but without appreciable sediment transport, and emerged zones). The active channel moved and evolved over time as a result of morphodynamic processes related to grain sorting and bedload variations.

Now that we clarified what we meant for flow measurements in contexts of low laterally confined configurations, we can describe frequency and methods of measurements.

As for the active channel width, we measured it during Run 1 and Run 2 (and not during Run 3 in which the flow width was constant and equal to the flume width). The monitoring of the active channel width was performed with a measuring tape; every 10 minutes all runs long at three cross-sections.

The flow depth as well was measured manually using a digital depth gauge. We measured it in various sections (several points per section) few times during the runs, and not with a precise sampling frequency. Indeed, as for the flow velocity, we just wanted a single average value: flow depth and flow velocity are not among the morphodynamic variables we are interested in monitoring all runs long in order to catch the evolution in time. Unfortunately the flow depth measurements are affected by a not slight uncertainty. The flow depth is measured by hand in conditions of very small flow depth (about 1-1.5 cm). Obviously higher water depth measured with probes would not present the same problem in measuring accuracy.

Lastly the flow velocity was measured through the Large Scale Particle Image Velocimetry, LSPIV, method. This is a non-intrusive, non-contact velocity measurement technique based on the analysis of photos sequences, it is able to provide the measurement of instantaneous surface velocities. The LSPIV estimates the displacement of tracer particles between photo pairs, taken with an appropriate time sampling, using a cross-correlation analysis. The tracers can be solid particles, bubbles or turbulence driven patterns; they are all advected with the flow (Le Coz et al., 2014) . In particular, we used the software Fudaa-LSPIV, based on the cross-correlation algorithm developed by Fujita et al. (1998) . The overall outcome of this algorithm is to detect the same tracers in two subsequent photos and hence determine the displacement vector of tracers. Knowing the time interval between the two images the velocity vectors are derived from the displacement vectors. Therefore, a potentially instantaneous 2D velocity field is obtained, time step being limited by the sampling

frequency of image pairs, which is adjusted according to the camera acquisition frequency and the magnitude of pattern movements. In Carbonari (2015) a detailed review and explanation of the LSPIV method is provided, as well as rules of thumb (both for the data capturing and image processing) for the best use of Fudaa-LSPIV in laboratory studies of low-submergence flows. We just recall two points of these good practices: water dyeing and seeding technique.

The water dyeing was necessary because in order to achieve a good tracking water must be completely opaque. Indeed, the flow was characterized by the absence of turbidity and very small water depth (maximum value of 3 centimeters) making clearly visible the sediment constituting the bed and bedload. In this condition, the LSPIV cross-correlation does not work because the velocity measured is related not to the displacement of the flow tracer but to the displacement of bedload materials leading to a wrong estimation of water velocity. We dyed water using titanium dioxide (TiO_2) which is a chemical product often used as a pigment. The seeding technique instead was necessary to create visible tracer in the form of floating patterns moving on the water surface. We used coal dust which is a suitable tracer since it has a good hydraulic behavior moving at the same velocity of water surface and not interacting with channel sides. Coal dust also has a high surface density forming a pattern easily framed also in a small interrogation area during the cross-correlation process.

As for the Fudaa-LSPIV processing, it consists of three main steps:

- extrapolation of an image sequence of the flow from a movie paying attention to the time sampling;
- orthorectification of the images using ground reference points to avoid perspective distortion;
- calculation of the displacement of flow tracers using a statistical analysis algorithm based on cross-correlation of moving patterns.

Hence, first of all we made high-quality movies using one of the two cameras Canon 100D which was utilized to take the photo for Structure from Motion photogrammetry. This camera recorded videos with a frame rate of 50 frames per second. The video itself can be processed with the latest version of Fudaa-LSPIV; in fact the software provides frames extractions as well.

The images orthorectification is the first step of calculations and it requires Ground Reference Points (GRPs). These points were used to solve the eight-parameter image orthorectification relation developed by Fujita and Komura (1994) and we positioned them on the flume walls. If the recorded area is small, as in our case, 6 GRPs are enough to allow a good geometrical transformation solving the algebraic system on which the orthorectification algorithm is based on. At the end of the transformation, all pixels have a known and constant size and are located on a perfectly flat plane.

Then on the orthorectified images we could achieve the analysis of tracers' displacement trough cross-correlation. The overall outcome is the instantaneous velocity field. Spatial and time average of velocity field can be easily computed. Figure 4.10 illustrates the good practices regarding data capturing (dying water and seeding technique) as well as a configuration in which a main active channel, a secondary channel, and an emerged zone are all present.

We took the flow velocity (the outcome of spatial and time averages) as the value

of the mean flow velocity. It is indeed a quite strong assumption but, to us, it was the most "fair" assumption we could do in the flow conditions characterizing our runs. Actually, because of the very small water depth, the velocity profile was not logarithmic, nor linearly increasing from the bed to the free surface. For these reasons we assumed the average surface velocity as the mean flow velocity (any possible reduction of the surface velocity in order to obtain the mean flow velocity would be arbitrary). To conclude the values we have for the flow velocity and the flow depth are affected by a certain inaccuracy because of the tricky floe conditions characterizing our runs. As a consequence the hydraulic characterisation of our runs (for instance the Froude number) is more indicative rather than an exact set of values (however dealing for instance with the Froude number we were certain that the regime was supercritical as photographical evidences showed free surface and bed undulation in phase).

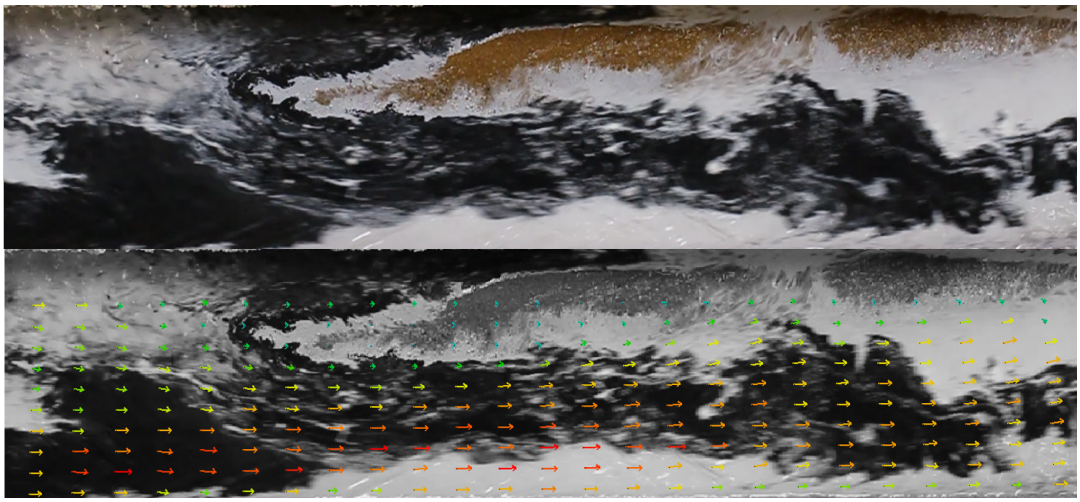

FIGURE 4.10: Velocity measurement using Fudaa-LSPIV in Run 2. In the top figure a frame extracted from the video: water is dyed in white and coal dust forms floating patterns; the main active channel is on the right, an emerged area on the left (orange sediments). In the bottom figure the orthorectified image with a time averaged velocity field superimposed.

4.3 Experimental procedure and conditions

We carried out some preliminary runs to define the ensemble of external parameters, namely the flow rate and the sediment feed rate, in equilibrium with the slope we set. The flume slope was set at the fixed value of 3.18 % (see subsection 4.1.2). The feeding sediment mixture is the one described in subsection 4.1.2 (60 % coarse fraction, 40 % fine fraction). At the end of the preliminary runs it appeared that the flow and sediment discharge in a dynamic equilibrium with $S = 3.18\%$ were 0.55 l/s and 8 g/s.

Hence all three experiments were performed with the same steady sediment feed rates: 0.55 l/s and 8 g/s; whereas we varied the flume width and consequently the flow confinement (table 4.4).

We modeled first, low constrained flows (Run 1 and Run 2) and then a confined flow (Run 3). Precisely Run 1 was characterized by a flume width of 0.5 m and a width to average flow depth ratio, hereinafter width-to-depth ratio, of about 100; Run 2 had a flume width of 0.25 m and a width-to-depth ratio of about 30; Run 3

had a flume width of 0.12 m and a width-to-depth ratio of about 8. We point out that for the determination of the width-to-depth ratio the flow depth taken into account is the average flow depth. For the sake of clarity, it means that over a section in which for instance emerged zones are present, the latter as well are considered with their zero flow depth and thus they contribute to the average flow depth of the cross-section. Indeed, the width-to-depth ratio is a non-dimensional number that indicatively classifies flow confinement from narrow configurations to very wide ones, such as braiding system in which the flow can greatly move in the lateral direction and form its active channel in a wide alluvial bed. (Conversely, as illustrated in subsection 4.2.4, the flow depth for the hydraulic characterization of the flows is determined only in the main active channel points of the cross-section).

The three runs reproduced three different morphodynamic configurations which are, respectively for Run 1, Run 2, and Run 3, a braiding system, a central/multiple bars configuration, a narrower configuration so narrow that alternate bars could not form (figure 4.9).

In the introduction of chapter 4 we illustrated the criterion we followed when varying the flow confinement from one run to another. Our decision about flow confinement variation was based on the observations of the width of the self-formed channel.

The first configuration had the lowest lateral constraint corresponding to a width equal to 0.5 m, the second experiment was performed with a halved width, ending with the third one corresponding to a 0.12 m large flume. These decreasing values till the one of 0.12 m were chosen after the observation and monitoring of Run 1's active channel width, whose average value was 0.12 m. The same average value was found monitoring the active channel width during Run 2. Therefore we interpreted this value as the average width of a self-formed channel free to wander in its alluvial bed (given certain conditions of bed slope and sediments). And we found interesting to observe a configuration in which the flow had exactly this space and thus no more the possibility of lateral mobility, hence Run 3 was performed with the flume width of 0.12 m.

In summary, here we give the detailed characteristics of the three runs. In the following list all the common conditions of the three runs are set out, namely the unchanged features, what we kept constant from one run to another. Conversely table 4.4 contains the characteristics in which the three runs differed.

All the runs were performed with:

- a constant water discharge of 0.55 l/s;
- a constant sediment discharge of 8 g/s;
- the same bimodal sediment mixture composed of 60% by a coarse fraction (d_{50} = 1.8 mm) and 40% by a fine fraction (d_{50} = 0.7 mm) as described in details in section 3.1.1;
- a duration of 60 hours;
- a flume setup consisting of the entire flume length (6 m) and a fixed slope of the flume structure of 3.18%.

In particular the slope set out in table 4.4 is the average bed slope, i.e the slope we measured all runs long on the entire flume bed length (see subsection 4.2.2). As for the flow depth, flow width, and flow velocity, they are the outcome of the hydraulic measurements widely outlined in subsection 4.2.4. In particular, the flow depth was

TABLE 4.4: Runs' characterization; what distinguish one run from another.

Run	Flume width	Slope	Flow width	Flow depth	Flow velocity	Fr	θ/θ_c
1	0.5 m	3.26%	0.12 m	0.01 m	0.443 m/s	1.4	1.568
2	0.25 m	2.85%	0.12 m	0.011 m	0.506 m/s	1.5	1.686
3	0.12 m	2.73%	0.12 m	0.012 m	0.6 m/s	1.6	1.838

measured in different cross-sections of the active channel, few times for each run; table 4.4 provides an average value. Flow velocity was measured in a 1-m-long sector of the flume; only non-zero values are considered, i.e. grid points in the active channel, see subsection 4.2.4). The LSPIV method gave a 2D velocity field; values in table 4.4 are the averages both in the streamwise and in the spanwise direction. Lastly, the Shields values, θ, are obtained considering the aforementioned average slope and the d_{84} of the sediment mixture; the critical Shields value, θ_c, is 0.6 after Ashida & Michiue.

4.4 Methodology

The monitoring, all runs long without interrupting the hydrograph, of the bed surface sediment composition (subsection 4.1.2), the bed slope (subsection 4.2.2), and the outlet solid discharge as a measure of the bedload transport rate (subsection 4.2.3) allowed us to obtain long time series of such physical quantities.

In particular, the time series concerning the bed sediment composition are of different types since we could perform different operations of data processing starting from the photos taken for the bed surface sediment composition measurements (subsection 4.2.1, appendix B). Indeed we could separate coarse and fine grains both at the grain scale, and thus obtain the percentages of the two fractions covering the framed area, and at the pattern scale, and thus obtain the area covered by patches of coarse grains and patches of fines. We provide here the explanation of why it is important to get the information consisting of the area covered by patches of fines, and we illustrate as well how such information is associated to other measurements such as the active channel width.

By analyzing the photos captured for the study of the bed surface sediment composition we found out that the bed of the main active channel was characterized by a rather homogeneous presence of fines. Indeed, within the wide unconfined bed, the main active channel was the place where the bedload transport was more intense than anywhere else, and thus, a relevant erosion took place. Hence the eroded zones, which manifested themselves as zones rather homogeneously composed by fines, could indicate the active channel itself and a state of the bed concerned by intense bedload transport. The greater was the extension of the zones rather homogeneously composed by fines (hereinafter patches of fines), the larger was the main active channel width, the more intense was the sediment transport. An example of this is shown in figure 4.11.

Hence we could use the area covered by patches of fines as a proxy for the active channel width.

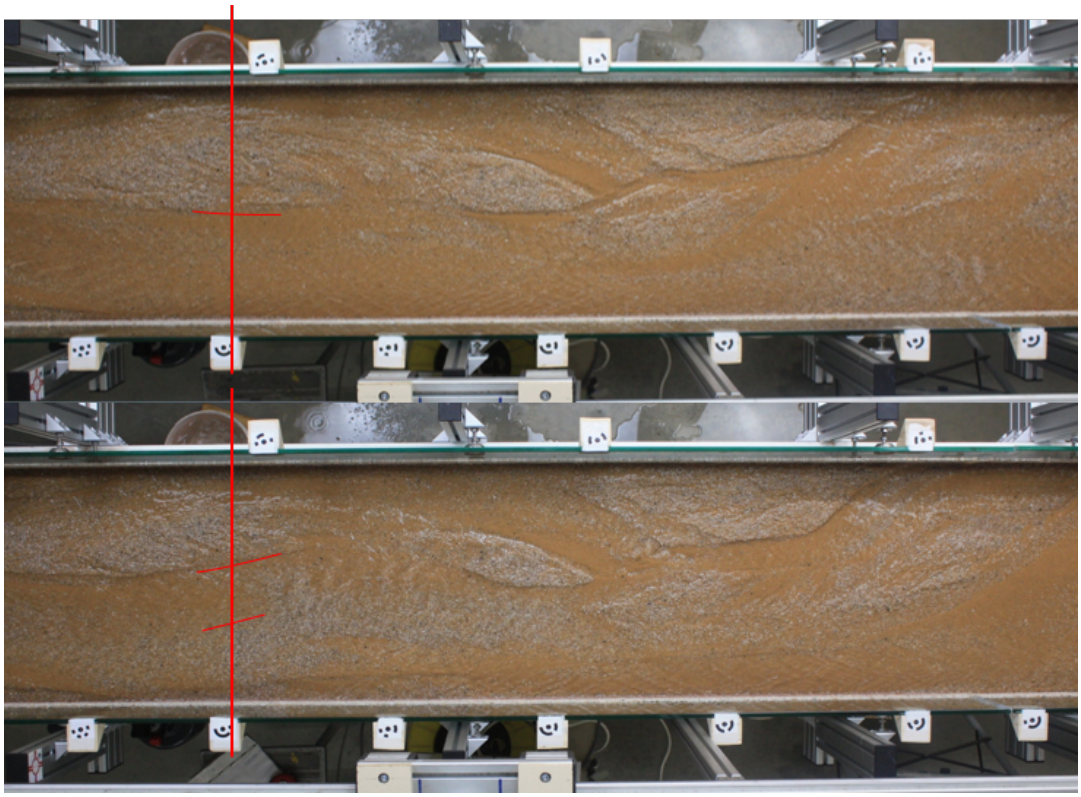

FIGURE 4.11: A photo taken during Run 1; the central part of the flume is framed, the flow is from left to right. The red line indicates a section at which we measured the main active channel width; emerged zones are mainly composed by patches of coarse grains. Top figure: the channel, on the right side, covers half width on the flume; the active channel bed is composed of fines. Bottom figure: the main active channel is narrower, concomitantly a greater amount of coarse grains covers the flume bed.

For this reason, among our image processing operations, we also performed the morphological operation consisting in identifying patches of fines (subsection 4.2.1, appendix B).

By achieving this operation for all the images captured for the analysis of the bed surface sediment composition, we obtained the time series called "% Area Fine"; precisely the patches of fines were detected, their areal extension was determined, the total area occupied by patches of fines was calculated by sum, the latter was expressed as the percentage of the total framed area.

Indeed it was strictly necessary to use the "% Area Fine" to asses the active channel width, since the metric measurements of the active channel width (flow width measurements are described in subsection 4.2.4) formed time series chaotic and not usable. We recall that we measured the active channel width in three cross-sections both during Run 1 and Run 2.[2] We obtained time series of the metric values of the channel width. These time series gave the interesting information of the average value of the main channel width: the time average in each cross-section both in Run 1 and Run 2 was 0.12 m[3] (table 4.4). Nevertheless, the entire time series of the channel width measurements showed no trend nor periodicities. There was not

[2] As described in the introduction of chapter 4, during Run 3 the flow width is equal to the flume width; the flow is from wall to wall, hence the active channel coincides with the flume.

[3] We interpreted the average channel width as the width of the self-formed channel; a more detailed explanation was provided in the introduction of chapter 4.

correlation between, for instance, the time series of the upstream cross-section and the time series of the two downstream cross-sections. Moreover, we could not establish any relation between the active channel width's signal and the time series of the other morphodynamic bed variables (i.e. the bed slope and the sediment transport rate).

Lastly, we provide a further remark about the measurements of the active channel width on one side, and of the area covered by patches of fines on the other. As we said, they both aim at identifying the eroded zones, i.e. the zones where sediment transport is intense, but the first is a local measurement, whereas the latter is a measurement in which a wide region is taken into account. Actually the active channel width was measured at three precise cross-sections, therefore this was an information concerning a single streamwise abscissa. Conversely the area covered by patches of fines concerned a region, precisely the area framed in the photos for the image processing (the entire flume width by the central 2.8 meters of the flume length); thus this was a more global information. And it was better (as results will show in the following) to deal with this kind of information since the other signals too were of this type. Indeed, the percentage of coarse grains composing the bed surface and its dual, the percentage of fines (see subsection 4.2.1, appendix B), were obtained by studying the same area; the bed slope concerned the entire flume length; and the sediment discharge is a global signal as well.

It is worth noting the difference between the signal "% Fines" and the signal "% Area Fine". "% Fines" just give the information of how many grains of the total are fine grains and it does not take into account if fine grains are aggregated or not.

We can visualize such difference by plotting for both Run 1 and Run 2 the time series % Fines and % Area Fine, figure 4.12.

The signals% Area Fine and % Fine get closer in Run2. In Run 2 they have similar values, whereas in Run1 % Area Fine and % Fine have different values, in particular % Area Fine has lower values than % Fine. Whereas in Run 3 it was not possible to perform any morphological operations able to identify patches of fines, and consequently to get % Area Fine.

The reason of that lies in the fact that the greater is the presence of forms and morphological patterns (coarse grains corresponding to depositional patterns; fines corresponding to eroded zones), the more significant and effective is the morphological operation of identification of patches of fines. The more the flows are wandering, with deposits and emerged zones, the more this condition of clear morphological patterns is present. This is what happen in Run 1, the lowest confined flow.

This fact does not mean that no sorting patterns take place in more confined flows like those of Run 2 and Run 3; in these configurations coarse grains and fines are segregated as well; focusing on patches of fines, they are more extended than in Run 1 and fine grains are more interconnected than in Run 1 (figure 4.13). In Run 1 there are more intrusions of fines in deposits of coarse grains; these small quantities of fines are detected in the counting of percentage of fines whereas are excluded from the identification of patches of fines (and thus from % Area Fine) since they are very small areas of fines subject to morphological erosion[4]. This is the reason why % Area Fine has lower values than % Fine in Run 2.

Hence we could investigate the overall behaviour of the "river bed system" by

[4]The detailed explanation of how the detection of patches works, and thus the functioning of morphological operations among which "erosion", was provided in appendix B.

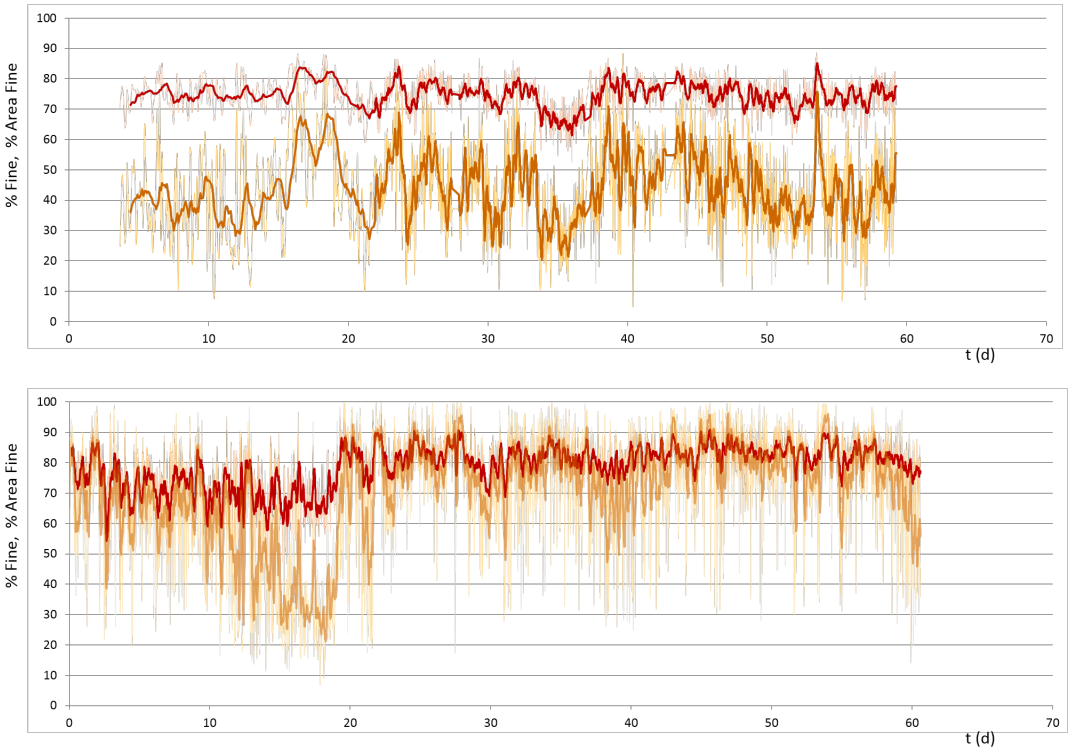

FIGURE 4.12: The signal % Fine is in red, the signal % Area Fine is in orange. Top figure: Run 1. Bottom figure: Run 2. Thin, light lines represent the original high-frequency signals; thick lines represent the Simple Moving Average (SMA) of the signals.

FIGURE 4.13: The three runs compared through demonstrative pictures aiming at illustrate the different "patchiness" of the three different configurations.

studying the ensemble of the time series of the bed surface sediment composition (signals % Coarse, % Fine, % Area Fine), the bed slope, and the outlet solid discharge. These information were completed with measures of vertical sorting. At the end of each run we took samples of the substrate. Precisely, for each run we took about 10 samples distributed along the flume obtained removing a 5-mm-thick superficial sediment layer. The samples were dried and sieved, and then the substrate sediment composition determined (volume fraction content).

4.5 Results and discussion

Results concern the time series (section 4.4) of the morphodynamic bed variables we monitored all runs long. The bed surface sediment composition, the bed slope, and the sediment transport rate have complex mutual dependence; their ensemble and feedbacks depict the morphodynamic evolution of the river bed. Together with the information of planimetric sorting (time series of the bed surface sediment composition) we provide information of vertical sorting, through the analysis of the substrate samples.

In this section we present first the three runs one by one, and then the comparison of the three runs. The flow configurations and their features are discussed through the use of linear stability analysis as well.

4.5.1 Run 1

The bed system was concerned by rapid dynamics of channels' self-formation accompanied by sorting processes. Bed states were characterized by the presence of multiple bars and braided patterns, whose formation and destruction generally took place rapidly producing on the bed surface well-defined patches of coarse sediments and fines. This continuous and rapid evolution and rearrangement of the bed surface took few minutes, as it is shown in figure 4.14, in which indeed we can notice how the bed dynamics was extremely fast and complex. In particular, we observed "sorting waves" (panel b of figure 4.14) leading to continuous changes in the superficial grain size distribution.

It appears that the granulometric sorting of the bed surface was very efficient both in the spanwise and streamwise direction, whereas vertical sorting was almost completely absent: samples of the substrate at the end of the run have indeed the same composition (about $\pm$ 2-3 %) of the initial bed state and of sediment fed.

Results concern the analysis and interpretation of the time series measured during the experiment (bed slope and outlet solid discharge) and detected through image processing techniques (surface texture in term of coarse/fine percentage and relative area occupied by fine sediment patches).

Albeit the run was conducted under constant feeding rate conditions, the outlet sediment discharge presented continuous fluctuations over time around the input value (figure 4.15) as already showed in other flume experiments (Recking et al., 2009; Bacchi et al., 2014) even if with a different lateral confinement, particularly narrow flow configurations.

The fluctuations around the $Q_{s,out}$ mean value ($Q_{s,out}$ mean value equals $Q_{s,in}$, given the dynamic equilibrium conditions characterizing the run) were of the order of the 50% of the average $Q_{s,out}$ (figure 4.15). Precisely the highest values of $Q_{s,out}$

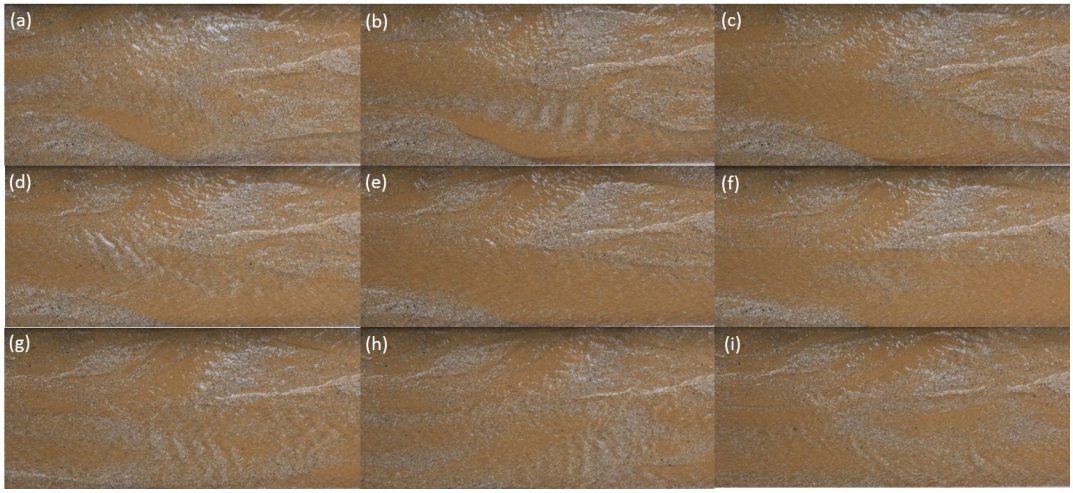

FIGURE 4.14: Panels from (a) to (i) all frame the same area of the flume, in particular a zoom of the central part of the flume photographed to study the granulometric composition of the bed surface. These photos are taken every minute and they revealed how rapid is the rearrangement of the bed surface in terms paving/fining processes.

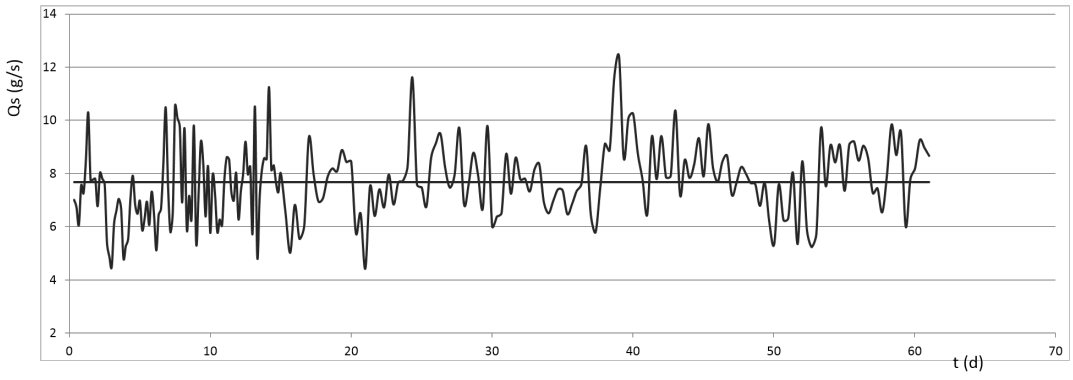

FIGURE 4.15: Run 1. The outlet solid discharge as a measure of the bedload transport. The average of the solid discharge is indicated as well (horizontal line) and it is in equilibrium with the constant value of the inlet solid discharge equal to 8 g/s.

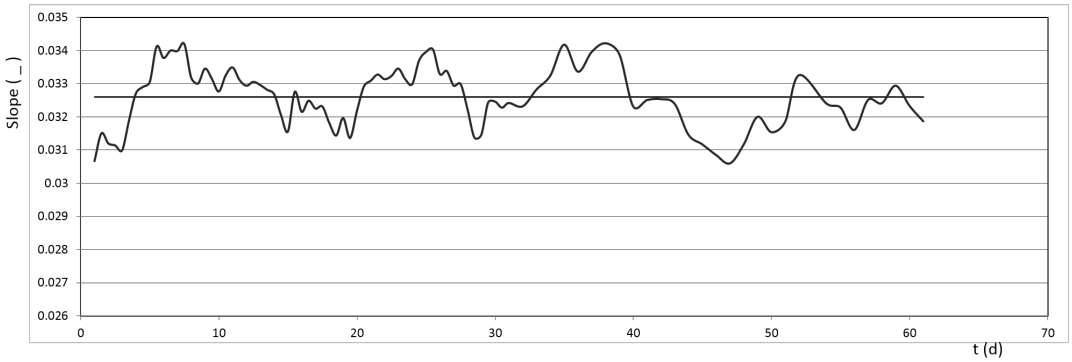

FIGURE 4.16: Run 1. The slope signal and its average value (horizontal line), the latter equal to 3.26 %.

and the lowest values of $Q_{s,out}$ were respectively about 60% higher and 40% smaller than the average $Q_{s,out}$.

We observed significant fluctuations of the bed slope (figure 4.16), and of the percentage of the granulometric fractions composing the surface texture (figure 4.17) as well.

As illustrated in subsection 4.2.2 the bed slope was obtained from the measurements of bed elevation in three cross-sections. In so doing we got also local bed slopes, precisely for three 2m-long reaches, as well as a total bed slope computed between the upstream section and the downstream one. The average of the slope of the three reaches was equal to the total upstream-downstream slope, and in any case, in the analyses we considered the total upstream-downstream slope, hereinafter just called slope.

The fluctuations around the average slope were of the order of the 6% of the average slope. The upper and lower peaks of the fluctuation had almost the same values, and a clear periodicity can be observed.

The signals of the bed surface composition are concerned by very intense and rapid fluctuations, we recall that the photos aimed at this bed surface texture analysis were taken with a frequency of one per minute.

More indicators and and descriptive statistics of all these signals now presented one by one are provided when we deal with the comparisons of the three runs. Now that we presented the time series separately we can put them together in order to analyse their trend and every dependence of one upon the other.

The evolution over time of the percentage of the coarse fraction was in opposition with the time trend of the sum of the surfaces covered by patches of fines, the sum of the aforementioned areas was expressed in terms of percentage of the total bed surface as well (figure 4.18, top plot). Patches of fine sediments constituted the zones where the channel was more active (in terms of transport rate).

It therefore turns out that when the patches of fines covered a wide area of the bed, the bed slope was low, corresponding to stages of fining and degradation of the bed; we observed indeed a concomitant increase of the outlet solid discharge. On the contrary, when the patches of fines covered a small area of the bed, a coarsening and aggradation bed state took place, in conjunction with a decrease of the outlet solid discharge; during this stage, the bed was characterized by higher values of the slope.

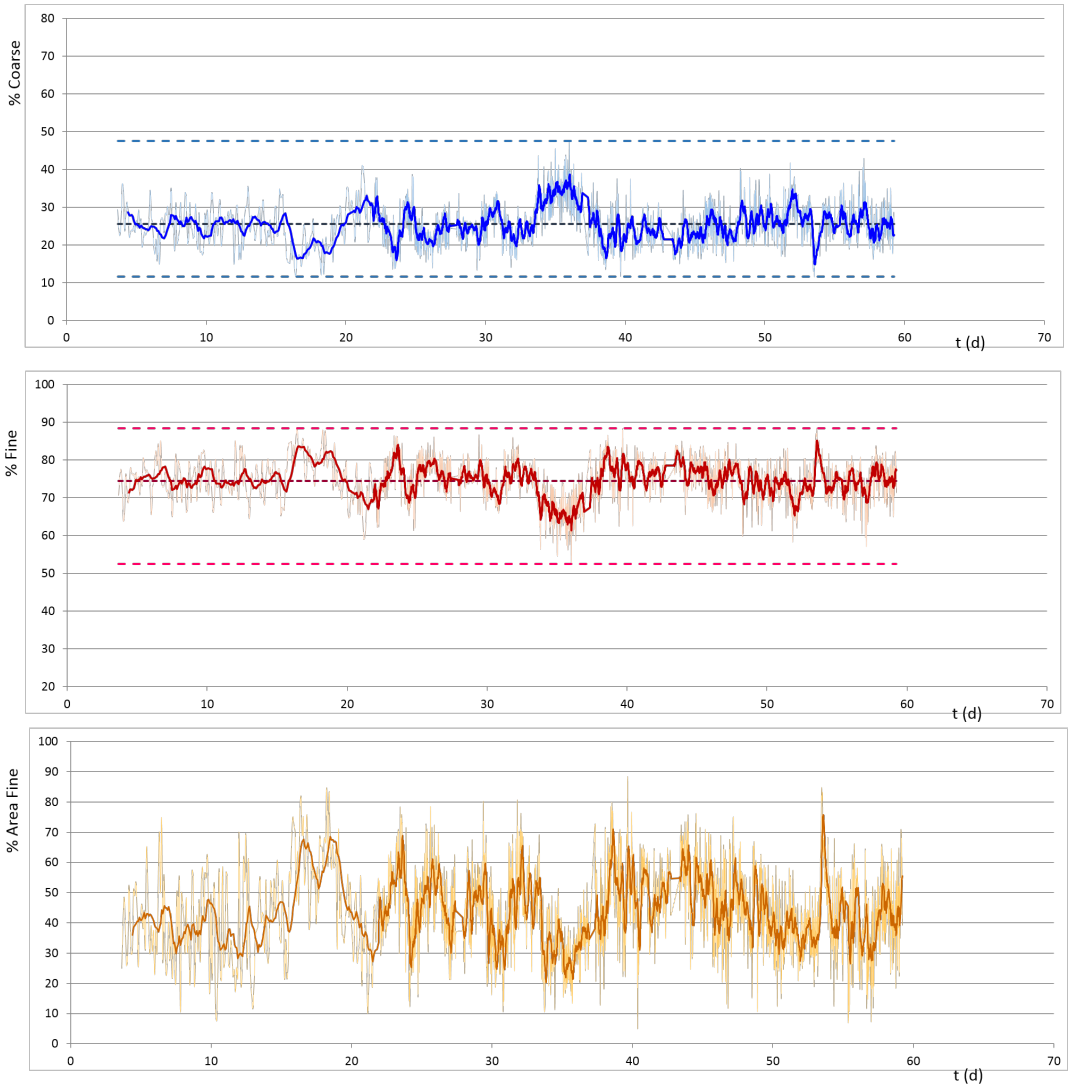

FIGURE 4.17: Run 1. The signals of the bed surface composition. The thin, light-coloured lines represent the signals themselves for which the "sampling frequency" is one value per minute (one value every 5 minutes during the first 20 hours, after which we realised that sediment surface rearrangement was so rapid that a more frequent data capturing was preferable. The thick lines are 10-values moving averages.

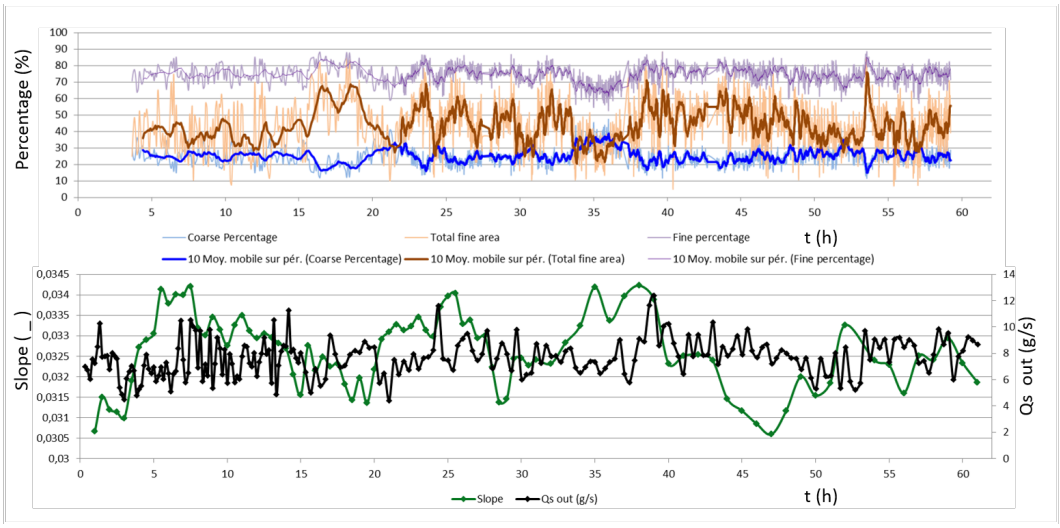

FIGURE 4.18: Run 1. Top figure: time series of the percentage of the coarse fraction of the bed surface, the fine fraction of the bed surface, and the total surface covered by patches of fines; Simple Moving Average (SMA) of each quantity is shown as well. Bottom figure: time series of the average bed slope and the outlet solid discharge.

We reaffirm the feedback between the slope and the solid discharge with the following description. During increasing phases of bed slope, we registered minimum values in the outlet solid discharge resulting in aggradation and low grain mobility, whereas just after the bed slope reached the maximum value equal to about 3.4 %, we registered high values in the outlet solid discharge associated to a high grain mobility. Subsequently we measured an upper-middle sediment discharge at the outlet which lasted even when the bed slope had already decreased its value meaning that the "bed system" needed some time to evacuate sediments previously stored.

Actually, this mutual dependence between the fluctuations of the solid discharge and the fluctuations of the slope were confirmed by Fourier analysis in the frequency domain. Indeed the two signals revealed similar periodicities, precisely they were characterized by similar frequency signature in particular for high frequencies, identifying in both the signals a period of about 15 hours.

The % Area Fine signal and the Q_s signal had a comparable trend with a lag of the latter respect to the former (figure 4.19). After the maximum bed slope was reached, the coarse pavement (relatively extensive) was suddenly destroyed resulting in a decrease of the coarse percentage and an increase of the fine patches accompanied by erosion episodes which led to high values of solid discharge registered in the outlet section with a lag time due to damping effect of the flume's wide lateral space.

Run 1 showed that, similarly to what was demonstrated in constrained flows, large bedload fluctuations also occur in non-constrained flows. However, they are not due to (only) vertical sorting and slope fluctuation, but also to large bed surface sorting producing highly mobile patches of fines. The coming results with same input conditions will show how this surface process is affected when the flume width is reduced.

4.5.2 Run 2

From Run 1 to Run 2 we halved the flume width (see table 4.4), in this configuration, maintaining the same feeding rates and the same flume slope of Run 1, we obtained

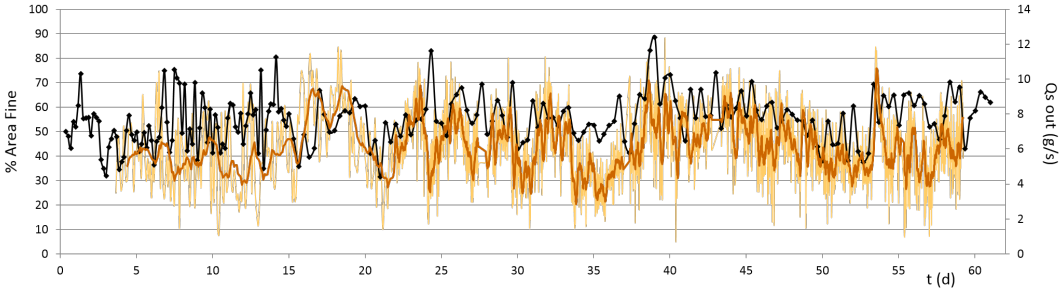

FIGURE 4.19: Run 1. Time series of the outlet solid discharge and the total surface covered by patches of fines.

a morphology of central/multiple bars (see figure 4.9).

Before the beginning of measurements used to achieve the time series described in section 4.4, we run the experiment for a few hours in order to let the bed adjust to the new width configuration. During this phase an upstream erosion took place, indeed the slope settled at an average value slightly smaller than that of Run 1 (see table 4.4). However, the first 20 hours of the signals of the bed surface sediment composition (figure 4.20) gave rise to doubts as to whether this initial adjustment phase was not long enough. Looking at these time series (figure 4.20) we can observe that the average value of both % Coarse (and its dual % Fine) and % Area Fine of the first almost 20 hours differed from the respective average value of the remaining almost 40 hours of the run.

We recall that the photos for the measurement of the bed surface sediment composition framed the central part of the flume (the central 2.8 meters of the flume length). Thus we did not have a recording of the bed sediment composition of the upstream part of the flume, and it is obviously this reach the one more affected by initial bed adjustments. We can notice that for the first 20 hours of the run the bed surface of the framed area was coarser with respect to the rest of the run. This could suggest that the transitory adjustment phase of erosion could not be over when we started recording the measurements. However, we do not have a clear explanation for the trend of these signals, but we verified that no external disturbances took place.

As in Run 1, in Run 2 too the signals of Q_s, S, % Coarse, % Fine, % Area Fine revealed significant fluctuations, see figures 4.21 and 4.20.

As in Run 1, concerning the outlet solid discharge, the average value of $Q_{s,out}$ coincided with the steady value of the sediment feeding rate (see table 4.4) and thus we can affirm that we reproduced dynamic equilibrium conditions. The fluctuations around the average value of $Q_{s,out}$ were of the order of the 10% of the average itself; precisely the highest values of $Q_{s,out}$ and the lowest values of $Q_{s,out}$ were respectively about 13% higher and 8% smaller than the average $Q_{s,out}$.

Now that we presented the time series separately we can study them in their ensemble in order to analyse their trends and feedbacks.

The top plot of figure 4.22 shows that the time series of bed slope and the time series of the outlet solid discharge had the same trend. An increase of the bed slope went together with an increase of the outlet solid discharge, whereas low stages of the slope were associated to low sediment transport rate. Moreover, between the two signals only a slight lag was present; the more the flow is confined, the smaller is the lag between the slope and the $Q_{s,out}$ signals (see figure 4.18).

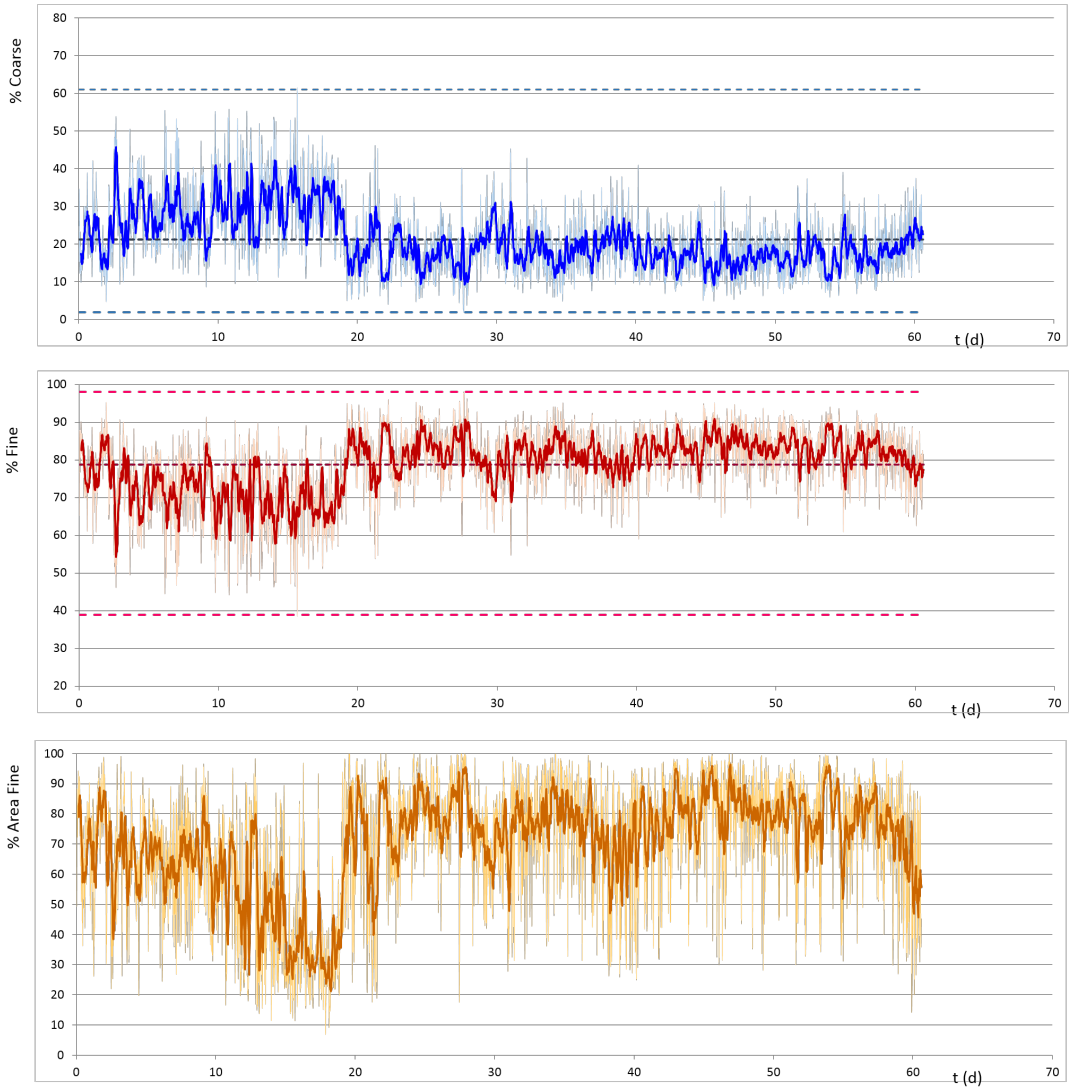

FIGURE 4.20: Run 2. The signals of the bed surface composition. The thin, light-colored lines represent the signals themselves for which the "sampling frequency" is one value per minute. The thick lines are 10-values moving averages.

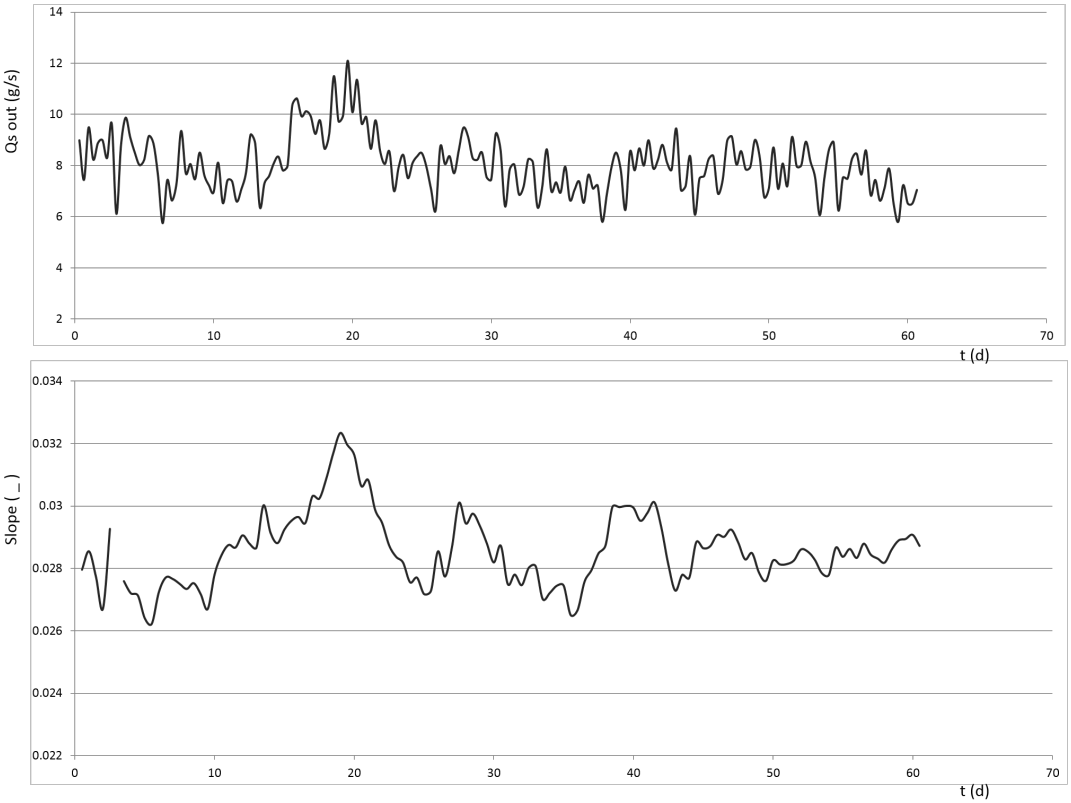

FIGURE 4.21: Run 2. The outlet solid discharge signal and the slope signal.

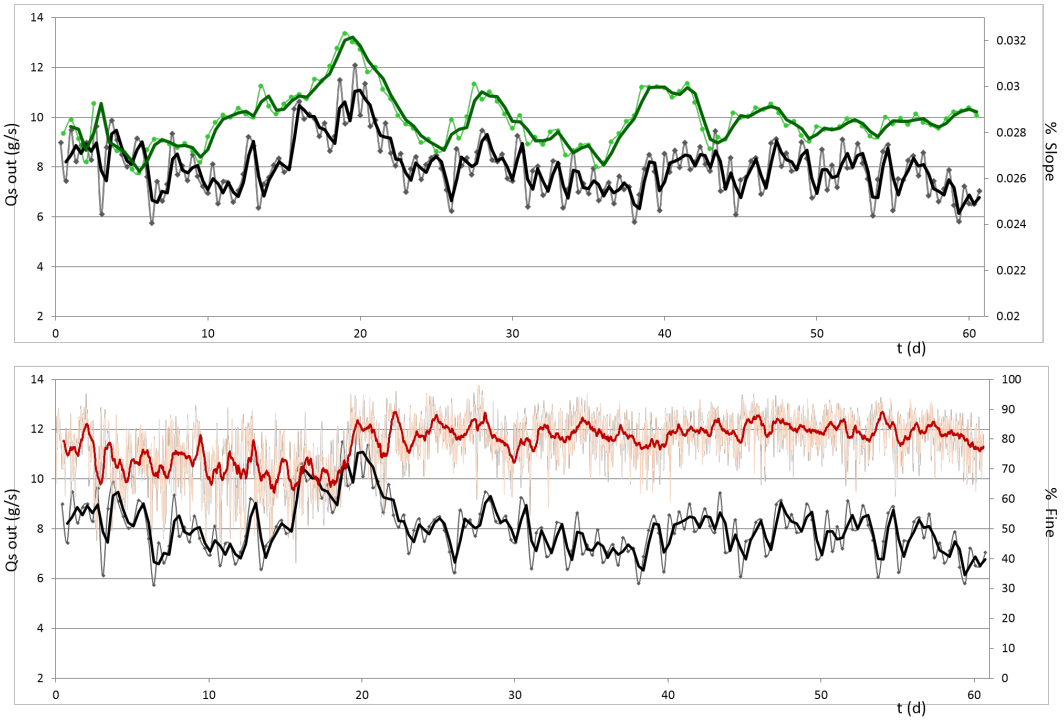

FIGURE 4.22: Run2. Top figure: the solid discharge and the slope signals. Bottom figure: the solid discharge and the % Fine signals. Both the signals themselves and their Simple Moving Average (SMA) are plotted.

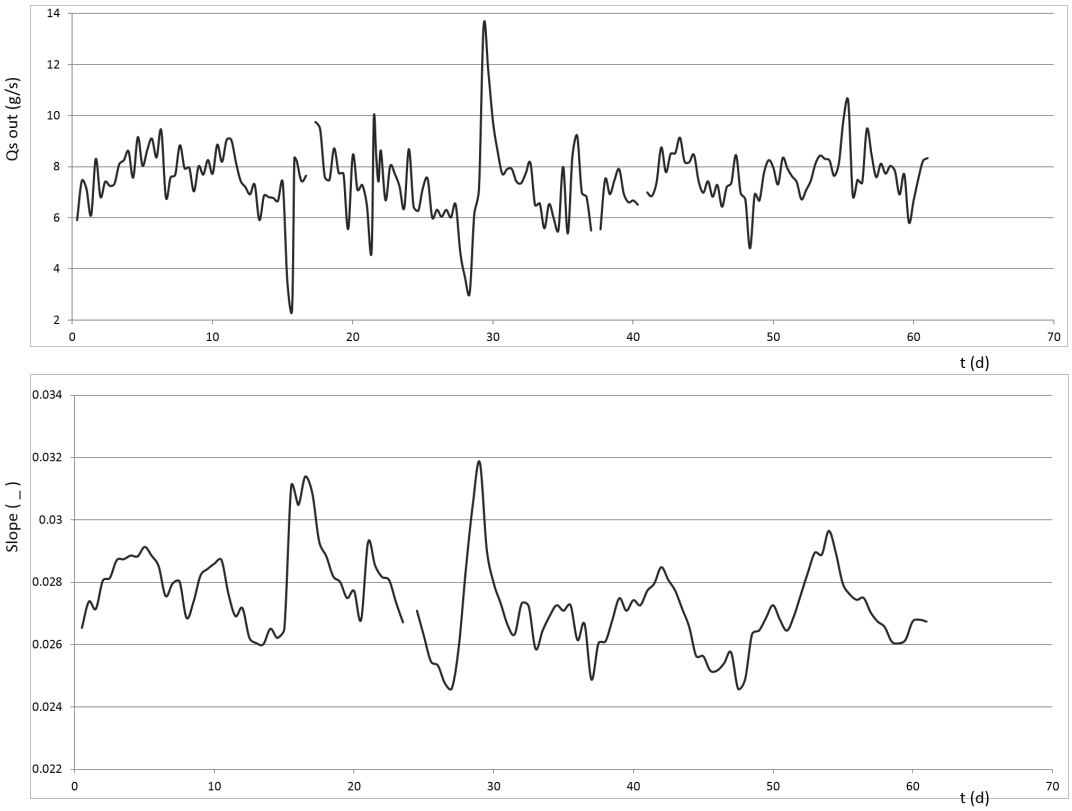

FIGURE 4.23: Run 3. The outlet solid discharge signal and the slope signal.

The bottom plot of figure 4.22 shows that fines (% Area Fine and% Fine) are a good indicator of bedload transport rate. High presence of fines went with intense bedload transport rate. In this plot the signal % Fine is represented, but similarly the signal % Area Fine would be a good indicator of the bedload transport rate, indeed figure 4.12 shows that for Run 2 the signals % Area Fine and % Fine tended to coincide, as illustrated in section 4.4. Hence the greater was the extension of the zones covered by patches of fines (eroded zones), the more intense was the sediment transport.

In Run 2 the planimetric sorting processes were intense, as the oscillation of the signals of the bed surface sediment composition showed (figure 4.20), and the mutual dependence of such signals with the slope signal and the solid discharge signal was the same of what we observed in Run 1. The efficient planimetric sorting of the bed material seemed the only relevant sorting process occurring, since the substrate samples taken at the end of the run (see section 4.4) had the same composition of the well-mixed sediment mixture (feeding sediment mixture, 4.1.2) with which the initial bed state was constituted. Precisely the substrate samples composition differed from the mixture (60% coarse, 40% fines) of $\pm 3\% - 4\%$.

4.5.3 Run 3

In Run 3 too the signals of Q_s, S, % Coarse, and % Fine revealed significant fluctuations, see figures 4.23 and 4.24, with the evident presence of intense and fast peaks.

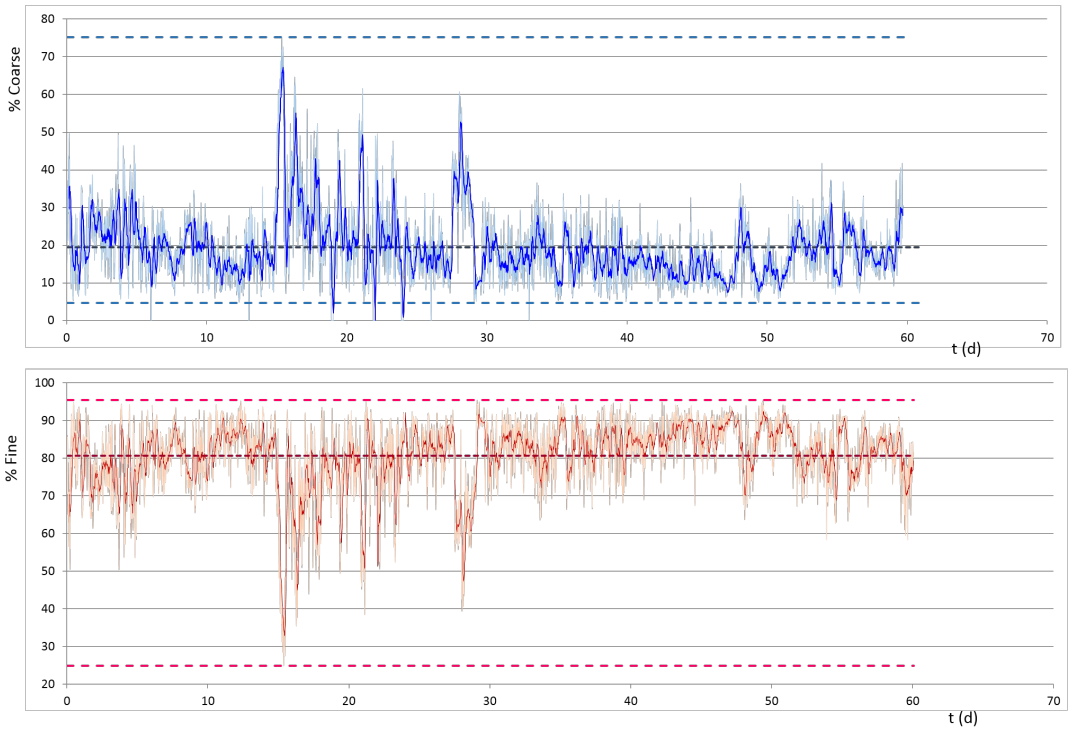

FIGURE 4.24: Run 3. The signals of the bed surface composition. The thin, light-colored lines represent the signals themselves for which the "sampling frequency" is one value per minute. The thick lines are 10-values moving averages.

Time series of slope and outlet solid discharge confirmed the magnitude of fluctuations observed for these physical quantities in comparable narrow flume experiments (Recking et al., 2009), see subsection 2.4.2. In particular in Run 3 the fluctuations around the average value of $Q_{s,out}$ were of the order of the 70-80% of the average itself; precisely the highest values of $Q_{s,out}$ and the lowest values of $Q_{s,out}$ were respectively about 80% higher and 68% smaller than the average $Q_{s,out}$.

Now we show the ensemble of Run 3's signals in order to observe the dependencies of one signal upon the other.

The plot of the solid discharge and the slope together (figure 4.25, top plot) reveals that the two signals had the same trend with a slight lag of $Q_{s,out}$ with respect to the slope. Rising parts of the slope signal were followed by rising parts of the $Q_{s,out}$ signal, and falling limbs of the slope signal were followed by falling limbs of the $Q_{s,out}$ signal. The lag was slight with respect of the lag between the homologous signals of Run 1 and Run 2 (see figures 4.18 and 4.22), since in the narrower Run 3 there was not the damping effect due to the flume's wide lateral space.

Aggrading bed was associated with low outlet solid discharge and aggrading stages went together with coarsening stages of the bed (figure 4.25, central plot). Indeed aggradation was associated to reduced gravel mobility (reduced transport rate) and efficient sediment sorting that manifests itself through a coarsening of the bed surface.

This behavior was particularly evident and intense in the time windows concerned by the peaks, around hour 15 and around hour 30. Actually at these moments of the run we observed bedload sheets as described in Recking et al. (2009)

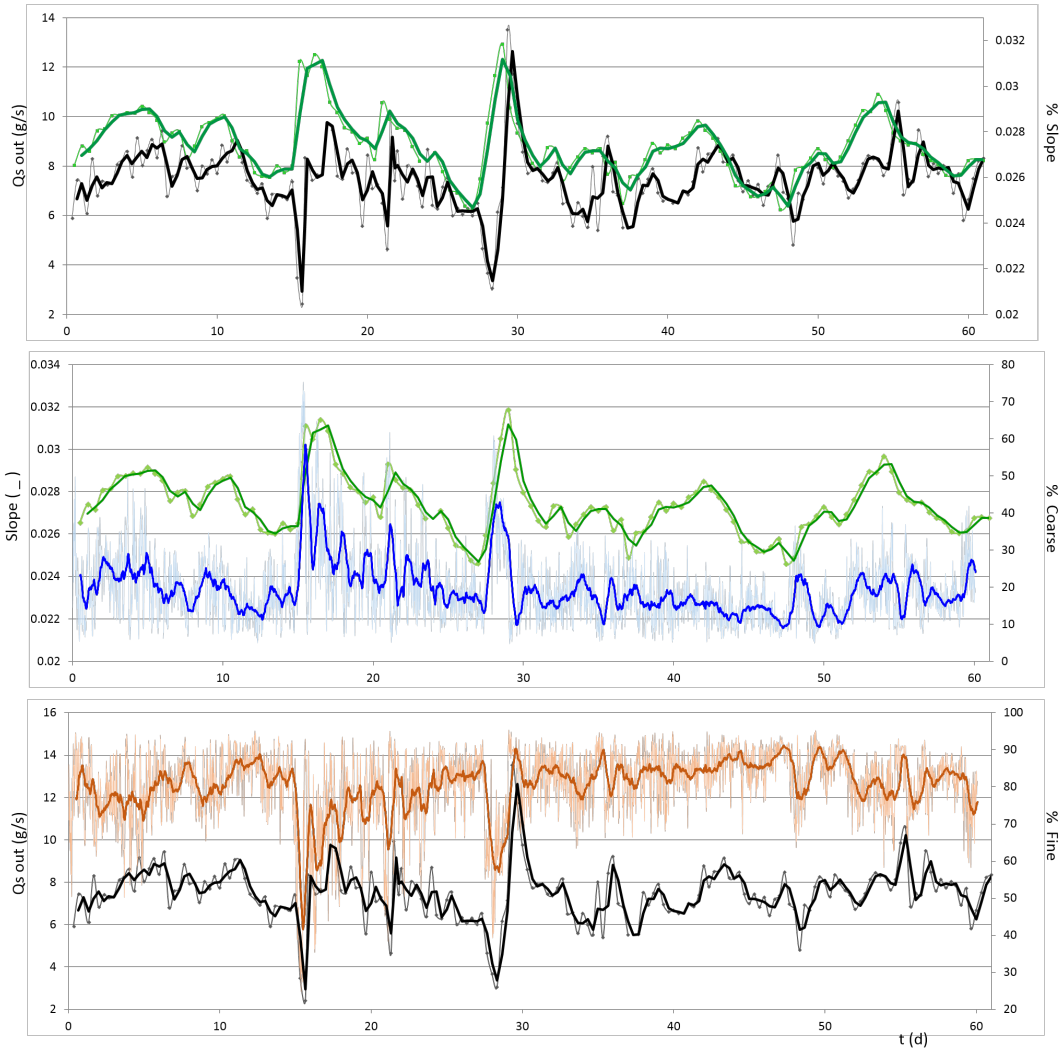

FIGURE 4.25: Run3. Top figure: the solid discharge and the slope signals. Central figure: the slope and the % Coarse signals. Bottom figure: the solid discharge and the % Fine signals. Both the signals themselves and their Simple Moving Average (SMA) are plotted.

and indeed a very efficient process of bed coarsening. This stage of rapid and intense aggradation and coarsening stopped with the attainment of a maximum slope; then sharp and rapid erosion episodes with pavement destruction took place; the bed surface composition was characterized by fine grains zones more and more extensive, and concomitantly the outlet solid discharge increased as well (figure 4.25, bottom plot).

The peaks of the time series % Coarse, top plot of figure 4.24 and central plot of figure 4.25, (corresponding to the minima of its dual % Fine, bottom plot of figure 4.24 and bottom plot of figure 4.25) reached such high values because coarse grains covered a very long reach of the flume. With respect to Run 1 and Run 2 the patches of coarse grains not only were more homogeneous (less intrusions of fines) but also they were much longer. Right picture of figure 4.26 and the second to last picture of figure 4.27 illustrate an example of this bed state.

During these stages of the bed, the extension (i.e. the length) of these coarse surfaces was so great that it seems no more appropriate to talk about patchiness. On the contrary Run 1 and Run 2 had patches of coarse grains which never were as long as the entire flume.

It seems that in our narrow flume experiment, without the degree of freedom consisting in transversal bed state variations, substantial sorting processes could affect longer spatial scales with respect to low confined flow configuration (Run 1 and Run 2). Indeed in Run 3 we observed substantial sorting processes also at the reach scale, a larger scale with respect to the one of patches of Run 1 and Run 2.

FIGURE 4.26: Run3. Photos of bedload sheets. Left picture: a view from upstream towards downstream; the most upstream part presents a coarsening of the reach, downstream trains of bedload sheets manifesting themselves as bands of coarse and fine grains are clearly visible in the downstream reach. Central picture: a view from the outlet in the upstream direction; the alternation of bands of coarse grains and fines is very pronounced. Right picture: the final step of a sequence of bedload sheets' trains, namely tha maximum aggradation and paving of the reach.

The same also applies to areas homogeneously covered by fines. In Run 1 and Run 2 these areas had a limited extension that made us label them patches, whereas during same phases of Run 3 these areas were much longer. A unique area of fines could cover almost the entire flume length, as for instance in the last picture of figure 4.27 where the fining of the surface concerned the entire framed area (about 3 meters long). This efficient bed fining corresponded to the peaks of the signal % Fine, which in turn were associated to peaks of $Q_{s,out}$ (bottom plot of figure 4.25): an intense bed erosion took place.

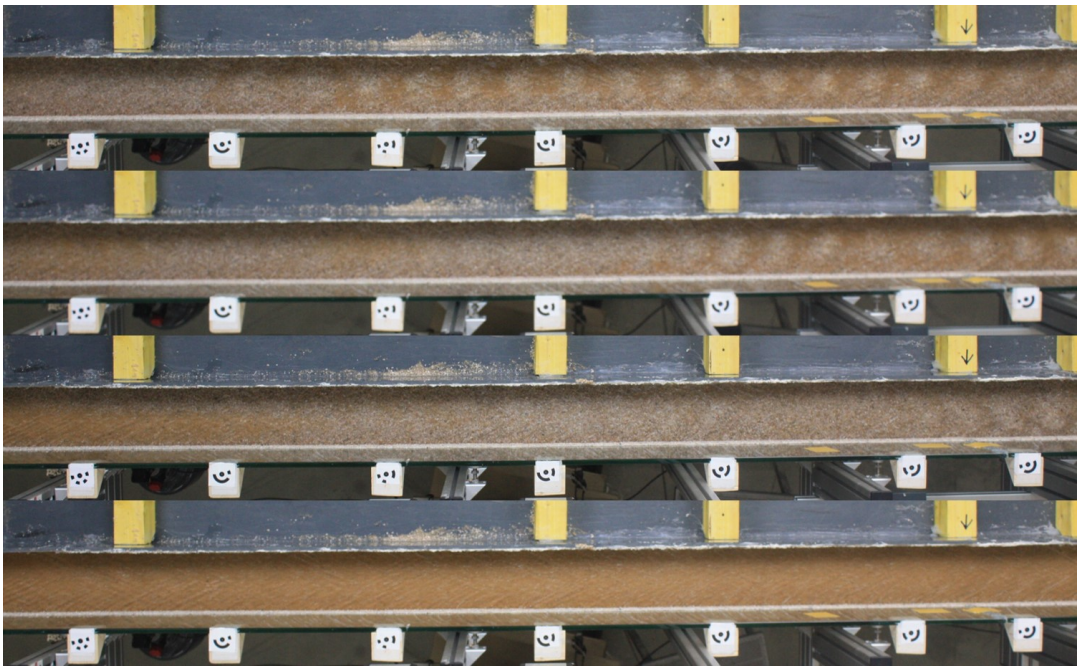

FIGURE 4.27: Run3. Top view of the central part of the flume, flow is from left to right. The time interval between the first photo, at the top of the figure, and the last one, at the bottom of the figure is about 30 minutes. In this half an hour, as well as for all run's duration, photos were taken with a frequency of one per minute.

We observed bedload sheets migrating rapidly downstream, hence our experimental observations are in accordance wit other laboratory and field observations (see subsections 2.3.1 and 2.4.2) which documented the same features in bedload sheets propagation. Moreover our observations on bedload sheets migration are confirmed by mathematical (Stecca et al., 2014) and numerical (Stecca et al., 2015) results, as well as by our stability analysis (chapter 3) for which sorting waves (nothing but bedload sheets!) propagate downstream at a fast pace, a wave speed faster than the one of topographic perturbations (bed waves), see section 3.5, in particular the comparison between figure 3.7 and figure 3.8. We could not measure the celerity of migration of these sorting waves of the bedload sheets kind, however their fast downstream migration was clear; that makes us affirm that the patterns we observed where not antidunes with the addition of sorting[5]. As for the wavelength of our bedload sheets we measured it from the aerial photos (see for instance the top pictures of figure 4.27) and we found quite short wavelength of the order of 12 cm; whereby having an average water depth of 1.4 cm the resulting wavenumber is found of about 1, which is a relatively large value. Unfortunately the measurements of the amplitude of bedload sheets was indeed a tricky operation and we could not carry it out.

We compared these characteristics of the bedload sheets observed in our Run 3 with the results of our linear stability analysis, i.e. we placed the experimental point representing Run 3 in a stability plot representing the parameter space with the values typical of Run 3. In particular the parameters relevant for stability analysis computed making use of the measured values of Run 3 are reported in table 4.5.

The parameters reported in table 4.5 are:

[5] And besides the patterns we observed were not even dunes with the addition of sorting since the flow regime was irrefutably supercritical, see table 4.4 and the central picture of figure 4.26.

TABLE 4.5: The parameters relevant for stability analysis with the measured values of Run 3.

K	0.8
d_{50}	0.107
Fr	1.6
C	9.3
θ/θ_c	3.682

- the wavenumber K computed with the values of wavelength and water depth reported in the previous paragraph; K is computed according to equation 3.4;
- the nondimensional grain size computed according to the last formula of equation 3.1 and making use of the dimensional average water depth and the median grain diameter of the mixture used in our experiments;
- the Froude number, see table 4.4;
- the Chézy coefficient computed according to equation 3.17;
- the ratio between the Shields stress and the critical Shields stress. The former is computed according to second formula of equation 3.2 and the latter is computed according to equation 3.53.

We performed the stability analysis described in chapter 3 in order to have a stability plot of the sorting eigenvalue, shown in figure 4.28, with which to compare the experimental data of table 4.5. Indeed the experimental point of Run 3 is in the unstable region provided by the stability analysis. Figure 4.28 shows that the unstable region for $C = 10$ do not present neither a cut-off nor a wavelength selection mechanisms: for large wavenumbers K the curves are horizontal. We illustrated this situation in section 3.5 (see figures 3.9 and 3.10). There, we first explained that the absence of cut-off and wavelength selection (flat isolines) is a sign of an inadequate functioning of the model, and then we outlined when and why this "failure" happens. We have determined that we have no cut-off nor wavelength selection for small values of the Chézy coefficient, which imply large values of roughness and small values values of water depth. Precisely we identified a lower limit for the Chézy coefficient, $C = 14$, in order to safely apply our stability analysis. Whereby the C value of our Run 3 is to low for an appropriate comparison with our stability analysis. Nonetheless the experimental data of Run 3 correspond to a positive growth rate of the sorting eigenvalue (see table 4.5 and figure 4.28) and we also had the good result of the observed rapid downstream migration in accordance with the celerity plot obtained with our stability analysis (figure 3.8).

After this discussion about bedload sheets characteristics (wavelength, propagation etc.) through the comparison of our experimental results with the tool consisting of the linear stability analysis we developed, we provide in the following further observations concerning the patterns we monitored during Run 3.

We observed bedload sheets as sequences of undulations (see top photos of figure 4.27) travelling downstream and covering all the flume length. While propagating downstream, they also evolved in the following way: coarse grains accumulated on the crests while fines were in the troughs, these alternation of bands of coarse and fine sediments moved downstream, and at the upstream location previously occupied by the undulations the bed coarsened. This process was as if the troughs with fines got filled with coarse material (see figure 4.27). Indeed bedload sheets passage was an efficient and rapid coarsening of the bed surface accompanied by

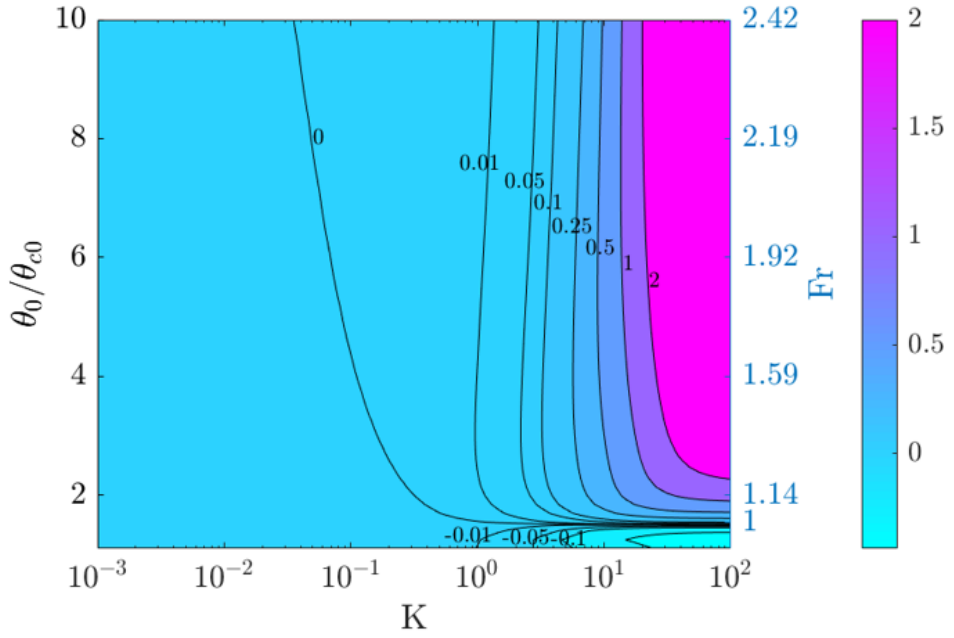

FIGURE 4.28: The linear stability analysis for sorting waves applied to Run 3. The growth rate of the sorting eigenvalue is represented in a stability plot for the quasi-steady simulation performed for a value of the Chézy coefficient of 10.

aggradation of the bed as illustrated in the description of figure 4.25. This process stopped when maximum aggradation was attained and subsequent strong erosion episodes took place (see bottom picture of figure 4.27). In this process it appeared obvious that also vertical sorting occurred since the other side of the bed surface coarsening was fine material embedded.

Finally we can conclude that in this narrow flume configuration not only surface sorting was very efficient, as showed by the great variations in the time series of the bed surface sediment composition (figure 4.24), but also vertical sorting took place. Actually the samples of the substrate taken at the end of the run had a different composition from the well-mixed sediment mixture (feeding sediment mixture, 4.1.2) with which the initial bed state was constituted. Precisely the substrate samples composition differed from the mixture (60% coarse, 40% fines) of about $\pm$25%. However our sampling technique was unfortunately rather rough (see section 4.4) and we did not sample the substrate making numerous layers; however when we sectioned the bed for sampling it was not visible a stratigraphy. Hence we can just state that relevant vertical sorting took place during Run 3, but our sampling procedure did not allow us to quantify it accurately.

4.5.4 Runs' comparison

Here we compare the three runs, mainly analysing the signal of each morphodynamic bed variable for the three runs together. For the set of the three runs, indicators and descriptive statistics of each morphodynamic bed variable are provided as well.

All the runs presented significant fluctuations of the "bed system" signals (% Coarse, its dual % Fine, % Area Fine, Slope, $Q_{s,out}$), however the amplitude and the main statistical features of such fluctuations varied from one run to another.

We start this analysis dealing with the % Coarse signal; figure 4.29 gathers the three runs' % Coarse signals; the basic indicators and descriptive statistics of these signals are reported in table 4.6 and graphically represented in box plots of figure 4.30.

TABLE 4.6: All runs. Descriptive statistics for the signal % Coarse.

		Run 1	Run 2	Run 3
% coarse	average	25.5	21.2	19.5
	median	25.2	19.8	17.7
	variance	28.5	77.5	92.7
	25^{th} percentile	21.9	14.8	12.7
	75^{th} percentile	28.6	26.0	24.1
	min	11.7	2.0	4.6
	max	47.4	61.1	75.2
	range	35.8	59.1	70.5
	coefficient of variation	0.2	0.4	0.5

The data summarised in table 4.6 show a precise trend of "increasing variability" of the bed signal % Coarse from Run 1 to Run 3; for instance the variance and the range increases significantly going from Run 1 to Run 3. In order to better depict this fact, we introduced a standardised measure of dispersion of the data making up the time series: the coefficient of variation (also named relative standard deviation). It is defined as the ratio of the standard deviation to the mean and it represents the extension of the variability in relation to the mean. The coefficient of variation is reported in table 4.6 as well; it represents a comprehensive indicator and it shows the trend we have just described: an increase of the variability of the signal % Coarse from the least confined flow configuration to the more confined one.

Indeed Run 3 was characterized by the most intense process of paving and fining of the bed, as described in subsection 4.5.3: with respect to the low confined flow configurations, areas covered homogeneously by coarse grains, and similarly by fines, were longer and occupied the entire flume.

When the channel had instead some lateral space and then could wander and adjust its width, areas covered homogeneously by coarse grains, and similarly by fines, were less extended (patch scale rather than reach scale); we did not observed the entire reach almost totally covered by coarse grains or similarly by fines.

The same trend of increasing variability characterized the slope signal; figure 4.31 gathers the three runs' slope signals; the basic indicators and descriptive statistics of these signals are reported in table 4.7 and graphically represented in box plots of figure 4.32.

From Run 1 to Run 3 the slope signal is characterized by a relevant increase of the range, the variance, and the more comprehensive coefficient of variation (see figure 4.31 and table 4.7). Run 3 showed the highest variability of the slope signal, being the experiment with the most intense and efficient aggradation and degradation process. Indeed in this confined flow configuration we documented the bed "breathing": the bed elevation increased and decreased significantly. Altimetric variations were relevant corresponding to a process of "storage and release" of sediments. Moreover altimetric variations were accompanied by vertical sorting; Run 3 was the only experiments presenting vertical sorting. The highest slope variability goes therefore

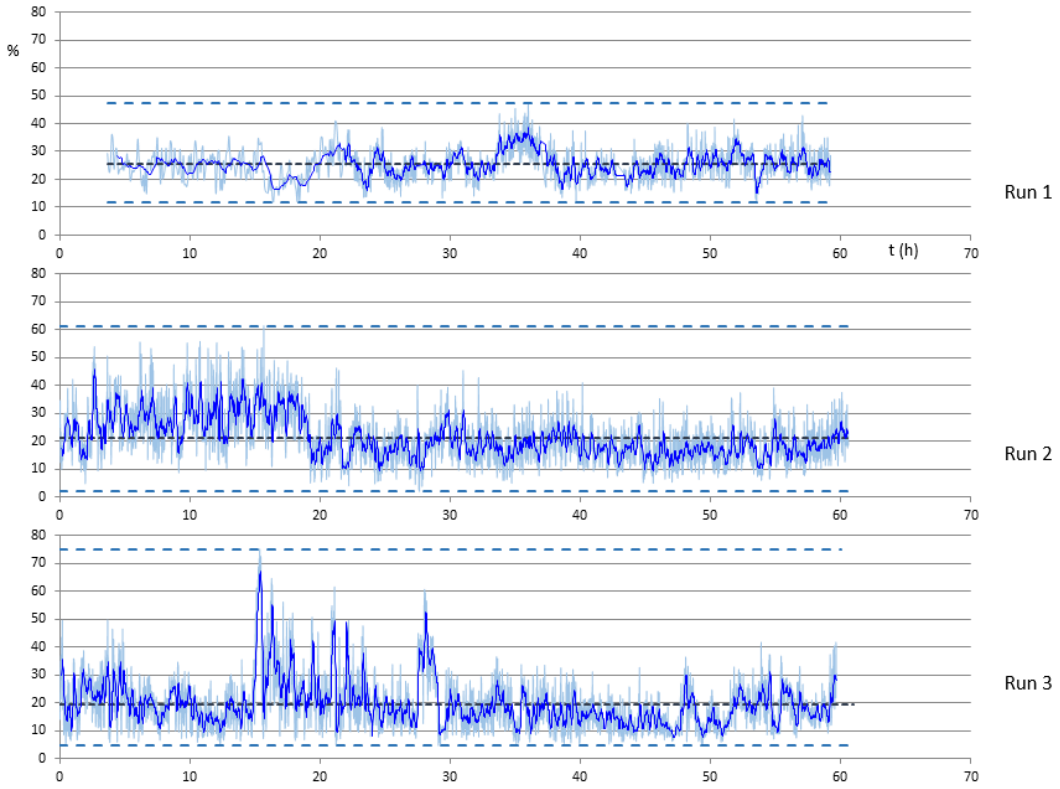

FIGURE 4.29: All runs. The signal % Coarse.

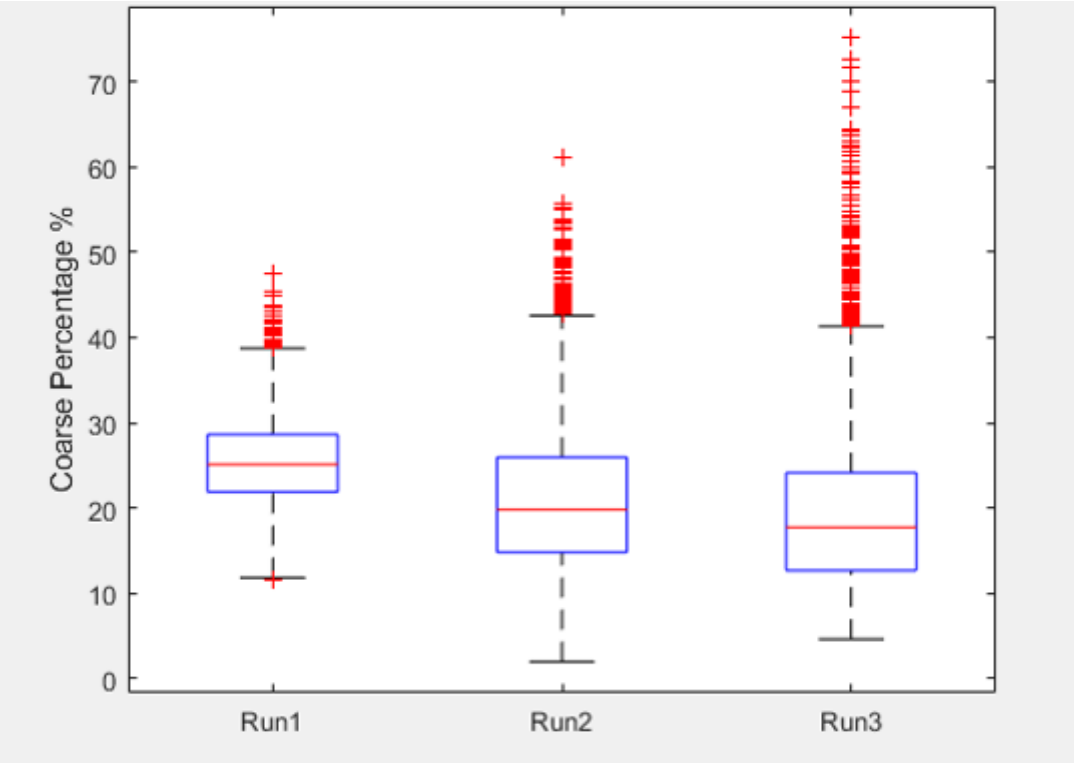

FIGURE 4.30: All runs. Box plots of the signal % Coarse.

together with vertical sorting.

As for the signal of the outlet solid discharge; figure 4.33 gathers the three runs'

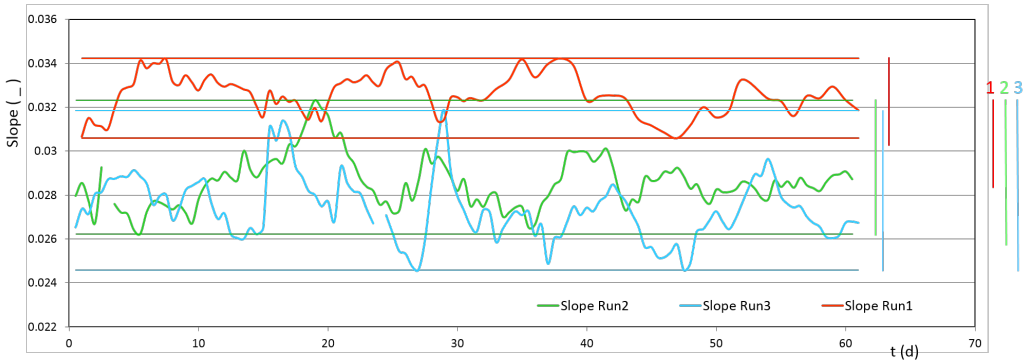

FIGURE 4.31: All runs. The slope signal.

TABLE 4.7: All runs. Descriptive statistics for the slope signal.

		Run 1	Run 2	Run 3
slope (_)	average	0.0326	0.0286	0.0274
	median	0.3270	0.0285	0.0273
	variance	7.94×10^{-7}	1.33×10^{-6}	1.96×10^{-6}
	25^{th} percentile	0.0317	0.0277	0.0265
	75^{th} percentile	0.0328	0.0292	0.0282
	min	0.0306	0.0262	0.0246
	max	0.0342	0.0323	0.0318
	range	0.0036	0.0061	0.0073
	coefficient of variation	0.0270	0.0400	0.0510

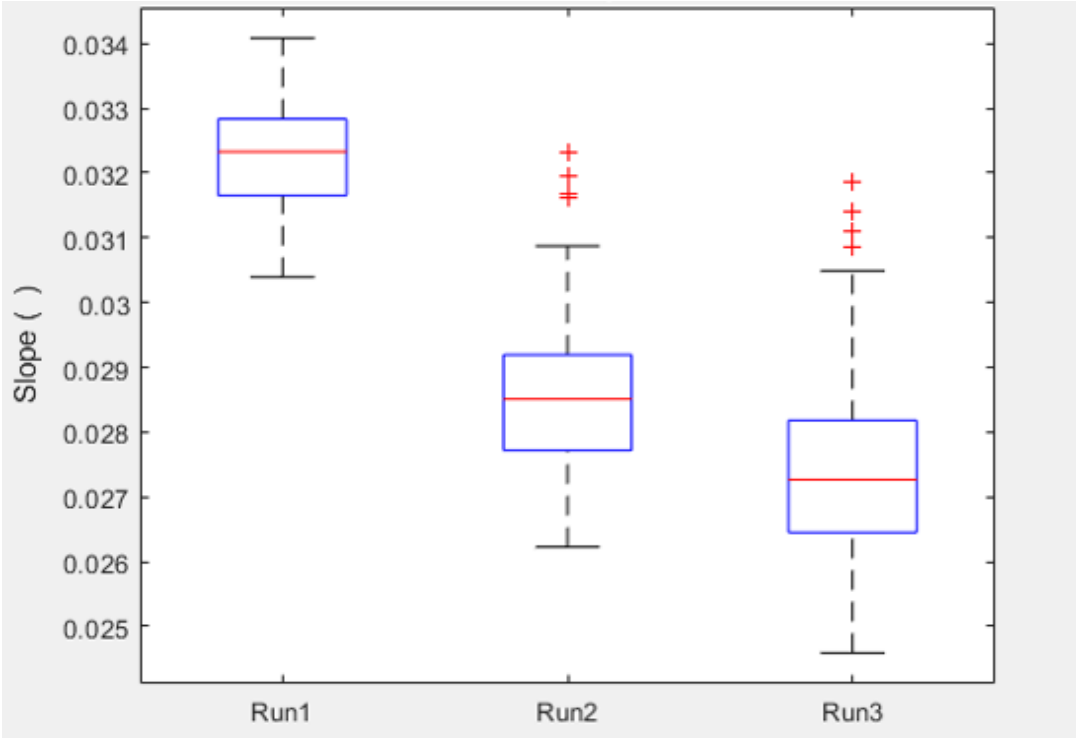

FIGURE 4.32: All runs. Box plots of the slope signal.

signals of the outlet solid discharge; the basic indicators and descriptive statistics of these signals are reported in table 4.8 and graphically represented in box plots of figure 4.34.

With respect to the signal % Coarse and to the slope signal, the signal of the outlet solid discharge presented a different behaviour: the variance and the more comprehensive coefficient of variation (table 4.8) do not present an increasing trend from Run 1 to Run 3. Precisely the coefficient of variation of the signal $Q_{s,out}$ has a high value for Run 1, a low value for Run 2, and a high value for Run 3, as shown in figure 4.35.

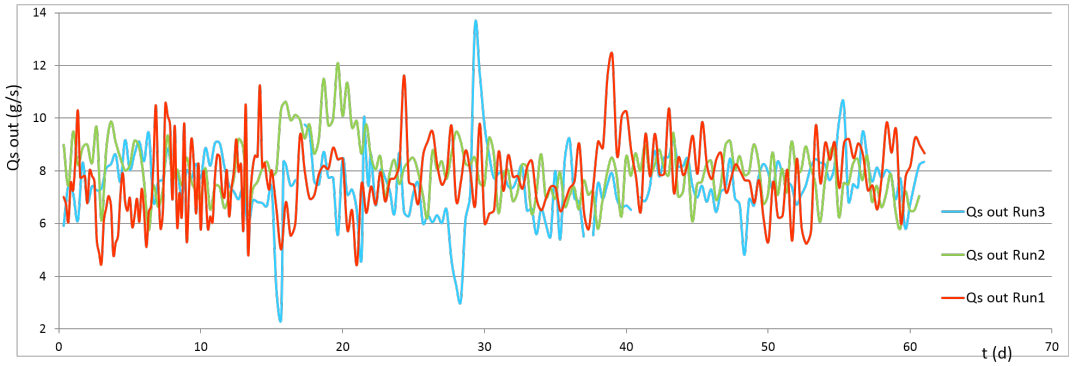

FIGURE 4.33: All runs. The signal of the outlet solid discharge.

TABLE 4.8: All runs. Descriptive statistics for the signal of the outlet solid discharge.

		Run 1	Run 2	Run 3
$Q_{s,out}$ (g/s)	average	7.64	8.04	7.47
	median	7.64	8.01	7.48
	variance	1.94	1.24	1.75
	25^{th} percentile	6.68	7.22	6.82
	75^{th} percentile	8.47	8.65	8.21
	min	4.42	5.74	2.41
	max	12.40	12.09	13.52
	range	7.98	6.35	11.11
	coefficient of variation	0.18	0.14	0.18

The trend of the variability of the $Q_{s,out}$ signal can be interpreted making use of the concept of storage and release of sediments. When the outlet solid discharge has a high variability (the $Q_{s,out}$ coefficient of variation has a high value) the process of storage and release of sediments is important, efficient. Actually if the bed is in conditions that promote a stockage of sediments then released after a while, the system encounters conditions of intermittent sediment transfer, or at least a sediment transfer that varies a lot in terms of magnitude and occurrence. On the contrary, when $Q_{s,out}$ has a low variability the process of storage and release is less important, whereas the solid transfer has an optimum. In other words, in this second case the bed has not relevant stocks of sediments cyclically formed and destroyed by the flow, and thus the channel is not affected by relevant discontinuous input of sediments, the channel rather transfers downstream a solid discharge not highly varying in terms of magnitude and occurrence. An optimum sediment transfer goes with a minimum storage and release process.

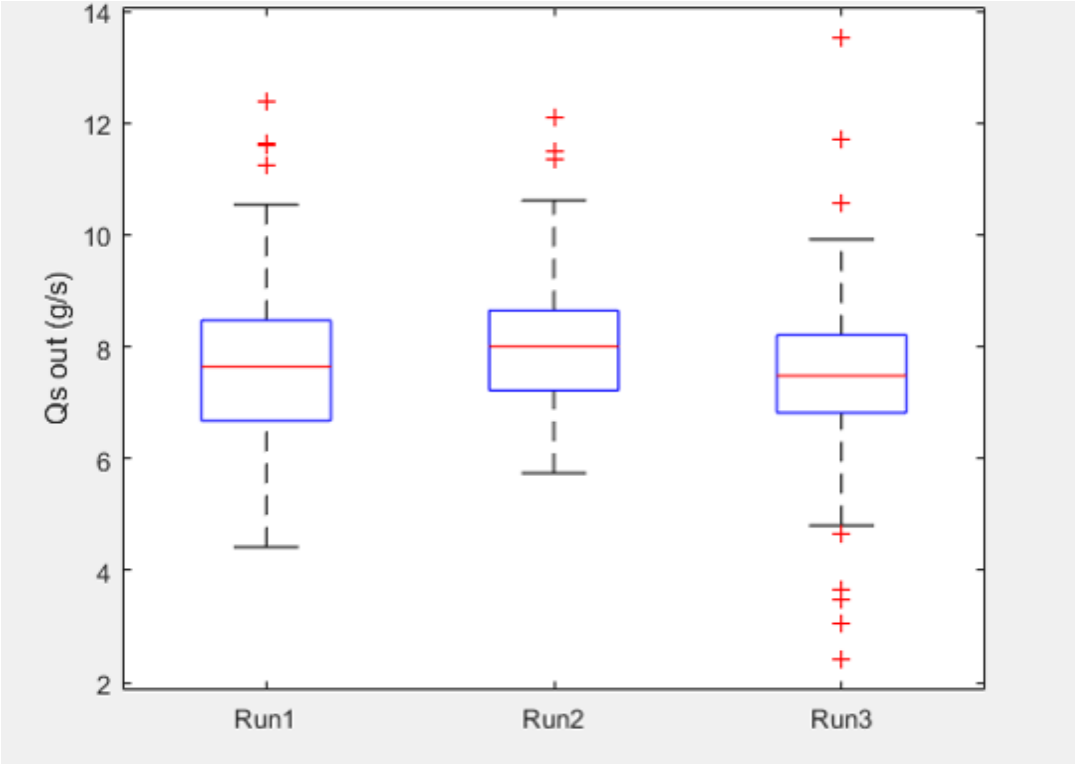

FIGURE 4.34: All runs. Box plots of the signal of the outlet solid discharge.

Run 1 and Run 3 were characterized by a high variability of $Q_{s,out}$ and by an efficient process of storage and release. However this effective storage and release process took place in different ways and with different features in these two experiments.

The significant storage and release process in Run 3 was characterized by an “altimetric functioning": the formation and destruction of sediments stocks occurred with altimetric variations and without variation in the spanwise direction. Evidences of this "altimetric functioning" were: the most intense and efficient aggradation and degradation process; the highest variability of slope; the most intense and efficient coarsening and fining of the bed surface (the first associated to aggradation and the second associated to degradation respectively); the substrate samples which proved the presence of vertical sorting.

The relevant storage and release process occurring in Run 1 took place in a very different, even opposite, way that we labelled "planimetric functioning". In this wide, unconfined flow configuration no vertical sorting took place; the variability of the bed slope was the lowest with respect to the other experiments; and above all a large lateral space let the main channel wander and build, destroy and rebuild depositional patterns.

In Run 2 the process of storage and release of sediments was not efficient nor particularly relevant since there was not neither a strong altimetric functioning, nor a strong planimetric one.

With respect to Run 1 and Run 3, Run 2 is the test in our set of experiments where the lateral constraint and the flow width (active channel width) implied the minimum storage and release of sediments which corresponded to an optimum downstream sediment transfer. In other words, with respect to Run 1 and Run 3, Run 2

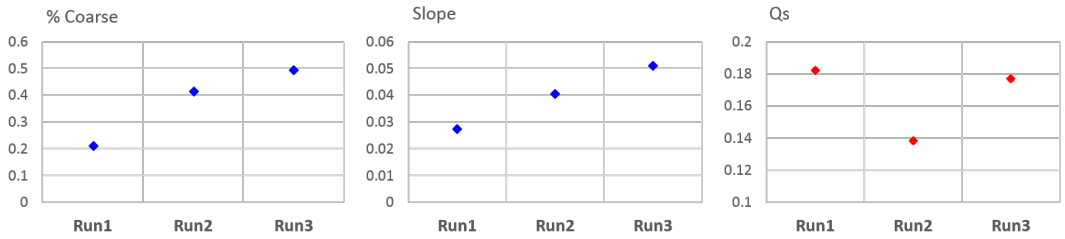

FIGURE 4.35: All runs. The coefficient of variation for the signals % Coarse, slope and outlet solid discharge.

was the configuration in which the main channel was the most efficient from a sediment transfer point of view; the channel conveyed sediments at the outlet section of the reach (i.e. the outlet of the flume) with the minimum solid discharge fluctuation.

But was Run 2 the configuration with the optimum sediment transfer and minimum stockage and release of all? Or rather Run 2 was "towards" the "most" optimum transfer and minimum stockage and release configuration? In other words, by extending the issue of optimum transfer and minimum stockage and release not only to our set of three experiments, we wondered what is the channel morphology that transfers the sediments downstream in the more "constant" way, hence not having a bed with periodical huge stocks of sediments. Which is the channel morphology with the less varying channel characteristics?

We observed that a braided pattern (Run 1), characterized by multi-threads channels and abundant medial bars, represented a morphology where the main active channel is ephemeral, this channel builds and wipes away sediment deposits, thus making the sediment transfer highly fluctuating.

We can then assume that a single thread channel morphology ensures a less fluctuating downstream sediment transfer; however a single thread channel like the confined flow configuration of Run 3 represented a case in which the sediments cyclically embedded and released made fluctuate significantly the sediment transport rate.

It is reasonable to assume that the optimum transfer occurs when the three following features are present simultaneously: a single thread channel morphology is present; a moderate lateral mobility of the channel is present (if not Run 3 configuration is recovered); the lateral wandering of the channel is anyway limited (if not we recover a braiding system case). We hence hypothesised that a single thread channel morphology as the one consisting in a channel with alternate bars is the intermediate flow configuration that makes the channel more stable and suitable to convey sediments downstream in a less fluctuating way.

Indeed our Run 2 configuration had an intermediate flow constraint with respect to Run 1 (braiding system) and Run 3 (confined single thread channel with intense altimetric variations), but it did not reproduce an alternate bar morphology, it was rather a central/multiple bars configuration and thus a configuration still quite close to the configuration of Run 1. We supposed therefore that with the external conditions characterising our set of experiments (feeding rates, slope, sediment mixture) an alternate bars configuration would take place reproducing an intermediate width with respect to Run 2 and Run 3.

Unfortunately we could not perform a fourth experiment with such conditions in the context of this thesis work. However we decided to verify that effectively Run

2 was too wide and Run 3 was too narrow for an alternate bars configuration. We carried out these checking performing a linear stability analysis for bars formation for both Run 2 and Run 3. Moreover we looked for other researchers studies on sediment transport rate in alternate bars configurations compared with sediment transport rate in different morphologies.

As for the check on bars formation in Run 2 and Run 3 configurations, we performed a linear stability analysis based on the classical theory of bars morphodynamics regime, indeed the regime controlled by the width-to-depth parameter.

For the theory of free bars formation we referred to Colombini et al. (1987) and for implementing such theory we used a free, open source matlab code developed by the researchers of the University of Trento, this tool has been named TREMTO (Theoretical RivEr Morphodynamics TOol).

Here we just recall the key dimensionless parameters of the bars formation theory: β, θ, and d_s.

β is a measure of the channel width-to-depth ratio

$$\beta = \frac{W_0^*}{2D_0^*}$$

where W_0^* and D_0^* are respectively the dimensional channel width and water depth of the reference uniform flow.

θ is the Shields parameter

$$\theta = \frac{\tau^*}{(\rho_s - \rho)g d_{50}^*}$$

in which τ^* is the dimensional mean shear stress that the flow exerts on the bottom and d_{50}^* is the median value of the bed surface grain size distribution.

d_s is the so called relative roughness: the ratio between the mean sediment diameter and the reference uniform water depth, expressed by:

$$d_s = \frac{d_{50}^*}{D_0^*}$$

Hence, getting back to dimensional quantities, by performing a linear stability analysis for bars we just want to know if in Run 2 and Run 3 bars are likely to form for our given discharge, slope, width, and grain size.

We apply first this analysis to Run 2.

First of all, we determined that the flume length is sufficient for bars formation: bars' wavelength is much shorter than flume length. Thus, if bars did not form the reason was not the fact that the flume was not long enough, the reason was rather that the flow configuration (water depth, flume width, average slope, grain size of the mixture) had not the characteristics for bar regime.

Basically, we followed two criteria to determine bars' wavelength, λ : one criterion comes from literature about experimental observations on bars both in the field and in the flume, and the second one comes from the outcomes of the stability analysis we performed. According to the first criterion the wavelength of migrating bars ranges between 7 and 9 times the channel width, thus our flume was long enough.

The second criterion will be illustrated in a little while, but we anticipate that according to this criterion too our flume length was greater than bars' wavelength.

We performed the linear stability analysis using the TREMTO tool whose input data are the following dimensional quantities: the water discharge, the channel width, the mean grain size, and the slope; for which we set respectively, Q=0.00055 m^3/s, W=0.25 m, d_{mean}=1.5 mm (namely the d_{50} of our bimodal mixture), S=0.0286 (the average slope of Run 2, see table 4.4). The code requires the user to specify also the roughness formula and the bedload formula to utilise, and we set respectively the Chézy formula and the Wong and Parker (2006) relation. Figure 4.36 collects the main output of such analysis.

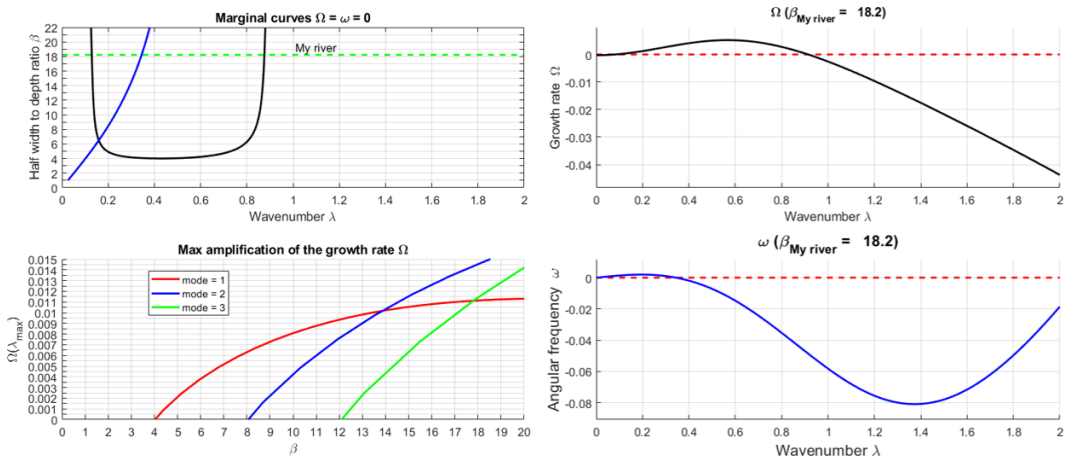

FIGURE 4.36: Main results of the linear stability analysis for bars formation performed for Run 2. The plots are obtained using the TREMTO tool.

The top left panel represents in the $\beta - \lambda$ plane the marginal curves of both the growth rate Ω in black, and the angular frequency ω, in blue; it represents the β value of Run 2 configuration as well, the green dashed line. On the left of the blue curve we have ω>0, on the right ω<0, see the bottom right panel. Inside the region bounded by the black curve we have Ω>0, outside that region Ω<0, see the top right panel. The shape of the black marginal curve is particularly relevant because it suggests that the channel aspect ratio is a key parameter for bar stability, because no free bars could form for relatively narrow and deep channel, i.e. having $\beta < \beta_c$ regardless of the length of the bars. Starting from a subcritical condition (flat bed) and increasing β, at limit of $\beta = \beta_c$ bars with $\lambda = \lambda_c$ start to develop. Note that while β_c has a well defined limit, λ_c has a smooth limit and can be found into a range.

In our case $\beta_c = 4$ and β my river =18.2, that is β my river > β_c and thus bars can form. However, the point is which kind of bars since β my river is significantly higher than β_c, meaning that we deal with a quite wide configuration.

To answer this question we just have to look at the plot in the bottom left panel. For $\beta = \beta$ my river = 18.2 all the three bar transversal modes are excited: m=1 alternate bars, m=2 mid-channel bars, m=3 multiple bars. More precisely for β= 18.2, m=2 is the more unstable mode, m=1 and m=3 are less unstable (and they have comparable values of the growth rate Ω, exactly we have $\Omega_{m2} > \Omega_{m3} > \Omega_{m1}$); in other words the mode of alternate bars is the less unstable, thus the less likely to take place.

We can conclude that the configuration of Run 2 (with the mixture we used, the

water discharge we set, and the slope we had) had a too large width and a too small water depth in order to have alternate bars.

Furthermore, as previously anticipated, the linear stability analysis confirmed that the flume length is greater than the bars' wavelength. Indeed, the range of unstable wavenumber λ (see the top left panel of figure 4.36) implies dimensional wavelength (much) shorter than our flume length ($\lambda = \pi W^*/L^*$ in which W^* = dimensional width = 0.25 m, L^* = dimensional wavelength (m)).

Lastly, another evidence that Run 2's configuration was too wide for alternate bars came from experimental observations from Run 2's videos. Actually, we took qualitative videos all runs long with a web-cam framing all the flume. These videos did not aim at quantitative measurements, they just provided movies of the runs.

Run 2's video showed sediment patterns that at first sight could be interpreted as alternate bars. But a deeper observation of these supposed bars revealed the ephemeral nature of such sediment patterns.

We could not observe a dimensional migration velocity to compare with the angular frequency resulting from the stability analysis. The dimensional migration velocity was not possible to observe because the supposed bars did not have a front which had a displacement in a certain time interval. The supposed bars did not migrate, they just had a short "life time" (from 12 to 33 minutes) and they were "built and destroyed" at a certain location in the flume.

In conclusion, Run 2 was a wide flow configuration in which the depositional patterns observed were not alternate bars.

On the other hand, performing a similar linear stability analysis for bars formation applied to Run 3's configuration, we found out that in this case the channel was too narrow for the formation of bars, figure 4.37.

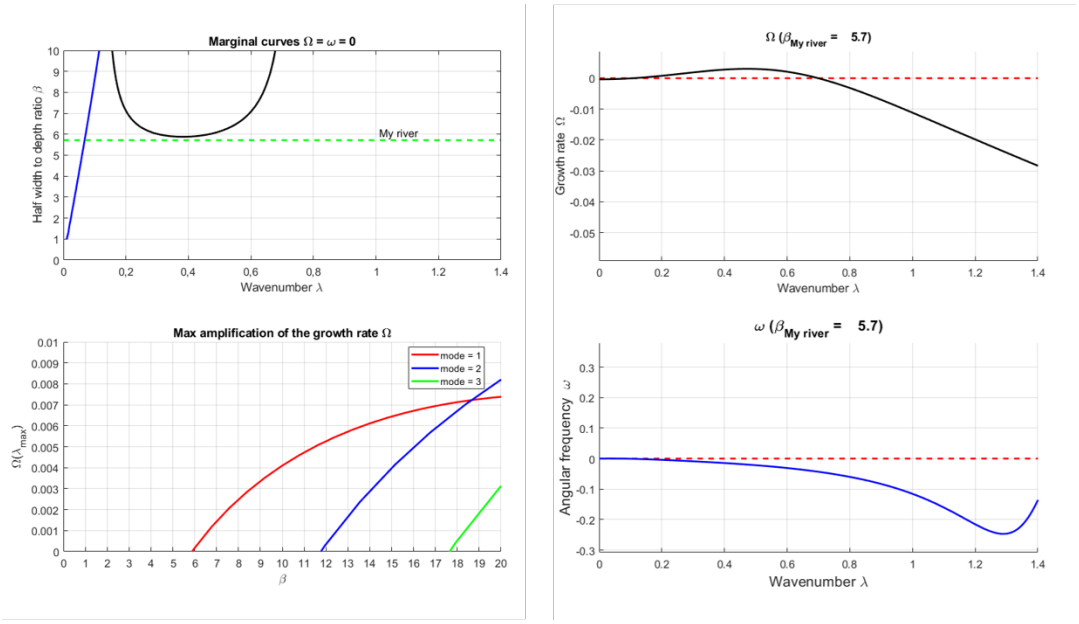

FIGURE 4.37: Main results of the linear stability analysis for bars formation performed for Run 3. The plots are obtained using the TREMTO tool.

The essential information that made us conclude that bars could not form for the conditions charcterizing Run 3 is contained is in the top left plot of figure 4.37:

$\beta < \beta_c$, the dashed green line representing the width-to-depth ratio of Run 3 configuration is smaller than the critical width-to-depth ratio.

Hence we confirmed that our runs configurations did not reproduced an alternate bars regime, the regime we suppose to be the most efficient is downstream sediment transfer having a less varying channel morphology which can convey the solid discharge with limited fluctuations with respect to wider and narrower flow configurations. Not being able to include in our experimental activity a further run reproducing an alternate bars configuration, we just looked in literature studies dealing with sediment transport in bars regime and we find an inspiring cue in the work by Francalanci et al. (2012). This study analyses sediment transport depending on the morphology where it takes place and it provides an analysis that can be linked to our concept optimum sediment transfer and minimum stockage and release concept applied to a bar regime.

Francalanci et al. (2012) study how alternate bars affect sediment transport and flow resistance in gravel bed rivers. The authors wonder what is the effect of the complex 3d morphology of alternate bars both on total drag resistance and sediment transport rate. In order to answer this question they carry out a comparison between a 3D numerical model with well developed alternate bars and an equivalent 1D case of flat bed (equivalent in terms of macroscopic roughness, slope, and mean velocity). In the two cases they infer the sediment transport rate and the flow resistance (the comparison is enabled by the fact that for the numerical model with bars the resulting sediment transport and the flow resistance are averaged over the bar wavelength).

We just focused on results by Francalanci et al. (2012) concerning sediment transport: the authors conclude that alternate bars strongly enhance bedload transport at low Shields stress, i.e. the flow conditions slightly greater than the conditions of incipient motion (exactly the flow conditions we are interested in dealing with sorting, see table 4.4).

We found this outcome in accordance with our hint about optimum sediment transfer characterising the bar morphology among all the other morphologies typical of gravel bed rivers (namely the single thread channel with a highly confined flow configuration and the braided configuration). Indeed optimum sediment transfer can be interpreted either way: considering the magnitude of the sediment transport rate (Francalanci et al., 2012) or considering fluctuations and possible intermittency of the sediment transport rate (as we suggested).

4.6 Conclusions and perspectives

We performed three long runs reproducing gravel bed rivers under dynamic equilibrium conditions.

The external conditions of the experiments were such that we could explore the effects of lateral confinement on river bed morphodynamics and in particular on grain sorting processes: feeding rates, slope, sediment mixture characteristics were kept constant; whereas the flume width, and thus flow confinement, varied.

In so doing we studied the morphodynamic evolution of different morphologies typical of gravel bed rivers: a braided system (Run 1), a central/multiple bars system (Run 2), and a highly confined single thread channel (Run 3).

In each experiment we could describe the morphodynamics of the overall "bed system" by establishing feedbacks between the bed slope, the sediment transport rate, the active channel width, and the sorting patterns.

In the morphology consisting in a confined flow (Run 3) we documented bedload sheets; we could confirm previous experimental observations of this kind of bed forms; and we could thoroughly monitor the bed surface sediment sorting characteristic of bedload sheets.

Lastly we studied the bedload sheets documented in Run 3 making use of our analytical model: actually the linear stability analysis we developed and we dealt with in chapter 3 was able to catch the morphodynamic instabilities sorting dominated, nothing but bedload sheets. Nonetheless the comparison between our experimental observations on bedload sheets and our stability analysis presents some limitations: our stability analysis has a range of applicability, a range we identified in terms of values of the Chézy coefficient, and Run 3 is characterized by a Chézy value smaller than the lower limit of the range we should respect for a proper application of our stability analysis.

5 Conclusions

We present the conclusions of this thesis work in the form of answers to the research questions presented in the introduction (chapter 1).

In the context of gravel bed rivers, we wondered what are the effects of flow lateral confinement on river bed morphodynamics and in particular on grain sorting processes; and more precisely what are these effects in presence of relevant variations of the river bed's width.

We investigated this issue carrying out an extended experimental activity, reproducing three different river morphologies typical of gravel bed rivers. The three different models we reproduced in the lab were actually characterized by a width-to-depth parameter with rather distant values from one experiment to another. Indeed, our goal was not to reproduce a single morphodynamic configuration even if with varying lateral confinement (for instance a range of conditions of different lateral confinement but always in the domain of an alternate bars configuration, or always in the domain of a braiding configuration). Starting from lowest confined flow configurations (Run 1) we decreased the flume width, corresponding to an increasing flow confinement (Run 2: configuration with an intermediate flow confinement; Run 3: confined flow). Our criterion in flow constraint variations had as guiding principle the "width of the self-formed channel". We could therefore explore what happens in a river system with unchanged hydrological and sedimentological upstream conditions when its lateral alluvial bed is drastically reduced, passing from an unconfined condition to a highly confined one, the latter with the flume width exactly equal to the active channel width (previously monitored in the low confined flows of Run 1 and Run 2).

We found that the more the river is confined the more intense are the fluctuations of all the bed parameters: more intense aggradation and degradation bed states, larger fluctuations of the bed slope, larger fluctuations of the sediments transfer downstream, more efficient grain segregation processes. In particular the latter take place with very efficient cyclical phenomena of paving and fining of the bed, and the spatial scales of such coarsening and fining of the bed were much longer than the spatial scales characterising sorting patterns of low confined flow configurations. Precisely in low confined flow configurations thanks to lateral space sorting patterns can take place in a plane, both in the streamwise and in the spanwise directions. In this case the characteristic spatial scale of sorting patterns is the patch scale. Instead in a highly confined flow the characteristic spatial scale of sorting patterns is the reach scale, being the flow able to act only in the longitudinal direction. In such case however the flow "reconquers" a degree of freedom provoking vertical sorting processes otherwise negligible in low confined flow conditions.

In this context of gravel bed rivers morphodynamics thus the role played by grains

sorting mechanisms is of great importance. We wonder therefore if we could develop a simple theoretical analyses and tools able to predict morphodynamic bed river variations driven by sorting. We therefore undertook a theoretical study in the context of sorting phenomena occurring in bedload transport of heterogeneous sediments; we found this theoretical effort important since we think that mathematical modelling to natural phenomena represents an approach allowing a deeper understanding of physical processes.

With this in mind we developed a simple but effective model consisting in a 1D linear stability analysis able to catch instabilities sorting dominated. We point out the fact we were able to describe sorting waves with the simplest (but not oversimplified!) possible model: the governing equations are in a simple form, actually we used the 1D shallow-water flow model and we did not need to implement a rotational 2D flow model, and not even a 2D model.

Our model gives a theoretical context for bedload sheets by providing a theoretical justification of depicting bedload sheets as bed forms sorting driven and with negligible amplitude (as described in field and laboratory observations).

We were able as well to map the field of applicability of our analytical model and to use it in the analysis of our experimental results of Run 3, the experiments in which bedload sheets took place.

Finally, with this work and with careful reflection, but above all thanks to our own experience, we understood that mathematical modelling of both low confined flows, such as braiding systems, and very steep streams, such as steep mountain river reaches, is really challenging. Actually, mathematical modelling through "classical flow equations", both numerically solved and analytically solved, do not suit well these cases.

As for very steep streams, flow governing equations are not suitable since they adequately apply to cases with large water depth with respect to grains diameter, and thus mountain rivers reaches characterized by macro-roughness regime are very tricky conditions to model at least with "classical flow equations".

"Classical flow equations" are not appropriate for unconfined flow configurations, either, since such equations do not adequately apply to flow conditions with emerged depositional patterns. Actually, analytical theories for river morphodynamics are based on the hypothesis that the entire channel width is actively transporting sediments; whereby their application in cases where the active width is smaller than the wetted width, and even dry areas are present in the river bed, is problematic.

We can conclude that "classical flow equations" are suitable for describing river morphodynamics of sub-aqueous sediments with rather significant flow depth compared to sediments size.

For this reason the domain of mountain rivers is still a challenging and complex field of study.

A Areal fraction content techniques for surface texture measurements

Our measures and data of bed surface sediment composition are areal fraction contents and not volume fraction contents. Indeed surface texture measurements with image processing, and in particular color detection, are among the areal fraction content techniques for measuring bed surface grain size distribution.

We briefly recall that the result of whichever areal sampling technique is not equivalent to the outcome of sieving, namely the volumetric sampling (Kellerhals and Bray, 1971). Indeed sieving provides the grain size distribution, i.e. frequency by number; and no areal sampling methods are based on frequency by number, with the exception of the grid by number technique (for which the frequency of each size fraction is expressed as the percentage by number compared to the total number of particles). Therefore, only the grid by number technique leads to a grain size distribution directly comparable to the one resulting from sieving; whereas the results of other areal sampling techniques have bias with respect to the outcome of sieving. Each sample has its own bias, which often not only depends on the sampling method, but also on the grain size distribution itself (for instance the areal sampling technique by image analysis based on detecting edges of individual grains becomes less accurate when many very small grains are present).

Orru et al. (2016) provide a complete review of the works that analyzed these intrinsic differences between areal and volumetric estimates of the grain size distribution. Moreover the authors outline the conversion models needed to convert areal fraction contents into volume fraction contents. However, the use of any of these conversion models lies outside the scope of our study.

Furthermore Orru et al. (2016) illustrate the different areal sampling techniques, and we shortly recall them in order to give some context to the areal sampling technique we adopted, namely image analysis based on color detection. The earlier methods are grid sampling (Kellerhals and Bray, 1971) and wax or clay sampling (Diplas and Sutherland, 1988). In the past years several digital image analysis techniques were developped: based on detecting edges of individuals grains (McEwan et al., 2000; Sime and Ferguson, 2003; Graham et al., 2005b; Graham et al., 2005a; Graham et al., 2010); based on color detection in the RGB space (Heays et al., 2010b; Heays et al., 2010a); based on color segmentation in the Lab space (Orru et al., 2014; Orru et al., 2016; Orru and Blom, 2016); based on spatial statistics (Rubin, 2004; Warrick et al., 2009).

Among all the areal sampling techniques, we used the image analysis based on color detection, and we illustrate here its basic principles.

Objects with different colors are basically different surfaces which have different

radiant flux emitted, reflected, transmitted or received, i.e. different colors have different radiances. An RGB color digital camera divides the light spectrum into broad overlapping red, green, and blue image slices that when combined seem realistic to the eye. Thus a digital photo is a multispectral image (a spectrum for each band, also called channel). The image is divided in a discrete number of pixels, and so for each band, thereby the image is a 3D (a slice for each band) array whose dimension is given by the number of pixels. Pixels (in each band) have their pixel value called Digital Number, DN; and the DNs have corresponding band specific radiance values. Given that a bit corresponds to a binary value, a 8-bit processor handles, for each band, $2^8 = 256$ possible values for each pixel, thereby the DN is a value ranging from 0 to 255 (in each band); the RGB $(0, 0, 0)$ corresponds to black and the RGB $(255, 255, 255)$ corresponds to white. Hence it is possible to treat images as statistic population of radiance values, and thus it is possible to determine for an interrogation area of an image the histogram representing the DNs distribution.

We point out that DNs are not radiance values, and thus histograms of DNs are not histograms of radiance values; there is, however, a one-to-one correspondence between DNs and radiance values. Indeed the generic term "Digital Number" is commonly used to describe pixel values that have not yet been calibrated into physically meaningful units. To convert the DN of a pixel to radiance it is necessary to multiply the DN value by a coefficient called radiometric scale factor, as shown in the following band specific formula:

$$RAD(i) = DN(i) * RadiometricScaleFactor(i)$$

where RAD is the radiance value of the pixel in watts per steradian per square meter ($Wsr^{-1}m^{-2}$) and i stands for the number of the spectral band (red i=1, green i=2, blue i=3); the radiometric scale factor for each band can be found in the image XML metadata file under the band specific metadata.

However, in our case study we were not interested in determining the radiance value of pixels representing coarse grains and fines, we just wanted a criterion for distinguishing the two fractions, and we found that the two fractions had different DNs' values in the blue channel. Indeed in the blue channel the two fractions had DNs' histograms with the minimum overlapping (see figure 4.4). Hence we could set a threshold value on DNs as illustrated in figure A.1; pixels with DN smaller than the threshold were identified as pixels representing fine grains, whereas pixels with DN greater than the threshold were set as pixels representing coarse grains.

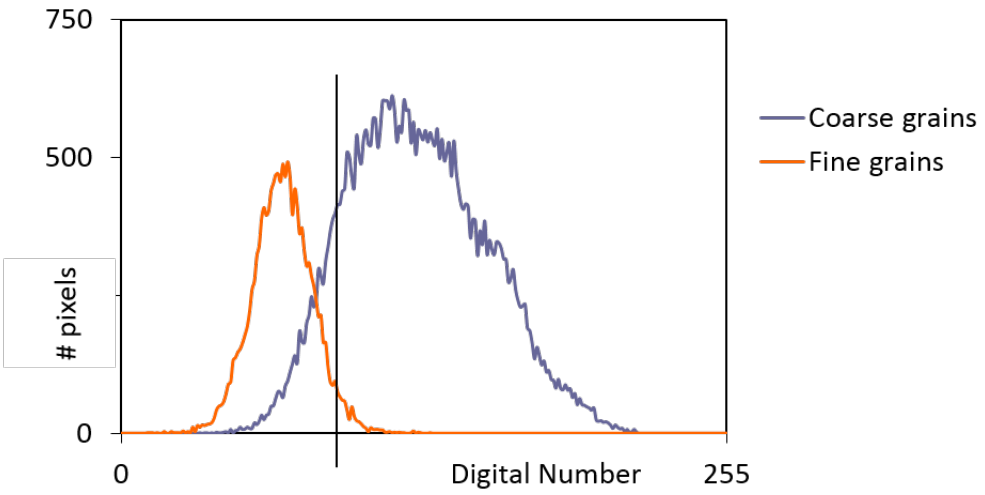

FIGURE A.1: Digital Numbers' histograms of the two fractions in the blue channel. A threshold value is set on DNs.

B Color detection operations

Here we provide the details of the image processing we performed in order to analyze the bed surface texture. In particular we illustrate the details of the operations aimed at determining the surface texture composition and at identifying homogeneous sediment patches.

The image processing workflow was the following:

- we extracted the blue channel from the original RGB image;
- the blue channel is one of the three layers of the 3D RGB array, and, as for the red channel and the green channel, it is a gray-scale image. The threshold value was set on pixels' DN of this particular gray-scale image;
- we created a binary image by applying the thresholding operation: we assigned 0 to pixels whose DN in the gray-scale image was lower than the threshold value, whereas we assigned 1 to pixels whose DN in the gray-scale image was higher than the threshold value;
- in the binary image we performed a counting of the pixels whose value was 1 (color white, pixels representing coarse grains). Then the percentage of the two kind of pixels, and thus the percentage of the two sediment fractions, was determined.

Figure B.1 shows the steps of the above workflow.

We remark that the threshold value was run specific: for Run 1 a certain threshold was applied to all the photos taken for its duration; for Run 2's photos a slight different threshold was used; for Run 3 we applied a third threshold. This because from one run to another we changed the flume width moving a flume wall, whereas the lighting system remained fixed, the lightening of the bed resulted therefore slightly different from one run to another and since light affects radiance run specific threshold was needed.

We hereby just accounted for the operations aimed at determining the bed surface fractions' percentage, but we performed not only this grain scale analysis but also a pattern scale analysis which enable us to catch patches of homogeneous sediments. As well as fractions' percentage determination, the image processing for pattern scale analysis was carried out on binary images.

For this purpose we carried out shape detection by morphological image processing based on mathematical morphology customarily used dealing with geometrical structures.

The basic functioning of these type of operations lies in the comparison between the value of each pixel and the value of its neighbors. This comparison is performed by applying a structural element as a control element, whose shape and size can be designed according to the type of image to treat. In fact, by appropriately choosing the size and shape of the neighborhood, it is possible to construct morphological operations that are sensitive to certain specific geometric structures.

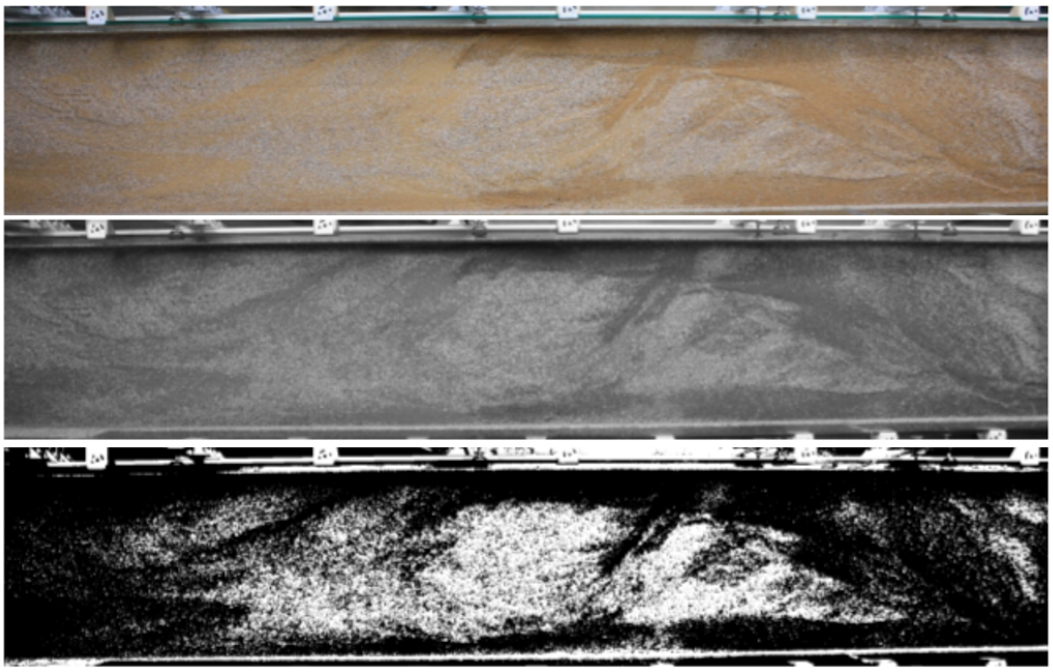

FIGURE B.1: A photo taken from the Run 1 configuration. Top figure: the original RGB photo in which coarse grains are white (light gray) and fine grains are orange. Central figure: the blue channel is a gray-scale image on which we performed thresholding. Bottom figure: the binary image resulting from the thresholded gray-scale image.

Therefore, the neighborhood is processed by a structural element (SE) whose dimension and format (diamond, square, circle) can be set ad hoc adapting it to the analyzed image.

Two fundamental morphological operations are dilation and erosion: dilation adds pixels to the contours of an object, while erosion removes them. Erosion is a filtering operation used to eliminate or thin the objects in a binary image; the details of the image that are deleted are the smaller ones detected within the structuring element. Instead, dilation is a morphological filtering operation used to increase and thicken the objects in a binary image; the dimensions of the thickening depend on the shape of the structuring element. For example, one of the simplest applications of this operation is filling the voids. The number of pixels added or removed depends on the shape and size of the structuring element.

The dilation and erosion operations are often combined in the image processing. If erosion is followed by dilation, it is called opening; whereas if dilation is followed by erosion we obtain the operation of closing.

In our code, many of these operations were carried out in a strict and precise order constituting a sequence whose outcome is the correct detection of the patches.

We found, after many tests, that the most appropriate structural element was the "diamond" shape, whose dimension was defined ad hoc depending on whether coarse patches' detection or fine patches' detection were concerned. In particular, our attention focused on the latter because it is the detection of fine patches that represents an indicator of the transport intensity and the erosion state of the bed.

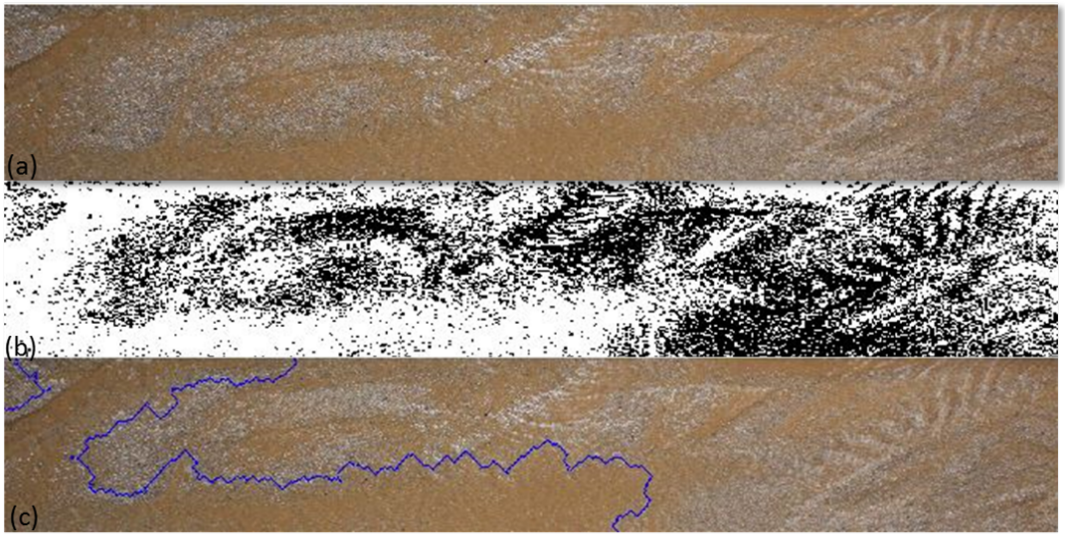

FIGURE B.2: A photo taken during Run 1. (a) The original RGB photo; coarse grains are white (light gray) and fines are orange. (b) The binary image resulting from the thresholding; coarse grains are black and fines are white (reversed with respect to figure B.2). (c) The delimitation of the detected zone of fines.

Bibliography

Allen, J. R. L. (1984). *Sedimentary structures: Their character and physical basis* (E. Science, Ed.).

Ashida, K. & Michiue, M. (1972). Study on hydraulic resistance and bed-load transport rate in alluvial streams. *Proceedings of the Japan Society of Civil Engineers*, *1972*(206), 59–69.

Ashida, K. & Michiue, M. (1973). Studies on bed-load transport rate in open channel flows. *Proceedings of the International Symposium on River Mechanics, IAHR*, (1), 407–417.

Bacchi, V., Recking, A., Eckert, N., Frey, P., Piton, G., & Naaim, M. (2014). The effects of kinetic sorting on sediment mobility on steep slopes. *Earth Surface Processes and Landforms*.

Bagnold, R. A. (1966). An approach to the sediment transport problem from general physics. U.S. Geological Survey Professional Paper 422-I.

Balmforth, N. J. & Vakil, A. (2012). Cyclic steps and roll waves in shallow water flow over an erodible bed. *695*, 35–62.

Bennett, S. & Bridge, J. (1995). The geometry and dynamics of low-relief bed forms in heterogeneous sediment in a laboratory channel, and their relationship to water flow and sediment transport. *Vol. 65A*, 29–39.

Birkhoff, G. (1954). Classification of partial differential equations. *Journal of the Society for Industrial and Applied Mathematics*, *2*(1), 57–67.

Blom, A. & Parker, G. (2004). Vertical sorting and the morphodynamics of bedform-dominated rivers: A modelling framework. *Journal of geophysical research. Earth surface*, *109*.

Blom, A., Ribberink, J. S., & Parker, G. (2008). Vertical sorting and the morphodynamics of bed form-dominated rivers: A sorting evolution model. *Journal of Geophysical Research: Earth Surface*, *113*(F1).

Bracken, L. J. & Wainwright, J. (2006). Geomorphological equilibrium: Myth and metaphor? *Transactions of the Institute of British Geographers*, *31*(2), 167–178.

Brayshaw, A. (1985). Bed microtopography and entrainment thresholds in gravel-bed rivers. *GSA Bulletin*, *96*(2), 218.

Bridge, J. S. (1993). The interaction between channel geometry, water flow, sediment transport and deposition in braided rivers. *Geological Society, London, Special Publications*, *75*(1), 13–71.

Carbonari, C. (2015). *Experimental observations on the functioning of sediment trap basins: Lspiv measurements of low subemrsion flows* (Master's thesis, Scuola di Ingegneria, Universit? degli Studi di Firenze).

Carling, P. (1999). Subaqueous gravel dunes. *69*, 534–545.

Church, M. (2006). Bed material transport and the morphology of alluvial river channels. *Annual Review of Earth and Planetary Sciences, vol. 34: 325-354*.

Church, M. & Ferguson, R. I. (2015). Morphodynamics: Rivers beyond steady state. *Water Resources Research*, *51*(4), 1883–1897.

Church, M. (2010). Mountains and montane channels. In *Sediment cascades: An integrated approach* (Chap. 2, pp. 17–53). Wiley-Blackwell.

Colombini, M. (2004). Revisiting the linear theory of sand dune formation. *Journal of Fluid Mechanics*, *502*, 1–16.

Colombini, M. & Parker, G. (1995). Longitudinal streaks. *Journal of Fluid Mechanics*, *304*, 161–183.

Colombini, M. & Stocchino, A. (2011). Ripple and dune formation in rivers. *Journal of Fluid Mechanics*, 121–131.

Colombini, M. & Stocchino, A. (2012). Three-dimensional river bed forms. *Journal of Fluid Mechanics*, *695*, 63–80.

Colombini, M., Seminara, G., & Tubino, M. (1987). Fnite-amplitude alternate bars. *Journal of Fluid Mechanics*, *181*, 213–232.

Cudden, J. R. & Hoey, T. B. (2003). The causes of bedload pulses in a gravel channel: The implications of bedload grain-size distributions. *Earth Surface Processes and Landforms*, *28*(13), 1411–1428.

Cui, Y., Parker, G., Lisle, T. E., Gott, J., Hansler-Ball, M. E., Pizzuto, J. E., … Reed, J. M. (2003). Sediment pulses in mountain rivers: 1. experiments. *Water Resources Research*, *39*(9).

Curran, J. C. & Wilcock, P. R. (2005). Effect of sand supply on transport rates in a gravel-bed channel. *Journal of Hydraulic Engineering*, *131*(11), 961–967.

Dhont, B. (2017). *Sediment pulses in a gravel-bed flume with alternate bars* (Doctoral dissertation, Ecole Polytechnique Federale de Lausanne).

Diplas, P. & Sutherland, J. A. (1988). Sampling techniques for gravel sized sediments. *Journal of Hydraulic Engineering*, *114*, 484–501.

Egiazaroff, V., I. (1965). Calculation of nonuniform sediment concentrations. *Journal of the Hydraulics Division, 1965, Vol. 91, Issue 4, 225-247*.

Einstein, H. A. (1950). The bed-load function for sediment transportation in open channel flows. *Technical Bulletin no. 1026, United States Department of Agriculture - Soil Conservation Service*.

Einstein, H. A. & Qian, N. (1953). *Transport of sediment mixtures with large ranges of grain sizes*. Berkeley, California : University of California, Institute of Engineering Research in co-operation with the Missouri River Division, Corps of Engineers, U.S. Army.

Ferguson, R. I., Prestegaard, K. L., & Ashworth, P. J. (1989). Influence of sand on hydraulics and gravel transport in a braided gravel bed river. *Water Resources Research*, *25*(4), 635–643.

Francalanci, S., Solari, L., Toffolon, M., & Parker, G. (2012). Do alternate bars affect sediment transport and flow resistance in gravel-bed rivers? *Earth Surface Processes and Landforms*, *37*(8), 866–875.

Fredsøe, J. (1974). On the development of dunes in erodible channels. *Journal of Fluid Mechanics*, *64*(1), 1–16.

Frey, P. & Church, M. (2011). Bedload: A granular phenomenon. *Earth Surface Processes and Landforms, 36, 58-69*.

Fujita, I. & Komura, S. (1994). Application of video image analysis for measurements of river-surface flows. *Proceedings of Hydraulic Engineering*, *38*, 733–738.

Fujita, I., Muste, M., & Kruger, A. (1998). Large-scale particle image velocimetry for flow analysis in hydraulic engineering applications. *Journal of Hydraulic Research*, *36*(3), 397–414.

Fujita, Y. (1989). Bar and channel formation in braided streams. In *River meandering* (Chap. 13, pp. 417–462). American Geophysical Union (AGU).

Garcia Lugo, G. A., Bertoldi, W., Henshaw, A. J., & Gurnell, A. M. (2015). The effect of lateral confinement on gravel bed river morphology. *Water Resources Research*, *51*(9), 7145–7158.

Gilbert, G. & Murphy, E. (1914). *The transportation of debris by running water*. Department of the Interior United States. Geological Survey. Professional Paper. U.S. Government Printing Office.

Gomez, B., Naff, R. L., & Hubbell, D. W. (1989). Temporal variations in bedload transport rates associated with the migration of bedforms. *Earth Surface Processes and Landforms*, *14*(2), 135–156.

Graham, D. J., Rice, S. P., & Reid, I. (2005a). A transferable method for the automated grain sizing of river gravels. *Water Resourcer Research*, *41*, W07020.

Graham, D. J., Rollet, A. J., Piegay, H., & Rice, S. P. (2010). Maximizing the accuracy of image-based surface sediment sampling techniques. *Water Resources Research*, *46*(2).

Graham, D., Reid, I., & Rice, S. (2005b). Automated sizing of coarse-grained sediments: Image-processing procedures. *Mathematical Geology*, *37*(1), 1–28.

Guy, H. P., Simons, D. B., & Richardson, E. V. (1966). Summary of alluvial channel data from flume experiments, 1956–61. *Geological Magazine, U.S. Geological Survey Professional Paper 462–I*, *104*(4), 408–409.

Hassan, M. A. & Church, M. (2000). Experiments on surface structure and partial sediment transport on a gravel bed. *Water Resources Research*, *36*(7), 1885–1895.

Heays, K., Friedrich, H., & Melville, B. W. (2010a). Advanced particle tracking for sediment movement on river beds: A laboratory study. *17th Australasian Fluid Mechanics Conference, Univ. of Auckland, Auckland, New Zealand*, 5–9.

Heays, K., Friedrich, H., & Melville, B. W. (2010b). Re-evaluation of image analysis for sedimentary process research. *International Association of Hydraulic Engineering-Asia Pacific Division, Auckland, 21?24 February, 2010*.

Hirano, M. (1971). River-bed degradation with armoring. *Transactions of the JSCE*, *1971*(195), 55–65.

Hoey, T. B. & Sutherland, A. J. (1991). Channel morphology and bedload pulses in braided rivers: A laboratory study. *Earth Surface Processes and Landforms*, *16*, 447–462.

Iseya, F. & Ikeda, H. (1987). Pulsations in bedload transport rates induced by a longitudinal sediment sorting: A flume study using sand and gravel mixtures. *Geografiska Annaler. Series A, Physical Geography, Vol. 69, No. 1 (1987), pp. 15-27 Published by: on behalf of the Wiley Swedish Society for Anthropology and Geography*.

Joseph, D. D. (1990). *Fluid dynamics of viscoelastic liquids*.

Kellerhals, R. & Bray, D. I. (1971). Sampling procedures for coarse fluvial sediments. *Journal of the Hydraulics Division*, *97*, 1165–1180.

Kinerson, D. (1990). *Surface response to sediment supply* (Master's thesis, University of California, Berkeley).

Kleinhans, M. (2002). *Sorting out sand and gravel: Sediment transport and deposition in sand-gravel bed rivers* (Doctoral dissertation, Universiteit Utrecht).

Kleinhans, M., Wilbers, A., A. De Swaaf, A., & J.H., V. D. B. (2002). Sediment supply-limited bedforms in sand-gravel bed rivers. *Journal of Sedimentary Research*, *vol. 72*(no. 5), 629–640.

Kuhnle, R. A. (1996). Unsteady transport of sand and gravel mixtures. *Advances in fluvial dynamics and Stratigraphy*, 183–201.

Kuhnle, R. A. & Southard, J. B. (1988). Bed load transport fluctuations in a gravel bed laboratory channel. *Water Resources Research*.

Kuhnle, R. A., Horton, J. K., Bennett, S. J., & Best, J. L. (2006). Bed forms in bimodal sand gravel sediments: Laboratory and field analysis. *Sedimentology*, *53*(3), 631–654.

Lane, E. W. (1954). *The importance of fluvial morphology in hydraulic engineering*. U.S. Department of the Interior, Bureau of Reclamation, Commissioner's Office.

Lanzoni, S. (2000a). Experiments on bar formation in a straight flume 1. uniform sediment. *Water Reseources Research*, *36*(11), 3337?3349.

Lanzoni, S. (2000b). Experiments on bar formation in a straight flume 2. graded sediment. *Water Resources Research*, *36*(11), 3351–3363.

Lanzoni, S. & Tubino, M. (1999). Grain sorting and bar instability. *Journal of Fluid Mechanics*, *393*, 149–174.

Lanzoni, S., Tubino, M., & Bruno, S. (1994). Formazione di barre alternate in alvei incoerenti a granulometria non uniforme. *aper presented at XXIII Convegno di Idraulica e Costruzioni Idrauliche, Naples, Italy, septembre 20-25, 1994*.

Lanzoni, S., Siviglia, A., Frascati, A, & Seminara, G. (2006). Long waves in erodible channels and morphodynamic influence. *Water Resources Research*, *vol. 42*.

Laronne, J. B. & Carson, M. A. (1976). Interrelationships between bed morphology and bed-material transport for a small, gravel-bed channel. *Sedimentology*, *23*(1), 67–85.

Le Coz, J., Jodeau, M., Hauet, A., Marchand, B., & Le Boursicaud, R. (2014). Image-based velocity and discharge measurements in field and laboratory river engineering studies using the free fudaa-lspiv software. *Proceedings of the International Conference on Fluvial Hydraulics, RIVER FLOW 2014*.

Leduc, P. (2013). *Etude experimentale de la dynamique sedimentaire des rivieres en tresses* (Doctoral dissertation, Ecole Doctorale Terre, Univers, Environnement, Universite de Grenoble).

Lisle, T. E., Ikeda, H., & Iseya, F. (1991). Formation of stationary alternate bars ina steep channel with mixed-size sediment: A flume experiment. *Earth Surface Processes and Landoforms*, *16*, 463–469.

Lisle, T. E., Iseya, F., & Ikeda, H. (1993). Response of a channel with alternate bars to a decrease in supply of mixed-size bed load: A flume experiment. *Water Resources Research*, *29*(11), 3623–3629.

Livesey, J., Bennett, S., Ashworth, P. J., & Best, J. L. (1998). Flow structure, sediment transport and bedform dynamics for a bimodal sediment mixture. *In: Klingeman, P.C., Bechta , R.L., Komar, P.D. and Bradley, J.B., eds. Gravel-bed rivers in the environment. Water Resources Publications, Colorado, USA*, 149–172.

Madej, M. A., Sutherland, D. G., Lisle, T. E., & Pryo, B. (2009). Channel responses to varying sediment input: A flume experiment modeled after redwood creek, california. *Geomorphology*, (103), 507–519.

Marti, C. & Bezzola, G. R. (2006). Bed load transport in braided gravel-bed rivers. In *Braided rivers* (pp. 199–215). John Wiley & Sons, Ltd.

McEwan, I. K., Sheen, T. M., Cunningham, G. J., & Allen, A. R. (2000). Estimating the size composition of sediment surfaces through image analysis. *Proceedings of the Institution of Civil Engineers - Water and Maritime Engineering*, *142*(4), 189–195.

Mosselman, E. (2012). *Modelling sediment transport and morphodynamics of gravel-bed rivers*. John Wiley & Sons.

Nelson, P. A., Venditti, J. G., Dietrich, W. E., Kirchner, J. W., Ikeda, H., Iseya, F., & Sklar, L. S. (2009). Response of bed surface patchiness to reductions in sediment supply. *Journal of Geophysical Research: Earth Surface*, *114*.

Nelson, P. A., McDonald, R. R., Nelson, J. M., & Dietrich, W. E. (2015). Coevolution of bed surface patchiness and channel morphology: 1. mechanisms of forced patch formation. *Journal of Geophysical Research: Earth Surface*, *120*(9), 1687–1707.

Orru, C. & Blom, A. (2016). Armor breakup and reformation in a degradational laboratory experiment. *Earth Surface Dynamics EGU*.

Orru, C., Chavarrias, V., Uijttewaal, W. S. J., & Blom, A. (2014). Image analysis for measuring the size stratification in sand-gravel laboratory experiments. *Earth Surface Dynamics*, *2*, 217–232.

Orru, C., Blom, A., Chavarrias Borras, V., Ferrara, V., & Stecca, G. (2016). A new technique for measuring the bed surface texture during flow and application to a degradational sand-gravel laboratory experiment. *Water Resources Research*, *52*(9), 7005–7022.

Parker, G. (1990). Surface-based bedload transport relation for gravel rivers. *Journal of Hydraulic Research*, *28*(4), 417–436.

Parker, G. (2008a). Chapter 17: Aggradations and degradetion of rivers transporting gravel. In *Sediment transport morphodinamics, e-book*. University of Minnesota.

Parker, G. & Klingeman, P. C. (1982). On why gravel bed streams are paved. *Water Resources Reserach*, *18*(5), 1409–1423.

Parker, G & Sutherland, A. J. (1990). Fluvial armor. *Journal of Hydraulic Research*.

Parker, G. & Toro-Escobar, C. M. (2002). Equal mobility of gravel in streams: The remains of the day. *Water Resources Research*, *38*(11), 1264.

Parker, G., Klingeman, P., & McLean, D. (1982). Bedload and size distribution in paved gravel-bed streams. *Journal of the Hydraulics Division (ASCE)*, *108*, 544–571.

Parker, G. (2008b). Transport of gravel and sediment mixtures. In *Sedimentation engineering: Theories, measurements, modeling and practice* (Chap. 3, pp. 165–251).

Parker, G., Paola, C., & Leclair, S. (2000). Probabilistic exner sediment continuity equation for mixtures with no active layer. *126*.

Pfeiffer, A. M., Finnegan, N. J., & Willenbring, J. K. (2017). Sediment supply controls equilibrium channel geometry in gravel rivers. *114*(13), 3346–3351.

Pitlick, J., Marr, J., & Pizzuto, J. (2013). Width adjustment in experimental gravel-bed channels in response to overbank flows. *Journal of Geophysical Research: Earth Surface*, *118*(2), 553–570.

Recking, A. (2006). *An experimental study of grain sorting effects on bedload* (Doctoral dissertation, INSTITUT NATIONAL DES SCIENCES APPLIQUEES DE LYON).

Recking, A. (2012). Influence of sediment supply on mountain streams bedload transport. *Geomorphology*, *vol. 175-176*, p. 139–150.

Recking, A. (2013). Relations between bed recharge and magnitude of mountain streams erosions. *Journal of Hydro-environment Research xx (2013) 1*.

Recking, A., Frey, P., Paquier, A., & Belleudy, P. (2009). An experimental investigation of mechanisms involved in bed load sheet production and migration. *Journal of Geophysical Research*.

Recking, A., Piton, G., Vazquez-Tarrio, D., & Parker, G. (2016). Quantifying the morphological print of bedload transport. *Earth Surface Processes and Landforms*, *41*(6), 809–822.

Reid, I., Frostick, L. E., & Layman, J. T. (1985). The incidence and nature of bedload transport during flood flows in coarse-grained alluvial channels. *Earth Surface Processes and Landforms*, *10*(1), 33–44.

Ribberink, J. S. (1987). *Mathematical modelling of one-dimensional morphological changes in rivers with non-uniform sediment* (Master's thesis, Civil Engineering and Geosciences, TU Delft).

Rice, S. P., Church, M., Wooldridge, C. L., & Hickin, E. J. (2009). Morphology and evolution of bars in a wandering gravel-bed river; lower fraser river, british columbia, canada. *Sedimentology*, *56*(3), 709–736.

Rohde, S., Schütz, M., Kienast, F., & Englmaier, P. (2005). River widening: An approach to restoring riparian habitats and plant species. *River Research and Applications*, *21*(10), 1075–1094.

Rohde, S., Kienast, F., & Bürgi, M. (2004). Assessing the restoration success of river widenings: A landscape approach. *Environmental Management*, *34*(4), 574–589.

Rubin, D. (2004). A simple autocorrelation algorithm for determining grain size from digital images of sediment. *Journal of Sedimentary Research*, *74*(1), 160–165.

Seminara, G. (1995). Effect of grain sorting on the formation of bedforms. *Applied Mechanics Reviews*, *48*(9).

Seminara, G., Colombini, M., & Parker, G. (1996). Nearly pure sorting waves and formation of bedload sheets. *Journal of Fluid Mechanics*, *312*, pp. 253–278.

Seminara, G. (1998). Stability and morphodynamics. *Meccanica*, *33*(1), 59–99.

Sieben, J. (1997). *Modelling of hydraulics and morphology in mountain rivers* (Doctoral dissertation, Delft University of Technology).

Sime, L. C. & Ferguson, R. I. (2003). Information on grain sizes in gravel-bed rivers by automated image analysis. *Journal of Sedimentary Research*, *73*(4), 630–636.

Singh, A., Fienberg, K., Jerolmack, D. J., Marr, J., & Foufoula-Georgiou, E. (2009). Experimental evidence for statistical scaling and intermittency in sediment transport rates. *Journal of Geophysical Research: Earth Surface*, *114*(F1).

Siviglia, A., Stecca, G., & Blom, A. (2017). Modelling of mixed-sediment morphodynamics in gravel-bed rivers using the active-layer approach: Insights from mathematical and numerical analysis. In *Gravel-bed rivers: Processes and disasters* (Chap. 26, pp. 703–728). John Wiley and Sons Ltd.

Smith, G. H. S., Nicholas, A. P., & Ferguson, R. I. (1997). Measuring and defining bimodal sediments: Problems and implications. *Water Resources Research*, *33*(5), 1179–1185.

Stecca, G., Siviglia, A., & Blom, A. (2014). Mathematical analysis of the saint-venant-hirano model for mixed-sediment morphodynamics. *Water Resources Research*.

Stecca, G., Siviglia, A., & Blom, A. (2015). An accurate numerical solution to the saint-venant-hirano model for mixed-sediment morphodynamics in rivers. *Advances in Water Resources*.

Truzzolillo, D. & Cipelletti, L. (2017). Hydrodynamic instabilities in miscible fluids. *Journal of Physics: Condensed Matter*, *30*(3), 033001.

Venditti, J. G., Nelson, J. M., & Dietrich, W. E. (2008). The domain of bedload sheets. In *Marine and river dune dynamics*.

Venditti, J. G., Nelson, P. A., Minear, J. T., Wooster, J., & Dietrich, W. E. (2012). Alternate bar response to sediment supply termination. *Journal of Geophysical Research: Earth Surface*, *117*(F2).

Venditti, J. G., Peter, A. N., Bradley, R. W., Haught, D., & Gitto, A. B. (2017). Bedforms, structures, patches, and sediment supply in gravel-bed rivers. In *Gravel-bed rivers: Processes and disasters* (Chap. 16, pp. 439–466). John Wiley and Sons Ltd.

Vericat, D., Batalla, R. J., & Garcia, C. (2006). Breakup and reestablishment of the armour layer in a large gravel-bed river below dams: The lower ebro. *Geomorphology*, *76*(1), 122 –136.

Viparelli, E., Blom, A., & Moreira, R. R. H. (2017). Modeling stratigraphy-based gravel-bed river morphodynamics. In *Gravel-bed rivers* (Chap. 23, pp. 609–637). Wiley-Blackwell.

Warrick, J., Rubin, D., Ruggiero, P., Harney, J., Draut, A., & D., B. (2009). Cobble cam: Grain-size measurements of sand to boulder from digital photographs and autocorrelation analyses. *Earth Surface Processes and Landforms*, *34*(13), 1811–1821.

Whiting, P. J., Dietrich, W. E., Leopold, L. B., Drake, T. G., & Shreve, R. L. (1988). Bedload sheets in heterogeneous sediment. *Geology*.

Wilcock, P. R. (1998). Two-fraction model of initial sediment motion in gravel-bed rivers. *Science*, *280*(5362), 410–412.

Wilcock, P. R., Kenworthy, S. T., & Crowe, J. C. (2001). Experimental study of the transport of mixed sand and gravel. *Water Resources Research*, *37*(12), 3349–3358.

Wohl, E. (2006). Human impacts to mountain streams. *Geomorphology*, *79*(3), 217 – 248. 37th Binghamton Geomorphology Symposium.

Wong, M. & Parker, G. (2006). Reanalysis and correction of bed-load relation of meyer-peter and muller using their own database. *Journal of Hydraulic Engineering*, *132*(11), 1159–1168.